FZD-528

Wissenschaftlich-Technische Berichte
FZD-528 2010 · ISSN 1437-322X

ANNUAL REPORT 2009

INSTITUTE OF ION BEAM PHYSICS AND MATERIALS RESEARCH

Wissenschaftlich-Technische Berichte
FZD – 528
2010

Annual Report 2009

Institute of Ion Beam Physics and Materials Research

Editors:

J. von Borany, V. Heera,
J. Faßbender, M. Helm, W. Möller

Cover Picture:

The inset graph shows the temperature dependence of the resistance R of a germanium (Ge) substrate (red line) and a heavily gallium (Ga) doped germanium layer (grey-blue line) measured in a four point probe arrangement (schematic as inset, U: voltage, I: current). While the Ge substrate exhibits an exponential increase of the resistance with decreasing temperature as typical for semiconductors, the heavily Ga doped Ge layer behaves "metallic" and becomes superconducting below 0.3 K. The background shows a high-resolution cross-sectional electron microscopy image of the superconducting Ge:Ga layer.

For further information see:
T. Herrmannsdörfer et al., Phys. Rev. Lett. **102**, 217 003 (2009),
reprinted at pp. 22 - 25 of this Annual Report.

Forschungszentrum Dresden - Rossendorf e.V.
Institute of Ion Beam Physics and Materials Research
P.O. Box 51 01 19
01314 Dresden
Germany

Directors	Prof. Dr. W. Möller	Prof. Dr. M. Helm	Prof. Dr. J. Faßbender
Phone	+ 49 (351) 260 2245	+ 49 (351) 260 2260	+ 49 (351) 260 3096
Fax	+ 49 (351) 260 3285	+ 49 (351) 260 3285	+ 49 (351) 260 3285
Email	w.moeller@fzd.de	m.helm@fzd.de	j.fassbender@fzd.de

Homepage http://www.fzd.de/FWI

Preface by the Directors

The Institute of Ion Beam Physics and Materials Research (IIM) is one of the six institutes of the Forschungszentrum Dresden-Rossendorf (FZD), and contributes the largest part to its Research Program "Advanced Materials", mainly in the fields of semiconductor physics and materials research using ion beams. The institute operates a national and international Ion Beam Center, which, in addition to its own scientific activities, makes available fast ion technologies to universities, other research institutes, and industry. Parts of its activities are also dedicated to exploit the infrared/THz free-electron laser at the 40 MeV superconducting electron accelerator ELBE for condensed matter research. For both facilities the institute holds EU grants for funding access of external users.

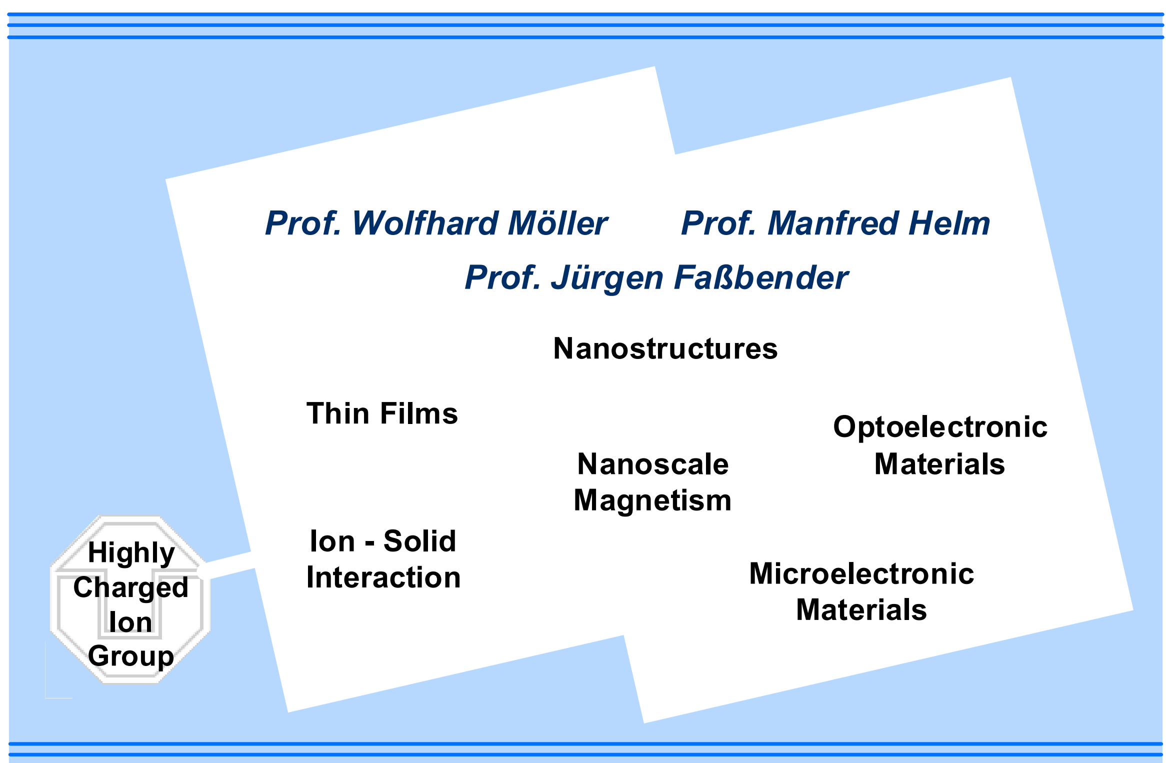

The diagram displays the presently six R&D topics of the institute, together with the associated Highly Charged Ion (HCI) Group of the TU Dresden. The research activities span a wide range of topics relevant for future information processing and energy technology, be it in the realm of nanoelectronics, optoelectronics, magnetoelectronics, spintronics, and future photovoltaics. Readers familiar with our institute will notice the appearance of a third director in the diagram, Prof. Jürgen Faßbender. He is the designated successor of Prof. Wolfhard Möller, who will retire in the course of the year 2010. In order to enable a smooth transition, Prof. Faßbender was instated, after a competitive selection process, as of Oct. 1, 2009, both as a director at the institute and as Professor for Applied Solid State Physics at the Technical University Dresden. He is a world-renowned expert for magnetic materials and structures and their modification by ion beams. Already since 2004 he was a group leader at the institute.

Highlights of last year's research are presented in this Annual Report through reprints of short papers that were published in leading international journals. In 2009, IIM staff published more than 190 papers in peer-reviewed journals, the highest number ever in its history. But since not only quantity counts, institute members were also co-authors of two publications in the prestigious journal

“Nature Materials” and of five papers in Physical Review Letters, apart from about 60 more papers published at journals with impact factor >3.

2009 has again been an excellent year with respect to third party funding. Besides the continuation of the large project "Concepts of multifunctional memories" funded by the German Federal Government, the institute was successful in acquiring the large collaborative EU grant SPIRIT (“Support of Public and Industrial Research using Ion beam Technology”) as a coordinator. This project constitutes a collaboration between the main ion beam laboratories in Europe and is granting transnational access to European users. Another essential part of funding arises from direct contracts with industry, including also local microelectronics and other high-tech industry. Thus also our funding spectrum reflects our span from successful basic science to relevant applied research.

An important milestone for the institute was the inauguration of a new 6 MV tandem accelerator on December 4, 2009, which was installed in a new, dedicated building. The machine will replace the outdated 5 MV Tandem for ion beam modification and analysis of materials, but additionally enable accelerator mass spectrometry (AMS). In relation to this, Dr. Silke Merchel, an AMS expert, joined the institute as a division head for ion beam analysis.

On the organizational side, FZD as a whole is preparing for its transition from being a member of the Leibniz Association of Research Institutes (WGL) to the Helmholtz Association of German Research Centers (HGF), which will formally take place in the beginning of 2011. This will require considerable changes in the way our research is funded, organized and administered. It will also open the way for new alliances and cooperations based on our scientific profile, and thus add to the stimulating atmosphere at the institute.

Finally we would like to cordially thank all partners, friends, and organizations who supported our progress in 2009. Special thanks are due to the Executive Board of the Forschungszentrum Dresden-Rossendorf, the Minister of Science and Arts of the Free State of Saxony, and the Minister of Education and Research of the Federal Government of Germany. Numerous partners from universities, industry and research institutes all around the world contributed essentially, and play a crucial role for the further development of the institute. Last but not least, the directors would like to thank all IIM staff for their efforts and excellent contributions in 2009.

Prof. Wolfhard Möller Prof. Manfred Helm Prof. Jürgen Faßbender

Contents

Selected Publications

Copyright Remarks 9

E.A. Zibik, T. Grange, B.A. Carpenter, N.E. Porter, R. Ferreira, G. Bastard, D. Stehr, S. Winnerl, M. Helm, H.Y. Liu, M.S. Skolnick, and L.R. Wilson 11
Long lifetimes of quantum-dot intersublevel transitions in the terahertz range

J. Seidel, L.W. Martin, Q. He, Q. Zhan, Y.H. Chu, A. Rother, M.E. Hawkridge, P. Maksymovych, P. Yu, M. Gajek, N. Balke, S.V. Kalinin, S. Gemming, F. Wang, G. Catalan, J.F. Scott, N.A. Spaldin, J. Orenstein, and R. Ramesh 16
Conduction at domain walls in oxide multiferroics

T. Herrmannsdörfer, V. Heera, O. Ignatchik, M. Uhlarz, A. Mücklich, M. Posselt, H. Reuther, B. Schmidt, K.-H. Heinig, W. Skorupa, M. Voelskow, C. Wündisch, R. Skrotzki, M. Helm, and J. Wosnitza 22
Superconducting state in a gallium-doped germanium layer at low temperatures

H. Bracht, S. Schneider, J.N. Klug, C.Y. Liao, J.L. Hansen, E.E. Haller, A.N. Larsen, D. Bougeard, M. Posselt, and C. Wündisch 26
Interstitial-mediated diffusion in germanium under proton irradiation

D. Golde, M. Wagner, D. Stehr, H. Schneider, M. Helm, A. M. Andrews, T. Roch, G. Strasser, M. Kira, and S. W. Koch 30
Fano signatures in the intersubband terahertz response of optically excited semiconductor quantum wells

A. Keller, A. Biermanns, G. Carbone, J. Grenzer, S. Facsko, O. Plantevin, R. Gago, and T. H. Metzger 34
Transition from smoothing to roughening of ion-eroded GaSb surfaces

S. Cornelius, M. Vinnichenko, N. Shevchenko, A. Rogozin, A. Kolitsch, and W. Möller 37
Achieving high free electron mobility in ZnO:Al thin films grown by reactive pulsed magnetron sputtering

M. Vinnichenko, A. Rogozin, D. Grambole, F. Munnik, A. Kolitsch, W. Möller, O. Stenzel, S. Wilbrandt, A. Chuvilin, and U. Kaiser 40
Highly dense amorphous Nb_2O_5 films with closed nanosized pores

S. Zhou, D. Bürger, M. Helm, and H. Schmidt 43
Anomalous Hall resistance in Ge:Mn systems with low Mn concentrations

G. Talut, J. Grenzer, H. Reuther, A. Shalimov, C. Baehtz, D. Novikov, and B. Walz 46
In-situ observation of secondary phase formation in Fe implanted GaN annealed in low pressure N_2 atmosphere

C. Wündisch, M. Posselt, B. Schmidt, V. Heera, T. Schumann, A. Mücklich, R. Grötzschel, W. Skorupa, T. Clarysse, E. Simoen, and H. Hortenbach 49
Millisecond flash lamp annealing of shallow implanted layers in Ge

X. Ou, R. Kögler, A. Mücklich, W. Skorupa, W. Möller, Xi Wang, and L.Vines 52
The use of nanocavities for the fabrication of ultrathin buried oxide layers

V. Beyer, B. Schmidt, K.-H. Heinig, and K.-H. Stegemann 55
Light emitting field effect transistor with two self-aligned Si nanocrystal layers

A. Kanjilal, L. Rebohle, M. Voelskow, W. Skorupa, and M. Helm ………………………………. 58
Enhanced blue-violet emission by inverse energy transfer to the Ge-related oxygen deficiency centers via Er^{3+} ions in metal-oxide semiconductor structures

M. Wagner, H. Schneider, S. Winnerl, M. Helm, T. Roch, A. M. Andrews, S. Schartner, and G. Strasser ………………………………………………………………………. 61
Resonant enhancement of second order sideband generation for intraexcitonic transitions in GaAs/AlGaAs multiple quantum wells

Statistics

Journal Publications ………………………………………………………………………... 67

Invited Conference Talks ……………………………………………………………………... 80

Conference Contributions ……………………………………………………………………. 82

Lectures / Talks ……………………………………………………………………………... 92

PhD and Diploma Theses ……………………………………………………………………. 95

Organization of Conferences / Workshops ……………………………………………………… 96

Laboratory Visits ……………………………………………………………………………… 96

Guests ………………………………………………………………………………………….. 98

AIM Visitors ……………………………………………………………………………………… 100

FEL Visitors …………………………………………………………………………………….. 101

ROBL-MRH Visitors …………………………………………………………………………... 101

Colloquium ……………………………………………………………………………………. 102

FZD Materials Science Seminar ……………………………………………………………… 103

Seminars ……………………………………………………………………………………….. 104

Projects …………………………………………………………………………………………. 105

Experimental Equipment ……………………………………………………………………... 109

User Facilities / Service ……………………………………………………………………….. 113

Organigram ……………………………………………………………………………………. 117

List of Personnel ………………………………………………………………………………. 118

Selected Publications

Copyright Remarks

The following journal articles are reprinted with kind permission from

E.A. Zibik, T. Grange, B.A. Carpenter, N.E. Porter, R. Ferreira, G. Bastard, D. Stehr, S. Winnerl, M. Helm, H.Y. Liu, M.S. Skolnick, and L.R. Wilson
Long lifetimes of quantum-dot intersublevel transitions in the terahertz range
Nature Materials, Vol. **8**, Issue 10, pp. 803-807, 2009.
Copyright 2009, Nature Publishing Group, a division of Macmillan Publishers Ltd.

J. Seidel, L.W. Martin, Q. He, Q. Zhan, Y.H. Chu, A. Rother, M.E. Hawkridge, P. Maksymovych, P. Yu, M. Gajek, N. Balke, S.V. Kalinin, S. Gemming, F. Wang, G. Catalan, J.F. Scott, N.A. Spaldin, J. Orenstein, and R. Ramesh
Conduction at domain walls in oxide multiferroics
Nature Materials, Vol. **8** , Issue 3, pp. 229-234, 2009.
Copyright 2009, Nature Publishing Group, a division of Macmillan Publishers Ltd.

T. Herrmannsdörfer, V. Heera, O. Ignatchik, M. Uhlarz, A. Mücklich, M. Posselt, H. Reuther, B. Schmidt, K.-H. Heinig, W. Skorupa, M. Voelskow, C. Wündisch, R. Skrotzki, M. Helm, and J. Wosnitza
Superconducting state in a gallium-doped germanium layer at low temperatures
Physical Review Letters, Vol. **102**, Issue 21, Art.-No.: 217 003, 2009.
Copyright 2009, The American Physical Society

H. Bracht, S. Schneider, J.N. Klug, C.Y. Liao, J.L. Hansen, E.E. Haller, A.N. Larsen, D. Bougeard, M. Posselt, and C. Wundisch
Interstitial-mediated diffusion in germanium under proton irradiation
Physical Review Letters, Vol. **103**, Issue 25, Art.-No.: 255 501, 2009.
Copyright 2009, The American Physical Society

D. Golde, M. Wagner, D. Stehr, H. Schneider, M. Helm, A. M. Andrews, T. Roch, G. Strasser, M. Kira, and S. W. Koch
Fano signatures in the intersubband terahertz response of optically excited semiconductor quantum wells
Physical Review Letters, Vol. **102**, Issue 12, Art.-No. 127 403, 2009.
Copyright 2009, The American Physical Society

A. Keller, A. Biermanns, G. Carbone, J. Grenzer, S. Facsko, O. Plantevin, R. Gago, and T. H. Metzger
Transition from smoothing to roughening of ion-eroded GaSb surfaces
Applied Physics Letters, Vol. **94**, Issue 19, Art.-No.: 193 103, 2009.
Copyright 2009, American Institute of Physics

S. Cornelius, M. Vinnichenko, N. Shevchenko, A. Rogozin, A. Kolitsch, and W. Möller
Achieving high free electron mobility in ZnO:Al thin films grown by reactive pulsed magnetron sputtering
Applied Physics Letters, Vol. **94**, Issue 4, Art.-No.: 042 103, 2009.
Copyright 2009, American Institute of Physics

M. Vinnichenko, A. Rogozin, D. Grambole, F. Munnik, A. Kolitsch, W. Möller, O. Stenzel, S. Wilbrandt, A. Chuvilin, and U. Kaiser
Highly dense amorphous Nb_2O_5 films with closed nanosized pores
Applied Physics Letters, Vol. **95**, Issue 8, Art.-No.: 081 904, 2009.
Copyright 2009, American Institute of Physics

S. Zhou, D. Bürger, M. Helm, and H. Schmidt
Anomalous Hall resistance in Ge:Mn systems with low Mn concentrations
Applied Physics Letters, Vol. **95**, Issue 17, Art.-No.: 172 103, 2009.
Copyright 2009, American Institute of Physics

G. Talut, J. Grenzer, H. Reuther, A. Shalimov, C. Baehtz, D. Novikov, and B. Walz
In-situ observation of secondary phase formation in Fe implanted GaN annealed in low pressure N_2 atmosphere
Applied Physics Letters, Vol. **95**, Issue 23, Art.-No.: 232 506, 2009.
Copyright 2009, American Institute of Physics

C. Wündisch, M. Posselt, B. Schmidt, V. Heera, T. Schumann, A. Mücklich, R. Grötzschel, W. Skorupa, T. Clarysse, E. Simoen, and H. Hortenbach
Millisecond flash lamp annealing of shallow implanted layers in Ge
Applied Physics Letters, Vol. **95**, Issue 25, Art.-No. 252 107, 2009.
Copyright 2009, American Institute of Physics

X. Ou, R. Kögler, A. Mücklich, W. Skorupa, W. Möller, Xi Wang, and L.Vines
The use of nanocavities for the fabrication of ultrathin buried oxide layers
Applied Physics Letters, Vol. **94**, Issue 1, Art.-No.: 011 903 (2009).
Copyright 2009, American Institute of Physics

V. Beyer, B. Schmidt, K.-H. Heinig, and K.-H. Stegemann
Light emitting field effect transistor with two self-aligned Si nanocrystal layers
Applied Physics Letters, Vol. **95**, Issue 19, Art.-No. 193 501, 2009.
Copyright 2009, American Institute of Physics

A. Kanjilal, L. Rebohle, M. Voelskow, W. Skorupa, and M. Helm
Enhanced blue-violet emission by inverse energy transfer to the Ge-related oxygen deficiency centers via Er^{3+} ions in metal-oxide semiconductor structures
Applied Physics Letters, Vol. **94**, Issue 5, Art.-No.: 051 903, 2009.
Copyright 2009, American Institute of Physics

M. Wagner, H. Schneider, S. Winnerl, M. Helm, T. Roch, A. M. Andrews, S. Schartner, and G. Strasser
Resonant enhancement of second order sideband generation for intraexcitonic transitions in GaAs/AlGaAs multiple quantum wells
Applied Physics Letters, Vol. **94**, Issue 24, Art.-No.: 241 105, 2009.
Copyright 2009, American Institute of Physics

nature materials

LETTERS

PUBLISHED ONLINE: 16 AUGUST 2009 | DOI: 10.1038/NMAT2511

Long lifetimes of quantum-dot intersublevel transitions in the terahertz range

E. A. Zibik[1*†], T. Grange[2*†], B. A. Carpenter[1], N. E. Porter[1], R. Ferreira[2‡], G. Bastard[2], D. Stehr[3], S. Winnerl[3], M. Helm[3], H. Y. Liu[4*], M. S. Skolnick[1] and L. R. Wilson[1‡]

Carrier relaxation is a key issue in determining the efficiency of semiconductor optoelectronic device operation. Devices incorporating semiconductor quantum dots have the potential to overcome many of the limitations of quantum-well-based devices because of the predicted long quantum-dot excited-state lifetimes. For example, the population inversion required for terahertz laser operation in quantum-well-based devices (quantum-cascade lasers[1,2]) is fundamentally limited by efficient scattering between the laser levels, which form a continuum in the plane of the quantum well. In this context, semiconductor quantum dots are a highly attractive alternative for terahertz devices, because of their intrinsic discrete energy levels. Here, we present the first measurements, and theoretical description, of the intersublevel carrier relaxation in quantum dots for transition energies in the few terahertz range. Long intradot relaxation times (1.5 ns) are found for level separations of 14 meV (3.4 THz), decreasing very strongly to ∼2 ps at 30 meV (7 THz), in very good agreement with our microscopic theory of the carrier relaxation process. Our studies pave the way for quantum-dot terahertz device development, providing the fundamental knowledge of carrier relaxation times required for optimum device design.

The predicted suppression of carrier relaxation rates in semiconductor quantum dots compared with quantum wells has motivated the study of quantum-dot carrier relaxation mechanisms and quantum-dot optoelectronic device development across a wide range of operating wavelengths[3–5]. The development of efficient devices based on intraband transitions operating at mid- and far-infrared wavelengths (terahertz range), such as quantum-cascade lasers, relies on a detailed knowledge of carrier relaxation processes. Direct measurements of intersubband relaxation times in quantum wells yield times of up to 500 ps in the terahertz range, showing a strong reduction to tens of picoseconds with increasing electron density in the excited sub-band[6]. This reduction is mainly due to electron–electron scattering in the upper sub-band[7] and heating of the two-dimensional electron gas, which permits efficient optical phonon scattering from the high-energy tail of the electron distribution[6]. In quantum dots these effects are suppressed because of the discrete nature of the energy levels. The potential for high-efficiency quantum-dot-based terahertz emitters has recently been highlighted by the record high-temperature operation of a quantum-well-based terahertz quantum-cascade laser in which extra lateral carrier confinement was provided by high magnetic fields in the growth direction[8].

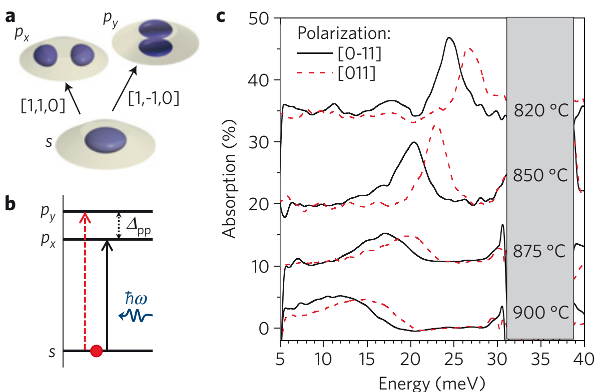

Figure 1 | Intersublevel transitions in quantum dots. a, Calculated wavefunctions for *s*-like ground and *p*-like first excited states in quantum dots. **b**, Schematic diagram of the energy levels of a quantum dot and allowed optical transitions. **c**, Normal-incidence absorption spectra (for two orthogonal linear light polarizations) of quantum-dot samples with different annealing temperatures measured at 10 K (the spectra are shifted for clarity).

Self-assembled quantum dots (SAQDs) are an appealing solution for device incorporation. However, carrier relaxation has been studied over only a limited range of sublevel energy separations. Typically, the transition energy between the ground and first excited conduction band states lies in the range 40–60 meV for InGaAs SAQDs, above the Reststrahlen band (36 meV ∼ 9 THz). Experimental studies[9,10] have demonstrated that the carrier relaxation in SAQDs occurs on a timescale of tens of picoseconds. This was explained in terms of anharmonicity of the polarons formed by the interaction between electrons and longitudinal optical phonons[10–13]. However, recent theoretical work based on a microscopic approach of polaron anharmonicity[13] has predicted a significantly longer lifetime for dots with sublevel spacing below the longitudinal optical phonon energy. Here, we report pump–probe investigations of the relaxation dynamics in InGaAs SAQDs in the few terahertz (sub-Reststrahlen) range. We show that the relaxation time shows a marked increase of three orders of magnitude over a narrow (∼15 meV) energy range up

[1]Department of Physics and Astronomy, University of Sheffield, Sheffield S3 7RH, UK, [2]Laboratoire Pierre Aigrain, Ecole Normale Supérieure, Centre National de la Recherche Scientifique, 24 Rue Lhomond, 75005 Paris, France, [3]Institute of Ion Beam Physics and Material Research, Forschungszentrum Rossendorf, PO Box 510119, 01314 Dresden, Germany, [4]EPSRC National Centre for III–V Technologies, Sheffield S1 3JD, UK. *Present addresses: Oclaro (Switzerland) AG, Binzstrasse 17, CH-8045 Zürich, Switzerland (E.A.Z.); Walter Schottky Institut, Technische Universität München, 85748 Garching, Germany (T.G.); Department of Electronic & Electrical Engineering, University College London, London WC1E 7JE, UK (H.Y.L.). †These authors contributed equally to this work. ‡e-mail: robson.ferreira@lpa.ens.fr; Luke.Wilson@sheffield.ac.uk.

© 2009 Macmillan Publishers Limited. All rights reserved.

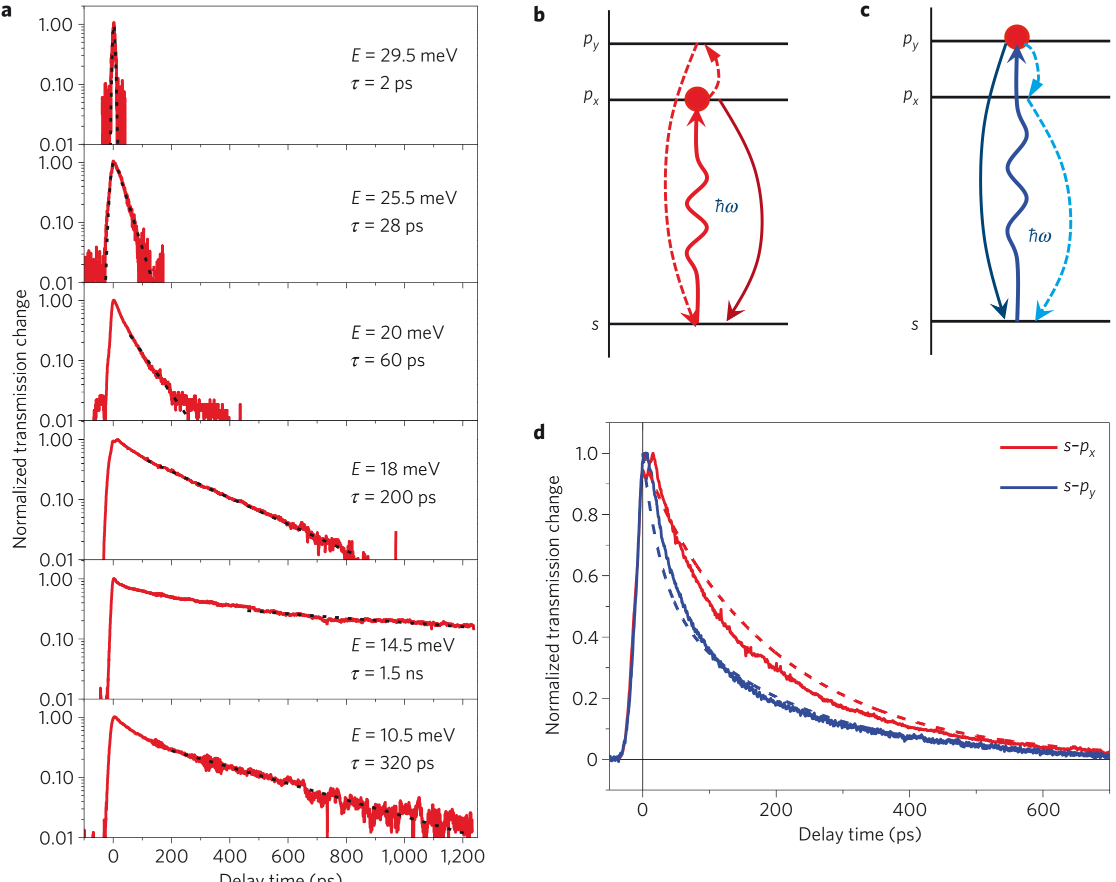

Figure 2 | Population dynamics in quantum dots. a, Normalized time evolution of the s–p_x intersublevel transmission change at different excitation energies at 10 K: pump–probe measurements at excitation energy E (red solid lines) and exponential fit with time constant τ (black dashed lines). **b**,**c**, Schematic of the possible relaxation paths after exciting either the p_x (**b**) or p_y (**c**) state. The solid arrows show the direct p-to-s intersublevel relaxation process, and the dashed arrows illustrate the relaxation path through acoustic-phonon-assisted transitions between p_x and p_y states. **d**, Pump–probe curves (solid line) for excitation into either the p_x or p_y state at the same energy of 18 meV and simulation (dashed line) taking into account the thermalization between the p states by acoustic phonon emission and absorption.

to a maximum of 1.5 ns, and we discuss model calculations that enable us to clearly identify the underlying mechanism responsible for the energy relaxation.

The investigated samples comprise 80 layers of SAQDs (areal density $\sim 4 \times 10^{10}$ cm^{-2}) separated by 50-nm-wide GaAs barriers, thus preventing both structural and electronic coupling between the layers. The dots of each layer are populated with electrons transferred from a Si-doped layer grown ~2 nm below them. The doping density was controlled in such a way as to charge each dot with at most one electron (see ref. 10 and references therein for more details). The fundamental intersublevel transitions occur in the mid-infrared region (around 50 meV) and involve one ground (s) state and a doublet (p_x and p_y) of excited levels (Fig. 1a). The absorption spectrum shows two inhomogeneously broadened peaks shifted by a small anisotropic splitting $\Delta_{pp} \sim 3.5$ meV, with each transition related to light polarized along either the [1, 1, 0] (s-to-p_x transition) or [1, −1, 0] (s-to-p_y transition) crystallographic direction (different effects have been invoked to explain the splitting of the p_x and p_y states: in-plane shape anisotropy[14], piezoelectric field effects[15] and atomistic symmetry[16]). To decrease the transition energy below the longitudinal optical phonon energy $\hbar\omega_{LO}$, we used the well-established method of post-growth thermal annealing[17–19] (see the Methods section). The absorption spectra of the annealed samples with temperatures ranging from 800 to 900 °C are shown in Fig. 1c (the absorption spectrum for the quantum-dot sample annealed at 800 °C is not shown because it overlaps strongly with the Reststrahlen band). The absorption spectra show several interesting features: (1) the absorption of annealed-sample peaks below the Reststrahlen band, with increasing redshift for increasing annealing temperature; (2) the material interdiffusion induced by the annealing does not eliminate the anisotropic splitting, which diminishes only slightly to about 2 meV; and (3) the lines become broader, indicating an enhancement of size and composition inhomogeneity of the dots during the annealing. These results clearly demonstrate that post-growth annealing provides a well-controlled means to obtain dots with average intersublevel spacing Δ_{sp} well below the Reststrahlen band (for example, $\Delta_{sp} \sim 10$ meV (2.4 THz) for the 900 °C sample).

The relaxation dynamics of excited carriers in quantum dots are studied using degenerate terahertz pump–probe spectroscopy. A free-electron laser 'FELBE' delivering linearly polarized picosecond pulses was used in the experiments[20]. An initial pulse excites the ground state to the p_x or p_y transition (the in-plane light polarization is chosen parallel to either of the crystallographic axes), and a second pulse probes the recovery of the absorption signal for this same transition as a function of the time delay between the pump and probe pulses. The results of low-temperature (10 K) pump–probe measurements for different excitation energies are shown in Fig. 2a. We observe a very strong variation in the recovery of the absorption bleaching when changing the transition energy. For transition energies close to the longitudinal optical

© 2009 Macmillan Publishers Limited. All rights reserved.

NATURE MATERIALS DOI: 10.1038/NMAT2511 LETTERS

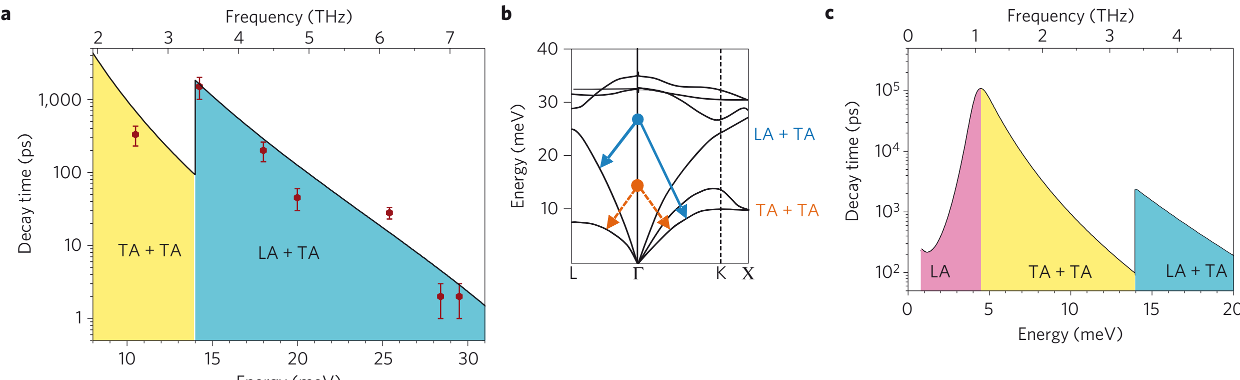

Figure 3 | Intersublevel lifetimes in the terahertz region. a, Variation of the decay time with the transition energy below the Reststrahlen band: experimental data (symbols) and theoretical calculations (solid line). The error bars are determined by the uncertainty in the mono-exponential decay fit. **b**, Schematic diagram of the different polaronic decay channels. **c**, Calculation of the relaxation time in an $In_{0.1}Ga_{0.9}As$/GaAs quantum dot of varying diameter showing the transition between electron relaxation by emission of one acoustic phonon (below ~1 THz) and the polaron anharmonic decay (above ~1 THz).

phonon energy, the decay curve is mono-exponential with a short time constant varying from 2 ± 1 ps for ~30 meV (≈7.2 THz) up to 60 ± 5 ps for 20 meV (≈4.8 THz). With a further decrease of the transition energy, the time dynamic presents a bi-exponential decay. The mono-exponential decay time as well as the extracted long time component in the bi-exponential case is plotted as a function of the transition energy in Fig. 3a. The decay time increases strongly with decreasing transition energy up to 1.5 ± 0.5 ns at ~15 meV (≈3.6 THz).

We assign the mono-exponential decay as well as the long time component in the bi-exponential case to the decay from the *p* to the *s* shells of the quantum-dot levels, whereas the short time component results from population interchanges among the *p* states (p_x and p_y) by absorption or emission of acoustic phonons with energy corresponding to the anisotropic splitting $\Delta_{pp} \approx 2$ meV (see Fig. 2b). This interpretation is corroborated by further measurements in the bi-exponential regime, using light with opposite in-plane polarization to probe also the p_y transition (see Fig. 2c). The initial decay is faster when exciting an upper (p_y) state than a lower (p_x) one, as expected because at low temperature, phonon emission is much more probable than absorption. This interpretation is confirmed in Fig. 2d when comparing the experimental data to simulations (dashed lines) that include the calculated rates for the thermal exchange between the p_x and p_y levels. This model also provides a clear explanation for the absence of bi-exponential behaviour for energies above ~20 meV, because the p_x to *s* relaxation time is shorter than or comparable to the $p_x - p_y$ thermalization time.

Let us focus now on the interpretation of the strong energy dependence of the *p*-to-*s* intersublevel relaxation time, reported in Fig. 3a as a function of the intersublevel detuning. We expect that the scattering mechanisms responsible for the energy relaxation in bulk and quantum wells are either forbidden (elastic) or greatly reduced (inelastic) in quantum dots, owing to the discrete nature of the energy levels[21,22]. Instead, as we show below, the anharmonic decay of quantum-dot polarons (electrons strongly coupled to longitudinal optical phonons[23–25]) is the dominant relaxation mechanism below the longitudinal optical phonon energy down to the 1 THz regime. This is the same physical mechanism that has been shown previously to lead to efficient relaxation at energies above the longitudinal optical phonon energy[9–13] (between 20 and 65 ps in the 40–60 meV energy range[10]), but producing here a much higher sensitivity of the cooling rate with the amount of relaxed energy. This demonstrates the generality of the polaron formation and decay mechanism for energy relaxation in systems with three-dimensional quantization of the electronic states. We have calculated the intersublevel relaxation time using the microscopic model of anharmonic polaron decay developed in ref. 13 (see the Methods section). The Fröhlich polar coupling between electrons and longitudinal optical phonons is taken into account and leads to the formation of polaron states. The anharmonic terms of the lattice vibrational potential energy then trigger the polaron disintegration into a two-phonon state. We incorporate the three possible channels for two-phonon disintegration allowed in the studied energy range: LA + LA, LA + TA and TA + TA, where LA corresponds to longitudinal acoustic and TA to transverse acoustic phonons, as shown schematically in Fig. 3b. The calculated lifetime is plotted in Fig. 3a as a function of the transition energy. For each decay channel, the relaxation rate strongly decreases with decreasing intersublevel energy. Three factors mainly contribute to this behaviour: the reduction of the available density of two-acoustic-phonon states, the decreasing strength of the anharmonic couplings involved and the increasing detuning with respect to the longitudinal optical phonon energy. We find that the LA + TA channel dominates for intersublevel energies below ~33 meV (8 THz) (the longitudinal acoustic Debye energy plus the transverse acoustic Debye energy) but larger than twice the transverse acoustic Debye energy (taken as 7 meV here). Below ~14 meV, the TA + TA path becomes available, which explains the non-monotonic variation in the calculated and measured times around this energy.

In addition, we carried out pump–probe measurements at a temperature higher than 10 K at energies of 25.4 meV and 14.25 meV (see Supplementary Information). At transition energies around 25.4 meV, the temperature dependence of the intersublevel lifetime, which decreases from 28 ± 2 ps at 10 K to 8 ± 3 ps at 170 K, can be well fitted considering polaron decay into two acoustic phonons (TA + LA). For a pump–probe energy of 14.25 meV, the intersublevel lifetime was measured to decrease from 1.5 ± 0.5 ns at 10 K to 560 ± 50 ps at 30 K and 260 ± 30 ps at 50 K. At this energy, a polaron decay time of 60 ps is expected at room temperature.

The overall close agreement between experiment and theory demonstrates that the energy relaxation in annealed SAQDs is governed by the anharmonic mechanism and becomes strongly inhibited when the level spacing decreases to the order of a few terahertz. However, it is known that in lithographically defined quantum dots, where the *s*–*p* transition energy is below 1 THz, an efficient cooling of carriers is ensured by the emission of one acoustic phonon[26,27]. To show the crossover between the two regimes, we have calculated the intersublevel lifetime for

© 2009 Macmillan Publishers Limited. All rights reserved.

transition energies between 1 and 5 meV in quantum dots with fixed composition ($In_{0.1}Ga_{0.9}As/GaAs$) and fixed height (5 nm) and varying diameter. As shown in Fig. 3c, one-phonon emission does provide an efficient relaxation channel in the sub-terahertz domain, but quickly becomes inoperative for larger intersublevel energies. As a consequence of this acoustic-phonon bottleneck, the anharmonic polaron decay mechanism governs the p-to-s energy relaxation in SAQDs down to the 1 THz regime.

Our studies demonstrate that carrier cooling in quantum dots in the terahertz domain is due to the mechanism of anharmonic polaron decay, and that its rate increases by about three orders of magnitude when the energy spacing varies between 7 and 3.5 THz. This extreme sensitivity is a consequence of the polaronic nature of the relaxation processes in fully confined quantum dots. Our results provide important new information for the design of quantum-dot-based terahertz optoelectronic devices. The long carrier relaxation times, and the ability to controllably alter the times by varying the sublevel spacing, provide strong motivation for the production of, for example, terahertz lasers, which require the inhibition of the upper-to-lower relaxation and a fast emptying of the lower level.

Methods

Annealing. The annealing was carried out in a rapid thermal annealer with temperatures ranging from 800 to 900 °C. The annealing time was fixed to 4 min. During the annealing process, the samples were sandwiched between two GaAs wafers to prevent As out-diffusion from the sample surface and were kept in a nitrogen ambient environment. We prepared several samples annealed at 800, 820, 850, 875 and 900 °C to cover the investigated spectral range.

Experimental set-up. The degenerate terahertz pump–probe measurements were carried out using the Free Electron Laser Facilities 'FELBE' located at Forschungszentrum Dresden-Rossendorf (Germany)[20]. The free-electron laser delivered linearly polarized picosecond pulses with a repetition rate of 13 MHz tunable in the 18–250 μm spectral range. The laser beam was split into pump and probe beams with pulse energies of ~1 and ~0.01 nJ correspondingly. The pump beam was modulated at a frequency of ~330 Hz using an optical chopper and a variable time delay between the pump and probe was introduced. An off-axis parabolic mirror of ~11 cm effective focal length was applied to focus both the pump and the probe beam onto the same spot on the sample, which was held in a He-flow cryostat with diamond windows. The pump and probe beams were hitting the sample at about a 10° angle to the normal. The change of the intensity of the probe beam after the sample was detected using a Ge:Ga detector and a lock-in amplifier, which was locked to the modulation frequency of the pump beam. Owing to the high repetition rate and stability of the laser, we were able to resolve an absorption change as small as ~0.05%. A mirror-based polarization rotator was also incorporated into the incident beam path to enable us to pump and probe either s–p_x or s–p_y quantum-dot transitions.

Modelling of the interdiffused quantum dots. We model both as-grown and annealed $In_xGa_{1-x}As/GaAs$ dots as truncated cones with in-plane (top) basis radius R ($R/2$), height h and uniform In fraction x in the dot region, residing on a thin wetting layer of the same In concentration, and surrounded by GaAs. The parameters of the as-grown quantum dots ($R_0 = 122$ A, $h_0 = 49$ A, $x_0 = 0.55$) were chosen to fit both intersublevel and interband transition energies ($\Delta_{sp} \approx 48$ meV and the photoluminescence peak is centred at 1,109 meV). For annealed dots, we assume that: (1) the In quantity inside the dot and the aspect ratio R/h are both preserved during the thermal process, which gives $R = R_0(x_0/x)^{1/3}$ for the annealed dot; (2) the confining potential depth ΔV varies linearly with the In content: $x_0\Delta V = x\Delta V_0$. Despite its simplicity, this model captures the main aspects of the interdiffusion, namely, an increase of the quantum-dot effective size and a decrease of its confinement potential, which both lead to a decrease of Δ_{sp}. We calculate that Δ_{sp} decreases from 48 to 10 meV on increasing the quantum-dot radius from $R \sim 12$ to ~ 25 nm with a corresponding decrease of the In fraction from $x \sim 0.55$ to 0.07. The corresponding electron wavefunctions are used to calculate the matrix elements related to the coupling of the confined electron to both the acoustical and optical phonons. In particular, the Fröhlich coupling V_{sp} (see ref. 13 for definition) varies from 3.2 meV for $\Delta_{sp} = 30$ to 2.5 meV when $\Delta_{sp} = 10$ meV.

Anharmonic decay of polarons. The intersublevel relaxation time is calculated using the microscopic model in ref. 13. We use channel-dependent Gruneisen constants to fit the present data: $\gamma = 1.3$ for the LA+LA channel (as in ref. 13), and $\gamma = 4.0$ for the TA+TA and TA+LA channels. The transverse acoustic and longitudinal acoustic Debye energies are taken respectively as 7 and 26 meV. In the present work, we take into account the non-resonant Fröhlich couplings between the ground state and the longitudinal optical phonon replicas of the p states. As a consequence, we find that the polaron decay time τ due to the anharmonic couplings is given by:

$$\frac{\hbar}{\tau} = \frac{4\Delta_{sp}^2}{(\hbar\omega_{LO}+\Delta_{sp})^2}\frac{V_{sp}^2}{(\Delta_{sp}-\hbar\omega_{LO})^2+V_{sp}^2}\Gamma^{ph}(\Delta_{sp}) \quad (1)$$

where the function $\Gamma^{ph}(E)$ is defined in ref. 13. The intersublevel transition energy Δ_{sp} corresponds to the optically probed transition energy between s-like and p-like polaron states with a dominant zero-phonon component. This formula is used here instead of formula (6) used in ref. 13, which is valid only close to the longitudinal optical phonon resonance. The first term in the above equation arises from the interference between the resonant and the non-resonant couplings. This interference is found to be destructive for intersublevel transition energies that are small compared with the longitudinal optical phonon one ($\Delta_{sp} \ll \hbar\omega_{LO}$). This effect contributes also to the inhibition of the polaron decay mechanism at low energies, in particular in the calculation shown in Fig. 3c.

Received 15 April 2009; accepted 14 July 2009; published online 16 August 2009

References

1. Faist, J. *et al.* Quantum cascade laser. *Science* **264,** 553–556 (1994).
2. Kohler, R. *et al.* Terahertz semiconductor-heterostructure laser. *Nature* **417,** 156–159 (2002).
3. Urayama, J., Norris, T. B., Singh, J. & Bhattacharya, P. Observation of phonon bottleneck in quantum dot electronic relaxation. *Phys. Rev. Lett.* **86,** 4930–4933 (2001).
4. Borri, P. & Langbein, W. Four-wave mixing dynamics of excitons in InGaAs self-assembled quantum dots. *J. Phys. Condens. Matter* **19,** 295201 (2007).
5. Botez, D. *et al.* Progress towards intersubband quantum-box lasers for highly efficient continuous wave operation in the mid-infrared. *J. Nanophoton.* **3,** 031606 (2009).
6. Murdin, B. N. *et al.* Direct observation of the LO phonon bottleneck in wide $GaAs/Al_xGa_{1-x}As$ quantum wells. *Phys. Rev. B* **55,** 5171–5176 (1997).
7. Hartig, M. *et al.* Efficient intersubband scattering via carrier–carrier interaction in quantum wells. *Phys. Rev. Lett.* **80,** 1940–1943 (1998).
8. Wade, A. *et al.* Magnetic-field-assisted terahertz quantum cascade laser operating up to 225 K. *Nature Photon.* **3,** 41–45 (2008).
9. Sauvage, S. *et al.* Long polaron lifetime in InAs/GaAs self-assembled quantum dots. *Phys. Rev. Lett.* **88,** 177402 (2002).
10. Zibik, E. A. *et al.* Intraband relaxation via polaron decay in InAs self-assembled quantum dots. *Phys. Rev. B* **70,** 161305(R) (2004).
11. Li, X.-Q., Nakayama, H. & Arakawa, Y. Phonon bottleneck in quantum dots: Role of lifetime of the confined optical phonons. *Phys. Rev. B* **59,** 5069–5073 (1999).
12. Verzelen, O., Ferreira, R. & Bastard, G. Polaron lifetime and energy relaxation in semiconductor quantum dots. *Phys. Rev. B* **62,** 4809–4812(R) (2000).
13. Grange, T., Ferreira, R. & Bastard, G. Polaron relaxation in self-assembled quantum dots: Breakdown of the semiclassical model. *Phys. Rev. B* **76,** 241304(R) (2007).
14. Nabetani, Y. *et al.* Initial growth stage and optical properties of a three-dimensional InAs structure on GaAs. *J. Appl. Phys.* **76,** 347–351 (1994).
15. Stier, O. *et al.* Electronic and optical properties of strained quantum dots modeled by 8-band k.p theory. *Phys. Rev. B* **59,** 5688–5701 (1999).
16. Bester, G. *et al.* Pseudopotential calculation of the excitonic fine structure of million-atom self-assembled $In_{1-x}Ga_xAs/GaAs$ quantum dots. *Phys. Rev. B* **67,** 161306 (2003).
17. Fafard, S. *et al.* Manipulating the energy levels of semiconductor quantum dots. *Phys. Rev. B* **59,** 15368–15373 (1999).
18. Fafard, S. & Allen, C. Nì. Intermixing in quantum-dot ensembles with sharp adjustable shells. *Appl. Phys. Lett.* **75,** 2374–2376 (1999).
19. Zibik, E. A. *et al.* Effects of alloy intermixing on the lateral confinement potential in InAs/GaAs self-assembled quantum dots probed by intersublevel absorption spectroscopy. *Appl. Phys. Lett.* **90,** 163107 (2007).
20. Lehnert, U. *et al. Proc. 29th FEL Conference, Novosibirsk, Russia* (2007); available at <http://accelconf.web.cern.ch/AccelConf/f07/PAPERS/MOPPH036.PDF>.
21. Bockelman, U. & Bastard, G. Phonon scattering and energy relaxation in two-, one-, and zero-dimensional electron gases. *Phys. Rev. B* **42,** 8947–8951 (1990).
22. Benisty, H., Sotomayor-Torres, C. M. & Weisbuch, C. Intrinsic mechanism for the poor luminescence properties of quantum-box systems. *Phys. Rev. B* **44,** 10945–10948 (1991).
23. Inoshita, T. & Sakaki, H. Density of states and phonon-induced relaxation of electrons in semiconductor quantum dots. *Phys. Rev. B* **56,** R4355–R4358 (1997).

© 2009 Macmillan Publishers Limited. All rights reserved.

NATURE MATERIALS DOI: 10.1038/NMAT2511

24. Hameau, S. *et al.* Strong electron–phonon coupling regime in quantum dots: Evidence for everlasting resonant polarons. *Phys. Rev. Lett.* **83,** 4152–4155 (1999).
25. Carpenter, B. A. *et al.* Intraband magnetospectroscopy of singly and doubly charged *n*-type self-assembled quantum dots. *Phys. Rev. B* **74,** 161302(R) (2006).
26. Garcia, C. P. *et al.* Evidence of correlation in spin excitations of few-electron quantum dots. *Phys. Rev. Lett.* **95,** 266806 (2005).
27. Fujisawa, T. *et al.* Allowed and forbidden transitions in artificial hydrogen and helium atoms. *Nature* **419,** 278–281 (2002).

Acknowledgements

Financial support was provided by the UK Engineering and Physical Sciences Research Council (EPSRC). The LPA (UMR 8551) is associated with the CNRS and the Universities Paris 6 and Paris 7. The free-electron laser 'FELBE' is supported by the Integrating Activity on Synchrotron and Free-Electron Laser Science (IA-SFS) under the EU contract RII3-CT-2004-506008 of the 6th Framework 'Structuring the European Research Area, Research Infrastructures Action'. We are grateful to P. Michel and the FELBE team for their dedicated support.

Author contributions

E.A.Z. and L.R.W. conceived the experiments; E.A.Z., L.R.W., B.A.C., N.E.P., D.S. and S.W. carried out the experiments; T.G., R.F. and G.B. made the theory and modelled the experiments; E.A.Z. and T.G. analysed the data; L.R.W., R.F., E.A.Z. and M.S.S. supervised the project; H.Y.L. grew the samples; T.G., E.A.Z., R.F. and L.R.W. wrote the paper with major input and edits from M.S.S. and M.H. All authors discussed the results and commented on the manuscript.

Additional information

Supplementary information accompanies this paper on www.nature.com/naturematerials. Reprints and permissions information is available online at http://npg.nature.com/reprintsandpermissions. Correspondence and requests for materials should be addressed to R.F. or L.R.W.

© 2009 Macmillan Publishers Limited. All rights reserved.

nature materials
ARTICLES
PUBLISHED ONLINE: 25 JANUARY 2009 | DOI: 10.1038/NMAT2373

Conduction at domain walls in oxide multiferroics

J. Seidel[1,2*†], L. W. Martin[2,3*], Q. He[1], Q. Zhan[2], Y.-H. Chu[2,3,4], A. Rother[5], M. E. Hawkridge[2], P. Maksymovych[6], P. Yu[1], M. Gajek[1], N. Balke[1], S. V. Kalinin[6], S. Gemming[7], F. Wang[1], G. Catalan[8], J. F. Scott[8], N. A. Spaldin[9], J. Orenstein[1,2] and R. Ramesh[1,2,3]

Domain walls may play an important role in future electronic devices, given their small size as well as the fact that their location can be controlled. Here, we report the observation of room-temperature electronic conductivity at ferroelectric domain walls in the insulating multiferroic $BiFeO_3$. The origin and nature of the observed conductivity are probed using a combination of conductive atomic force microscopy, high-resolution transmission electron microscopy and first-principles density functional computations. Our analyses indicate that the conductivity correlates with structurally driven changes in both the electrostatic potential and the local electronic structure, which shows a decrease in the bandgap at the domain wall. Additionally, we demonstrate the potential for device applications of such conducting nanoscale features.

Correlated oxide systems are an exciting and challenging area of condensed-matter research, with their interacting and competing charge, spin, orbital and lattice degrees of freedom forming new electronic and magnetic phases[1,2]. These phases can be controlled through stress, optical excitation and electric and magnetic fields and have great potential for applications in the fields of spintronics, information storage and communications. Among the correlated oxides, the multiferroics, which show more than one type of ferroic order in the same phase, are attracting particular interest[3–6]. The defining characteristic of a ferroic material is an order parameter (electric polarization in ferroelectrics, magnetization in ferromagnets or spontaneous strain in ferroelastics) that has different, energetically equivalent orientations, the orientation of which can be selected using an applied field. This often leads to the appearance of domains of differently oriented regions, separated by domain walls, coexisting in a sample[7]. Such domain walls will become more technologically important as the dimensions of individual elements in devices continue to shrink.

Although the morphology and properties of domains and their walls have been studied for more than 50 years, in recent times there has been increasing focus on novel functionality at domain walls[8–12]. For example, it has been predicted theoretically that the ferroelectric walls in magnetoelectric multiferroics can be ferromagnetic even if the domains themselves are antiferromagnetic[9–11]. Conversely, spin rotation across ferromagnetic domain walls in insulating ferromagnets can induce a local polarization in the walls of an otherwise non-polar material[5,12]. Experimentally, unusual functional properties of domain walls have also been observed: preferential doping along domain walls has been reported to induce two-dimensional superconductivity in WO_{3-x} (ref. 13) and enhanced resistivity in phosphates[14], whereas in paraelectric, non-polar $SrTiO_3$ the ferroelastic domain walls seem to be ferroelectrically polarized[15]. Local probes, particularly those based on scanning probe microscopy[14], are invaluable in observing such effects at the nanoscale.

Here we describe the observation of a new behaviour—room-temperature electrical conductivity—at ferroelectric domain walls in the prototypical multiferroic $BiFeO_3$ (BFO). BFO is a room-temperature G-type antiferromagnet ($T_N \sim 650$ K) and a rhombohedral ferroelectric ($T_C \sim 1{,}103$ K), with a large spontaneous ferroelectric polarization ($\sim 90\,\mu\mathrm{C\,cm^{-2}}$) along the pseudocubic 111 directions[16,17]. Such rhombohedral ferroelectrics possess 71°, 109° and 180° domain walls forming on {101}, {100} and planes that satisfy the requirement that $\pm h \pm k + l = 0$, respectively[18]. All three wall orientations have been observed in BFO (refs 19,20).

Epitaxial BFO films (~100 nm thick) were grown using laser molecular-beam epitaxy in (111), (110) and (100) orientations, using carefully controlled single-crystal $SrTiO_3$ substrates. A thin 50 nm layer of epitaxial $SrRuO_3$ was used as a bottom electrode for electrical-contact purposes. Ferroelectric domains were imaged using piezoresponse force microscopy (PFM) as described previously[19]. Controlled ferroelectric domain patterns were written using PFM by applying a d.c. voltage to the probe tip. Local electrical conductivity was measured using high-resolution conductive atomic force microscopy (c-AFM) (details of measurements are provided in the Methods section) by applying a bias voltage (below the polarization switching voltage) between the conductive AFM tip and the bottom electrode of the sample.

100-nm-thick epitaxial films grown on (110) surfaces show a two-variant ferroelectric domain structure in the as-grown states with average domain sizes between 5 and 10 μm. On electrical switching at high fields, all three variations of domain walls can be created[21]; therefore, we begin our study on these (110)-oriented films. The typical morphology is shown in Fig. 1a. We measured the RMS roughness of the films to be ~0.5 nm and there are no observable surface features, either before or after switching,

[1]Department of Physics, University of California, Berkeley, 94720 California, USA, [2]Materials Sciences Division, Lawrence Berkeley National Laboratory, 94720 California, USA, [3]Department of Materials Science and Engineering, University of California, Berkeley, 94720 California, USA, [4]Department of Materials Science and Engineering, National Chiao Tung University, HsinChu, 30010, Taiwan, [5]Institute of Structure Physics, Triebenberg Laboratory, Technische Universität Dresden, DE-01062, Germany, [6]Center for Nanophase Materials Science, Oak Ridge National Laboratory, 37831 Tennessee, USA, [7]Forschungszentrum Dresden-Rossendorf, 01314 Dresden, Germany, [8]Department of Earth Sciences, University of Cambridge, Cambridge CB2 3EQ, UK, [9]Materials Department, University of California, Santa Barbara, 93106 California, USA. *These authors contributed equally to this work. †e-mail: jseidel@berkeley.edu.

NATURE MATERIALS DOI: 10.1038/NMAT2373

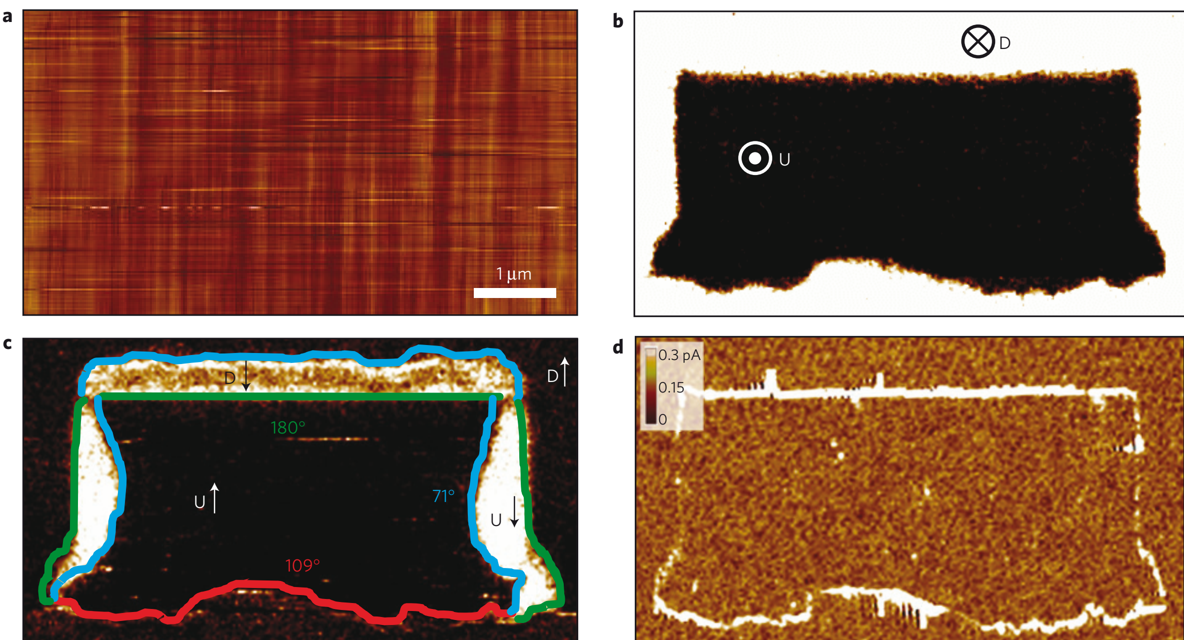

Figure 1 | Conductivity at different wall types. a, Topography of a BFO(110) thin film, r.m.s. roughness of 0.5 nm. **b**, Out-of-plane PFM image of a written domain pattern in a monodomain BFO(110) film showing the out-of-plane polarization component of the domains to be either down, labelled as 'D' (white), or up, labelled as 'U' (black). **c**, In-plane PFM image of a written domain pattern in a monodomain BFO(110) film showing all three types of domain wall, that is, 71° (blue), 109° (red) and 180° (green), as inferred from the combination of both out-of-plane and in-plane PFM images. In these images, both the out-of-plane (U or D) component and the in-plane projection of the polarization direction (shown as an arrow) are also labelled. **d,** Corresponding c-AFM image showing conduction at both 109° and 180° domain walls; note the absence of conduction at the 71° domain walls.

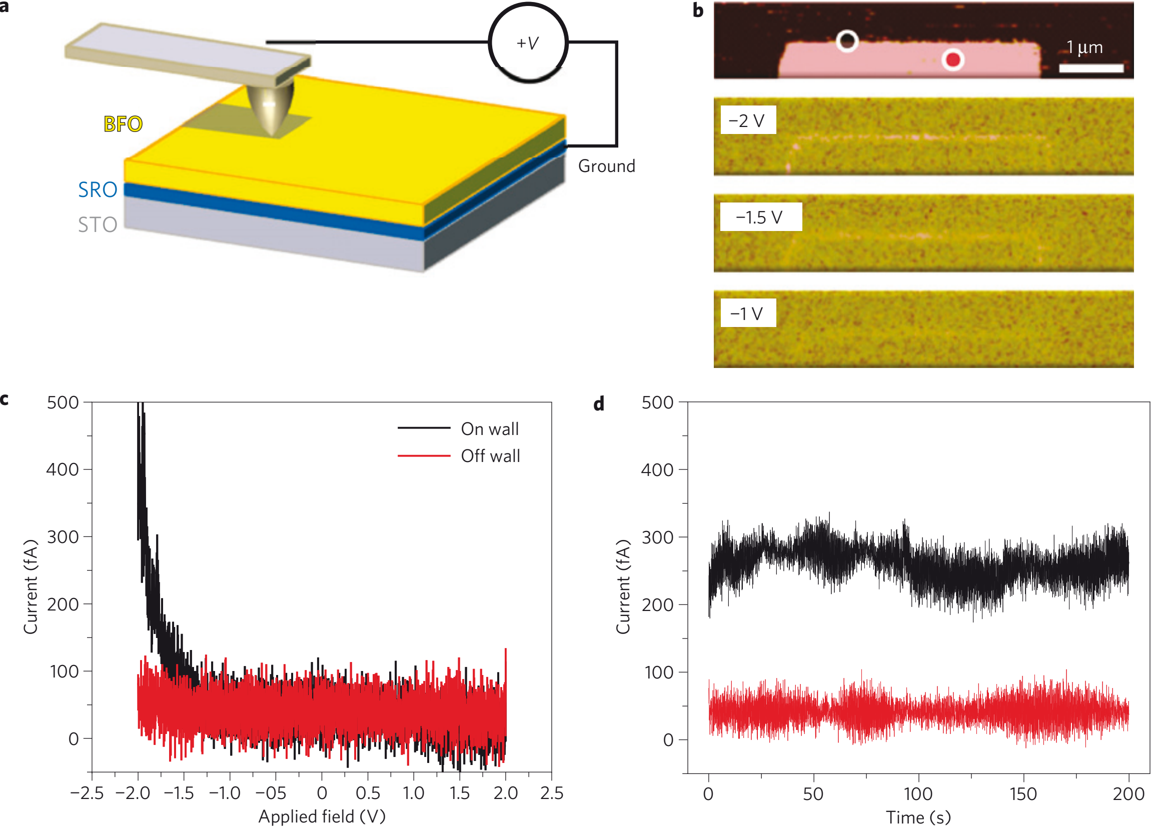

Figure 2 | Conduction at domain walls. a, Schematic illustration of the experimental c-AFM set-up. **b**, (Top) Out-of plane PFM image of a written 180° domain in a monodomain BFO(110) sample and (lower) corresponding c-AFM current maps for −1, −1.5 and −2 V sample bias made with a Pt-coated tip. **c**, *I*–*V* curves taken both on the domain wall (black) and off the domain wall (red) reveal Schottky-like behaviour. **d**, Time dependence of the current both on the wall (black) and off the wall (red) at an applied sample bias of −2 V. Results are qualitatively similar for N-doped diamond tips.

NATURE MATERIALS DOI: 10.1038/NMAT2373 ARTICLES

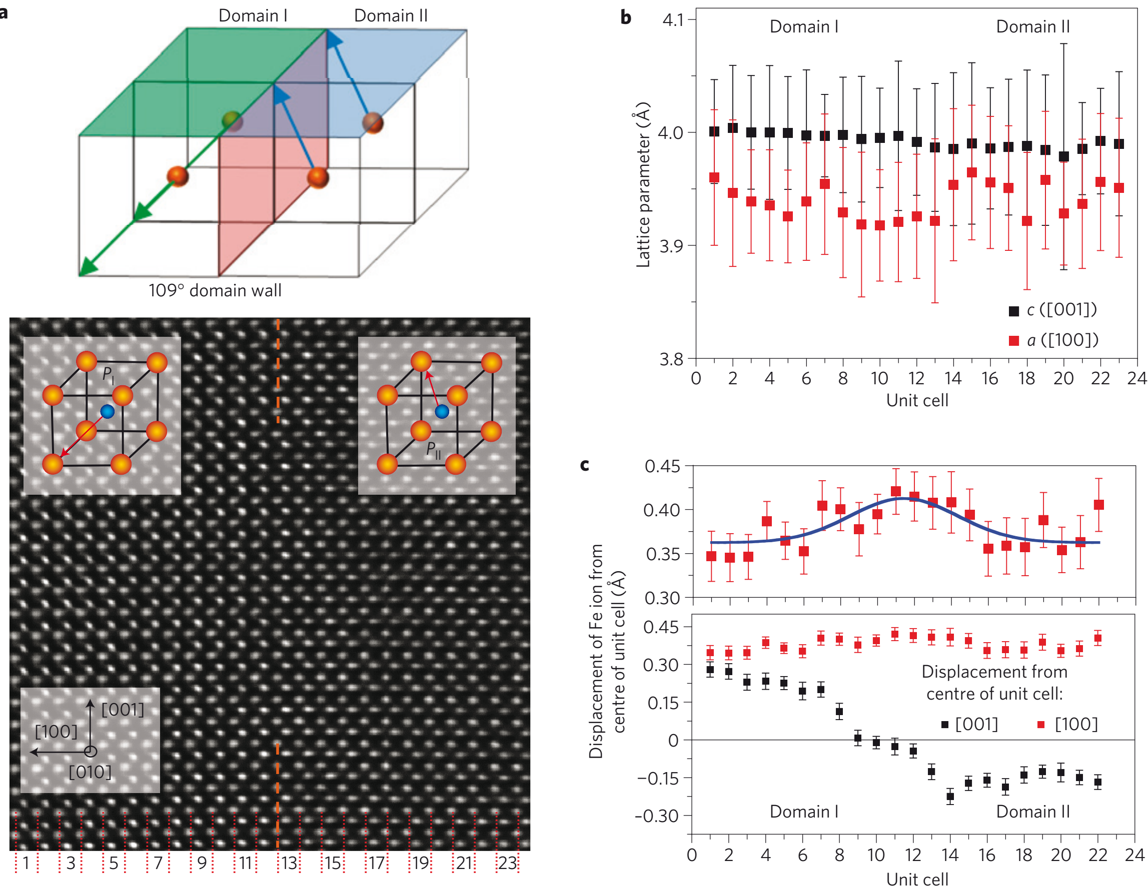

Figure 3 | Structural analysis of domain walls. a, Schematic diagram of 109° domain wall and exit-wave-reconstructed HRTEM image of a 109° domain wall imaged along the [010] zone axis. **b**, Extracted *a* and *c* lattice parameters for each unit cell across the domain wall. **c**, Extracted Fe-ion displacement relative to the Bi lattice for each unit cell across the domain wall. A close-up (upper panel) reveals an increase in the component of polarization perpendicular to the domain wall.

corresponding to the conducting features. In Fig. 1c, we show the in-plane PFM image of a written domain pattern controlled to have all three domain-wall types. The complicated domain shapes occur only when the high voltages required to stabilize all three domain-wall variants are applied[21]. The various domain-wall types are determined using both in-plane (Fig. 1c) and out-of-plane (Fig. 1b) PFM images and are labelled accordingly. Our main result is shown in the corresponding c-AFM trace (Fig. 1d): the occurrence of electrical conduction at 109° and 180° domain walls, and the absence of conduction at 71° domain walls. BFO films grown on (001)- and (111)-oriented substrates also consistently show conduction at 109° and 180° domain walls (Supplementary Information, Fig. S1); in no cases do 71° domain walls show conduction within the resolution of our measurements.

Next we discuss in detail our c-AFM measurements on the (110)-oriented BFO films. A schematic diagram of the experimental set-up is shown in Fig. 2a. The spatial resolution of the technique is limited by the tip radius of ~20 nm. Figure 2b (top panel) shows a PFM image of two domains separated by a 180° domain wall. The corresponding c-AFM images (lower panels) show enhanced conduction at the domain wall for applied bias voltages of −1 to −2 V. Current–voltage (I–V) curves (Fig. 2c) show resistive behaviour within the domain (red data) and Schottky-like behaviour suggesting activated conduction at the domain wall (black data). We repeated our I–V measurements with a number of different c-AFM tip materials—including Pt and N-doped diamond—and found similar Schottky-like behaviour with slightly shifted conduction onsets. Furthermore, the current is persistent over a timescale of at least 3 min, which is limited by the drift in our scanning system (Fig. 2d). These time-dependent data indicate that the origin of this current is not displacement of domain walls. Additional details of conduction at domain walls are provided in the Supplementary Information (Supplementary Information, Fig. S2). Ultrahigh-vacuum-based c-AFM measurements were used to further probe the nature of conduction and I–V characteristics of the conducting domain walls—including the observation of enhanced current values.

Table 1 | Electronic structure at ferroelectric domain walls.

Domain wall type (°)	Electrostatic potential step (eV)	Change in bandgap (eV)
71	0.02	0.05
109	0.15	0.10
180	0.18	0.20

Calculated values of the potential step and reduction in bandgap at all three domain-wall types.

To understand the observed electrical conductivity, we performed a combined transmission electron microscopy (TEM) and density functional theory (DFT) study of the domain-wall structure and properties. The structure of domain walls in ferroelectric perovskites and related materials has been the focus of several recent DFT (refs 18,22) and TEM (refs 23–25) studies, and the structural distortions associated with ferroelectric domain

ARTICLES NATURE MATERIALS DOI: 10.1038/NMAT2373

walls are now reasonably well characterized. However, studies of the associated electronic properties are in their infancy[26]. We chose the 109° domain wall (shown schematically in Fig. 3a) for our study because we do not obtain conduction at 71° domain walls and because imaging of 180° domain walls with high-resolution TEM (HRTEM) presents practical problems in terms of locating the wall. (For completeness, HRTEM images of 71° domain walls are shown in Supplementary Information, Fig. S3.) We use (001)-oriented samples for the TEM analysis, because we can easily control the density of 109° domain walls during growth for this orientation. TEM images were acquired using the exit-wave reconstruction approach to eliminate the effects of objective-lens spherical aberrations; such images can be directly interpreted in terms of the projection of the atomic columns[27]. A representative image for such a 109° domain wall taken along the [010] zone axis of a cross-sectioned BFO/SRO/STO(001) film, where SRO is $SrRuO_3$ and STO is $SrTiO_3$, is shown in Fig. 3a. Analysis of this image enables us to determine the lattice parameter in the plane of the film (a) ([100]) and the lattice parameter out of the plane of the film (c) ([001]) (Fig. 3b). As expected, the in-plane lattice parameter is slightly smaller and the out-of-plane lattice parameter larger than the values in bulk BFO (3.96 Å; ref. 16) owing to the strain inherent in the epitaxial films. In addition, we find that both the in-plane and out-of-plane film lattice parameters are unchanged in the vicinity of the domain wall. We also extract the relative displacement of the Fe ion with respect to the Bi sublattice, and resolve it into components parallel ([001]) and perpendicular ([100]) to the domain wall (which lies in a (100) plane running vertically across the image and labelled with a dashed orange line) by quantitative analysis of the HRTEM data (Fig. 3c); this distance is representative of the local polarization. The component of the displacement parallel to the domain wall (along [001]) decreases in magnitude to zero at the centre of the domain wall before changing to the same magnitude (but opposite sign) on the other side of the wall, reflecting the change in polarization orientation of the domain. Interestingly, the perpendicular displacement component (along [100]) shows a small increase at the domain wall; we return to the implications of this later. Similar studies were completed on a 71° domain wall as well (Supplementary Information, Fig. S2). Again, only minor variation in lattice parameters was observed across the domain wall. In this case a similar step in Fe-ion displacement is observed parallel to the domain wall, but we are unable to resolve a step in the perpendicular component across the wall.

To investigate the influence of these structural changes on the electronic properties, we next performed a density functional study of the structure and electronic properties for all three ferroelectric domain-wall variants (details in the Methods section). First we performed full structural optimizations of the ionic positions with the lattice parameters fixed to their experimental bulk values; in particular, the oxygen polyhedral rotations around the polar axis, which are known to have a profound effect on both the magnetic[28] and electronic[29] properties and cannot be easily extracted from the HRTEM data, were accurately calculated. As the sense of the oxygen rotations around the polar axis is independent of the direction of polarization along the axis[28] we studied two scenarios: first we initialized the sense of rotation to be continuous across the domain boundary and second we changed the rotation sense when the polarization direction changed. As expected, we found that domain walls with continuous oxygen rotations are considerably lower in energy, because this avoids formation of an antiphase boundary associated with the octahedral rotations. In addition, we investigated domain-wall configurations centred at both the Bi–O and Fe–O planes and found the Bi–O walls to be slightly lower in energy, confirming the findings of the HRTEM analysis. Our lowest-energy calculated configuration for the 109° domain wall has a domain-wall energy of 206 mJ m^{-2}.

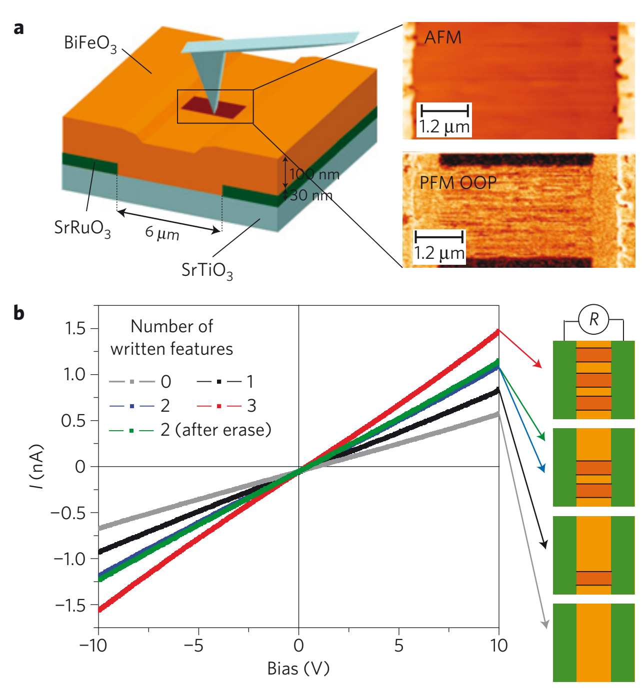

Figure 4 | Proof of concept for device application. a, Schematic illustration (left) of in-plane electrode structure (green) and how scanning probe tips can be used to controllably create conductive domain-wall features between electrodes. The images on the right show AFM (top) and out-of-plane PFM (bottom) contrast for this written domain area on a BFO(110) sample. **b**, I–V characteristics of the devices measured between the two in-plane electrodes show that the current can be incrementally controlled through creating or erasing the conducting domain walls.

To confirm that our calculated structure is consistent with our TEM data, we analysed the layer-by-layer polarization, defined as the sum over the bulk Born effective charges[29] multiplied by the displacements of the ions from their centrosymmetric reference positions in each layer. As expected, the local polarization in the middle of the domain is close to the value calculated for bulk BFO using the same computationally and experimentally determined lattice parameters (~93 µC cm^{-2}; refs 29–32), confirming that our supercell is large enough to capture the essential physics. Consistent with our TEM analysis, we find an abrupt change in the parallel polarization component across the domain wall and a small change in the normal component at the domain wall.

Our calculations indicate that this small change in the normal component of the polarization across the 109° domain wall leads to a step in the electrostatic potential (planar and macroscopically averaged) of 0.15 eV across the domain wall (Table 1); a similar step was computed and explained previously across 90° domain walls in $PbTiO_3$ (ref. 22). Such a potential step should enhance the electrical conductivity by causing carriers in the material to accumulate at the domain wall to screen the polarization discontinuity. Our calculations for the 180° domain wall also yield a variation in the normal component of the polarization, and a corresponding potential step of 0.18 eV (Table 1). The normal component results from the polarization rotating towards successive adjacent corners of the perovskite unit cell, through a 71° and than a 109° change in the polarization direction before reaching the reversed polarization[16]. This behaviour is in striking contrast to the 180° polarization reversal in tetragonal ferroelectrics[22], where the polarization changes in only one direction within the wall plane and no normal component occurs. The 71° wall, however, exhibits no anomaly in the perpendicular component of the ion displacement at the centre of the wall, again consistent with our

TEM data, and therefore exhibits a negligible electrostatic potential step at the domain wall (Table 1).

Finally, we calculate the electronic properties of our structurally optimized domain walls, in particular by comparing the layer-by-layer densities of states in the domain wall and mid-domain regions. Within the central region of the domain, we find, as expected, that the local density of states resembles that of bulk BFO, and the local Kohn–Sham bandgap is equal to the value of 1.3 eV obtained for bulk BFO with the same choice of Hubbard parameter U and exchange interaction J, 3 and 1 eV, respectively[29]. (We emphasize that, although the DFT Kohn–Sham bandgaps do not correspond to experimental bandgaps, changes in DFT gaps caused by changes in bandwidth as a consequence of small changes in structure for the same DFT implementation are qualitatively meaningful.) As the domain wall is approached, we find that the changes in the structure do indeed cause changes in the band width and the positions of the band edges. This leads in the 109° (180°) case to a 0.1 eV (0.2 eV) reduction in the bandgap in the domain-wall layer from the mid-domain calculated value of 1.3 eV (Table 1). For activated conduction at room temperature, such a change in bandgap, or in band-edge offset relative to the Fermi energy of the tip, should lead to considerable changes in conductivity. Consistent with its absence of conduction, the reduction in bandgap in the 71° case is smaller (0.05 eV) (Table 1). Interestingly, the magnitude of the bandgap reduction is sensitive to the details of the lattice parameters used in the calculation; if we constrain the lattice parameters to the bulk values, the changes in the bandgap are larger than those for the relaxed structures given in Table 1. This suggests that band-structure changes at domain walls might be tunable by epitaxial strain.

Our conductivity measurements, TEM analysis and DFT calculations therefore suggest two mechanisms, which probably combine to yield the observed conductivity at the 109° and 180° domain walls: (1) an increased carrier density as a consequence of the electrostatic potential step at the wall and (2) a decrease in the bandgap within the wall and corresponding reduction in band offset with the c-AFM tip. Both factors are the result of structural changes at the wall.

The potential of these conducting domain walls for possible device applications is illustrated in Fig. 4. By creating a simple device structure consisting of in-plane electrodes of SRO separated by a 6 µm spacing (Fig. 4a), we can measure the I–V characteristics of BFO films and domain walls macroscopically. Additionally, the SRO provides nearly Ohmic contacts with the BFO films and thus we can gain further insight into the conduction of the walls in the gap, without any interference from the AFM tip during the measurement process. Monodomain (110)-oriented BFO films were grown on top of the SRO in-plane electrode device structures on STO(110) substrates. Conducting domain-wall features (here are shown 180° domain walls, Fig. 4a, right) that connect the two in-plane electrodes were written using PFM. Again, no morphological surface features were observed that correspond to the written domain pattern. I–V measurements (Fig. 4b) reveal a step-like increase in the measured current between the two in-plane electrodes on addition of a controlled number of conducting domain walls. The steps in conduction are essentially equidistant, increase proportionally to the total number of domain walls written and show completely reversible behaviour on erasing a given feature. I–V curves for zero, one, two and three domain features are shown in Fig. 4b. Such material functionality has potential application in both logic and memory applications, as the wall location (and hence electronic conduction) can be precisely controlled on the nanoscale. This demonstrates a possible rewritable, multiconfiguration device set-up that uses nanoscale conductive channels (that is, conducting domain walls). Finally, on the basis of a simple sheet-resistance model, we can estimate the resistivity of a single domain wall in BFO to be of the order of 1–10 Ω m, which is between five and six orders of magnitude lower than for bulk BFO.

In summary, our results show that ferroelectric domain walls in multiferroic BFO show unusual local electronic transport behaviour that is quite different from that in the bulk of the material or in conventional ferroelectrics. The conductivity is consistent with our observed changes in structure at the domain wall and can be activated and controlled on the scale of the domain wall width—about 2 nm in BFO. The present work represents a 'proof of concept' that domain walls are discrete functional entities, which may be addressed and sensed, suggesting potential utility in novel nanoelectronic applications.

Methods

Nanoscale conductivity measurements were performed on a Digital Instruments Nanoscope-IV Multimode atomic force microscope equipped with a c-AFM application module (TUNA). The investigations were performed with commercially available N-doped diamond-coated Si tips (NT-MDT) and Ti/Pt-coated Si tips (MikroMasch). Current-amplification settings of the c-AFM equipment of 1 and 10 V pA^{-1} at an applicable voltage range of ±12 V were used. For a typical scan rate of 0.5–1.0 µm s^{-1}, the noise level was of the order of 50 fA at a bandwidth of 250 Hz. All data were acquired under ambient conditions and at room temperature and all such c-AFM measurements were made within a few minutes after the domain wall was created by electrical switching.

Structural investigations have been carried out using a Philips CM300 field emission gun microscope with a point-to-point resolution of 1.7 Å and information resolution of 0.8 Å. The domain structure was investigated in cross-section [010] orientation. The reconstructed phase of the complex electron exit wave, as shown in Fig. 3a, was reconstructed from a series of 20 high-resolution images of the BFO 109° domain wall using the TrueImage software package[33,34]. According to the weak phase-object approximation for a thin object, the heavy Bi columns projected along the [010] direction correspond to the brightest dots and the less bright ones represent Fe in the phase.

DFT calculations were performed using the projector augmented wave implementation of the VASP code[35] with standard projector augmented wave potentials (Bi, $6s^25d^{10}6p^3$; Fe, $3p^64s^23d^6$; O, $2s^22p^4$) and the local spin density approximation (LSDA) $+U$ method to describe the exchange–correlation potential[36]. We used a cut-off energy of 550 eV and U/J values of 3/1 eV; these values were shown in previous work[29] to give a bandgap of 1.3 eV for bulk rhombohedral BFO and to yield a small bandgap even in the high-symmetry cubic perovskite phase. We constructed supercells containing two oppositely polarized domains and two domain walls; each domain contained six $Bi_2Fe_2O_6$ units initially set to the bulk $BiFeO_3$ structure. Note that the systems in our calculations are in all cases electrically neutral with uncharged domain walls. We used the experimental bulk lattice parameters, with the rhombohedral angle set to 60° so that the supercell could accommodate the broken symmetry of the domain wall. The Brillouin zone integration was performed on a $5\times5\times1$ Γ-centred Monkhorst–Pack grid incorporating a Gaussian averaging, with an energy width of 0.05 eV. Ionic positions were relaxed within the local minimum of maintaining two domains and domain walls per supercell until the total energy of the supercell converged to within 0.01 eV and the forces acting on individual ions were below 0.03 eV Å^{-1}. The magnetism was set to the G-type antiferromagnetic ordering observed in bulk BFO and remained unchanged throughout the relaxation of the domain boundary. All parameters chosen for the supercell calculations were tested in calculations for single unit cells and shown to yield well-converged total energies, with atom positions and band structures in good agreement with previous work.

Received 12 May 2008; accepted 22 December 2008; published online 25 January 2009

References

1. Tsuda, N., Nasu, K., Yanase, A. & Siratori, K. *Electronic Conduction in Oxides* (Springer, 2000).
2. Imada, M., Fujimori, A. & Tokura, Y. Metal–insulator transitions. *Rev. Mod. Phys.* **70**, 1039–1263 (1998).
3. Spaldin, N. A. & Fiebig, M. The renaissance of magnetoelectric multiferroics. *Science* **309**, 391–392 (2005).
4. Eerenstein, W., Mathur, N. D. & Scott, J. F. Multiferroic and magnetoelectric materials. *Nature* **442**, 759–765 (2006).
5. Cheong, S.-W. & Mostovoy, M. Multiferroics: A magnetic twist for ferroelectricity. *Nature Mater.* **6**, 13–20 (2007).
6. Ramesh, R. & Spaldin, N. A. Multiferroics: Progress and prospects in thin films. *Nature Mater.* **6**, 21–29 (2007).
7. Roytburd, A. Elastic domains and polydomain phases in solids. *Phase Transit.* **45**, 1–34 (1993).
8. Thomas, L. *et al.* Resonant amplification of magnetic domain-wall motion by a train of current pulses. *Science* **315**, 1553–1556 (2007).

9. Přívratská, J. & Janovec, V. Pyromagnetic domain walls connecting antiferromagnetic non-ferroelastic magnetoelectric domains. *Ferroelectrics* **204**, 321–331 (1997).
10. Přívratská, J. & Janovec, V. Spontaneous polarization and/or magnetization in non-ferroelastic domain walls: Symmetry predictions. *Ferroelectrics* **222**, 23–32 (1999).
11. Goltsev, V. *et al*. Structure and interaction of antiferromagnetic domain walls in hexagonal $YMnO_3$. *Phys. Rev. Lett.* **90**, 177204 (2003).
12. Mostovoy, M. Ferroelectricity in spiral magnets. *Phys. Rev. Lett.* **96**, 067601 (2006).
13. Aird, A. & Salje, E. K. H. Sheet superconductivity in twin walls: Experimental evidence of WO_{3-x}. *J. Phys. Condens. Matter* **10**, L377–L380 (1998).
14. Bartels, M. *et al*. Impurity-induced resistivity of ferroelastic domain walls in doped lead phosphate. *J. Phys. Condens. Matter* **15**, 957–962 (2003).
15. Zubko, P. *et al*. Strain-gradient-induced polarization in $SrTiO_3$ single crystals. *Phys. Rev. Lett.* **99**, 167601 (2007).
16. Kubel, F. & Schmid, H. Structure of a ferroelectric and ferroelastic monodomain crystal of the perovskite $BiFeO_3$. *Acta Crystallogr. B* **46**, 698–702 (1990).
17. Lebeugle, D. *et al*. Very large spontaneous electric polarization in $BiFeO_3$ single crystals at room temperature and its evolution under cycling fields. *Appl. Phys. Lett.* **91**, 022907 (2007).
18. Streiffer, S. K. *et al*. Domain patterns in epitaxial rhombohedral ferroelectric films. I. Geometry and experiments. *J. Appl. Phys.* **83**, 2742–2753 (1998).
19. Zavaliche, F. *et al*. Multiferroic $BiFeO_3$ films: Domain structure and polarization dynamics. *Phase Transit.* **79**, 991–1017 (2006).
20. Béa, H. *et al*. Influence of parasitic phases on the properties of $BiFeO_3$ epitaxial thin films. *Appl. Phys. Lett.* **87**, 072508 (2005).
21. Cruz, M. P. *et al*. Strain control of domain-wall stability in epitaxial $BiFeO_3$ (110) films. *Phys. Rev. Lett.* **99**, 217601 (2007).
22. Meyer, B. & Vanderbilt, D. Ab initio study of ferroelectric domain walls in $PbTiO_3$. *Phys. Rev. B* **65**, 104111 (2002).
23. Stemmer, S., Streiffer, S. K., Ernst, F. & Rühle, M. Atomistic structure of 90° domain walls in ferroelectric $PbTiO_3$ thin-films. *Phil. Mag. A* **71**, 713–724 (1995).
24. Floquet, N. & Valot, C. Ferroelectric domain walls in $BaTiO_3$: Structural walls model interpreting fingerprints in XRPD diagrams. *Ferroelectrics* **234**, 107–122 (1999).
25. Jia, C.-L. *et al*. Atomic-scale study of electric dipoles near charged and uncharged domain walls in ferroelectric films. *Nature Mater.* **7**, 57–61 (2008).
26. Wu, X. & Vanderbilt, D. Theory of hypothetical ferroelectric superlattices incorporating head-to-head and tail-to-tail 180 degree domain walls. *Phys. Rev. B* **73**, 020103(R) (2006).
27. Allen, L. J., McBride, W., O'Leary, N. L. & Oxley, M. P. Exit wave reconstruction at atomic resolution. *Ultramicroscopy* **100**, 91–104 (2004).
28. Ederer, C. & Spaldin, N. A. Weak ferromagnetism and magnetoelectric coupling in bismuth ferrite. *Phys. Rev. B* **71**, 060401(R) (2005).
29. Neaton, J. B. *et al*. First-principles study of spontaneous polarization in multiferroic $BiFeO_3$. *Phys. Rev. B* **71**, 014113 (2005).
30. Li, J. F. *et al*. Dramatically enhanced polarization in (001), (101), and (111) $BiFeO_3$ thin films due to epitiaxial-induced transitions. *Appl. Phys. Lett.* **84**, 5261 (2004).
31. Ravindran, P. *et al*. Theoretical investigation of magnetoelectric behavior in $BiFeO_3$. *Phys. Rev. B* **74**, 224412 (2006).
32. Lebeugle, D. *et al*. Electric-field induced spin flop in $BiFeO_3$ single crystals at room temperature. *Phys. Rev. Lett.* **100**, 227602 (2008).
33. Coene, W. M. J., Thust, A., Op de Beeck, M. & Van Dyck, D. Maximum-likelihood method for focus-variation image reconstruction in high resolution transmission electron microscopy. *Ultramicroscopy* **64**, 109–135 (1996).
34. Thust, A., Coene, W. M. J., Op de Beeck, M. & Van Dyck, D. Focal-series reconstruction in HRTEM: Simulation studies on non-periodic objects. *Ultramicroscopy* **64**, 211–230 (1996).
35. Kresse, G. & Furthmüller, J. Efficient iterative schemes for ab initio total-energy calculations using a plane-wave basis set. *Phys. Rev. B* **54**, 11169–11186 (1996).
36. Anisimov, V. I., Aryasetiawan, F. & Liechtenstein, A. I. First-principles calculations of the electronic structure and spectra of strongly correlated systems: The LDA+U method. *J. Phys. Condens. Matter* **9**, 767–808 (1997).

Acknowledgements

The work at Berkeley is supported by the Director, Office of Science, Office of Basic Energy Sciences, Materials Sciences Division of the US Department of Energy under contract No DE-AC02-05CH1123. The authors from Berkeley would like to acknowledge the support of the National Center for Electron Microscopy, Lawrence Berkeley National Laboratory. J.S. acknowledges support from the Alexander von Humboldt Foundation. Y.H.C. would also like to acknowledge the support of the National Science Council, R.O.C., under contract No NSC 97-3114-M-009-001. A.R. and S.G. acknowledge support from Deutsche Forschungsgemeinschaft through FOR 520 and Deutsche Akademische Austauschdienst through GE 1202/5-1, and N.A.S. acknowledges support from NSF DMR Award No DMR-0605852 and the Miller Institute for Basic Research in Science, UC Berkeley.

Additional information

Supplementary Information accompanies this paper on www.nature.com/naturematerials. Reprints and permissions information is available online at http://npg.nature.com/reprintsandpermissions. Correspondence and requests for materials should be addressed to J.S.

PRL **102,** 217003 (2009) PHYSICAL REVIEW LETTERS week ending 29 MAY 2009

Superconducting State in a Gallium-Doped Germanium Layer at Low Temperatures

T. Herrmannsdörfer, V. Heera, O. Ignatchik, M. Uhlarz, A. Mücklich, M. Posselt, H. Reuther, B. Schmidt, K.-H. Heinig, W. Skorupa, M. Voelskow, C. Wündisch, R. Skrotzki, M. Helm, and J. Wosnitza

Dresden High Magnetic Field Laboratory (HLD) and Institute of Ion Beam Physics and Materials Research, Forschungszentrum Dresden-Rossendorf (FZD), P.O. Box 51 01 19, D-01314 Dresden, Germany

(Received 29 January 2009; published 27 May 2009)

We demonstrate that the third elemental group-IV semiconductor, germanium, exhibits superconductivity at ambient pressure. Using advanced doping and annealing techniques of state-of-the-art semiconductor processing, we have fabricated a highly Ga-doped Ge (Ge:Ga) layer in near-intrinsic Ge. Depending on the detailed annealing conditions, we demonstrate that superconductivity can be generated and tailored in the doped semiconducting Ge host at temperatures as high as 0.5 K. Critical-field measurements reveal the quasi-two-dimensional character of superconductivity in the ~60 nm thick Ge:Ga layer. The Cooper-pair density in Ge:Ga appears to be exceptionally low.

DOI: 10.1103/PhysRevLett.102.217003 PACS numbers: 74.10.+v, 74.78.−w

Since the first observation of superconductivity in 1911, the search for new superconducting materials has offered quite a few surprises, such as the discovery of several classes of high-T_c compounds [1], but recently also the observation of superconductivity in the doped elemental semiconductors diamond [2] and silicon [3]. Although superconductivity has been observed in several doped binary semiconductors already starting in the 1960s, e.g., in doped tellurides such as GeTe [4], in $SrTiO_3$ [5], flanked and motivated by a considerable amount of theoretical work [6], as well as in SiC [7] recently, it has not been seen in the simple elemental representatives at ambient-pressure conditions before. Superconductivity of Si and Ge in their metallic high-pressure phases has been reported by Wittig already in 1966 [8]. However, it needed more than four decades to drive Si and diamond superconducting at ambient-pressure conditions, owed to the sophisticated preparation techniques required and maybe due to the prejudice that superconductivity might not be possible in the archetypical semiconductors. Compared to Si and diamond, Ge seems to be even less promising for the search of superconductivity as theoretical studies predict only a weak tendency towards superconductivity in heavily n-type [9] and p-type doped Ge [10].

In order to obtain superconductivity in group-IV semiconductors, heavy p-type doping well above the metal-insulator transition is required. Otherwise the charge-carrier density of these materials is too low to create a superconducting state at low temperatures. Ekimov *et al.* have observed superconductivity in diamonds containing high boron (B) concentrations prepared by a high-pressure and high-temperature technique at temperatures up to $T_c = 2.3$ K [2]. Bustarret *et al.* [3] have investigated boron-supersaturated Si layers processed by ultra-short-time laser melting and found superconductivity at $T_c = 0.34$ K. For this work, Ga has been chosen as acceptor atom due to its high solid solubility in Ge (up to ~1 at. % at 700 °C). Ion implantation as an effective method for introducing high concentrations of dopants has been used. The ion-beam technique is highly selective since it allows for a precise control of the amount of the implanted species and its depth distribution. Here, we have succeeded in producing samples with a peak concentration of 8 at. % Ga in a thin layer of Ge with a full width at half maximum of approximately 60 nm (see Fig. 1). However, high-dose ion implantation causes severe lattice damage which may be difficult to anneal as observed for B-doped diamond where the formation of graphite may further complicate a reconstruction of the lattice [11,12] and where the superconducting phase might be located in amorphous boron-rich intergranular layers and pockets [13]. In Ge (and Si), annealing of implantation damage is easier to achieve than in diamond. Here, the challenge is to reconstruct the crystalline structure without causing long-range diffusion, precipitation, and subsequent clustering of acceptor atoms in the supersaturated semiconductor. Flashlamp annealing in the millisecond range is known to be a versatile tool to remove the implantation damage and to achieve dopant activation in thin semiconductor layers [14–16]. Because of the short thermal-processing time, this method is much less affected by diffusion and precipitation problems. Depending on light-pulse energy and duration, flashlamp annealing leads to solid-phase epitaxial or liquid-phase epitaxial regrowth of the amorphous layers formed during the high-dose implantation. Here, we have treated samples using various flashlamp fluences Φ after implanting. This resulted in samples with a slightly decreased peak concentration of 6 at. % Ga after annealing (see Fig. 1), corresponding to 2.6×10^{21} Ga atoms/cm^3. No evidence for the formation of Ga clusters or filaments has been found during careful sample analysis. The charge-carrier concentration of the Ge:Ga samples has been determined at low temperatures, $T \leq 2.5$ K, by means of Hall-effect measurements (see inset of Fig. 3). A summary of the most important parameters of five samples is given in Table I. The hole concentration extracted from Hall measurements

 © 2009 The American Physical Society

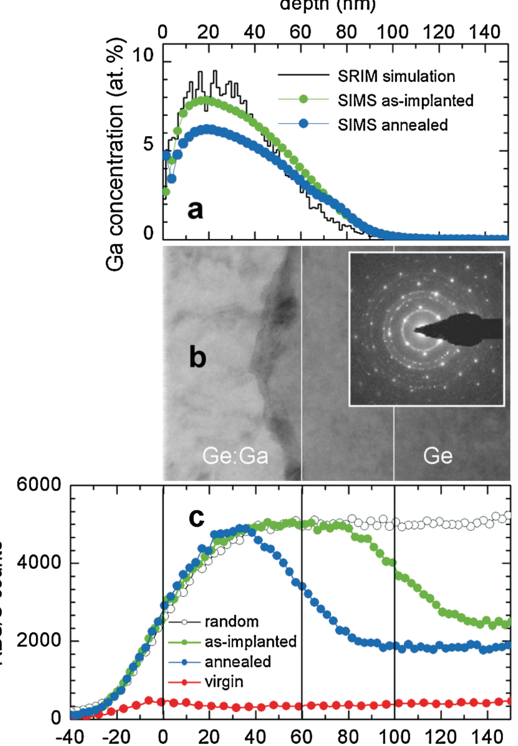

FIG. 1 (color). (a) Ga depth distribution obtained by secondary ion mass spectrometry (SIMS) of a Ge:Ga sample before and after annealing ($\Phi = 50.8$ J/cm^2) compared to a Ga profile simulated for an as-implanted Ge:Ga sample using the SRIM code [22]. (b) The cross-sectional transmission electron micrograph and the diffraction pattern (inset) from the same region demonstrate that the implanted layer is completely (poly)recrystallized after flashlamp annealing down to about 50–60 nm, followed by $\approx$ 10 nm thin wavy interface (indicated by the left white line) between the polycrystalline layer and the single-crystalline region. The initial amorphous-crystalline interface is indicated by the right white line. (c) Results of a channeled-ion Rutherford backscattering (RBS/C) analysis confirm the random orientation of the Ge grains. The backscattering signal for the annealed sample reaches the same value as in random orientation. For comparison the RBS/C results of unimplanted (virgin) and as-implanted Ge are shown.

varies considerably with the flashlamp fluence. At a small fluence, $\Phi = 45.5$ J/cm^2, the hole concentration is up to 1 order of magnitude smaller than the Ga concentration determined from secondary ion mass spectrometry (SIMS), indicating the only partial electrical activation of the dopants. With increasing fluence, the hole concentration also increases to 1.4×10^{21} cm^{-3} reflecting that half of the implanted Ga atoms have been activated.

Measurements of the electrical-transport properties were carried out from 300 K to 20 mK and are presented in Fig. 2. Data were taken using low ac-excitation currents (down to 10 nA) in order to keep the electrical current density in the thin Ge:Ga layer moderate. The unimplanted sample exhibits the typical behavior of semiconducting

TABLE I. Fluence Φ used during 3 ms of flashlamp annealing, critical superconducting transition temperature T_c (taking the 50% drop of R), critical magnetic field aligned in plane, $B_{c\parallel}$, and perpendicular to the Ge:Ga layer, $B_{c\perp}$, as well as charge-carrier concentration obtained from Hall-effect measurement, n_{Hall}, of five Ge:Ga samples.

Ge:Ga sample	a	b	c	d	e
Φ (J/cm^2)	45.5	48.1	50.8	53.6	62.4
T_c (K)	···	0.14[a]	0.45	0.19	···
$B_{c\parallel}$ (T)	···	···	1.1	0.18	···
$B_{c\perp}$ (T)	···	···	0.30	0.025	···
n_{Hall} (10^{21} cm^{-3})	0.28	0.32	0.43	1.4	1.0

[a]For sample b, a nonzero residual resistance was measured at $T < T_c^*$.

bulk n-type Ge with a resistance drop due to the increasing mobility upon lowering the temperature, and a subsequent resistance increase due to carrier freeze-out. The as-implanted Ge:Ga sample also shows an increasing resistance below about 40 K despite the high doping level. This is due to the large damage induced by implantation and implies that the dopants are not electrically activated. In contrast, the sample which has been flashlamp annealed (fluence $\Phi = 53.6$ J/cm^2) for $t = 3$ ms exhibits metallic behavior, indicating that a significant part of the dopants has been electrically activated. Below $T = 0.5$ K, the resistivity drops to zero (Fig. 2) indicating the onset of superconductivity. In more detail, in the inset of Fig. 2 it is shown how the annealing conditions influence the normal and superconducting properties of the Ge:Ga samples. The residual normal-state resistivity is clearly affected by the annealing conditions. Upon increasing flashlamp fluence, the residual resistivity drops by a factor of 3. Compared to that, we observed a more elaborate dependence of the superconducting properties on the annealing conditions (see Table I). By keeping the flashlamp expo-

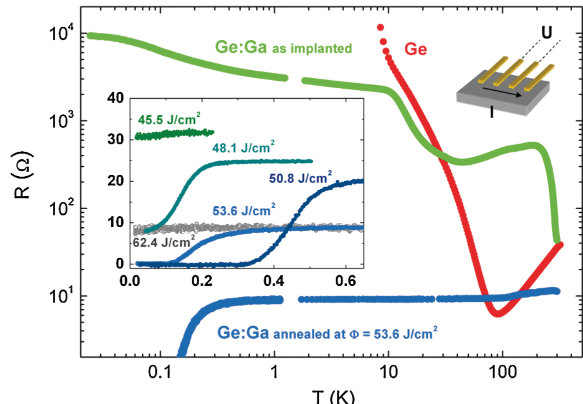

FIG. 2 (color). Temperature dependence of the electrical resistance of unimplanted Ge and as-implanted as well as annealed Ge:Ga ($\Phi = 53.6$ J/cm^2, $t = 3$ ms) taken in $B = 0$. Only annealed Ge:Ga exhibits superconductivity below 0.5 K, depending on the flashlamp fluence Φ (see inset).

sure time constant (3 ms) but varying the fluence stepwise in the range $45 \leq \Phi \leq 62.4$ J/cm^2, and consequently varying the maximum annealing temperature, the occurrence of superconductivity can be triggered and, when further increasing Φ, even suppressed. The fluence of 45.5 J/cm^2 is not yet sufficient to induce a sample modification which allows for the creation of a superconducting state. At $\Phi = 48.1$ J/cm^2, the onset of superconductivity is visible (inset of Fig. 2) and the highest transition temperature, $T_c = 0.45$ K, is achieved at $\Phi = 50.8$ J/cm^2. Tuning the annealing conditions to higher fluences, superconductivity starts to disappear. At $\Phi = 53.6$ J/cm^2, T_c is reduced to about 0.2 K and at $\Phi = 62.4$ J/cm^2 a superconducting transition has not been observed in the temperature range accessible to us, i.e., at $T \geq 20$ mK. The reproducibility of the annealing process with respect to the creation of superconductivity has been verified for several samples prepared separately under identical conditions. Thus superconductivity only occurs in a narrow region of optimized parameters; in particular, the activation of charge carriers appears to be rather delicate. It should be mentioned that the maximum T_c is not observed in the sample with the largest charge-carrier concentration 1.4×10^{21} cm^{-3}, but in the sample that has only one third, 0.43×10^{21} cm^{-3}, of the highest level of activated Ga atoms instead. The width of the superconducting transition is rather broad, reflecting the inhomogeneous charge-carrier profile of the Ge:Ga layers.

The superconducting transition temperature of Ge:Ga, $T_c \leq 0.45$ K, compares well to the one of B-doped diamond [2], C:B, taking into account the qualitative expectation of phonon-mediated superconductors, $T_c \sim \Theta_D$. Whereas the ratios of the superconducting transition temperatures, $T_c(\text{C:B})/T_c(\text{Ge:Ga}) = 5.1$, and of the Debye temperatures, $\theta_D(\text{C:B})/\theta_D(\text{Ge:Ga}) = 1860\text{ K}/374\text{ K} = 5.0$, match well, the comparison of these properties with the data of B-doped Si [3] ($T_c = 0.34$, $\Theta_D = 645$ K) is less striking and might emphasize the influence of doping levels and individual electron-phonon coupling on the superconducting state of group-IV semiconductors. However, a reasonable scaling of T_c and Θ_D might support the notion of phonon-mediated superconductivity in this material class. Although the critical temperature of Ge:Ga is about 0.5 K, the critical magnetic field, B_c, reaches a value slightly above 1 T (see Table I). Both samples that undergo a complete superconducting transition exhibit a distinct dependence of the superconducting critical field on its orientation relative to the Ge:Ga layer. Superconductivity remains stable to clearly higher critical magnetic fields, $B_{c\parallel}$, when aligned in plane compared to when aligned perpendicular to the Ge:Ga plane, $B_{c\perp}$. The anisotropy reaches a maximum in the sample which has been annealed at $\Phi = 53.6$ J/cm^2 where $B_{c\parallel}/B_{c\perp} = 7$ (see Fig. 3). From a qualitative point of view, this strong anisotropy of the critical magnetic field is typical for a thin-layered superconductor and may be considered as proof

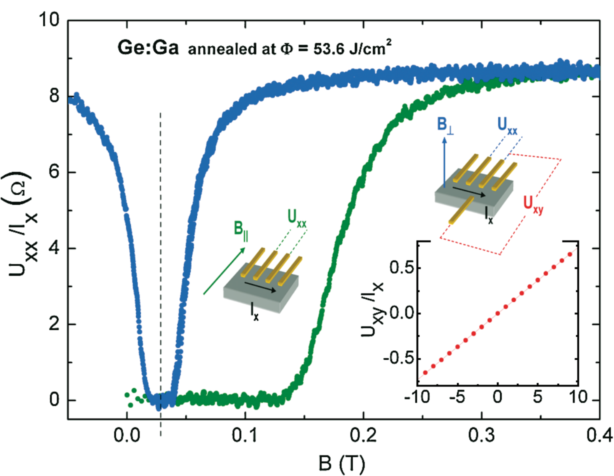

FIG. 3 (color). Electrical-transport data of a Ge:Ga sample (flashlamp annealed at $\Phi = 53.6$ J/cm^2) as function of the magnetic field aligned in plane $B_\parallel$ (green), and perpendicular $B_\perp$ (blue). The offset of B (dashed line at ~27 mT) results from frozen flux in the superconducting 20 T magnet after Hall-effect measurements (red data in inset).

that Ga is incorporated in the Ge matrix homogeneously in a thin layer in agreement with our structural analysis. The anisotropy of the superconducting critical field also allows for excluding superconductivity mediated by Ga clusters in the samples. The maximum possible in-plane fields, $B_{c\parallel}$, are attributed to the so-called Pauli limit where the high polarization of the electron spins is responsible for Cooper-pair breaking, whereas $B_{c\perp}$ is considered to be related to the orbital-limiting fields. It is remarkable that the theoretical Pauli limit in simple approximation [17], $B_P/T_c = 1.84$ (T/K), is exceeded in the sample with the highest T_c (0.45 K) and $B_{c\parallel}$ (~1.1 T) annealed at 50.8 J/cm^2, where $B_\parallel/T_c = 2.4$ (T/K) (see Fig. 4). However, the large relative width of the superconducting transition hinders further conclusions. The temperature dependences of $B_{c\parallel}(T)$ and $B_{c\perp}(T)$ clearly deviate from the one of a simple bulk BCS superconductor, $B_c(T) = B_{c0}[1 - (T/T_{c0})^2]$. Even the Werthamer-Helfand-Hohenberg (WHH) theory [18] as a quantitative approach for type-II superconductors with a linear upper critical field, $B_{c2}(T) \sim T$ at $T > 0.5T_{c0}$, does not reasonably describe the critical field of Ge:Ga as $B_{c\parallel}(T)$ is linear down to lower temperatures, $0.1T_{c0}$, and $B_{c\perp}(T)$ is even superlinear at $T < T_{c0}$. A more detailed study of the curvature of $B_{c\parallel,\perp}(T)$ will be the subject of a more extended work on Ge:Ga where various scenarios for deviations from WHH theory (see, e.g., Boebinger *et al.* [19]) will be taken into account. From the orbital-limiting critical field, we deduce the coherence length as in the case of bulk superconductors according to $\xi = (\phi_0/2\pi B_{c\perp})^{1/2}$, where $\phi_0 = h/2e = 2.068 \times 10^{-15}$ Wb is the flux quantum. From $B_{c\perp}$, one obtains $\xi = 33$ (115) nm for $\Phi = 50.8$ (53.6) J/cm^2. These values may be taken to estimate the in-plane critical field, $B_{c\parallel}(\xi) = \sqrt{6}\phi_0/(\pi\xi d)$, where d

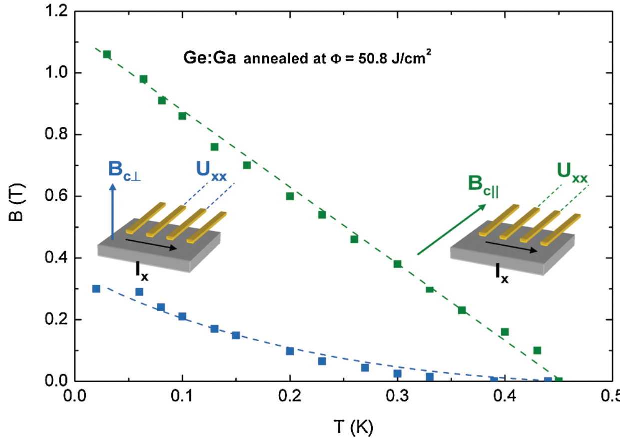

FIG. 4 (color). Field-temperature phase diagram of the Ge:Ga sample (flash lamp annealed at $\Phi = 50.8\ \mathrm{J/cm^2}$) with the highest T_c at 0.45 K for two magnetic-field orientations relative to the Ge:Ga plane (see illustrations).

is the thickness of the Ga-doped layer and $\sqrt{6}$ is a correction factor for a thin-plate geometry [20]. Using $d = 60$ nm leads to $B_{c\|}(\xi) = 0.81$ (0.23) T for $\Phi = 50.8$ (53.6) $\mathrm{J/cm^2}$, in reasonable agreement with the experimental values (Table I). By use of the nonlinear Ginzburg-Landau theory, the critical-current density J_c of a thin-film superconductor may be estimated [21] using $J_c = ehn_s/(3\pi\sqrt{3}m\xi)$. We have measured a critical superconducting current of about 10 μA. Using the superconducting critical-current density, $J_c = 10\ \mu\mathrm{A}/(1\ \mathrm{cm} \times 60\ \mathrm{nm}) = 1.7 \times 10^4\ \mathrm{A/m^2}$ (spanned by the 60 nm thick Ga-doped Ge layer and the sample width of 1 cm) and the above calculated coherence length ξ, allows for an estimate of n_s. We obtain a superconducting charge-carrier density, $n_s = 2.7 \times 10^{14}\ \mathrm{cm^{-3}}$ ($\Phi = 53.6\ \mathrm{J/cm^2}$), which is by orders of magnitude smaller than the normal-conducting charge-carrier density, deduced from Hall measurements, $n \approx 1 \times 10^{21}\ \mathrm{cm^{-3}}$. In this context, an effective mass of the charge carriers equal to the bare mass of free electrons, $m = m_e$, has been used for simplicity. In the case of light holes, $m \ll m_e$, n_s would be even smaller. Using $\lambda_L = \sqrt{m/(\mu_0 n_s e^2)}$ for the calculation of the London penetration depth leads to λ_L of the order of $10^2\ \mu$m. Such a large London penetration depth makes the detection of superconductivity by inductive measurements virtually impossible in our thin Ge:Ga layers. Also the observation of a superconducting transition of Ge:Ga by means of heat capacity and NMR will be challenging as only a tiny jump of specific heat and an exiguous decrease of Pauli susceptibility and NMR Knight shift can be expected due to the very low Cooper-pair density. Therefore, the transport measurements reported here appear to be the only reliable means for the proof of superconductivity. According to λ_L/ξ of about 10^3–10^4, Ge:Ga may be considered as a superconductor in the extreme type-II limit.

In summary, the finding of superconductivity in Ga-doped Ge layers sheds new light on doped elemental semiconductors which might even serve as superconducting model systems as they allow for a tuning of their superconducting parameters via a modification of their hole concentration. The combination of ion implantation and subsequent flashlamp annealing can be employed to fabricate tailored thin-layer superconductors. Although the critical superconducting temperatures of Ge:Ga are far below those of high-temperature superconductors, there is a qualitative relationship between these systems concerning their $T_c(x)$-phase diagrams. Both in the high-temperature superconductors and in Ge:Ga, there is a limited range of the charge-carrier (hole) concentration x which allows for the occurrence of superconductivity, and there is an optimum concentration where $T_c(x)$ is maximum. For further conclusions, of course, it would be of interest to explore the detailed relation between annealing parameters, carrier density, as well as critical temperatures and to also try other dopants in order to generate superconductivity in Ge.

The authors acknowledge the support of F. Arnold, M. Bartkowiak, and R. Beyer (FZD) for transport measurements as well as of H. Hortenbach and S. Teichert (Qimonda Dresden) for SIMS analysis. Part of this work was supported by EuroMagNET.

[1] J. Bednorz and K. A. Müller, Z. Phys. B **64**, 189 (1986).
[2] E. A. Ekimov *et al.*, Nature (London) **428**, 542 (2004).
[3] E. Bustarret *et al.*, Nature (London) **444**, 465 (2006).
[4] R. A. Hein *et al.*, Phys. Rev. Lett. **12**, 320 (1964).
[5] J. F. Schooley *et al.*, Phys. Rev. Lett. **12**, 474 (1964).
[6] C. S. Koonce *et al.*, Phys. Rev. **177**, 707 (1969).
[7] Z. Ren *et al.*, J. Phys. Soc. Jpn. **76**, 103710 (2007).
[8] J. Wittig, Z. Phys. **195**, 215 (1966).
[9] W. Klose, Adv. Solid State Phys. **7**, 1 (1967).
[10] L. Boeri *et al.*, Phys. Rev. Lett. **93**, 237002 (2004).
[11] T. Tshepe, *et al.*, Phys. Rev. B **70**, 245107 (2004).
[12] V. Heera *et al.*, Diam. Relat. Mater. **17**, 383 (2008).
[13] N. Dubrovinskaia *et al.*, Proc. Natl. Acad. Sci. U.S.A. **105**, 11 619 (2008).
[14] W. Skorupa *et al.*, J. Electrochem. Soc. **152**, G436 (2005).
[15] M. Voelskow *et al.*, Appl. Phys. Lett. **87**, 241901 (2005).
[16] R. A. McMahon *et al.*, Vacuum **81**, 1301 (2007).
[17] A. M. Clogston, Phys. Rev. Lett. **9**, 266 (1962).
[18] E. Helfand *et al.*, Phys. Rev. Lett. **13**, 686 (1964); Phys. Rev. **147**, 288 (1966); N. R. Werthamer *et al.*, Phys. Rev. **147**, 295 (1966).
[19] G. Boebinger *et al.*, Phys. Rev. B **46**, 5876 (1992).
[20] M. Tinkham, Phys. Rev. **129**, 2413 (1963).
[21] L.-P. Levy, *Magnetism and Superconductivity* (Springer, New York, 2000).
[22] J. F. Ziegler *et al.*, *The Stopping and Range of Ions in Solids* (Pergamon, New York, 1985); www.SRIM.org.

PRL 103, 255501 (2009) PHYSICAL REVIEW LETTERS week ending 18 DECEMBER 2009

Interstitial-Mediated Diffusion in Germanium under Proton Irradiation

H. Bracht,[1,*] S. Schneider,[1] J. N. Klug,[2] C. Y. Liao,[3] J. Lundsgaard Hansen,[4] E. E. Haller,[3] A. Nylandsted Larsen,[4] D. Bougeard,[5] M. Posselt,[6] and C. Wündisch[6]

[1]*Institute of Materials Physics, University of Münster, Wilhelm-Klemm-Straße 10, D-48149 Münster, Germany*
[2]*RUBION, Ruhr-Universität Bochum, Universitätsstraße 150, D-44780 Bochum, Germany*
[3]*MS&E Department, University of California at Berkeley, and Lawrence Berkeley National Laboratory, 1 Cyclotron Road, Berkeley, California 94720, USA*
[4]*Department of Physics and Astronomy, Aarhus University, Ny Munkegade, DK-8000 Aarhus, Denmark*
[5]*Walter Schottky Institute, Technical University of Munich, Am Coulombwall 3, D-85748 Garching, Germany*
[6]*Forschungszentrum Dresden-Rossendorf, Institute of Ion Beam Physics and Materials Research, D-01314 Dresden, Germany*

(Received 26 August 2009; published 16 December 2009)

We report experiments on the impact of 2.5 MeV proton irradiation on self-diffusion and dopant diffusion in germanium (Ge). Self-diffusion under irradiation reveals an unusual depth independent broadening of the Ge isotope multilayer structure. This behavior and the observed enhanced diffusion of *B* and retarded diffusion of *P* demonstrates that an interstitial-mediated diffusion process dominates in Ge under irradiation. This fundamental finding opens up unique ways to suppress vacancy-mediated diffusion in Ge and to solve the donor deactivation problem that hinders the fabrication of Ge-based nanoelectronic devices.

DOI: 10.1103/PhysRevLett.103.255501 PACS numbers: 61.80.Jh, 61.72.jj, 61.82.Fk, 81.40.Wx

Over the past few years the elemental semiconductor Ge has been the subject of many experimental [1–13] and theoretical investigations [14–25] to elucidate the electronic and diffusion properties of point defects as well as their interaction. Understanding these properties helps to develop strategies for efficient defect engineering that are crucial for the fabrication of the next generation of nanoelectronic devices. Utilizing Ge instead of silicon (Si) for complementary metal oxide semiconductors (CMOS) technology one can take advantage of the higher electron and hole mobilities in Ge compared to Si [26]. Whereas the *p*-channel Ge-MOSFET (metal oxide semiconductor field-effect transistor) made of heavily *B* doped source and drain regions was already demonstrated [27], the *n*-channel MOSFET remains a challenge due to the enhanced diffusion of *n*-type dopants such as *P*, As, and Sb under extrinsic doping conditions and the deactivation of the donors for concentrations exceeding 10^{19} cm^{-3} [7,9,27]. The enhanced diffusion is a consequence of the singly negatively charged donor-vacancy $(AV)^-$ pair that mediates donor diffusion in Ge according to the reaction [7,9]

$$(AV)^- \leftrightarrow A_s^+ + V^{2-} \quad (1)$$

where A_s^+ and V^{2-} are the singly positively charged substitutional donor with $A \in \{\mathrm{P, As, Sb}\}$ and the doubly negatively charged vacancy (V^{2-}), respectively. The deactivation is related to the formation of inactive donor-vacancy clusters whose formation is favored due to Coulomb attraction between A_s^+ and $(AV)^-$ via the reaction [9]

$$(AV)^- + A_s^+ \leftrightarrow (A_2V)^0. \quad (2)$$

The formation of A_2V and even bigger clusters A_nV_m is consistent with the predictions of density functional theory calculations [23]. Reactions (1) and (2) indicate that the donor-vacancy pair mediates both the diffusion and deactivation of *n*-type dopants in Ge. Effective defect engineering that aims to suppress the enhanced diffusion and deactivation of donors in Ge should reduce the concentration of the *AV* pairs. In this letter we demonstrate that defect engineering with Ge interstitials makes it possible to effectively suppress the enhanced diffusion of donor atoms.

The formation enthalpy of interstitials is predicted to be much higher than that of vacancies in Ge [19,20]. Accordingly, atomic transport in Ge under thermal equilibrium is mainly mediated by vacancies [7]. However, interstitials in Ge can be formed under irradiation as demonstrated in previous studies [10,13]. Stimulated by these results and the understanding on the evolution of interstitial clusters in Si [28], the impact of implantation damage on the diffusion in Ge was investigated by several research groups [11,12,29]. However, post anneals of dopant implanted Ge did not reveal any significant TED or transient retarded diffusion (TRD) [29,30]. Instead, it is generally observed, that the implantation damage in Ge recovers fast even at low temperatures [29,30].

In order to investigate the impact of interstitials on diffusion in Ge we performed diffusion experiments under proton irradiation. For these experiments we utilized a single crystalline Ge isotope multilayer structure consisting of 20 alternating enriched ^{70}Ge (96% enrichment) and natural Ge layers. With a thickness of 15 nm for each layer a total thickness of 300 nm is obtained. The isotope struc-

 © 2009 The American Physical Society

ture was grown by molecular beam epitaxy (MBE) on a (100)-oriented Ge wafer at 250 °C. The distribution of ^{74}Ge within the multilayer measured with secondary ion mass spectrometry (SIMS) is illustrated in Fig. 1. In addition, we used a MBE grown structure with six *B*-doped Ge layers. The *B*-doped layers are each about 25 nm thick and separated by 100 nm undoped Ge. With a 100 nm thick undoped Ge cap and a buffer layer of 100 nm the total thickness of the single crystalline *B*-doped Ge structure is about 800 nm. A SIMS analysis of the as-grown *B*-doped structure is illustrated in Fig. 2. Finally, a Ge sample implanted with *P* at 30 keV to a dose of 3×10^{15} cm^{-2} was prepared. In order to prevent outdiffusion of *P* during annealing a 10 nm thick SiO_2 layer was sputter deposited on the Ge sample before implantation. A SIMS analysis of the as-implanted *P* profile is illustrated in Fig. 3.

Samples with lateral dimensions of 4×4 mm^2 were cut from the as-grown or as-implanted Ge wafers, thinned to a thickness of 30(±5) μm, and polished with Nalco 2360 (Bucher AG, Switzerland) to obtain a scratch free and specular surface on the back. The samples were mounted on a graphite holder and fixed via a graphite plate with a circular aperture of 3 mm in diameter. In this way the outer part of the Ge sample was covered with graphite and not exposed to the proton beam. The graphite holder was placed on a boron nitride heating plate that enables heating of the Ge sample during irradiation. The temperature was controlled with a thermocouple mounted 1 mm below the sample in the graphite holder. The whole sample holder was attached to a high vacuum chamber. Protons of 2.5 MeV were supplied via a beam line from a dynamitron accelerator. The beam was defocused and swept to achieve a homogeneously irradiated circular area with a diameter of 1 cm. An electron suppression, which consists of a negatively biased (600 V) screen, ensures that the measurement of the proton current is not hampered by secondary electrons. Proton irradiations were performed at 570 and 600 °C with a proton flux of 1.5 μA. The high energy of the protons assures that the protons penetrate through the Ge sample as this is ascertained by simulations of the "stopping and range of ions in matter" (SRIM [31]). After annealing under proton irradiation the respective concentration profiles of ^{74}Ge, *B*, and *P* were measured with SIMS. The depth of the SIMS craters was determined using an optical profilometer.

Figure 1 shows the concentration profile of ^{74}Ge after proton irradiation at 600 °C for 90 min (see red circles). The broadening of the isotope structure under thermal equilibrium measured with SIMS at the outer part of the samples is illustrated by the blue squares. The Ge profile from the proton exposed inner part of Ge isotope sample

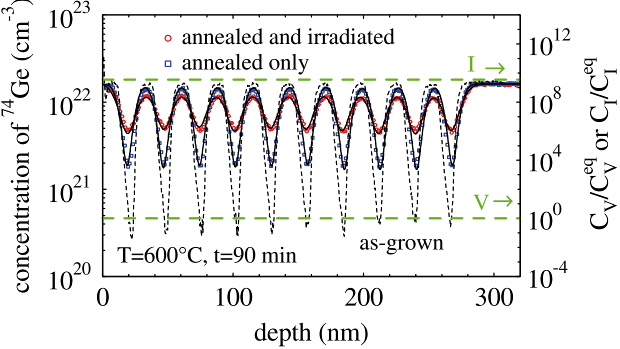

FIG. 1 (color online). Concentration profiles of ^{74}Ge measured with TOF-SIMS before (as-grown: thin dashed line) and after annealing (symbols) at the temperature and time indicated. Only every 6th data point is shown for clarity. The ^{74}Ge profile from the covered part of the sample (blue squares) represents Ge diffusion under equilibrium condition. The corresponding black solid line shows the expected Ge diffusion profile for self-diffusion under equilibrium conditions at 600 °C taking into account published self-diffusion data [34]. The ^{74}Ge profile obtained from the proton irradiated area of the sample (red circles) indicates an enhanced Ge diffusion under irradiation with respect to equilibrium conditions. The corresponding black solid line shows the numerical simulation of self-diffusion under irradiation assuming different boundary conditions for vacancies and self-interstitials (see text for details). The corresponding concentration profiles of vacancies and self-interstitials normalized to the respective equilibrium concentration (see right *y* axis) are displayed by the lower and upper green dashed lines, respectively.

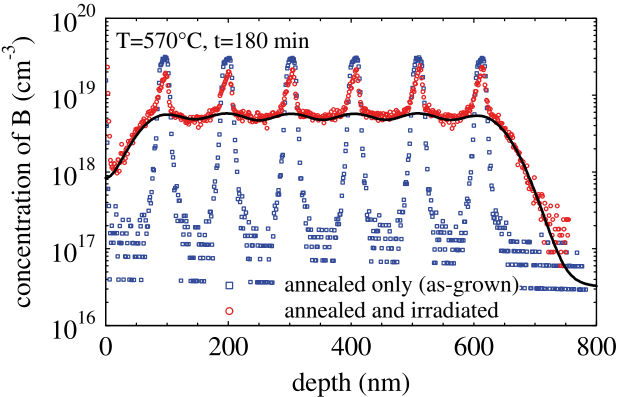

FIG. 2 (color online). Concentration profiles of *B* in Ge measured with TOF-SIMS after diffusion annealing at the temperature and time indicated. For clarity only every 6th data point is shown. The *B* profile from the covered part of the sample (blue squares) represents *B* diffusion under equilibrium conditions. This profile equals the as-grown profile because *B* diffusion in thermal equilibrium is very slow [4]. The *B* profile obtained from the proton irradiated area of the sample (red circles) indicates an enhanced *B* diffusion under irradiation with respect to equilibrium conditions. The black solid line shows a simulation of *B* diffusion based on Fick's second law with a concentration independent effective diffusion coefficient of 7.5×10^{-16} cm^2 s^{-1} which exceeds the equilibrium diffusion of *B* by several orders of magnitude.

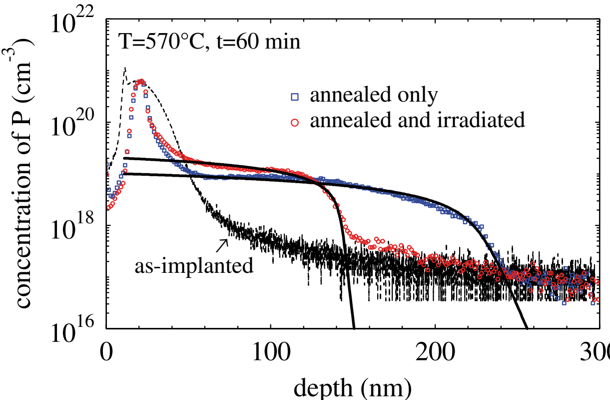

FIG. 3 (color online). Concentration profiles of P-implanted Ge measured with TOF-SIMS before (thin black dashed line) and after diffusion annealing (symbols) at the temperature and time indicated. Only every 6th data point is shown for clarity. The P profile from the covered part of the sample (blue squares) represents P diffusion under equilibrium conditions. The corresponding black solid line shows the expected P profile for diffusion under equilibrium conditions at 600 °C taking into account published data [7]. The P profile obtained from the proton irradiated area of the sample (red circles) indicates a retarded P diffusion under irradiation with respect to equilibrium conditions. The corresponding black solid line is a numerical simulation of the concentration dependent P diffusion that reveals a factor of 20 lower effective diffusion coefficient of P under irradiation compared to equilibrium conditions. Note, the 10 nm thick SiO_2 cap layer was not removed for the SIMS analysis and considered in the simulations of P diffusion by an offset in the profile. The high P concentrations in the peak region of the implanted P profiles likely reflect the formation of P clusters.

shows a more pronounced intermixing. This unambiguously demonstrates an enhanced self-diffusion under irradiation. The homogenous broadening of the isotope structure under irradiation is, however, very unusual. This reveals that no gradient in the concentration of the native point defects versus depth exists. Usually the free surface acts as sink for vacancies and self-interstitials that are formed by proton irradiation in equal numbers and concentrations (see, e.g., [32]). The homogenous broadening of the Ge isotope structures reflects that thermal equilibrium is disturbed at the surface. The Ge profile alone can not tell us whether this holds for both vacancies and self-interstitials or just for one of these defects. In order to identify the surface condition, we performed additional experiments with B-doped and P-implanted Ge samples. Under thermal equilibrium the diffusion of B in Ge is very low; its diffusion coefficient is several orders of magnitude smaller than the self-diffusion coefficient [4]. This behavior is in accord with theoretical calculations [18] that predict a repulsive interaction between substitutional B and the vacancy. Annealing of the B-doped multilayer structure at 570 °C under proton irradiation leads to a very strong intermixing as illustrated by Fig. 2. For comparison, the B profile beneath the outer part of the Ge sample, covered by a graphite plate, did not show any broadening at all, i.e., the as-grown B profile is reproduced. The strong enhancement of B diffusion under irradiation is likely caused by interstitials whose concentration under irradiation exceeds their thermal equilibrium concentration by several orders of magnitude. The B spikes with a concentration of 3×10^{19} cm^{-3} that interfere with the diffusion profile reveal an immobile fraction of B in Ge. This is similar to the behavior of B in Si where B-interstitial clusters have been identified as the origin of the immobile B fraction [28]. The concept of an interstitial-mediated diffusion in Ge under irradiation is confirmed by the diffusion behavior of P. P diffusion is mediated by donor-vacancy pairs via the vacancy mechanism [see Eq. (1)] [7,9]. In the case interstitials dominate under proton irradiation the diffusion of P should be retarded. Indeed, Fig. 3 demonstrates a reduced penetration depth of P compared to the profile measured beneath the covered part of the same Ge sample.

The results of the impact of proton irradiation on self- and dopant diffusion in Ge show that the Ge surface is not an efficient sink for interstitials. The interstitials created during irradiation are assumed to be reflected at the Ge surface. The vacancies that are produced in equal number are annihilated at the surface and in the bulk via recombination with interstitials. During irradiation the concentration of interstitials increases and, finally, dominates over the vacancy concentration, and promotes an interstitial-mediated diffusion. This diffusion behavior can be modeled on the basis of a continuum theoretical approach that considers the formation of point defects by irradiation and their annihilation via the Frenkel pair reaction [10]. Numerical simulations provide an accurate description of the experimental Ge profile when reflecting boundary conditions for the Ge interstitials are assumed. The calculated profile is given by the black solid line in Fig. 1. Analysis of the B profile reveals an enhancement factor of 2.8×10^7 for B diffusion under irradiation compared to equilibrium diffusion [4] (see Fig. 2). The analysis of the P profiles shown in Fig. 3 yields a retardation factor of about 20 for P diffusion under irradiation.

The inability of the Ge surface to annihilate interstitials leads to the interstitial-mediated diffusion under irradiation. Recently, interstitials in Ge were formed via electron irradiation and directly observed by means of HRTEM [33]. Their direct observation would be hardly possible in the case the Ge surface is a perfect sink for interstitials. The property of the Ge surface seems to hold for bare surfaces like those prepared in Ref. [33] and surfaces covered with impurities. Our samples were annealed and proton irradiated in a vacuum of about 10^{-6} mbar. Under these conditions they certainly do not exhibit bare surfaces. This also applies to the P-implanted sample with a thin SiO_2 layer on top.

In conclusion, our experiments on self- and dopant diffusion in Ge under proton irradiation clearly demonstrate that interstitial-mediated diffusion is favored under irradiation that promotes *B* diffusion and retards *P* diffusion. These findings open up new strategies to effectively suppress vacancy-mediated diffusion in Ge that prevails under thermal equilibrium conditions. Thermal treatments under irradiation are proposed to solve the diffusion and also the doping issues that limit today the fabrication of Ge *n*-channel MOSFET's.

This work was supported by the Deutsche Forschungsgemeinschaft under contract number BR 1520/6-2.

*Corresponding author.
bracht@uni-muenster.de

[1] *Germanium-Based Technologies—From Materials to Devices*, edited by C. Claeys and E. Simoen (Elsevier, Amsterdam, 2007).
[2] H. Häßlein, R. Sielemann, and C. Zistl, Phys. Rev. Lett. **80**, 2626 (1998).
[3] V.P. Markevich, I.D. Hawkins, A.R. Peaker, K.V. Emtsev, V.V. Emtsev, V.V. Litvinov, F.L.I. Murin, and L. Dobaczewski, Phys. Rev. B **70**, 235213 (2004).
[4] S. Uppal, A.F.W. Willoughby, J.M. Bonar, N.E.B. Cowern, T. Grasby, R.J.H. Morris, and M.G. Dowsett, J. Appl. Phys. **96**, 1376 (2004).
[5] C.E. Lindberg, J. Lundsgaard Hansen, P. Bomholt, A. Mesli, K. Bonde Nielsen, A. Nylandsted Larsen, and L. Dobaczewski, Appl. Phys. Lett. **87**, 172103 (2005).
[6] V. Emtsev, Mater. Sci. Semicond. Process. **9**, 580 (2006).
[7] S. Brotzmann and H. Bracht, J. Appl. Phys. **103**, 033508 (2008).
[8] A. Mesli, L. Dobaczewski, K. Bonde Nielsen, V. Kolkovsky, M. Christian Petersen, and A. Nylandsted Larsen, Phys. Rev. B **78**, 165202 (2008).
[9] S. Brotzmann, H. Bracht, J. Lundsgaard Hansen, A. Nylandsted Larsen, E. Simoen, E.E. Haller, J.S. Christensen, and P. Werner, Phys. Rev. B **77**, 235207 (2008).
[10] S. Schneider, H. Bracht, M.C. Petersen, J. Lundsgaard Hansen, and A. Nylandsted Larsen, J. Appl. Phys. **103**, 033517 (2008).
[11] G. Impellizzeri, S. Mirabella, E. Bruno, A.M. Piro, and M.G. Grimaldi, J. Appl. Phys. **105**, 063533 (2009).
[12] P. Tsouroutas, D. Tsoukalas, I. Zergioti, N. Cherkashin, and A. Claverie, J. Appl. Phys. **105**, 094910 (2009).
[13] E. Bruno, S. Mirabella, G. Scapellato, G. Impellizzeri, A. Terrasi, F. Priolo, E. Napolitani, D. De Salvador, M. Mastromatteo, and A. Carnera, Phys. Rev. B **80**, 033204 (2009).
[14] A. Fazzio, A. Janotti, Antonio J.R. da Silva, and R. Mota, Phys. Rev. B **61**, R2401 (2000).
[15] M. Dionízio Moreira, R.H. Miwa, and P. Venezuela, Phys. Rev. B **70**, 115215 (2004).
[16] H. Höhler, N. Atodiresei, K. Schroeder, R. Zeller, and P.H. Dederichs, Phys. Rev. B **71**, 035212 (2005).
[17] J. Coutinho, S. Öberg, V.J.B. Torres, M. Barroso, R. Jones, and P.R. Briddon, Phys. Rev. B **73**, 235213 (2006).
[18] A. Chroneos, B.P. Uberuaga, and R.W. Grimes, J. Appl. Phys. **102**, 083707 (2007).
[19] J. Vanhellemont, P. Śpiewak, and K. Sueoka, J. Appl. Phys. **101**, 036103 (2007).
[20] A. Carvalho, R. Jones, C. Janke, J.P. Goss, P.R. Briddon, J. Coutinho, and S. Öberg, Phys. Rev. Lett. **99**, 175502 (2007).
[21] A. Chroneos, H. Bracht, R.W. Grimes, and B.P. Uberuaga, Appl. Phys. Lett. **92**, 172103 (2008).
[22] J. Coutinho, C. Janke, A. Carvalho, S. Öberg, V.J.B. Torres, R. Jones, and P.R. Briddon, Defect and Diffusion Forum **273–276**, 93 (2008).
[23] A. Chroneos, R.W. Grimes, B.P. Uberuaga, and H. Bracht, Phys. Rev. B **77**, 235208 (2008).
[24] C. Janke, R. Jones, S. Öberg, and P.R. Briddon, Phys. Rev. B **77**, 195210 (2008).
[25] C. Janke, R. Jones, S. Öberg, and P.R. Briddon, Phys. Rev. B **77**, 075208 (2008).
[26] S.M. Sze, *Physics of Semiconductor Devices* (John Wiley and Sons, New York, 2001).
[27] D.P. Brunco, B. De Jaeger, G. Eneman, J. Mitard, G. Hellings, A. Satta, V. Terzieva, L. Souriau, F.E. Leys, G. Pourtois, M. Houssa, G. Winderickx, E. Vrancken, S. Sioncke, K. Opsomer, G. Nicholas, M. Caymax, A. Stesmans, J. Van Steenbergen, P.W. Mertens, M. Meuris, and M.M. Heyns, J. Electrochem. Soc. **155**, H552 (2008).
[28] S.C. Jain, W. Schoenmaker, R. Lindsay, P.A. Stolk, S. Decoutere, M. Willander, and H.E. Maes, J. Appl. Phys. **91**, 8919 (2002).
[29] A. Satta, E. Simoen, T. Janssens, T. Clarysse, B. De Jaeger, A. Benedetti, I. Hoflijk, B. Brijs, M. Meuris, and W. Vandervorst, J. Electrochem. Soc. **153**, G229 (2006).
[30] M. Posselt, B. Schmidt, W. Anwand, R. Grötzschel, V. Heera, A. Mücklich, C. Wündisch, W. Skorupa, H. Hortenbach, S. Gennaro, M. Bersani, D. Giubertoni, A. Möller, and H. Bracht, J. Vac. Sci. Technol. B **26**, 430 (2008).
[31] J.F. Ziegler, J.P. Biersack, and U. Littmark, *The Stopping and Range of Ions in Solids, Stopping and Ranges of Ions in Matter* (Pergamon, New York, 1984), Vol. 1.
[32] H. Bracht, J. Fage Pedersen, N. Zangenberg, A. Nylandsted Larsen, E.E. Haller, G. Lulli, and M. Posselt, Phys. Rev. Lett. **91**, 245502 (2003).
[33] D. Alloyeau, B. Freitag, S. Dag, Lin W. Wang, and C. Kisielowski, Phys. Rev. B **80**, 014114 (2009).
[34] E. Hüger, U. Tietze, D. Lott, H. Bracht, D. Bougeard, E.E. Haller, and H. Schmidt, Appl. Phys. Lett. **93**, 162104 (2008).

PRL 102, 127403 (2009) PHYSICAL REVIEW LETTERS week ending 27 MARCH 2009

Fano Signatures in the Intersubband Terahertz Response of Optically Excited Semiconductor Quantum Wells

D. Golde,[1,*] M. Wagner,[2] D. Stehr,[2] H. Schneider,[2] M. Helm,[2] A. M. Andrews,[3] T. Roch,[3] G. Strasser,[3] M. Kira,[1] and S. W. Koch[1]

[1]*Department of Physics and Materials Sciences Center, Philipps-University, Renthof 5, 35032 Marburg, Germany*
[2]*Institute of Ion Beam Physics and Materials Research, Forschungszentrum Dresden-Rossendorf, P.O. Box 510119, 01314 Dresden, Germany*
[3]*Solid State Electronics Institute, Micro- & Nanostructure Center, TU Wien, Floragasse 7, 1040 Vienna, Austria*
(Received 12 December 2008; published 24 March 2009)

Absorption and transmission spectra of broadband terahertz pulses are measured to probe the intersubband response of an optically excited quantum-well heterostructure. While the terahertz absorption shows the single peak of the resonant intersubband transition, the transmission spectra display strong Fano signatures due to the phase sensitive superposition of ponderomotive and terahertz currents as predicted by our microscopic theory.

DOI: 10.1103/PhysRevLett.102.127403 PACS numbers: 78.67.De, 42.25.Bs, 73.21.Fg

Terahertz (THz) experiments on optically excited or doped semiconductors provide unique opportunities to analyze and manipulate low-energy excitations or quasiparticle states, like intersubband transitions between quantum confined states [1–5], excitons, or plasmons, and monitor their dynamical evolution [6–10]. With sufficiently strong THz pulses, one can even reach the regime of "extreme nonlinear optics" leading to effects such as Rabi flopping [5,11,12], ac-Stark splitting [13], or the dynamical Franz-Keldysh effect [14,15]. The microscopic analysis of these experiments shows that the THz wave propagating through the semiconductor is determined by the combined response of the so-called ponderomotive current and the true THz transitions. Here, the ponderomotive contribution refers to the charge current generated by the classical field that causes a wiggling motion of the carriers according to the acceleration theorem $\hbar\dot{\mathbf{k}} = -e\mathbf{E}_{\mathrm{THz}}$ [16,17]. This part of the light-matter interaction, often thought to be relevant only at high intensities [15], produces the simple response $\chi(\omega) = -\frac{\omega_{\mathrm{PL}}^2}{\omega^2}$ with the plasma frequency ω_{PL}. Because of the factor ω^{-2}, the ponderomotive contribution can usually be neglected in the analysis of interband optical excitation; however, it is of relevance in the THz regime even at the lowest intensities. Thus, the THz response of an excited semiconductor is influenced by ponderomotive effects plus the true THz transitions. When both contributions are of equal strength, one expects a strong interplay. In the experiments reported in Refs. [12,18] the evidences for the role of the ponderomotive current are rather indirect. Their influence could only be seen by virtue of a theoretical switch-off analysis.

To clearly expose the interplay of ponderomotive and true THz response, one needs an experimental method that makes it possible to observe both effects directly. In this Letter, we study the intersubband transition of photoexcited semiconductor quantum wells using linear THz spectroscopy. Monitoring the transmission of a broadband THz pulse, we directly observe signatures of the ponderomotive motion of the excited carriers. We show that interference of ponderomotive and resonant contributions produces a characteristic Fano-like line shape in the differential transmission spectrum.

Asymmetric Fano line shapes are known to result from quantum interference of discrete energy levels coupled to a nearby continuum [19] and have been observed in semiconductor heterostructures under various conditions [20–23]. Whereas the relevant continuum in typical Fano configurations is an integral part of the probed quantum object, in our system an effective continuum is provided by the light-matter interaction through the ponderomotive contribution.

Figure 1(a) shows the basic concept of our experiment where spectrally broadband THz pulses probe the sample's intersubband transition after resonant photoexcitation. The THz pulses are generated in a 55 μm thin z-cut GaSe crystal by phase-matched difference frequency mixing [24] within the broad spectrum of 12 fs optical pulses, delivered by a 78 MHz Ti:sapphire oscillator (Femtolasers: Femtosource Scientific sPro). The THz beam is focused by off-axis parabolic mirrors on the multi-quantum-well (MQW) sample, with the THz field having a strong component perpendicular to the MQW plane to couple effectively to the intersubband transition [25]. For THz-field-resolved detection, phase-matched electro-optic sampling [26,27] is applied. To this end, a weak component of the 12 fs laser beam goes through a delay stage and samples the THz-field induced polarization change in a second 30 μm thin z-cut GaSe crystal as a function of the time delay between THz pulse and sampling pulse [Fig. 1(c)].

The sample studied consists of 60 periods of 8.2-nm-thick undoped GaAs quantum wells, separated by 19.6-nm-thick barriers of $Al_{0.34}Ga_{0.66}As$. The sample was prepared

 © 2009 The American Physical Society

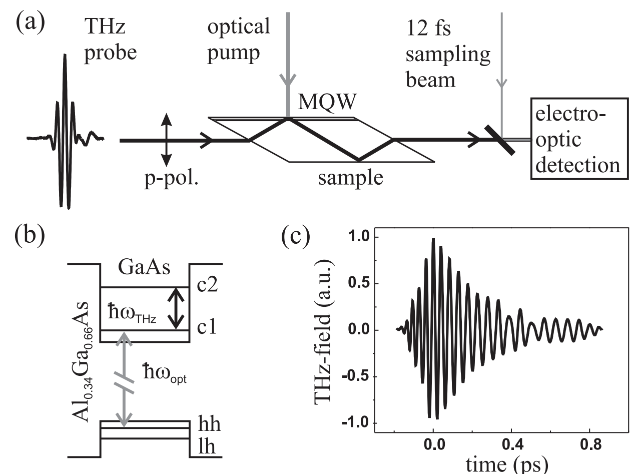

FIG. 1. (a) Optical interband pump intersubband THz probe experiment. (b) The transition from the heavy-hole (hh) state to the first conduction state (c1) in the $Al_{0.34}Ga_{0.66}As/GaAs$ multi-quantum-well (MQW) sample is resonantly excited, either by a ps or a fs laser. THz pulses probe the c1-to-c2 transition 25 ps after photoexcitation. (c) The field transients of the transmitted THz pulses are detected by phase-matched electro-optic sampling with a sampling beam. The reference without photoexcitation is shown.

in a 38-degree wedged-waveguide geometry, as shown in Fig. 1(a). To ensure optimized overlap between MQW region and THz standing wave [25], an additional $Al_{0.34}Ga_{0.66}As$ spacer layer of 300 nm thickness was grown on top of the sample. The experiments are performed at a temperature of 6 K.

The photoexcitation scheme is illustrated in Fig. 1(b). An optical interband pump pulse excites the MQW resonantly at the 1s heavy-hole exciton and creates carriers in the first conduction band. We choose either spectrally narrow 2.5 ps or broadband 100 fs optical excitation centered at $\hbar\omega_{opt} = 1.56$ eV. Both lasers are 78 MHz Ti:sapphire oscillators (Spectra Physics: Tsunami), locked to the repetition rate of the THz generating laser. In each case, only the first conduction subband of the MQW is populated. After a time delay of 25 ps during which the optically induced interband coherences disappear, the weak broadband THz-pulse probes the c1-to-c2 intersubband transition. In all the experiments, the photoexcited carrier density is 2×10^{10} cm^{-2} per quantum well.

A two-lock-in technique is employed to measure the transmitted THz transients with and without excitation. The visible pump and THz probe beams are chopped simultaneously at different frequencies around 2 kHz. The first lock-in amplifier locks on the modulation of the optical pump beam. Since the THz beam is also chopped at the same time, twice the signal obtained by the first lock-in amplifier yields the differential transmission $\Delta E(t)$, i.e., the pump-induced change in the transmitted THz field. The second lock-in amplifier detects the mean value between transmission with and without photoexcitation, leading to the reference $E_{ref}(t)$ without excitation by subtracting the signal of the first lock-in amplifier. This allows us to record $\Delta E(t)$ and $E_{ref}(t)$ simultaneously under the same conditions, preventing a drift in the relative phase between them. Such a phase drift would strongly affect the computed total THz absorption of the quantum wells $\alpha(\omega)$, where the complex valued Fourier transforms of $\Delta E(t)$ and $E_{ref}(t)$ enter in the following way: $\alpha(\omega) = 2\text{Im}[-i\Delta E(\omega)/E_{ref}(\omega)]$. This relation follows from Maxwell's equations and the assumptions that (i) $|\Delta E| \ll |E_{ref}|$, (ii) the unexcited sample is nonabsorptive in the investigated frequency range, and (iii) only the single-pass signal is measured.

Figure 1(c) shows the reference transient $E_{ref}(t)$. Compared with the incident THz transient [Fig. 1(a)], the field oscillations last longer in time due to dispersion in the sample. The differential THz transmission transients $\Delta E(t)$ are presented in Figs. 2(a) and 2(b) for ps and fs excitation, respectively. First, one observes that the signal has 440 fs

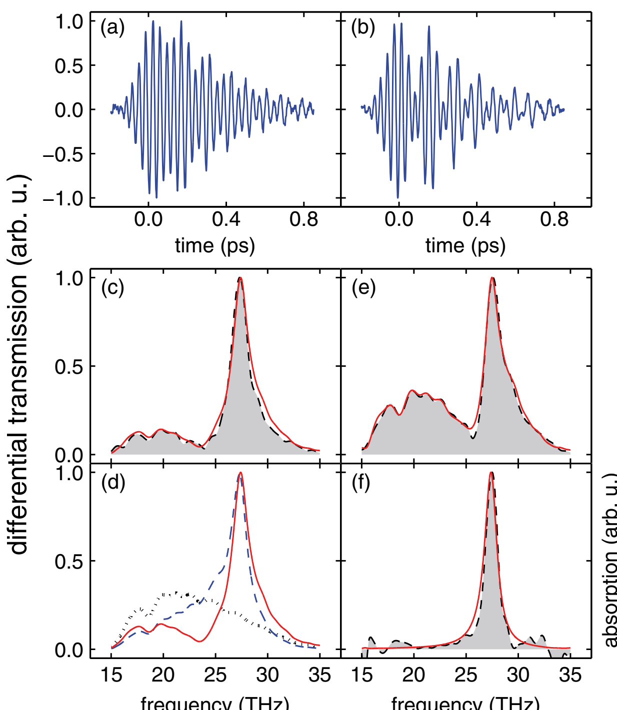

FIG. 2 (color online). Experiment-theory comparison of the THz intersubband response. (a),(b) Measured time-resolved differential transmission signals $\Delta E(t)$ for ps and fs excitation, respectively. (c) Measured spectral amplitude of differential transmission $|\Delta E(\omega)|$ (shaded area) and calculated current density $|J_{tot}(\omega)|$ (red solid line) after optical ps excitation. (d) shows the decomposition of the computed total current density (red solid line) into the ponderomotive contribution $|J_A|$ (black dotted line) and the intersubband current $|J_{THz}|$ (blue dashed line). (e), (f) Measured (shaded area) and computed (red solid line) differential transmission and THz absorption, respectively, after fs excitation. Here, J_A has been enhanced by 1.85 in order to account for substrate excitations.

PRL **102,** 127403 (2009) PHYSICAL REVIEW LETTERS week ending 27 MARCH 2009

decay constant for both ps and fs excitation, whereas a decay of 240 fs is observed for the reference $E_{\rm ref}(t)$ [see Fig. 1(c)]. This reveals the dephasing of the reradiated THz-induced intersubband polarization [2,3,28]. Second and more interesting, one observes a clear beating compared to the reference $E_{\rm ref}(t)$, superimposed on the dephasing and being more pronounced for fs photoexcitation.

We first address the ps excitation to analyze the origin of the observed beating. Figure 2(c) shows the spectral amplitude of the measured differential THz transmission $|\Delta E(\omega)|$ after optical excitation at the $1s$ position of the heavy-hole exciton resonance. We see that the spectrum consists of two major contributions: (i) a sharp resonance peak at the transition frequency of the conduction subbands $\nu_{1,2} = 27.3$ THz and (ii) a broad contribution centered at roughly 20 THz, being responsible for the beating in the time domain. These features remind us of a typical Fano spectrum, i.e., an undershoot at the low-frequency side of the peak followed by an asymmetric line shape.

When the system is excited with a 100 fs pulse, the broad contribution and the Fano signatures are more pronounced than in the ps case [Fig. 2(e)]. To check whether the broad feature in the differential transmission is caused by an additional carrier transition besides the intersubband resonance, we measure the THz absorption. Figure 2(f) shows that the absorption is single peaked; i.e., only the intersubband resonance appears and no Fano-like signature is observed.

In order to explain the experimental findings, we compute the THz transmission of a quantum well positioned at $z = 0$ (where z is the growth direction of the quantum well). The THz response follows from the wave equation

$$\left(\nabla^2 - \frac{n_b^2}{c^2}\frac{\partial^2}{\partial t^2}\right)E(\mathbf{r}, t) = \mu_0 \delta(z)\frac{\partial}{\partial t}(J_{\rm A}(t) + J_{\rm THz}(t)), \quad (1)$$

where n_b is the background refractive index, c is the speed of light, and μ_0 is the permeability of free space. The delta function arises due to the fact that the quantum-well width is much smaller than the wavelength of the THz field. The induced current density appearing as source term on the right-hand side of Eq. (1) consists of two terms: $J_{\rm THz}$ is the current due to the intersubband transitions and $J_{\rm A}$ describes the ponderomotive motion of the excited carriers due to the THz field. Solving Eq. (1), one finds that the differential transmission, i.e., the field that is reemitted by the current density, is directly proportional to the induced current [29]: $\Delta E \propto J_{\rm A} + J_{\rm THz}$.

The ponderomotive contribution to the current density is given by $J_{\rm A} = -\sum_\lambda \frac{e^2 n_\lambda}{m_\lambda} A_{\rm THz}$ [30] where n_λ is the carrier density in band λ and m_λ is the effective mass. The vector potential $A_{\rm THz}$ of the THz pulse is defined via $E_{\rm THz} = -\frac{\partial}{\partial t} A_{\rm THz}$. Here, λ includes both bulk-band index and subband index. Obviously, the ponderomotive current directly follows $A_{\rm THz}$ with an opposite phase due to the minus sign in $J_{\rm A}$. The linear susceptibility $\chi_{\rm A}(\omega) = -\frac{\omega_{\rm PL}^2}{\omega^2}$ following from the ponderomotive current is a real-valued quantity. Consequently, $J_{\rm A}$ does not contribute to the absorption $\alpha(\omega) \propto \omega {\rm Im}[\chi(\omega)]$, but simply introduces a refractive index change to the excited material.

The THz current is computed via $J_{\rm THz} = \frac{1}{S}\sum_{\lambda,l,l',\mathbf{k}} j^\lambda_{l',l} p^\lambda_{l,l',\mathbf{k}}$ with the quantization area S and the matrix elements $j^\lambda_{l,l'}$. The quantity $p^\lambda_{l,l',\mathbf{k}}$ represents the microscopic intersubband polarization between subbands l and l' of bulk-band λ. The intersubband matrix element is given by $j^\lambda_{l,l'} = -\frac{i\hbar e}{m_\lambda}\int dz \xi^*_{\lambda,l}(z)\frac{\partial}{\partial z}\xi_{\lambda,l'}(z)$ where $\xi_{\lambda,l}(z)$ is the confinement wave function of the carriers.

The intersubband polarization $p^\lambda_{l,l',\mathbf{k}}$ in $J_{\rm THz}$ is computed microscopically with an equation-of-motion approach. Since we are interested only in the c1-to-c2 transition, we can restrict the sum to $\lambda = c$ and $l,\ l' \in \{1, 2\}$. In analogy to the semiconductor Bloch equations [31], one finds for the time evolution of the intersubband polarization

$$\begin{aligned} i\hbar\frac{\partial}{\partial t}p^c_{1,2,\mathbf{k}} &= (\tilde{\varepsilon}^c_{2,\mathbf{k}} - \tilde{\varepsilon}^c_{1,\mathbf{k}})p^c_{1,2,\mathbf{k}} + \frac{\partial}{\partial t}p^c_{1,2,\mathbf{k}}\bigg|_{\rm scatt} \\ &\quad + (f^{c1}_{\mathbf{k}} - f^{c2}_{\mathbf{k}})\Big[j^c_{2,1}A_{\rm THz} - \sum_{\mathbf{q}\neq\mathbf{k}} V_{\mathbf{k}-\mathbf{q}}p^c_{1,2,\mathbf{q}}\Big] \\ &\quad + S^{\rm coh}_{\mathbf{k}}, \end{aligned} \quad (2)$$

where $\tilde{\varepsilon}^c_{l,\mathbf{k}}$ are the renormalized single-particle energies, $f^{c,l}_{\mathbf{k}}$ are the optically excited carrier distributions in the conduction bands, and $V_{\mathbf{q}}$ is the Coulomb matrix element. The term $\frac{\partial}{\partial t}p^c_{1,2,\mathbf{k}}|_{\rm scatt}$ formally contains all scattering effects and $S^{\rm coh}_{\mathbf{k}}$ includes the coupling to optically excited interband coherences via the Coulomb interaction. The scattering terms are modeled by a phenomenological dephasing constant γ to match the measured 440 fs decay, i.e., $\frac{\partial}{\partial t}p^c_{1,2,\mathbf{k}}|_{\rm scatt} \approx -i\gamma p^c_{1,2,\mathbf{k}}$. This approximation is justified since in our case, the intersubband transitions are not affected by excitonic effects due to large experimental linewidths (roughly 3.3 meV). For large time delays of optical pump and THz probe pulses, the optically excited coherences have decayed such that $S^{\rm coh}_{\mathbf{k}}$ does not contribute.

In our numerical evaluations, we compute the single-particle energies of the quantum-well system using standard $\mathbf{k}\cdot\mathbf{p}$ perturbation theory. For the THz response, we include the first two conduction subbands and the first heavy-hole and light-hole subband [Fig. 1(b)]. As input for the time-dependent fields, we use the experimental THz-pulse shapes of the reference pulse.

The theoretical results are superimposed to the experimental results in Fig. 2. The (red) solid line in Figs. 2(c) and 2(e) represents the absolute value of the computed current density, i.e., the differential transmission for the ps (c) and fs excitation (e). Figure 2(d) separates the two contributions $J_{\rm A}$ (dotted line) and $J_{\rm THz}$ (blue dashed line) to the total current for the case of ps excitation. The solid line in Fig. 2(f) shows the computed absorption spectrum.

PRL 102, 127403 (2009) PHYSICAL REVIEW LETTERS week ending 27 MARCH 2009

In all cases, an excellent experiment-theory agreement is obtained.

As in the measurement, we clearly notice the double peaked Fano-like feature in the transmission spectra, whereas the absorption is only single peaked. In our theory, the origin of the Fano-like feature can be investigated looking at the individual contributions separately. J_A directly reflects the vector potential of the THz probe pulse while J_{THz} consists of the intersubband resonance weighted with the pulse spectrum. The broad feature in the transmission spectrum is a direct consequence of the broad probe pulse. The Fano-like line shape is caused by the phase sensitive superposition of the broad ponderomotive and the sharp intersubband contribution, $|J_{tot}| = |J_A + J_{THz}|$. A further analysis reveals that for frequencies smaller than $\nu_{1,2}$, both contributions partially compensate each other while they interfere constructively for larger frequencies. As for typical Fano situations, this kind of superposition leads to narrowing of the resonance at the low-frequency side and a broadening at the high-frequency side, resulting in the characteristic asymmetric Fano line shape. Since the ponderomotive current leads to a real-valued susceptibility, there is no Fano-like behavior in the THz absorption [Fig. 2(f)].

In order to explain the more pronounced ponderomotive feature in the fs experiment, we had to extend our model beyond the single-quantum-well response. Since the fs pump pulse is spectrally significantly broader than the line width of the 1s exciton resonance (18.2 meV vs 3.3 meV), some frequency components are transmitted through the quantum wells and excite carriers in the substrate. These carriers contribute to J_A but not to J_{THz}, since there are no subbands in bulk material. A quantitative investigation of the interband optical excitation shows that 46% of the pump pulse is transmitted through the quantum wells and absorbed by the substrate. Hence, the total carrier density (in the wells plus substrate) is 1.85 times larger than the density in the quantum wells alone. Since J_A is proportional to the carrier density, we can model the substrate contribution to the THz response simply by enhancing J_A relative to J_{THz} by 1.85. The resulting current density is shown as the red solid line in Fig. 2(e). In the ps experiment, substrate excitations can be neglected since only 1.4% of the pump pulse reaches the substrate.

In summary, we have shown how the emission by the ponderomotive motion of the excited carriers can directly be identified in the linear THz response. Using a microscopic theory for the THz response, the observed Fano-like features in the transmission spectrum can unambiguously be attributed to the phase sensitive superposition of the intersubband resonance and the ponderomotive carrier dynamics. Our results are connected to the typical Fano situation because the system has a sharp discrete intersubband resonance that interferes with a broad continuous contribution, i.e., the ponderomotive current density. However, one of the contributions in our case is nonabsorptive such that we do not observe the Fano resonance in the absorption spectrum but in the differential transmission spectrum only.

The authors from Forschungszentrum Dresden-Rossendorf are grateful to Dr. Stephan Winnerl for critical discussions. The Marburg work is supported by the Quantum Optics in Semiconductors DFG Research Group. The Vienna group is supported by the Austrian FWF.

*daniel.golde@physik.uni-marburg.de

[1] A. Bonvalet *et al.*, Phys. Rev. Lett. **76**, 4392 (1996).
[2] J.N. Heyman, R. Kersting, and K. Unterrainer, Appl. Phys. Lett. **72**, 644 (1998).
[3] R. Kersting *et al.*, Opt. Lett. **25**, 272 (2000).
[4] T. Müller *et al.*, Phys. Rev. B **70**, 155324 (2004).
[5] C.W. Luo *et al.*, Phys. Rev. Lett. **92**, 047402 (2004).
[6] R.H.M. Groeneveld and D. Grischkowsky, J. Opt. Soc. Am. B **11**, 2502 (1994).
[7] J. Cerne *et al.*, Phys. Rev. Lett. **77**, 1131 (1996).
[8] R. Huber *et al.*, Nature (London) **414**, 286 (2001).
[9] R.A. Kaindl *et al.*, Nature (London) **423**, 734 (2003).
[10] I. Galbraith *et al.*, Phys. Rev. B **71**, 073302 (2005).
[11] B.E. Cole *et al.*, Nature (London) **410**, 60 (2001).
[12] S. Leinß *et al.*, Phys. Rev. Lett. **101**, 246401 (2008).
[13] J.F. Dynes *et al.*, Phys. Rev. Lett. **94**, 157403 (2005).
[14] K.B. Nordstrom *et al.*, Phys. Rev. Lett. **81**, 457 (1998).
[15] A.H. Chin, J.M. Bakker, and J. Kono, Phys. Rev. Lett. **85**, 3293 (2000).
[16] J.B. Krieger and G.J. Iafrate, Phys. Rev. B **33**, 5494 (1986).
[17] F. Bloch, Z. Phys. **52**, 555 (1929).
[18] J.R. Danielson *et al.*, Phys. Rev. Lett. **99**, 237401 (2007).
[19] U. Fano, Phys. Rev. **124**, 1866 (1961).
[20] J. Faist *et al.*, Opt. Lett. **21**, 985 (1996).
[21] J. Faist *et al.*, Nature (London) **390**, 589 (1997).
[22] H. Schmidt *et al.*, Appl. Phys. Lett. **70**, 3455 (1997).
[23] H.C. Liu *et al.*, Appl. Phys. Lett. **91**, 131121 (2007).
[24] R.A. Kaindl *et al.*, Opt. Lett. **23**, 861 (1998).
[25] M. Helm, in *Semiconductors and Semimetals*, edited by H.C. Liu and F. Capasso (Academic Press, San Diego, 2000), Vol. 62, Chap. 1.
[26] K. Liu, J. Xu, and X.-C. Zhang, Appl. Phys. Lett. **85**, 863 (2004).
[27] C. Kübler *et al.*, Appl. Phys. Lett. **85**, 3360 (2004).
[28] R.A. Kaindl *et al.*, Phys. Rev. B **63**, 161308(R) (2001).
[29] M. Kira and S.W. Koch, Prog. Quantum Electron. **30**, 155 (2006).
[30] The electrons experience a wiggling motion also in the growth direction due to the tilting of the confinement potential.
[31] H. Haug and S.W. Koch, *Quantum Theory of the Optical and Electronic Properties of Semiconductors* (World Scientific, Singapore, 2009), 5th ed.

APPLIED PHYSICS LETTERS **94**, 193103 (2009)

Transition from smoothing to roughening of ion-eroded GaSb surfaces

A. Keller,[1,a)] A. Biermanns,[2] G. Carbone,[3] J. Grenzer,[1,b)] S. Facsko,[1] O. Plantevin,[4] R. Gago,[5] and T. H. Metzger[3]

[1]*Institute of Ion Beam Physics and Materials Research, Forschungszentrum Dresden-Rossendorf, P.O. Box 510119, 01314 Dresden, Germany*
[2]*Festkörperphysik, Universität Siegen, 57068 Siegen, Germany*
[3]*European Synchrotron Radiation Facility, F-38043 Grenoble Cedex, France*
[4]*Centre de Spectrométrie Nucléaire et de Spectrométrie de Masse, CNRS/IN2P3, Univ. Paris-Sud, UMR 8609, F-91405 Orsay, France*
[5]*Instituto de Ciencia de Materiales de Madrid, Consejo Superior de Investigaciones Científicas, E-28049 Madrid, Spain*

(Received 11 March 2009; accepted 24 April 2009; published online 13 May 2009)

During ion sputtering of GaSb(100) surfaces a transient behavior from initial smoothing to roughening accompanied by self-organized pattern formation has been observed using *in situ* x-ray reflectivity and grazing incidence small angle scattering. The induced patterns show hexagonally ordered nanodot arrays with a spatial periodicity of 30 nm. The correlation length of the pattern increases with ion fluence. In the framework of the Bradley–Harper model [R. M. Bradley and J. M. E. Harper, J. Vac. Sci. Technol. A **6**, 2390 (1988)], where the dot pattern formation results from an interplay of surface roughening due to sputtering and surface smoothing due to diffusion, the initial smoothing behavior is explained by the same surface diffusion processes as the pattern formation.
© *2009 American Institute of Physics*. [DOI: 10.1063/1.3136765]

The roughness of surfaces and interfaces strongly influences many properties of thin films and surfaces, among them the electrical, optical and magnetic properties.[1] Therefore controlling the roughness is an important issue in a broad variety of technological applications. In addition, by controlling the roughness down to the nanoscale the structure and properties of films deposited on these surfaces can be tuned. For example, nanostructured surfaces can be used as templates for the growth of thin magnetic films with a predefined anisotropy[2] and metallic thin films exhibiting dichroitic plasmonic properties.[3] When materials are bombarded with energetic ions the surface is eroded by the sputtering process. Ion beam sputtering (IBS) is often used to modify the roughness of solid surfaces on lateral scales ranging from a few nanometers up to micrometers.[4] Under certain sputtering conditions (energy, ion mass, incidence angle, fluence, etc.), IBS leads to a smoothing of the surface, whereas at other parameters the surface roughness is increased, leading eventually to periodic patterns, i.e., ripple or dot patterns.[5] Recently, it has also been shown that the pattern formation might be accompanied by an actual decrease of the surface roughness.[6]

In this letter we report on *in situ* x-ray scattering measurements of the morphology of GaSb (100) surfaces during Ar^+ IBS at normal incidence. Especially, the early time regime is addressed, which gives insight into the detailed mechanisms governing the dynamics in the beginning of the pattern formation process. The roughness and morphology of the sample surface are measured by *in situ* x-ray reflectivity (XRR) and grazing incidence small angle x-ray scattering (GISAXS). This experimental approach, i.e., *in situ* x-ray scattering, has proven to be a valuable tool to investigate the surface evolution and transient behaviors in the early time regime of the ion erosion process, which would be difficult to access with other *ex situ* techniques.[7,8] In contrast to earlier investigations of the roughening behavior of ion eroded GaSb surfaces[9] where only an increase in the roughness with the formation of a dot pattern has been measured, we observe a transition behavior of the surface morphology: an initial smoothing regime is followed by a subsequent roughening of the GaSb surface and the formation of a dot pattern. Simulations of the dynamics of the surface morphology with a continuum approach show that the initial smoothing results from the same relaxation mechanism leading to the formation of the periodic dot structure.

Ion erosion was performed in a compact high vacuum chamber with a base pressure of 10^{-7} mbar with a Kaufman type ion source. The chamber, equipped with a 360° beryllium window for the x-ray scattering measurements,[10] is mounted on a goniometer at the ID01 synchrotron beam line at the ESRF in Grenoble (France). Sputtering was done with Ar^+ ions at normal incidence with an energy of 450 eV and ion flux of 1×10^{15} cm^{-2} s^{-1}. XRR and GISAXS spectra were measured at an x-ray energy of 8 keV after consecutive steps of sputtering, stopping the erosion process during the measurements. The sample temperature was always below 60 °C during each sputtering step. At these conditions the GaSb surface should be amorphized and in sputter equilibrium after an ion fluence of approx. 1×10^{16} cm^{-2}.[11]

Figure 1(a) shows XRR measurements of the initial, untreated surface and after sputtering with fluences between 3.6×10^{16} and 6.8×10^{17} cm^{-2}. In general, the decay of specular reflected intensity with increasing incidence angle α above the critical angle $\alpha_c \approx 0.32°$ reflects the penetration of the x-ray beam in the material and is, for a perfectly flat surface, given by the Fresnel equations. Surface roughness leads to offspecular diffuse scattered intensity and hence to a faster decay of the specular signal with incidence angle. Finally, the presence of a layer with different optical properties

a)Electronic mail: a.keller@fzd.de.
b)Electronic mail: j.grenzer@fzd.de.

 © 2009 American Institute of Physics

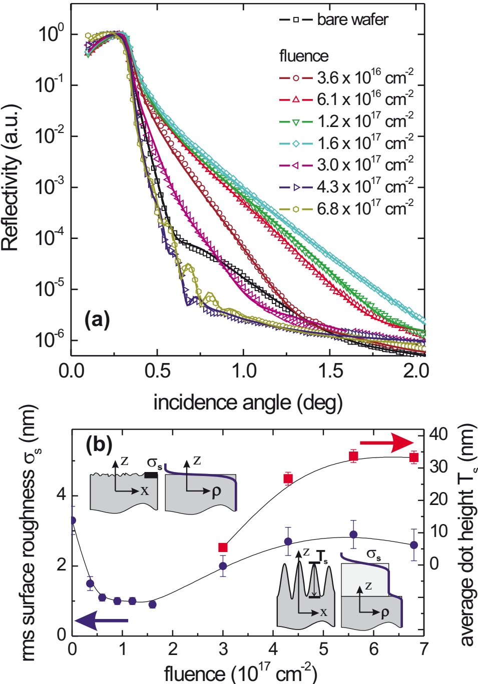

FIG. 1. (Color online) (a) XRR (symbols) of the GaSb surface sputtered with 450 eV Ar^+ ions at different ion fluences. The rough initial surface is smoothed in the beginning, followed by a strong roughening process. (b) Evolution of the roughness σ_s and the thickness T_s of the transition layer, respectively, as obtained from a simulation [solid lines in (a)] of the reflectivity curves. Insets illustrate the nature of the transition layer at low and high fluences, respectively.

on top of the surface leads to interference fringes whose angular distance is inversely proportional to the layer thickness.

Prior to sputtering, the XRR measurements reveal a rather rough surface with a thin surface layer which probably corresponds to the native oxide on top of the GaSb.[19] During ion erosion up to a fluence of 1.6×10^{17} cm^{-2} the reflectivity at angles $\alpha > \alpha_c$ increases significantly indicating a smoothing of the surface due to the ion irradiation. The roughening observed for higher fluence can be associated with the onset of a dot pattern formation as visible by GISAXS measurements (see text below). Moreover, the interference fringes observed in the XRR curves in this fluence region indicate the development of a layer with an electron density reduced with respect to the bulk value of GaSb. In order to quantify the surface evolution the reflectivity data are analyzed assuming a transition layer on top of a GaSb substrate that is characterized by a constant (lower) electron density, by its thickness T_s, and by introducing a surface roughness σ_s as a Gaussian-like density gradient into the Fresnel formula [insets in Fig. 1(b)]. Figure 1(b) shows the evolution of σ_s and of T_s, respectively.

At the beginning of sputtering the oxide layer is removed almost immediately and the GaSb surface can be modeled by the surface roughness only, i.e., $T_s=0$. The initial decrease of σ_s reflects the reduction of the surface roughness. With the onset of pattern formation at a fluence of 3×10^{17} cm^{-2} T_s starts to grow until it reaches a stable value of 30 nm, giving a measure for the averaged height of the dot pattern. The simultaneous increase of σ_s can be interpreted as height fluctuations of the dot pattern.

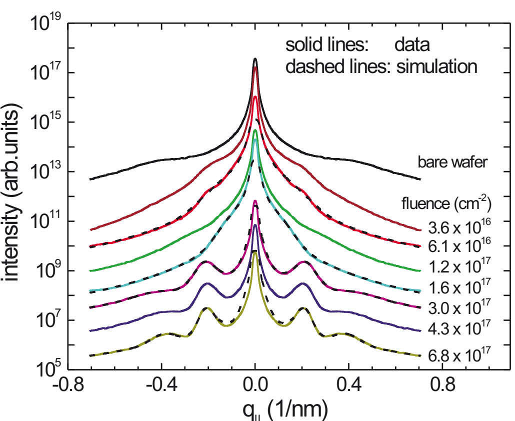

FIG. 2. (Color online) GISAXS spectra of the GaSb sample at different ion fluences.

In addition to XRR, GISAXS spectra were recorded between the sputtering cycles (Fig. 2). Complementary to XRR, these measurements contain information about the lateral height correlations along the surface. At the beginning of the erosion process, the strong diffuse scattering of the substrate is reduced, reaching a minimum at a fluence of 1.6×10^{17} cm^{-2}. At a fluence of 3×10^{17} cm^{-2}, corresponding to the increase of surface roughness as obtained by XRR, satellite peaks appear, indicating the onset of the formation of a periodic pattern. The position of these peaks is related to the mean interdot distance (wavelength) l, whereas number and width of the satellite peaks are related to the correlation length ξ.[12] The dashed lines in Fig. 2 show simulations of the scattered intensity. During the smoothing regime, the diffuse scattering can be modeled taking into account the nonspecular component of the structure factor of a rough surface.[13] For a quantitative analysis of the GISAXS spectra from the periodic dot pattern, the data has been fitted with the program ISGISAXS,[14] using a model of cone-shaped particles and the two-dimensional hexagonal paracrystal model to describe their correlation in a short-range order scenario.[14] The fitting results for the mean wavelength l and the correlation length ξ (not shown) revealed that the wavelength increases only slightly from 30 to 32 nm, whereas the correlation length increases with fluence by about a factor of 2 from roughly 10 to about 20 periods. This increase of ξ is reflected in the decrease of FWHM of the first-order satellite peak and the appearance of second-order peaks in Fig. 2.

In the Bradley–Harper (BH) model of IBS, pattern formation is explained by the interplay of two processes: first, roughening by the curvature dependent sputter yield and second, surface relaxation by surface diffusion.[15] In order to elucidate the smoothing and pattern formation mechanisms at the beginning of the ion sputtering, numerical integrations of a nonlinear extension of the BH model, the Kuramoto–Sivashinsky (KS) equation,[16]

$$\frac{\partial h}{\partial t} = -v_0 + \nu \nabla^2 h - D_{\mathrm{eff}} \nabla^4 h + \frac{\lambda}{2} (\nabla h)^2, \qquad (1)$$

have been performed. Here, v_0 is the constant erosion velocity of the planar surface. The second term represents the curvature dependence of the erosion velocity and the third term the effective surface relaxation. The nonlinear fourth term incorporates the dependence of the local erosion velocity on the surface slopes and is responsible for the formation

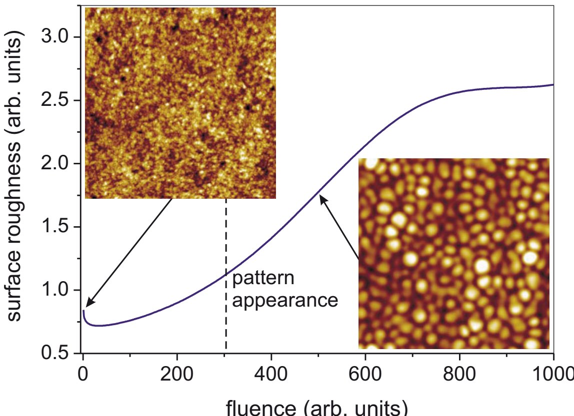

FIG. 3. (Color online) Root mean square roughness and surface morphology obtained by numerical integration of the KS Eq. (1). Note the good qualitative agreement with the measured results [Fig. 1(b)]. X and y scales depend only on simulation parameters and can be rescaled arbitrarily. The size of the AFM type images is 500×500 nm^2.

of ordered dot patterns at intermediate times.[17,18] However, for long sputtering times, in the nonlinear regime the pattern evolves to kinetic roughening which is not observed experimentally for GaSb. In our integration of the continuum equation a real atomic force microscopy (AFM) image of the virgin GaSb(100) wafer was used as the starting surface (left inset in Fig. 3). The coefficients $\nu=0.15$, $D_{\mathrm{eff}}=1$, and $\lambda=0.1$ were chosen such that the periodicity l is close to the experimental measured periodicity of 30 nm and that the initial dynamics of the pattern evolution can be followed easily. In this way the scales of the initial surface are mapped to the simulation.

Figure 3 shows the evolution of the surface roughness in the simulation. In the initial phase of the simulation the diffusion term leads to a reduction of the roughness at length scales smaller than the wavelength l of the system, whereas at larger length scales roughness is not affected. Therefore, the net effect of the diffusion term is to reduce the rms roughness, calculated as the integral of the power spectral density (PSD), in the beginning. At longer simulation times, the KS instability starts to grow and the pattern exhibits dot features with the wavelength l (right inset in Fig. 3). At fluences around 300 an ordered dot pattern appears which can be identified by a pronounced peak in the PSD. Now the surface is dominated by the pattern and the roughness increases again due to the formation of dots. The wavelength l is given by the ratio between the roughening coefficient ν and the diffusion coefficient D_{eff}. Thus, the same diffusion mechanism that determines the formation of periodic patterns is also responsible for the initial surface smoothing.

In summary, we presented *in situ* measurements of the nanodot formation on an Ar-eroded GaSb(100) surface using XRR and GISAXS. We showed that the sputtering process leads to an initial smoothing of the surface, followed by a roughening process associated with the formation of nanodots. Both the smoothing and roughening behavior can be modeled using the KS equation and are the result of the same diffusion mechanisms.

This work has been partially supported by Grant No. FIS2006-12253-C06-02 (MEC, Spain).

[1] G. Palasantzas, J. T. M. De Hosson, and J. Barnas, Surf. Sci. **507**, 541 (2002).
[2] M. O. Liedke, B. Liedke, A. Keller, B. Hillebrands, A. Mücklich, S. Facsko, and J. Fassbender, Phys. Rev. B **75**, 220407 (2007).
[3] T. W. H. Oates, A. Keller, S. Facsko, and A. Mucklich, Plasmonics **2**, 47 (2007).
[4] F. Frost, R. Fechner, D. Flamm, B. Ziberi, W. Frank, and A. Schindler, Appl. Phys. A: Mater. Sci. Process. **78**, 651 (2004).
[5] W. L. Chan and E. Chason, J. Appl. Phys. **101**, 121301 (2007).
[6] V. Mussi, F. Granone, C. Boragno, F. B. de Mongeot, U. Valbusa, T. Marolo, and R. M. Montereali, Appl. Phys. Lett. **88**, 103116 (2006).
[7] D. Carbone, A. Alija, O. Plantevin, R. Gago, S. Facsko, and T. H. Metzger, Nanotechnology **19**, 035304 (2008).
[8] O. Plantevin, R. Gago, L. Vazquez, A. Biermanns, and T. H. Metzger, Appl. Phys. Lett. **91**, 113105 (2007).
[9] T. Bobek, S. Facsko, H. Kurz, T. Dekorsy, M. Xu, and C. Teichert, Phys. Rev. B **68**, 085324 (2003).
[10] D. Carbone, O. Plantevin, R. Gago, C. Mocuta, O. Bikondoa, A. Alija, L. Petit, H. Djazuli, and T. H. Metzger, J. Synchrotron Radiat. **15**, 414 (2008).
[11] H. Gnaser, *Low-Energy Ion Irradiation of Solid Surfaces, Springer Tracts in Modern Physics* (Springer, New York, 1999), Vol. 146.
[12] M. Schmidbauer, *X-Ray Diffuse Scattering from Self-Organized Mesoscopic Semiconductor Structures, Springer Tracts in Modern Physics* (Springer, New York, 2004).
[13] S. K. Sinha, E. B. Sirota, S. Garoff, and H. B. Stanley, Phys. Rev. B **38**, 2297 (1988).
[14] R. Lazzari, J. Appl. Crystallogr. **35**, 406 (2002).
[15] R. M. Bradley and J. M. E. Harper, J. Vac. Sci. Technol. A **6**, 2390 (1988).
[16] R. Cuerno and A. L. Barabasi, Phys. Rev. Lett. **74**, 4746 (1995).
[17] B. Kahng, H. Jeong, and A. L. Barabasi, Appl. Phys. Lett. **78**, 805 (2001).
[18] S. Facsko, T. Bobek, A. Stahl, H. Kurz, and T. Dekorsy, Phys. Rev. B **69**, 153412 (2004).
[19] The initial root mean square (rms) roughness of commercially available GaSb(100) has a value of ~0.8 nm and is thus much higher than that of, e.g., commercial Si(100) with ~0.2 nm.

APPLIED PHYSICS LETTERS **94**, 042103 (2009)

Achieving high free electron mobility in ZnO:Al thin films grown by reactive pulsed magnetron sputtering

S. Cornelius,[a)] M. Vinnichenko, N. Shevchenko, A. Rogozin, A. Kolitsch, and W. Möller
Institute of Ion Beam Physics and Materials Research, Forschungszentrum Dresden-Rossendorf, P.O. Box 510119, 01314 Dresden, Germany

(Received 17 November 2008; accepted 23 December 2008; published online 26 January 2009)

The study is focused on the improvement of the free electron mobility in Al-doped ZnO films grown by reactive pulsed magnetron sputtering. At optimum growth conditions low-absorbing films are obtained with a Hall mobility of 46 $cm^2 V^{-1} s^{-1}$, a free electron density of 6.0×10^{20} cm^{-3}, and an electrical resistivity of 2.26×10^{-4} Ω cm. The relation between the mobility and free electron density for different growth conditions is discussed in terms of ionized impurity scattering, impurity clustering, and grain boundary limited transport. © *2009 American Institute of Physics*.
[DOI: 10.1063/1.3074373]

The need to establish a cost-effective replacement of tin-doped indium oxide as a transparent electrode material for thin-film solar cells has stimulated substantial research efforts to decrease both optical absorption in the near infrared (down to 1 eV) and electrical resistivity of Al-doped ZnO (AZO).[1–6] This can be accomplished by increasing the free electron mobility (μ_e) while maintaining the maximum free electron density (N_e) below 1×10^{21} cm^{-3}. The combination of lowest electrical resistivity ($\rho \sim 0.85-4 \times 10^{-4}$ Ω cm), highest mobility ($\mu_e \sim 40-50$ $cm^2 V^{-1} s^{-1}$), and a low optical absorption coefficient $\alpha \sim 500$ cm^{-1} in the visible spectral range is usually achieved by pulsed laser deposition (PLD)[2,3] or radio frequency magnetron sputtering (rf MS)[4,5] using ceramic targets and deposition at substrate temperatures $T_S > 200$ °C. Films grown by reactive pulsed MS (RP MS), which would override both PLD and rf MS in terms of scalability and cost efficiency, respectively, by now showed mobilities limited to $\mu_e \sim 28$ $cm^2 V^{-1} s^{-1}$.[6,7] In contrast to PLD and rf MS, the RP MS uses metallic targets being sputtered in a mixture of Ar and O_2. This offers the possibility to precisely vary the oxygen to metal flux ratio, which may serve as an additional optimization parameter to increase μ_e by controlling the film stochiometry and the local bonding arrangement around the dopant atom. Nevertheless, this potential advantage remained unexplored due to limited understanding of the mechanisms that control the generation and transport of the free electrons in AZO and their relation to the deposition conditions. The present study focuses on the effect of *in situ* controlled variation in the oxygen partial pressure during RP MS on the free electron mobility of AZO thin films grown at different Al concentrations and substrate temperatures.

AZO films were deposited by RP MS using two 2 in. unbalanced magnetrons (FHR, Germany) operated in parallel.[8] Three sets of Zn–Al alloy targets were used with different Al concentrations (c_{Al}) of ~1.7, 4.7, and 8.7 at. %, as determined by energy dispersive x-ray spectrometry (EDX). All films were grown on fused silica $7 \times 7 \times 0.5$ mm^3 substrates, whose temperature was varied in the range of $T_S = 22-520$ °C using a substrate holder with a boralectric heater (Tectra, Germany). Before each deposition run, the chamber was baked for several hours at ~90 °C and then cooled down to RT to reach a base pressure of 1.0×10^{-7} mbar. With the substrate covered by a closely mounted shutter, the magnetron targets were initially presputtered in pure Ar for 5 min, followed by a stabilization of the discharge current and the gas partial pressures under the addition of O_2. A fixed Ar flow rate of 105 sccm was employed. Using a capacitance gauge (Pfeiffer CMR 275) the total Ar and O_2 pressure was monitored precisely. For each run, the total pressure during presputtering in Ar only (p_1), during deposition in Ar and O_2 (p_2), and after deposition in Ar and O_2 with switched off magnetrons (p_3) was determined. Depositions were carried out at p_2 values in the range of $1.85-2.00 \times 10^{-2}$ mbar. The oxygen partial pressure during film growth was calculated as $p_{O_2} = p_2 - p_1$. An error of ~5% in p_{O_2} is attributed mainly to a limited stability of the gas flow controllers. The long-term stability of the Ar and O_2 partial pressures during deposition was controlled by a differentially pumped quadrupole mass spectrometer (HIDEN RGA 201).

The magnetrons were operated in constant voltage mode (cathode voltage $U \leq 750$ V) with a pulse frequency of $f = 2$ kHz. At fixed pumping speed the resulting discharge current and power depend strongly on the oxygen partial pressure p_{O_2}. While the oxygen gas flow (Φ_{O_2}) controls the total amount of oxygen available for the reactive process, a fine tuning of p_{O_2} was performed by varying the magnetron voltage at constant Φ_{O_2}. This is based on the gettering of reactive gas by the sputtered metal, a characteristic feature of reactive MS. The final p_{O_2} value depends on the total amount of sputtered metal, which can be controlled by changing U, because the sputtering yield of Zn and Al monotonically increases with rising energy of the Ar ions below 1 keV.[9,10] After determining the optimum p_{O_2} value, denoted as $p_{O_2}^*$, corresponding to a certain magnetron voltage at given Φ_{O_2}, it was used to grow samples at different substrate temperatures.

The film thickness (300–400 nm), the refractive index, and the extinction coefficient were determined by spectroscopic ellipsometry (M-2000, J.A Woolam, Inc.). Hall effect measurements in van der Pauw geometry (HMS 3000, ECO-

[a)]Author to whom correspondence should be addressed. Electronic mail: s.cornelius@fzd.de. Tel.: +49 (0) 351 260 2039. FAX: +49 (0) 351 260 2703.

 © 2009 American Institute of Physics

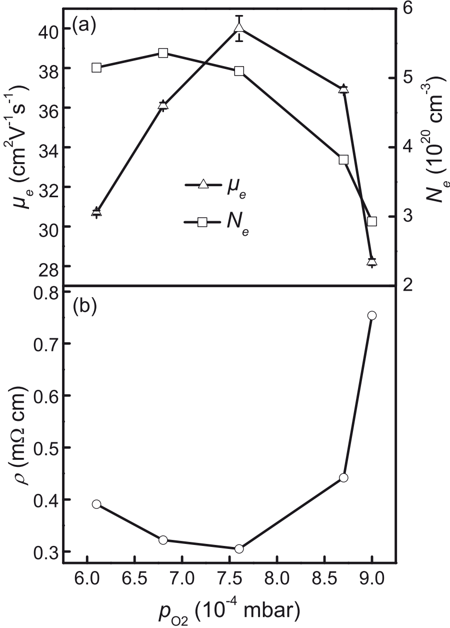

FIG. 1. Free electron mobility μ, density N_e (a), and film resistivity ρ (b) vs oxygen partial pressure at a fixed substrate temperature of T_S =350 °C, a target Al-content of c_{Al}=1.7 at. %, and an oxygen flow of Φ_{O_2}=3.1 SCCM.

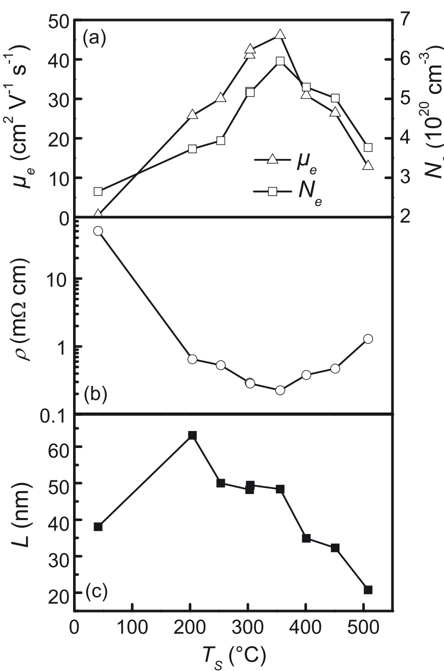

FIG. 2. [(a) and (b)] As for Fig. 1(c) coherence length L vs substrate temperature at an oxygen partial pressure of $p_{O_2}{}^*$=8.7±0.4×10^{-4} mbar, an oxygen flow of Φ_{O_2}=3.5 SCCM, and a target composition of c_{Al} =1.7 at. %.

PIA) were carried out at a magnetic flux density of 0.51 T and RT, from which the free electron density N_e, the Hall mobility μ_e, and the film electrical resistivity ρ were derived. The samples were contacted by gold-plated clamps providing Ohmic contacts without any additional contact deposition or bonding. Compositional analysis of the films was performed by means of elastic recoil detection analysis (ERDA) using 35 MeV Cl^{7+} ions. The film structure was analyzed by x-ray diffraction (XRD) using a D8 (BRUKER AXS) step scan diffractometer with Cu $K\alpha$ radiation The size of coherently diffracting domains, i.e., the coherence length L indicative of the grain size, was estimated from the wurtzite ZnO (002) peak using the Scherrer formula.

Figure 1 shows a typical dependence of the AZO film N_e, μ_e (a), and ρ (b) on the oxygen partial pressure p_{O_2} adjusted by a variation in the target voltage in the range from 540 to 660 V using a constant oxygen flow of Φ_{O_2} =3.1 SCCM. The data are shown for films grown at T_S =350 °C from targets with c_{Al}=1.7 at. %. In this case, a maximum of $\mu_e \sim 40$ cm^2 V^{-1} s^{-1} together with a minimum resistivity of $\rho \sim 3\times10^{-4}$ Ω cm is achieved at $p_{O_2}{}^*$ $\sim(7.6\pm0.4)\times10^{-4}$ mbar. The electrical resistivity of the AZO films increases rapidly when increasing $p_{O_2} > p_{O_2}{}^*$ due to a decrease in both μ_ε and N_ε. This can be attributed either to Al dopant deactivation or to a decreasing density of oxygen vacancies acting as electron donors caused by an excess of oxygen during film formation. Similar dependences on p_{O_2} were observed at other Φ_{O2} and T_S.

Figure 2 shows the dependence of the electrical properties [(a) and (b)] and coherence length L (c) on T_S for another set of films grown at c_{Al}=1.7 at. % with optimum parameters of $p_{O_2}{}^*=(8.7\pm0.4)\times10^{-4}$ mbar, U=680 V, and Φ_{O_2}=3.5 SCCM. The best electrical properties, ρ $\sim 2.26\times10^{-4}$ Ω cm, $\mu_e\sim 46$ cm^2 V^{-1} s^{-1}, and $N_e \sim 6.0$ $\times 10^{20}$ cm^{-3}, are achieved at an optimum substrate temperature of $T_S{}^*$=350 °C. The present free electron mobility is significantly higher than the highest value of 28 cm^2 V^{-1} s^{-1} reported before for AZO films grown by reactive MS (Ref. 7) and is essentially identical to the best values achieved for PLD (47 cm^2 V^{-1} s^{-1}) (Ref. 3) and rf MS (44 cm^2 V^{-1} s^{-1}).[4] A steep decrease in the mobility is observed both below and above the optimum temperature with a similar trend for the free electron density. This leads to a characteristic $\rho(T_S)$ dependence with a minimum resistivity at $T_S{}^*$. Strongly absorbing films form at $T_S \leq 100$ °C, while at higher temperatures low resistivity and transparent films are obtained. The AZO film with the lowest resistivity exhibits an absorption coefficient of α=460 cm^{-1} at a wavelength of 550 nm.

According to the XRD data all AZO films show a pronounced c-axis texture, resulting in a strong (002) peak corresponding to wurtzite ZnO. The dependence of the coherence length L on T_S [Fig. 2(c)] qualitatively resembles that of electrical properties, but the maximum L is reached already at $T_S < T_S{}^*$. Thus, although the decreasing μ_e values above $T_S{}^*$ are consistent with a decreasing crystallite size, the observed $\mu_e(T_S)$ cannot be directly related to the change in crystallinity.

Figure 3 sorts all present data for different target compositions and depositions conditions in a plot of the free electron mobility versus the free electron density. The figure shows a semiempirical model for ionized impurity scattering and impurity clustering developed by Masetti *et al.*,[11] which has been evaluated using parameters for AZO given in Ref. 5. At free electron densities between 10^{19} and 10^{21} cm^{-3}, the result sets a practical limit of $\mu_e \sim 55$ cm^2 V^{-1} s^{-1} to the ionized impurity scattering mobility, which is consistent with the highest value achieved in our work. The model even slightly underestimates the attainable mobility at $N_e \sim 6$ $\times 10^{20}$ cm^{-3}, while at higher free electron densities the calculated mobility is limited to $\sim$15 cm^2 V^{-1} s^{-1} due to the onset of ionized impurity clustering. A competing description

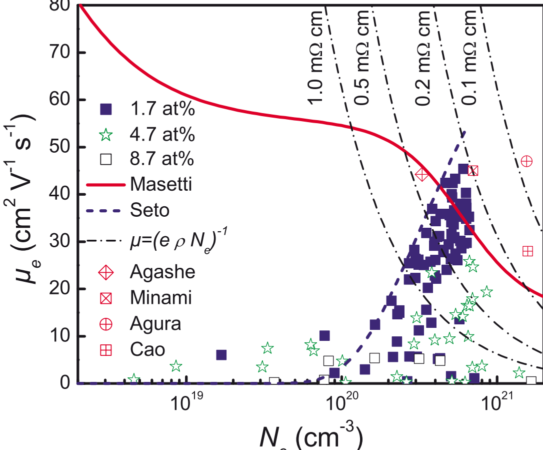

FIG. 3. (Color online) Scatter plot of free electron mobility vs free electron density from present data at different target compositions and from literature for PLD (Ref. 3), rf MS (see Refs. 4 and 16), and RP MS (Ref. 7). The solid line represents a semiempirical curve for ionized impurity scattering and impurity clustering from Ref. 12 with parameters from Ref. 5; the dashed line is from an approximate description of grain barrier limited transport (see Ref. 13). The dash-dotted lines represent contours of constant resistivity.

of grain barrier limited transport in polycrystalline materials has been published by Seto.[12] Depending on the areal density of traps N_T in the disturbed regions between the grains and the carrier density inside the grains, the traps can be partly or completely filled, leading to varying barrier heights φ_B and widths. Electrons can surmount these barriers by thermionic emission. In the case of TCOs ($LN_e > N_T$), the mobility is given by[12]

$$\mu_{\text{Seto}} = \mu_0 \exp(-\varphi_B/kT) = eL(2\pi m^* kT)^{-1/2} \exp(-e^2 N_T^2/8\varepsilon\varepsilon_0 N_e kT), \quad (1)$$

where μ_0 represents the in-grain mobility. In contrast to the model of Masetti *et al.*,[11] Eq. (1) results in a decreasing mobility with decreasing N_e values and is valid only at $N_e < 6\times10^{20}$ cm^{-3}, where impurity clustering does not occur.

As can be seen in Fig. 3, most of the $\mu_e(N_e)$ data for the target composition of $c_{\text{Al}}=1.7$ at. % are limited by either mechanism. The limiting data points for $c_{\text{Al}}=1.7$ at. % below $N_e=6\times10^{20}$ cm^{-3} have been fitted using the Seto[12] model (1). Although μ_0 and N_T are interdependent, it is possible to extract both values because they affect slope and position of $\mu_{\text{Seto}}(N_e)$, respectively. A rough best fit yields $\mu_0=75-90$ cm^2 V^{-1} s^{-1} and $N_T=(1.60-1.75)\times10^{13}$ cm^{-2}. The latter is in good agreement with data reported by Ellmer and co-worker[5,13] for AZO films grown by MS. Still, our highest mobility values are about a factor of two smaller than the in-grain mobility μ_0 due to the contribution of electron scattering inside the bulk of the grains at dislocations and point defects, which is not considered in the idealized Seto[12] model. Similar experimental in-grain mobilities of $\sim$100 cm^2 V^{-1} s^{-1}, which are close to our estimated μ_0 values, have been obtained by spectroscopic ellipsometry.[14] Finally, the significant decrease in the maximum attainable mobility at $N_e \geq 6\times10^{20}$ cm^{-3} for the larger Al fractional compositions is qualitatively consistent with the harmful role of Al impurity clustering.

A general trend of increasing optimum μ_e values along with improving of the film crystallinity toward lower c_{Al} has been observed (Table I). According to ERDA data, the Al concentration in the films at $T_S=T_S^*$ agrees with that in the target within the error limits. Thus, the Al donor activation rate even decreases with increasing c_{Al} because higher c_{Al} does not lead to higher optimum N_e values. Taking into account recent studies suggesting a solubility limit of 3 at. % for Al in ZnO,[15] the trend in μ_e can be understood assuming that at $c_{\text{Al}} > 3$ at. %, there is an excess of electrically inactive Al, which might locally drive the formation of $ZnO-Al_2O_3$ homologous phases[15] and affect film electrical properties by increasing the free electron scattering.

TABLE I. Optimum values of the AZO film electrical parameters and corresponding coherence length values obtained for different target Al concentrations.

c_{Al} (at %)	L (nm)	μ_e (cm^2 V^{-1} s^{-1})	N_e (10^{20} cm^{-3})	ρ (10^{-4} Ω cm)
8.7 ± 1.7	19	7.0	4.3	20.7
4.7 ± 1.7	34	24.6	6.9	3.62
1.7 ± 0.5	48	46.6	6.0	2.26

In summary, a fine tuning of the oxygen partial pressure using gettering of O_2 by sputtered metal atoms, along with substrate temperature variation, yielded AZO films with the highest mobility values so far reported for the present deposition technique. The best value of 46 cm^2 V^{-1} s^{-1} is comparable to the highest values achieved in AZO films grown by techniques that are less efficient in terms of either scalability or cost, and is approaching the practical limit of 55 cm^2 V^{-1} s^{-1}. Depending on the free electron density and the aluminum content, the electron mobility is either controlled by ionized impurity scattering in connection with impurity clustering or grain boundary limited transport.

The authors gratefully acknowledge the EDX analysis of the targets by H. Reuther and E. Christalle and ERDA analysis by F. Munnik. This work was supported in part by the Free State of Saxony (SMWA/SAB Project No. 11815/1854).

[1] G. J. Exarhos and X.-D. Zhou, Thin Solid Films **515**, 7025 (2007).
[2] A. V. Singh, R. M. Mehra, N. Buthrath, A. Wakahara, and A. Yoshida, J. Appl. Phys. **90**, 5661 (2001).
[3] H. Agura, A. Suzuki, T. Matsushita, T. Aoki, and M. Okuda, Thin Solid Films **445**, 263 (2003).
[4] C. Agashe, O. Kluth, J. Hüpkes, U. Zastrow, B. Rech, and M. Wuttig, J. Appl. Phys. **95**, 1911 (2004).
[5] K. Ellmer and R. Mientus, Thin Solid Films **516**, 4620 (2008).
[6] B. Szyszka, V. Sittinger, X. Jiang, R. J. Hong, W. Werner, A. Pflug, M. Ruske, and A. Lopp, Thin Solid Films **442**, 179 (2003).
[7] H. T. Cao, C. Sun, Z. L. Pei, A. Y. Wang, L. S. Wen, R. J. Hong, and X. Jiang, J. Mater. Sci.: Mater. Electron. **15**, 169 (2004).
[8] A. I. Rogozin, M. V. Vinnichenko, A. Kolitsch, and W. Möller, J. Vac. Sci. Technol. A **22**, 349 (2004).
[9] S. M. Rossnagel, *Handbook of Vacuum Science and Technology* (Academic, San Diego, 1998), p. 609.
[10] R. Bunshah, *Handbook of Deposition Technologies for Films and Coatings* (Park Ridge, New Jersey, 1984).
[11] G. Masetti, M. Severi, and S. Solmi, IEEE Trans. Electron Devices **30**, 764 (1983).
[12] J. Y. Seto, J. Appl. Phys. **46**, 5247 (1975).
[13] K. Ellmer, *Transparent Conductive Zinc Oxide* (Springer, Berlin, 2008), p. 53.
[14] I. Volintiru, M. Creatore, and M. C. M. van de Sanden, J. Appl. Phys. **103**, 033704 (2008).
[15] S. Yoshioka, F. Oba, R. Huang, I. Tanaka, T. Mizoguchi, and T. Yamamoto, J. Appl. Phys. **103**, 014309 (2008).
[16] T. Minami, H. Sato, K. Ohashi, T. Tomofuji, and S. Takata, J. Cryst. Growth **117**, 370 (1992).

APPLIED PHYSICS LETTERS **95**, 081904 (2009)

Highly dense amorphous Nb_2O_5 films with closed nanosized pores

M. Vinnichenko,[1,a)] A. Rogozin,[1] D. Grambole,[1] F. Munnik,[1] A. Kolitsch,[1] W. Möller,[1] O. Stenzel,[2] S. Wilbrandt,[2] A. Chuvilin,[3] and U. Kaiser[3]
[1]*Institute of Ion Beam Physics and Materials Research, Forschungszentrum Dresden-Rossendorf, 01314 Dresden, Germany*
[2]*Fraunhofer Institut Angewandte Optik und Feinmechanik, 07745 Jena, Germany*
[3]*Universität Ulm, 89069 Ulm, Germany*

(Received 17 May 2009; accepted 5 August 2009; published online 24 August 2009)

This study is focused on tailoring the porosity of Nb_2O_5 films during reactive pulsed magnetron sputtering. Dense amorphous films containing nanopores only in deeper regions have been grown at a high rate using substrate temperatures below 60 °C. The films exhibit a high refractive index, $n_{400}=2.54$, a low extinction coefficient, $k_{400}\sim 6\times 10^{-4}$, a low mechanical stress (−90 MPa), and a negligible thermal shift. The specific depth distribution of the nanopores is believed to be the reason for the optimum trade-off between a high refractive index and low mechanical stress. © *2009 American Institute of Physics*. [DOI: 10.1063/1.3212731]

The need for cost-effective materials combining a high refractive index, low optical extinction, low mechanical stress, and amorphous homogeneous microstructure for optical applications has stimulated active research on thin films of oxides such as HfO_2, Ta_2O_5, and Nb_2O_5.[1–3] Films of Nb_2O_5 produced by magnetron sputtering remain amorphous up to a temperature of 500 °C.[4,5] In addition, their refractive index $n(\lambda=400\ \text{nm})\sim 2.60$ (Refs. 6 and 7) is significantly higher than that of HfO_2 and Ta_2O_5. However, Nb_2O_5 films with the highest refractive index, produced by either reactive pulsed magnetron sputtering (RPMS)[4] or ion plating,[8] often exhibit a relatively high compressive stress ($\sigma > 300$ MPa) (Ref. 9) and an extinction coefficient $k(\lambda=400\ \text{nm}) > 0.002$ (Refs. 6 and 7) leading to inferior performance of the resulting optical devices. There is evidence in the literature that the incorporation of nanopores may cause relaxation of the mechanical stresses in amorphous films,[4] but the pores may absorb atmospheric water, which will then lead to a thermal shift, i.e., to a thermally variable refractive index. Tailoring film porosity would enable one to achieve an optimum trade-off between mechanical and optical film properties. The volume fraction of pores in the growing film may be reduced by increasing surface adatom mobility.[10] Such an increase can be accomplished by either energetic particle bombardment or raising substrate temperature. The present study focuses on the porosity control of Nb_2O_5 films using high-growth rate RPMS with variable oxygen partial pressure, different magnetron-substrate configurations, and substrate temperatures.

Nb_2O_5 films of a thickness of 490 to 550 nm were deposited by RPMS using two 2 in. unbalanced magnetrons (MightyMAK, U.K.) operated in parallel[11] and equipped with high purity (99.95%) Nb metallic targets (Kurt J. Lesker, U.K.). The films were grown using either two magnetrons with axes directed to the sample holder edges (off-normal deposition, with the angle between the magnetron axis and the substrate normal being 17°)[11] or a single magnetron with an axis perpendicular to the substrate. The substrates were either $(10\times 10\times 0.5)$ mm^3 plates of UV-grade fused silica, $(20\times 20\times 0.3)$ mm^3 plates of crystalline Si(100), or 3 –in. wafers of crystalline Si. The substrates were at floating potential while their temperature, T_S, was kept either below 60 °C (no intentional heating) or at a fixed value of 370 °C by means of a sample holder with a boralectric heater (Tectra, Germany). In both cases, the distance from the magnetron to the substrate was 55 mm. The magnetrons were operated in a constant power mode (400–625 W per magnetron), with voltage and current values in the range of 175–500 V and 0.8–3.6 A, respectively, and frequencies of 5 and 16.67 kHz. The chamber was baked to reach a base pressure of 3.0×10^{-7} mbar before deposition. The magnetron targets were initially presputtered in pure Ar for 5 min followed by stabilization of the discharge current and gas partial pressures upon addition of O_2. Before striking the magnetron discharge, the partial pressures of Ar ($p_{Ar}=2.29\times 10^{-2}$ mbar) and O_2 [$p_{O_2}=(3.03-6.68)\times 10^{-3}$ mbar] were monitored precisely with a capacitance gauge (Pfeiffer CMR 275).

An automated Langmuir probe (SmartProbe, Scientific Systems Ltd., USA) was employed to determine the spatial distribution of the plasma ion density, N_i, with a resolution of 1 cm in the plane parallel to the substrate at a distance of 3 cm from the latter. The film optical properties were characterized using an M-2000 spectroscopic ellipsometer (J.A. Woolam Co Inc., USA) at a photon energy of 1.24–3.4 eV. Spectroscopic ellipsometry (SE) data were processed with the aid of WVASE software, and were fitted to a four-layer model involving air, surface roughness, the oxide film, and the substrate. The surface roughness was modeled using a 50% air and 50% bulk oxide Bruggeman effective medium approximation.[12] The Nb_2O_5 complex refractive index, $N=n+ik$, being consistent with the Kramers–Kronig relations, was obtained using a Cody–Lorentz parameterized model.[3] Adding a linear grading of n and k values does not improve substantially fit results for optimized Nb_2O_5 films; however, it decreases the fit mean square error by a factor of 2–3 for unoptimized ones. In the latter case, the film parameters, including thickness-averaged n values, match (within the experimental error) those obtained by a simpler model. The

a)Author to whom correspondence should be addressed. Electronic mail: m.vinnichenko@fzd.de. Tel.: +49 (0) 351 260 2374. FAX: +49 (0) 351 260 2703.

 © 2009 American Institute of Physics

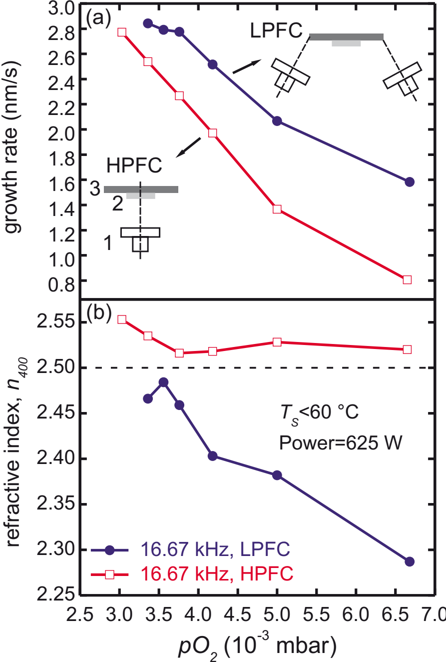

FIG. 1. (Color online) Growth rate (a) and refractive index, n_{400} (b), of films produced at different oxygen partial pressures, a substrate temperature of $T_s < 60$ °C, and magnetron power of 625 W. The insets show the configuration of the magnetron (1) with respect to the substrate (2) fixed to the substrate holder (3).

values of the refractive index and the extinction coefficient at a wavelength of 400 nm (3.1 eV), n_{400} and k_{400}, respectively, were compared for different samples, and the error involved in the former did not exceed $\Delta n_{400} \sim \pm 0.01$. The sensitivity limit of the SE measurement of the extinction coefficient was estimated to be about $k_{400} \sim 5 \times 10^{-4}$. For selected samples, the thermal shift was determined from transmission measurements with an OptiMon spectrophotometer as the relative change in the refractive index due to heating in a vacuum from room temperature to 100 °C.[13] The film stress was evaluated with Stoney's equation measuring the change in the curvature of the 3 in. Si wafers.[13] Negative and positive values correspond to tensile and compressive stress, respectively.

The hydrogen depth profile in the films was determined by nuclear reaction analysis (NRA) using $^{15}N^{2+}$ ions at energies above 6.3 MeV. The microstructure of selected films was characterized by high-resolution cross-sectional transmission electron microscopy (X-TEM) using a CM20 instrument (Philips, Netherlands) at an acceleration voltage of 200 kV, resulting in a point-to-point resolution of 0.25 nm. X-TEM specimen preparation followed a standard procedure described in more detail elsewhere.[14] The ion energy and the angle were chosen in such a way as to minimize ion milling artifacts.

Figure 1 shows the dependence of the growth rate (a) and the refractive index, n_{400}, (b) on the oxygen partial pressure p_{O_2} for films grown using two different magnetron-substrate configurations. The films were deposited on unheated substrates ($T_S < 60$ °C) at the highest magnetron power of 625 W. In the case of two magnetrons and off-normal deposition, the ion density at the substrate center is $N_i \sim 3 \times 10^{10}$ cm^{-3}. This is denoted as a low plasma flow configuration (LPFC). In the high plasma flow configuration (HPFC) for a single magnetron with an axis perpendicular to the substrate surface, the central beam of the unbalanced magnetron provides an ion density at the substrate of $N_i \geq 2.8 \times 10^{11}$ cm^{-3} for the entire range of p_{O_2} and at the two frequencies used. Increasing p_{O_2} causes a reduction in the film growth rate from 2.84 to 1.58 nm/s for LPFC, and a decrease from 2.77 to 0.80 nm/s for HPFC due to stronger coverage of the Nb magnetron target with an oxide layer resulting from an increased supply of oxygen.[15] For LPFC, the films grown at $p_{O_2} = 3.56 \times 10^{-3}$ mbar exhibit a highest refractive index of $n_{400} = 2.48$ and a relatively high extinction coefficient $k_{400} = 0.02$ (not shown). These parameters decrease to $n_{400} = 2.29$ and $k_{400} < 0.001$ at $p_{O_2} = 6.68 \times 10^{-3}$ mbar. In contrast, films grown at HPFC have a refractive index $n_{400} = 2.52 - 2.55$ and $k_{400} < 6 \times 10^{-4}$ over the whole range of p_{O_2}. In case of deposition onto heated substrates ($T_S = 370$ °C) at LPFC, a reduced magnetron power of 500 W and operation frequency of 5 kHz ($p_{O_2} = 3.36 \times 10^{-3}$ mbar) were necessary to achieve an optimum combination of a high refractive index ($n_{400} = 2.46$) and a low extinction coefficient ($k_{400} < 5 \times 10^{-4}$).

The films grown for HPFC without substrate heating (Table I) have a low tensile stress of −90 MPa and a negligible thermal shift in +0.06% in addition to high n. In contrast, the films grown for LPFC, but at an elevated substrate temperature, show a higher tensile stress (−132 MPa) and a much larger thermal shift in −2.0%.

Figure 2 shows X-TEM images of the films grown without heating for HPFC [(a)–(c)] and onto heated substrates for LPFC [(d)–(f)]. The common feature of both types of films is the dense nonporous amorphous layer near the Nb_2O_5/Si interface, with a thickness of ~5 nm [sample A, Fig. 2(c)] and ~5 nm [sample B, Fig. 2(f)]. Then, in the first case, a 10 nm thick layer consisting of isolated pores [Fig. 2(c)] forms followed by a dense amorphous microstructure with discontinuous vertical arrays of pores [Fig. 2(a)]. The characteristic pore size is 2 nm. The NRA depth profile shows that the hydrogen content in the film decreases from 1.2 at. % at the surface to values below the detection limit inside the film. The low hydrogen content is mainly attributed to atmospheric water adsorption at the surface rather than to water uptake by the pores. Accordingly, the thermal shift becomes negligible.

Conversely, for LPFC on heated substrates, no such a porous layer is observed near the film-substrate interface, and vertical arrays of pores start to form directly from the

TABLE I. Deposition parameters, thermal shift, and stress of the two different series of Nb_2O_5 samples.

Sample	T_S (°C)	P_m (W)	V_m (V)	f_m (kHz)	No. of magnetrons	N_i (10^{11} cm^{-3})	Configuration	Thermal shift (%)	Stress (MPa)
A	<60	625	175	16.67	1	2.8	HPFC	+0.06	−90
B	370	500	500	5	2	0.08	LPFC	−2.0	−132

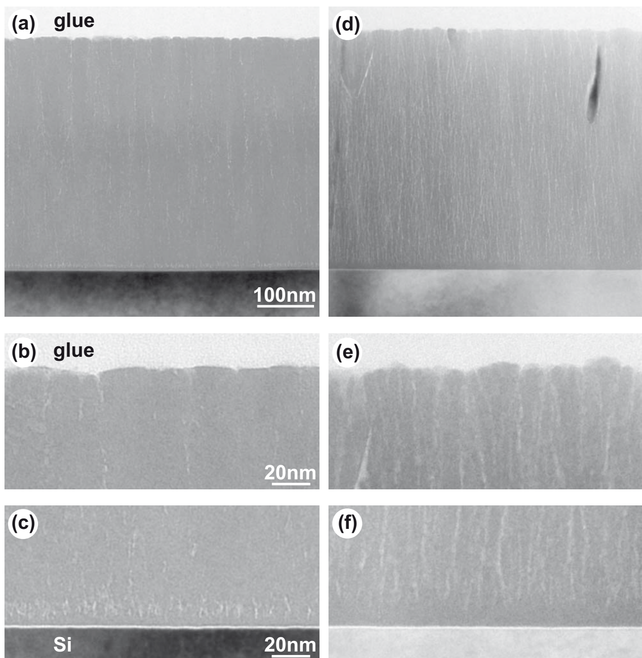

FIG. 2. X-TEM images of films grown onto unheated substrates in HPFC mode [(a)–(c)], and at T_S=370 °C in LPFC mode [(d)–(f)].

dense area [Figs. 2(d) and 2(f)], then continue through the film and, finally, open at the film surface [Fig. 2(e)]. The characteristic pore size is a little larger than described above, i.e., ~3 nm, while the pore density is significantly higher. These findings are in agreement with the NRA depth profile showing a high H concentration decreasing from 11 to 7 at. % with film thickness. The significant uptake of atmospheric water by the open pores explains the high thermal shift observed in these films.

The increased particle bombardment for HPFC at normal incidence is the reason for the observed formation of a dense amorphous microstructure with a small volume fraction of closed nanosized pores. In our case of reactive unbalanced magnetron sputtering, positive plasma ions contribute appreciably to the thermal power at the substrate[16] for plasma ion densities higher than 10^{11} cm^{-3}. In addition, energetic reflected neutral particles of Ar might play a role because their mass is appreciably lower than that of Nb target atoms. Since the refractive index of the material correlates with its density,[5] the densification of the amorphous film produces the high n values obtained irrespectively of p_{O_2}, and occurs for $N_i > 10^{11}$ cm^{-3}. The decreased particle bombardment for LPFC, as indicated by the low plasma ion density ($N_i \sim 10^{10}$ cm^{-3}), in conjunction with off-normal deposition, favors shadowing effects which in turn lead to the porous microstructure observed even in the case of growth at an elevated substrate temperature T_S=370 °C. A higher degree of porosity explains the lower refractive index values of the films grown for LPFC in comparison with those for HPFC (Fig. 1).

The influence of the nanosized pores on the film refractive index, thermal shift, and mechanical stress in the amorphous Nb_2O_5 films is interpreted in light of a recently developed model.[17] It is assumed that nonporous films show a high refractive index and a zero thermal shift while having a high compressive stress. The model suggests that there is an optimum volume fraction of closed pores of about 1% and, while the refractive index is still high, the film has a low stress and a thermal shift close to zero. The properties of the Nb_2O_5 samples deposited for HPFC match closely the predictions of this model, thus providing an optimum trade-off between the discussed optical and mechanical film parameters. Further enhancement in porosity and dominance of open pores increase the tensile stress, reduce significantly the refractive index, and lead to a substantial negative thermal shift. This situation corresponds to the films produced at LPFC.

n_{400}=2.54 (n_{550}=2.36) is among the highest refractive index values achieved to date using magnetron sputtering[4] and is only a little below the value n_{550}=2.40 for films produced by ion plating.[8] However, the films with the highest refractive index in Ref. 4 exhibit a mechanical stress of −200 MPa while ion plated films show an extinction coefficient in the visible spectral range of $k_{515}=5\times10^{-4}$ (Ref. 8) which is commensurate with our values in the UV spectral range. In addition, the growth rate of the films studied in the present work is the highest compared to the values available in literature.[4,8]

In summary, adjusting the deposition geometry and plasma ion density during RPMS enables one to tailor the porosity of amorphous Nb_2O_5 thin films using a three-dimensional growth mode. Films with a low extinction coefficient, a high refractive index, low tensile stress and negligible thermal shift have been obtained during deposition for plasma ion densities above 10^{11} cm^{-3} and substrate temperatures below 60 °C. These properties have been explained by the formation of a dense amorphous microstructure with a specific depth distribution of closed nanopores. In contrast, films grown at 370 °C using low plasma ion densities (~10^{10} cm^{-3}) are less dense with pores being open at the film surface, and show a significant thermal shift, higher tensile stress and lower refractive index.

The authors gratefully acknowledge assistance of R. Yankov and financial support by the EFDS and AiF Project No. 15042 BR “NANOMORPH.”

[1] L. Martinu and D. Poitras, J. Vac. Sci. Technol. A **18**, 2619 (2000).
[2] J. M. Ngaruiya, O. Kappertz, S. H. Mohamed, and M. Wuttig, Appl. Phys. Lett. **85**, 748 (2004).
[3] J. Price, P. Y. Hung, T. Rhoad, B. Foran, and A. C. Diebold, Appl. Phys. Lett. **85**, 1701 (2004).
[4] B. Hunsche, M. Vergöhl, H. Neuhäuser, F. Klose, B. Szyszka, and T. Matthee, Thin Solid Films **392**, 184 (2001).
[5] S. Venkataraj, R. Drese, Ch. Liesch, O. Kappertz, R. Jayavel, and M. Wuttig, J. Appl. Phys. **91**, 4863 (2002).
[6] M. G. Krishna and A. K. Bhattacharya, Int. J. Mod. Phys. B **13**, 411 (1999).
[7] M. Vergöhl, B. Hunsche, N. Malkomes, T. Matthee, and B. Szyszka, J. Vac. Sci. Technol. A **18**, 1709 (2000).
[8] A. Hallbauer, D. Huber, G. N. Strauss, S. Schlichtherle, A. Kunz, and H. K. Pulker, Thin Solid Films **516**, 4587 (2008).
[9] C.-C. Lee, C.-L. Tien, and J.-C. Hsu, Appl. Opt. **41**, 2043 (2002).
[10] R. W. Smith and D. J. Srolovitz, J. Appl. Phys. **79**, 1448 (1996).
[11] A. I. Rogozin, M. V. Vinnichenko, A. Kolitsch, and W. Möller, J. Vac. Sci. Technol. A **22**, 349 (2004).
[12] D. E. Aspnes, J. B. Theeten, and F. Hottier, Phys. Rev. B **20**, 3292 (1979).
[13] O. Stenzel, S. Wilbrandt, N. Kaiser, M. Vinnichenko, F. Munnik, A. Kolitsch, A. Chuvilin, U. Kaiser, J. Ebert, S. Jakobs, A. Kaless, S. Wüthrich, O. Treichel, B. Wunderlich, M. Bitzer, and M. Grössl, Thin Solid Films **517**, 6058 (2009).
[14] J. C. Bravman and R. Sinclair, J. Electron Microsc. Tech. **1**, 53 (1984).
[15] S. Berg and T. Nyberg, Thin Solid Films **476**, 215 (2005).
[16] A. Rogozin, M. Vinnichenko, N. Shevchenko, A. Kolitsch, and W. Moeller, Thin Solid Films **496**, 197 (2006).
[17] O. Stenzel, J. Phys. D **42**, 055312 (2009).

APPLIED PHYSICS LETTERS **95**, 172103 (2009)

Anomalous Hall resistance in Ge:Mn systems with low Mn concentrations

Shengqiang Zhou (周生强),[a] Danilo Bürger, Manfred Helm, and Heidemarie Schmidt
Institute of Ion Beam Physics and Materials Research, Forschungszentrum Dresden-Rossendorf, P.O. Box 510119, 01314 Dresden, Germany

(Received 15 September 2009; accepted 9 October 2009; published online 27 October 2009)

Taking Mn doped Germanium as an example, we evoke the consideration of a two-band-like conduction in diluted ferromagnetic semiconductor (FMS). The main argument for claiming Ge:Mn as a FMS is the occurrence of the anomalous Hall effect (AHE). Usually, the reported AHE (1) is observable at temperatures above 10 K, (2) exhibits no hysteresis, and (3) changes the sign of slope. We observed a similar Hall resistance in Mn implanted Ge with the Mn concentration as low as 0.004%. We show that the puzzling AHE features can be explained by considering a two-band-like conduction in Ge:Mn. © *2009 American Institute of Physics*. [doi:10.1063/1.3257363]

Diluted ferromagnetic semiconductors (FMSs) exhibit strong magnetotransport effects, namely negative magnetoresistance (MR) and anomalous Hall effect (AHE),[1–3] and provide the possibility to control the spin by an external electric field. Ferromagnetic GaMnAs reveals hysteretic AHE, which mimics its magnetization, and allows the determination of its magnetic parameters by measuring the Hall resistance. The observation of AHE is considered as one of the important criteria for FMS to be intrinsic.[4] Mn doped Germanium provides an alternative of FMS, as predicted by Dietl *et al.*[5] Its compatibility with conventional microelectronics makes it more promising for industry application. We notice that pronounced MR and AHE have been reported in the Ge:Mn system[6–13] independent of the formation of MnGe precipitates or not, as well as in Cr doped Ge.[14] By scrutinizing the published data on Ge:Mn, one can observe three features in the reported AHE. First, most of the AHE curves shown were recorded at temperatures above 10 K. Indeed, Riss *et al.*[9] reveal only ordinary Hall effect below 10 K. Second, no hysteresis in AHE curves has been observed, despite the observation of a clear hysteresis in magnetization, which is much different from the case of III-Mn-V and ZnMnTe.[1–3] Third, the Hall curve changes the sign of slope at lower temperatures, usually between 10 and 50 K. Obviously, the correlation between magnetization, MR, and AHE, which is a hallmark of III-Mn-V and ZnMnTe FMS,[1–3] has not been proven for Ge:Mn. In this letter, we report the observation of an anomalous Hall resistance in Mn implanted Ge with the Mn concentration as low as 0.004%, in which neither ferromagnetism nor paramagnetism has been measured. By considering two types of carriers, all the puzzling Hall-resistance features can be explained. Moreover, the two-band-like conduction probably also explains the Hall resistance at large fields for InMnAs (Ref. 15) and InMnSb.[16]

Intrinsic Ge(001) wafers were implanted with Mn ions at 300 °C to avoid amorphization. We varied the ion fluence to get samples with a large range of Mn concentrations and correspondingly different structural and magnetic properties (see Table I). Magnetotransport properties were measured using Van der Pauw geometry with a magnetic field applied perpendicular to the film plane.

[a]Electronic mail: s.zhou@fzd.de.

As shown in Table I, we examined samples with a wide range of Mn concentration. Mn_5Ge_3 precipitates have been observed in sample Ge02 and Ge03 by synchrotron radiation x-ray diffraction (SR-XRD) (Ref. 17) at the Rossendorf beamline (BM20) at the ESRF, but not in sample Ge01, and are not expected in sample Ge19. SR-XRD has been proved to be sensitive for detecting nanocrystalline precipitates.[18,19] Correspondingly, ferromagnetism was observed only in sample Ge02 and Ge03. Down to 5 K, only diamagnetism was probed for sample Ge01, identical to a virgin Ge sample. Note that independent of the formation of precipitates, a fraction of Mn ions has been confirmed by spectroscopic methods to be diluted inside the Ge matrix, resulting in p-type doping,[20–22] as well as by electrical transport measurements as shown in Fig. 1(a). In sharp contrast to the structural and magnetic properties, similar Hall effects are probed for all samples as shown in Fig. 1. Indeed, the shape and temperature dependence of the Hall-resistance curves are similar to those reported in literature.[7–13] Deng *et al.*[12] attribute the sign change in Hall curves to the hopping conductivity. However, this cannot explain the vanishing of AHE below 10 K.

The nonferromagnetic nature of sample Ge19 and Ge01 indicates that the observation of anomalous Hall resistance is not necessarily related to ferromagnetism. Actually, similar Hall curves have been observed in materials with a two-band-like conduction.[23–25] Figure 2 shows the resistance versus temperature for all samples. Basically, below 10 K the resistance is weakly dependent on temperature and a transition occurs above 10 K. The activation energy is only several meV for all samples. It cannot be the thermal activation of holes from the Mn acceptor levels in Ge since the Mn single and double acceptor level is as deep as 160 meV from the valence band and 370 meV from the conduction band,[26] re-

TABLE I. Sample identification (ID), Mn concentration (Mn conc.), sheet hole concentration (hole conc.), and magnetic properties.

ID	Mn conc. (%)	Hole conc. (cm^{-2})	Properties	
			Precipitates?	Ferromagnetic?
Ge19	0.004		No	No
Ge01	0.2	6.5×10^{12}	No	No
Ge02	2	1.1×10^{13}	Mn_5Ge_3	Yes
Ge03	10	2.0×10^{13}	Mn_5Ge_3	Yes

 © 2009 American Institute of Physics

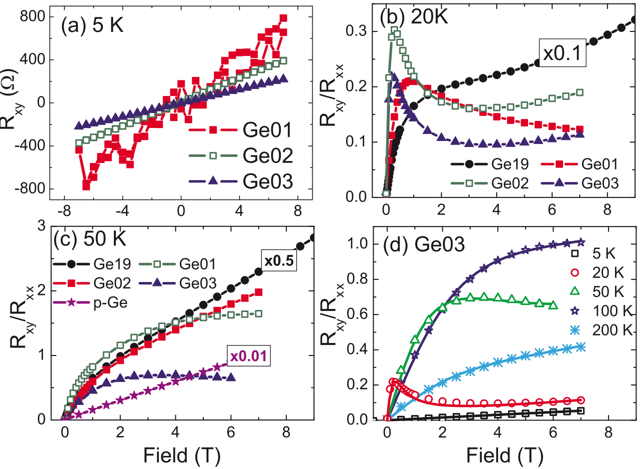

FIG. 1. (Color online) (a) Hall resistance (R_{xy}) at 5 K: only ordinary Hall effect has been observed. [(b) and (c)] The ratio between R_{xy} and sheet resistance at zero field (R_{xx}) at 20 and 50 K, respectively. An anomalous Hall resistance appears and the sign of slope is changed at lower fields (20 K) or at larger fields (50 K). (d) R_{xy}/R_{xx} at different temperatures for sample Ge03: the symbols are experimental data, while the solid lines are fits using Eq. (1). A Ga-doped Ge wafer with a hole concentration of 1.5 $\times 10^{16}$ cm^{-3} was measured for comparison and only ordinary Hall effect is observed as shown in (c). For better visibility some curves are multiplied by the factors indicated.

spectively. The small activation energy also cannot be a shallow acceptor level due to the large difference in the magnitude and temperature-dependence of resistance compared to Ga or In-doped Ge.[27] Moreover, between 10 and 50 K the temperature dependence of the resistance is rather a universal feature in Mn doped Ge.[6,7,9,28,29] An interpretation of the transition at around 10 K is plausible by considering the ground and the first excited states of $Mn^{2+}(d^5+2h)$.[30] Within such a scenario, a two-band-like conduction (or two types of carriers) is expected at above 10 K or even lower if the Mn concentration is very small as shown in Fig. 2. In the next step we fit the Hall curves using a two-band model described in Refs. 23 and 24.

The dependence of the ratio between Hall and sheet resistance (R_{xy}/R_{xx}) on the magnetic field B is given by

$$R_{xy}/R_{xx} = \frac{x_1\mu_1(1+\mu_1^2B^2) + x_2\mu_2[1+\mu_2^2B^2]}{1+(x_1\mu_2+x_2\mu_1)^2B^2}B, \quad (1)$$

where

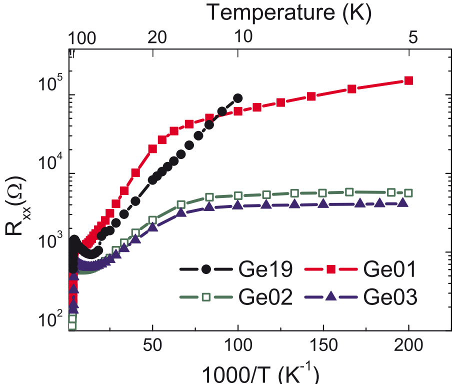

FIG. 2. (Color online) Temperature dependent sheet resistance at zero field (R_{xx}). For sample Ge19 the resistance is too large and can only be measured down to 10 K. Basically, below 10 K the resistance of sample Ge02 and Ge03 is weakly dependent on temperature.

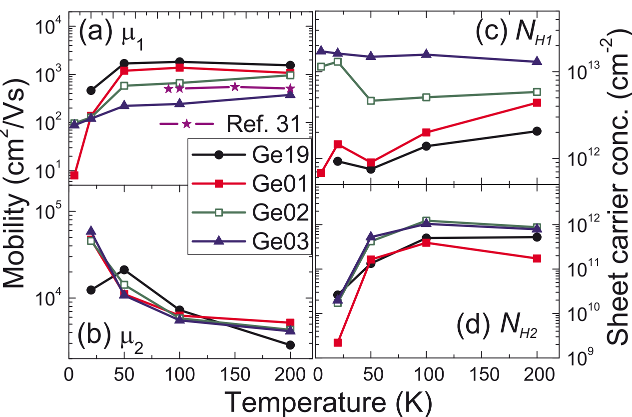

FIG. 3. (Color online) Fitting results of Hall curves at different temperatures. [(a) and (b)] Temperature dependent mobilities, data extracted from Ref. 31 is shown for comparison. [(c) and (d)] Temperature dependent sheet carrier concentrations. Lines are guides for eyes.

$$x_1 = \frac{G_1}{G_1+G_2}, \quad x_2 = \frac{G_2}{G_1+G_2}, \quad (2)$$

G and μ are conductance and mobility, respectively. The subscript numbers denote the two types of carriers. Numbers "1" and "2" label the carriers in the ground and the first excited state, respectively. In this formula, we assume spherical Fermi surfaces and use the zero-field sheet resistance (R_{xx}) to relate the two-carrier conductance,[23]

$$1/R_{xx} = G = G_1 + G_2, \quad (3)$$

where x_1, μ_1, and μ_2 in Eq. (1) are fitting parameters. At 5 K, for sample Ge01, Ge02, and Ge03 we only have carriers of type 1. With increasing temperature carriers of type 2 are activated and x_1 decreases. Taking this as a restriction, we can fit all measured results. Figure 1(d) shows the comparison between experiments and fitting. All the features are reproduced. In Fig. 3 we list the fitting results, i.e., temperature dependent mobility and sheet carrier concentration for two types of carriers. Despite the number of fitting parameters, it is plausible to draw conclusions according to the overall trend by examining all samples. The sheet carrier concentration (N_{H1}) of type 1 carriers is weakly dependent on temperature [Fig. 3(c)], while N_{H2} is increased above 10 K and becomes saturated at high temperatures [Fig. 3(d)]. The dependence of μ_1 on temperature is nonmonotonic. This is expected given the fact of a large hole concentration in those samples. The ion implantation results in an effective Ge:Mn layer thickness of around 100 nm. Then the concentration of type 1 carriers is in the range between 10^{17} and 10^{18} cm^{-3}. In this range a peak of hole mobility in Ge depending on temperature was observed.[31] The concentration of type 2 carriers is mostly below 10^{17} cm^{-3} and μ_2 increases monotonically with decreasing temperature.

Equation (1) neglects the influence of a possible paramagnetism inside the samples. The paramagnetism can be included as an anomalous Hall term using a Brillouin function.[24] However, we have not observed any paramagnetic component using superconducting quantum interference device magnetometry down to 5 K with fields up to 7 T for sample Ge19 and Ge01. The quench of the magnetic moments from Mn ions is somehow surprising, and has also been observed in Mn doped Si.[32] Nevertheless, we also refined Eq. (1) by including a Brillouin function in order to

account for possible magnetic field dependent mobilities. However, using the Brillouin function the fitting of the Hall curve at large fields is not possible because the fitted Hall curve changes the sign of slope with increasing field. This is in contrast to the Hall data probed on Mn implanted Ge where the sign of slope remains positive at large fields.[9] The simple two-band-like picture described by Eq. (1) also qualitatively explains the saturation of the positive MR at large fields. Namely, above 10 K a large positive MR is usually observed in Ge:Mn (also in our samples) and saturates at large fields,[7,9,13,28] which is a typical feature of the two-band MR.[23]

In summary, we observed an anomalous Hall resistance in Mn implanted Ge with the Mn concentration as low as 0.004%. By considering two types of carriers participating in the conduction, we can explain the puzzling Hall-resistance curves reported in the literature and in this letter. A multiple-path-like conduction can mislead the interpretation of materials as FMS. Possibly, it also can make an add-on effect to the AHE observed in InMnAs (Ref. 15) and InMnSb,[16] as well as in $Zn_{0.9}Mn_{0.075}Cu_{0.025}O$.[33]

The authors (S.Z. and D.B.) thank financial support from the Bundesministerium für Bildung und Forschung (Grant No. FKZ13N10144). We thank Carsten Timm from TU Dresden for fruitful discussion.

[1]T. Hayashi, M. Tanaka, T. Nishinaga, and H. Shimada, J. Appl. Phys. **81**, 4865 (1997).
[2]H. Ohno, H. Munekata, T. Penney, S. von Molnár, and L. L. Chang, Phys. Rev. Lett. **68**, 2664 (1992).
[3]D. Ferrand, J. Cibert, A. Wasiela, C. Bourgognon, S. Tatarenko, G. Fishman, T. Andrearczyk, J. Jaroszyński, S. Koleśnik, T. Dietl, B. Barbara, and D. Dufeu, Phys. Rev. B **63**, 085201 (2001).
[4]H. Ohno, A. Shen, F. Matsukura, A. Oiwa, A. Endo, S. Katsumoto, and Y. Iye, Appl. Phys. Lett. **69**, 363 (1996).
[5]T. Dietl, H. Ohno, F. Matsukura, J. Cibert, and D. Ferrand, Science **287**, 1019 (2000).
[6]Y. D. Park, A. T. Hanbicki, S. C. Erwin, C. S. Hellberg, J. M. Sullivan, J. E. Mattson, T. F. Ambrose, A. Wilson, G. Spanos, and B. T. Jonker, Science **295**, 651 (2002).
[7]F. Tsui, L. He, L. Ma, A. Tkachuk, Y. S. Chu, K. Nakajima, and T. Chikyow, Phys. Rev. Lett. **91**, 177203 (2003).
[8]M. Jamet, A. Barski, T. Devillers, V. Poydenot, R. Dujardin, P. Bayle-Guillemaud, J. Rothman, E. Bellet-Amalric, A. Marty, J. Cibert, R. Mattana, and S. Tatarenko, Nature Mater. **5**, 653 (2006).
[9]O. Riss, A. Gerber, I. Y. Korenblit, A. Suslov, M. Passacantando, and L. Ottaviano, Phys. Rev. B **79**, 241202(R) (2009).
[10]C. Zeng, Z. Zhang, K. van Benthem, M. F. Chisholm, and H. H. Weitering, Phys. Rev. Lett. **100**, 066101 (2008).
[11]R. R. Gareev, Y. V. Bugoslavsky, R. Schreiber, A. Paul, M. Sperl, and M. Döppe, Appl. Phys. Lett. **88**, 222508 (2006).
[12]J. X. Deng, Y. F. Tian, S. M. He, H. L. Bai, T. S. Xu, S. S. Yan, Y. Y. Dai, Y. X. Chen, G. L. Liu, and L. M. Mei, Appl. Phys. Lett. **95**, 062513 (2009).
[13]A. P. Li, J. F. Wendelken, J. Shen, L. C. Feldman, J. R. Thompson, and H. H. Weitering, Phys. Rev. B **72**, 195205 (2005).
[14]Y. Yamamoto, S. Itaya, K. Suga, T. Takenobu, Y. Iwasa, M. Hagiwara, K. Kindo, and H. Hori, J. Phys.: Conf. Ser. **51**, 115 (2006).
[15]A. Oiwa, A. Endo, S. Katsumoto, Y. Iye, H. Ohno, and H. Munekata, Phys. Rev. B **59**, 5826 (1999).
[16]G. Mihály, M. Csontos, S. Bordács, I. Kézsmárki, T. Wojtowicz, X. Liu, B. Jankó, and J. K. Furdyna, Phys. Rev. Lett. **100**, 107201 (2008).
[17]S. Zhou, A. Shalimov, K. Potzger, M. Helm, J. Fassbender, and H. Schmidt (unpublished).
[18]K. Potzger, S. Q. Zhou, H. Reuther, A. Mücklich, F. Eichhorn, N. Schell, W. Skorupa, M. Helm, J. Fassbender, T. Herrmannsdorfer, and T. P. Papageorgiou, Appl. Phys. Lett. **88**, 052508 (2006).
[19]S. Zhou, K. Potzger, G. Zhang, A. Mücklich, F. Eichhorn, N. Schell, R. Grötzchel, B. Schmidt, W. Skorupa, M. Helm, J. Fassbender, and D. Geiger, Phys. Rev. B **75**, 085203 (2007).
[20]S. Picozzi, L. Ottaviano, M. Passacantando, G. Profeta, A. Continenza, F. Priolo, M. Kim, and A. J. Freeman, Appl. Phys. Lett. **86**, 062501 (2005).
[21]P. Gambardella, L. Claude, S. Rusponi, K. J. Franke, H. Brune, J. Raabe, F. Nolting, P. Bencok, A. T. Hanbicki, B. T. Jonker, C. Grazioli, M. Veronese, and C. Carbone, Phys. Rev. B **75**, 125211 (2007).
[22]E. Biegger, L. Stäheli, M. Fonin, U. Rüdiger, and Y. S. Dedkov, J. Appl. Phys. **101**, 103912 (2007).
[23]S. M. Watts, S. Wirth, S. von Molnár, A. Barry, and J. M. D. Coey, Phys. Rev. B **61**, 9621 (2000).
[24]D. W. Jung, J. P. Noh, A. Z. M. T. Islam, and N. Otsuka, J. Appl. Phys. **103**, 043703 (2008).
[25]D. C. Look, D. C. Walters, M. O. Manasreh, J. R. Sizelove, C. E. Stutz, and K. R. Evans, Phys. Rev. B **42**, 3578 (1990).
[26]H. H. Woodbury and W. W. Tyler, Phys. Rev. **100**, 659 (1955).
[27]H. Fritzsche, Phys. Rev. **99**, 406 (1955).
[28]Y. D. Park, A. Wilson, A. T. Hanbicki, J. E. Mattson, T. Ambrose, G. Spanos, and B. T. Jonker, Appl. Phys. Lett. **78**, 2739 (2001).
[29]N. Pinto, L. Morresi, M. Ficcadenti, R. Murri, F. D'Orazio, F. Lucari, L. Boarino, and G. Amato, Phys. Rev. B **72**, 165203 (2005).
[30]S. Zhou, D. Bürger, C. Baumgart, W. Skorupa, C. Timm, P. Oesterlin, M. Helm, and H. Schmidt (unpublished).
[31]A. Golikova, B. Y. Moizhez, and L. S. Stilbans, Sov. Phys. Solid State **3**, 2259 (1962).
[32]L. Zeng, E. Helgren, M. Rahimi, F. Hellman, R. Islam, B. J. Wilkens, R. J. Culbertson, and D. J. Smith, Phys. Rev. B **77**, 073306 (2008).
[33]Q. Xu, L. Hartmann, H. Schmidt, H. Hochmuth, M. Lorenz, A. Setzer, P. Esquinazi, C. Meinecke, and M. Grundmann, Thin Solid Films **516**, 1160 (2008).

APPLIED PHYSICS LETTERS **95**, 232506 (2009)

In situ observation of secondary phase formation in Fe implanted GaN annealed in low pressure N_2 atmosphere

G. Talut,[1,a)] J. Grenzer,[1] H. Reuther,[1] A. Shalimov,[1] C. Baehtz,[1] D. Novikov,[2] and B. Walz[2]
[1]*Institute of Ion Beam Physics and Materials Research, Forschungszentrum Dresden-Rossendorf e.V., P.O. Box 510119, 01314 Dresden, Germany*
[2]*Deutsches Elektronen-Synchrotron DESY, Notkestraße 85, 22607 Hamburg, Germany*

(Received 26 October 2009; accepted 16 November 2009; published online 8 December 2009)

The formation of secondary phases in Fe implanted GaN upon annealing in low pressure N_2-atmosphere was detected by means of *in situ* x-ray diffraction and confirmed by magnetization measurements. A repeatable phase change from Fe_3N at room temperature and $Fe_{3-x}N$ at 1023 K was observed *in situ*. The phase transformation is explained by the change of lattice site and concentration of nitrogen within nitrides. The diffusion of Fe toward sample surface and oxidation with increasing annealing cycles limits the availability of secondary phase and hence the repeatability. At high temperature GaN dissolves and Ga as well as Fe oxidize due to presence of residual oxygen in the process gas. The ferromagnetism in the samples is related to nanometer sized interacting $Fe_{3-x}N$ crystallites. © *2009 American Institute of Physics*. [doi:10.1063/1.3271828]

GaN is a wide band gap semiconductor that has been studied intensively in the last years because of its potential field of applications like in optoelectronics, plasmonics, as well as for high power electronics. By doping with transitional metals like Fe it might also be a diluted magnetic semiconductor (DMS) with a Curie temperature above room temperature (RT) and could then be used for spintronics.[1] There are many experimental studies reporting ferromagnetism at RT in Fe doped GaN. In a real DMS, with magnetic atoms randomly substituting cation sites, ferromagnetic coupling is supposed to be due to the indirect exchange coupling between magnetic impurities mediated by holes.[1–4] Experimental observation of strong-coupling effects in a DMS $Ga_{1-x}Fe_xN$ was reported by Pacuski *et al.*[5] Robust ferromagnetism in the region of insulator-to-metal transition was predicted for high hole densities. However, there are also other possible sources of ferromagnetism like spinodal decomposition of Fe or ferromagnetic secondary phases. The detection of those is rather difficult. Bonanni *et al.*[6] prepared GaN:Fe layers by metalorganic chemical vapor deposition (MOCVD) and observed ferromagnetism that was partially accounted to the spinodal decomposition and non-uniform distribution of Fe-rich magnetic nanocrystals. Kuwabara *et al.*[7] reported the formation of nanoclusters and superparamagnetic behavior in GaN:Fe epilayers prepared by rf-plasma-assisted molecular beam epitaxy. In case of ion implantation the reports from different groups are quite controversial. Theodoropoulou *et al.*[8] and Shon *et al.*[9,10] did not relate ferromagnetic response to secondary phases after transition ion implantation into semiconductors. In our experiments, however, the formation of α-Fe nanoclusters, that were responsible for ferromagnetic response, was observed.[11] Though the appearance of such precipitates is not desired in a DMS they might be useful for certain applications.[12] Li *et al.*[13] detected co-occurrence of α-Fe and ε-Fe_3N in MOCVD prepared GaN:Fe films and pointed out the role of nitrogen pressure and structural disorder in the formation of Fe-rich phases. Bonanni *et al.*[14] have shown that the controlled aggregation of magnetic ions in a semiconductor can be affected by the growth rate and doping with shallow impurities.

Recently we reported predominant formation of epitaxially oriented α-Fe nanoclusters if Fe-doped samples were annealed in a N_2 flow at 1.1 bar pressure.[11] In this paper we report the formation of ε-$Fe_{3-x}N$ with $x<1$ that builds up during annealing at 1073 K in 0.5 bar N_2 and the reversible transformation to ε-Fe_3N during cooling down to RT.

P-type (Mg) doped ($\sim 2\times 10^{17}$ cm^{-3}) single crystalline wurtzite GaN(001) films of about 3 μm thickness epitaxially grown by metal organic vapor phase epitaxy on sapphire (001) were used. Samples, 7° tilted relative to the ion beam to avoid channeling, were implanted with 195 keV ^{57}Fe ions with fluence $\Phi=4\times 10^{16}$ cm^{-2} (peak Fe concentration of 4 at. % at the projected range $R_p=85$ nm according to TRIM[15]), keeping the samples at RT. In order to reduce the implantation damage and to investigate the formation of secondary phases the implanted samples were annealed at 1073 K in a low pressure N_2-atmosphere(0.5 bar) within several minutes. The annealing experiments along with the *in situ* x-ray diffraction characterization were performed at the Rossendorf beamline at the ESRF in Grenoble with a x-ray wavelength of $\lambda=0.124$ nm. The annealing chamber was equipped with a boron nitride heater, controlled by a Eurotherm controller, gas inlet and a half sphere beryllium dome. The temperature was measured by a PtRh/Pt thermocouple placed on top of the heater. The gas pressure in the chamber was limited to 0.5 bar with a flow of about 40 $l\cdot min^{-1}$. The purity of the N_2 gas (99.9999%) was limited by the setup with an oxygen contamination in the ppm range.

A Pilatus 100 K two-dimensional (2D) pixel detector was used to record 2D diffraction pattern. Additionally, a scintillation counter was used for 2θ-ω-scans. Generally, for clusters in the range of some nm the signal to background ratio is very low. In order to increase the signal to background ratio to an acceptable level the acquisition time of the 2D detector was set to 10 s and those of the scintillation counter to 5 s per point. The investigations of the magnetic properties were performed with a Quantum Design MPMS

[a)]Electronic mail: g.talut@fz-rossendorf.de.

 © 2009 American Institute of Physics

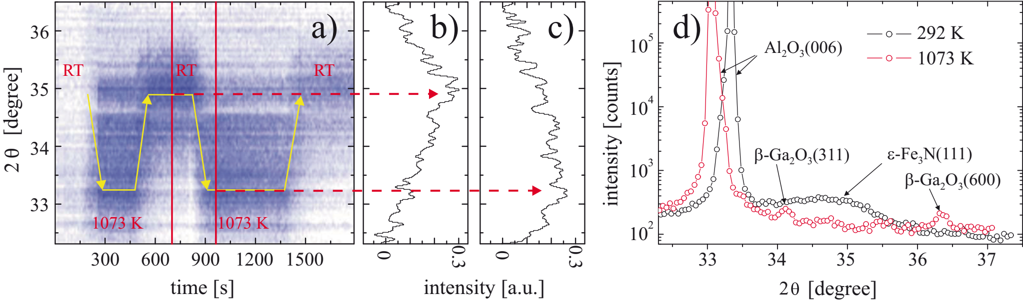

FIG. 1. (Color online) (a) Time dependent 2θ-scans between 32.3° and 36.5° at $\omega = 17.7°$. The presentation is based on the line profiles from the 2D detector with an 10 s acquisition time each. Intensity is color/grayscale coded with dark color representing higher intensity. On the right two profiles are presented for the (b) RT and (c) 1073 K scans. (d) 2θ-ω coupled scans at RT and 1073 K recorded after third cycle with a scintillation counter.

superconducting quantum interference device magnetometer. For the evaluation of the 2D detector exposures rectangular areas with dimensions 2θ from 32.3° to 36.5° and $\chi = \pm 0.2°$ (angle ⊥ to the scattering plane) were integrated over χ and assumed as line scans. Those line scans are represented over annealing/cooling time with the color/grayscale coded intensity in Fig. 1(a). Single examples of line scans are given in Figs. 1(b) and 1(c) for RT and 1073 K, respectively. Prior to the annealing procedure (time t=0 at RT) no reflexes from secondary phases were detected [see Fig. 1(a)]. After about 200 s annealing, at 1073 K, a broad reflex starts to evolve in the region between 32.5° and 35° with a local maximum at about 33.3°. The peak shift due to the lattice expansion from RT to 1073 K is in the order of 0.1° and can be neglected. The position of the maximum fits well to the pattern of FeN(200) (33.46° at RT). However, because of the broadness of the reflex, other nitrides like disordered ε-$Fe_{3-x}N(002)$ or ζ-$Fe_2N(102)$ can also be taken into account. Disordered in this sense means the redistribution of mainly N atoms within the structure and can be described by the transfer of N from Fig. 2(b) and 2(c) Wyckoff site position in the ε-$Fe_{3-x}N$-phase.[16] From symmetry reasons the formation of ε-$Fe_{3-x}N$ is more probable since it features the same type of structure (wurtzite) as GaN. The strain caused by the lattice mismatch is supposed to relax by generating misfit dislocations, as was shown in Ref. 13.

During cooling down (t=500 s) from 1073 K to RT the reflex shifts consistently toward higher angular values as represented by arrows. At RT the maximum of the peak ends up at about 34.9° and can be assigned to ε-$Fe_3N(111)$. This is shown in a selected plot at RT in Fig. 1(b). The presence of ε-Fe_3N correspond with the results in Refs. 13 and 14 However the change of symmetry cannot be explained up to now. The mean size of clusters, calculated with Scherrer formula using the full width at half maximum, is about 5 nm. However, the values calculated by means of Scherrer formula should be treated carefully. Because of the weak scattering intensity of the only secondary phase reflex no statement about the microstrain or mosaicity can be made.

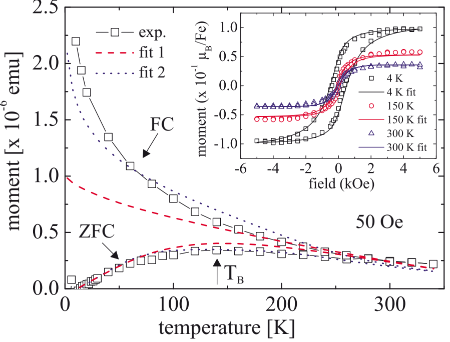

FIG. 2. (Color online) ZFC/FC measurement performed at 50 Oe on the sample implanted with 3×10^{16} cm^{-2} and annealed at 1073 K for one cycle along with the fitting results using Preisach model. The inset shows magnetization curves recorded at 4, 150, and 300 K.

The following annealing sequence, starting now from the already formed ε-$Fe_3N(111)$ phase lead to a peak shift from 34.9° at RT to 33.3° at 1073 K; cooling down to RT reverses the phase transformation again. Hence, the process of phase transformation from a partially disordered ε-$Fe_{3-x}N$ to an ordered ε-Fe_3N is reproducible.

The process of secondary phase formation is suggested as follows. After the ion implantation a highly defective GaN with broken Ga–N bonds is present. During annealing in low pressure N_2 atmosphere atomic nitrogen can escape from the surface region leading to a further dissolution of GaN. Considering the energies of formation if atomic nitrogen is available the formation of iron nitrides rather than of GaN is preferable. Once ε-$Fe_{3-x}N$ is formed the transformation between the ε-$Fe_{3-x}N$ and ε-Fe_3N phases occur over the N exchange and lattice site change. In contrast to that, the annealing in a high pressure N_2 atmosphere (at 1.1 bar) prevents the out-diffusion of nitrogen out of the damaged region, thus reducing the dissolution of GaN. In this case bcc-Fe is formed predominantly.

At this point it should be mentioned, that the reversibility is limited by the out-diffusion of Fe and gradual oxidation of Fe and Ga. During annealing the reflex intensities of the secondary phases decreases and after some repetitions reflexions from nitrides disappeared completely. This can be seen in Fig. 1(d), that shows two coupled 2θ-ω line scans recorded with the scintillation counter at RT after first annealing cycle and at 1073 K during the third annealing cycle. The shift of Al_2O_3 is due to its thermal expansion and is consistent with Ref. 17 this confirms proper temperature control. The additional small reflexes in the 1073 K spectrum are related to the β-Ga_2O_3 reflexes. The full set of β-Ga_2O_3 reflexes was found in this sample (not shown), referring to the polycrystallinity of the oxide layer.[18]

Magnetic measurements were performed on the samples in virgin and as implanted state, then after annealing at 1073 K for one cycle and after three cycles annealing accordingly. Virgin as well as implanted samples show no ferromagnetic response. The sample annealed for one cycle show a characteristic behavior of superparamagnetic nanoparticles. Figure 2 shows a zero-field-cooled/field-cooled (ZFC/FC)

measurement along with the magnetization curves (inset) of this sample recorded at 4, 150, and 300 K. The broad maximum in the ZFC part of the curve gives a hint of a large size distribution of the nanoparticles with the mean blocking temperature T_B of about 130 K. Using a formalism for the relaxation time τ of the particle magnetization with the anisotropy energy density E_A (2×10^4 J/m^3),[19] the attempt frequency f_0 (typically 10^9–10^{11} Hz), measurement time 100 s, Boltzmann constant k_B the volume V of the mean sized cluster can be calculated. From that a diameter of about 16 nm is estimated, assuming a spherical shape of clusters

$$\tau^{-1} = f_0 \cdot \exp\left(-\frac{E_A V}{k_B T_B}\right). \quad (1)$$

However, the blocking temperature may be influenced by magnetic interactions between the particles.[6] This can lead to an overestimation of cluster size. A Preisach model was applied to fit the ZFC/FC as well as the magnetization loops.[20,21] The model assumes the decomposition of magnetic system into an ensemble of bistable units characterized by a temperature dependent spontaneous moment μ, two possible magnetic states $\pm\mu$, and two characteristic values of coercive h_c and asymmetry h_i fields. Best fitting results were obtained by using Lorentz type functions for the coercive and asymmetry field distributions. The average spontaneous moment of the clusters at 0 K μ_0, mean coercive field h_{c0}, power law temperature dependence parameter σ_c and σ_i as well as the critical temperature T_c were best fitted using $\mu_0=7.7\times10^{-16}$ emu ($\cong 8.3\times10^4$ μ_B), $h_{c0}=150$ Oe, $\sigma_c=800$ Oe, $\sigma_i=900$ Oe, and $T_c=480$ K, respectively (fit 1). With 1.9 μ_B/Fe for the magnetic moment of Fe in ε-Fe_3N (Ref. 22) and 3 Fe atoms in a unit cell the number of unit cells and out of it the cluster volume can be calculated. Again, assuming the spherical shape of the cluster its diameter can be calculated to about 9 nm. This model describes the ZFC curve as well as the hysteresis loops very precise. An indication of superparamagnetic behavior of clusters is the breakdown of the coercive field with increasing temperatures (see inset in Fig. 2). It has to be noted that the moment per Fe atom in μ_B is by a factor 20 lower than of pure ε-Fe_3N.[16] This means that not all Fe are incorporated in the formation of ε-Fe_3N. Unfortunately, the mean size cluster approach is not able to describe the enhanced magnetization in the FC curve at low temperatures, related to the response from those magnetic clusters which are larger than 9 nm. Using two mean moments $\mu_0=7\times10^{-16}$ and 14×10^{-16} emu ($\cong$ mean sizes 9 and 11 nm) and different cluster concentrations the fit approaches the experimental curve (fit 2). This bimodal size distribution hint that clusters are in a coalescent regime, since the volume of a 11 nm sized cluster is close to the volume of two merged 9 nm sized clusters.

After annealing for three cycles at 1073 K no ferromagnetic response was detected. Because of the oxidation of Ga as well as of Fe the layer can be regarded as Ga_2O_3 with inclusions of some iron oxide. This result is in contrast to the results from Lee *et al.*,[23] where Fe doped β-Ga_2O_3 was found to be ferromagnetic.

In summary, reversible phase transition of Fe implanted GaN was observed upon annealing in 0.5 bar N_2 at 1073 K by means of *in situ* x-ray diffraction and discussed in terms of N exchange. After annealing ε-Fe_3N was found to be formed predominantly and is responsible for ferromagnetic response. It demonstrates that by variation of annealing conditions specific secondary phases can be created, leading to different electronic, magnetic and other properties. Preisach model yields an reasonable estimation of magnetic quantities and cluster size. The cluster size is in a good agreement with the calculation using Scherrer formula. No DMS related phenomena have been observed.

The annealing process is accompanied by a strong diffusion of N and dissolution of GaN, mediated by the formation of nitrides and oxides. Oxygen contamination further promotes the dissolution of GaN and the formation of β-Ga_2O_3. Hence, it acts as a further limiting aspect and need to be excluded in the following experiments. Fe doped β-Ga_2O_3 was found to be paramagnetic which is in contrast with the findings in Ref. 12.

G. Talut acknowledges the Deutsche Forschungsgemeinschaft (German Research Foundation) for the financial support under Contract No. Re 868/8-2.

[1] T. Dietl, H. Ohno, and F. Matsukura, Phys. Rev. B **63**, 195205 (2001).
[2] K. Sato and H. Katayama-Yoshida, Jpn. J. Appl. Phys., Part 2 **40**, L485 (2001).
[3] K. Sato and H. Katayama-Yoshida, Semicond. Sci. Technol. **17**, 367 (2002).
[4] T. Dietl, Phys. Rev. B **77**, 085208 (2008).
[5] W. Pacuski, P. Kossacki, D. Ferrand, A. Golnik, J. Cibert, M. Wegscheider, A. Navarro-Quezada, A. Bonanni, M. Kiecana, M. Sawicki, and T. Dietl, Phys. Rev. Lett. **100**, 037204 (2008).
[6] A. Bonanni, M. Kiecana, C. Simbrunner, T. Li, M. Sawicki, M. Wegscheider, M. Quast, H. Przybylińska, A. Navarro-Quezada, R. Jakieła, A. Wolos, W. Jantsch, and T. Dietl, Phys. Rev. B **75**, 125210 (2007).
[7] S. Kuwabara, T. Kondo, T. Chikyow, P. Ahmet, and H. Munekata, Jpn. J. Appl. Phys., Part 2 **40**, L724 (2001).
[8] N. Theodoropoulou, A. F. Hebard, S. N. G. Chu, M. E. Overberg, C. R. Abernaty, S. J. Pearton, R. G. Wilson, and J. M. Zavada, J. Appl. Phys. **91**, 7499 (2002).
[9] Y. Shon, Y. H. Kwon, Y. S. Park, Sh. U. Yuldashev, S. J. Lee, C. S. Park, K. J. Chung, S. J. Yoon, H. J. Kim, W. C. Lee, D. J. Fu, T. W. Kang, X. J. Fan, Y. J. Park, and H. T. Oh, J. Appl. Phys. **95**, 761 (2004).
[10] Y. Shon, S. Lee, H. C. Jeon, Y. S. Park, D. Y. Kim, T. W. Kang, J. S. Kim, E. K. Kim, D. J. Fu, X. J. Fan, Y. J. Park, J. M. Baik, and J. L. Lee, Appl. Phys. Lett. **89**, 082505 (2006).
[11] G. Talut, H. Reuther, S. Zhou, K. Potzger, F. Eichhorn, and F. Stromberg, J. Appl. Phys. **102**, 083909 (2007).
[12] S. Zhu, Y. Li, C. Fan, D. Zhang, W. Liu, Z. Sun, and S. Wei, Physica B **364**, 199 (2005).
[13] T. Li, C. Simbrunner, A. Navarro-Quezada, M. Wegscheider, M. Quast, D. Litvinov, D. Gerthsen, and A. Bonanni, J. Cryst. Growth **310**, 3294 (2008).
[14] A. Bonanni, A. Navarro-Quezada, M. Tian, L. Wegscheider, Z. Matěj, V. Holý, R. T. Lechner, G. Bauer, M. Rovezzi, F. D'Acapito, M. Kiecana, M. Sawicki, and T. Dietl, Phys. Rev. Lett. **101**, 135502 (2008).
[15] Part of the SRIM program package by J. F. Ziegler at http://www.srim.org/.
[16] A. Leineweber, H. Jacobs, F. Huning, H. Lueken, H. Schilder, and W. Kockelmann, J. Alloys Compd. **288**, 79 (1999).
[17] G. Fiquet, P. Richet, and G. Montagnac, Phys. Chem. Miner. **27**, 103 (1999).
[18] K. H. Jack, Proc. R. Soc. London, Ser. A **208**, 200 (1951).
[19] R. S. Ningthoujam and N. S. Gajbhiye, Mater. Res. Bull. **43**, 1079 (2008).
[20] T. Song, R. M. Roshko, and E. Dan Dahlberg, J. Phys.: Condens. Matter **13**, 3443 (2001).
[21] A. Shalimov, K. Potzger, D. Geiger, H. Lichte, G. Talut, A. Misiuk, H. Reuther, F. Stromberg, S. Zhou, C. Baehtz, and J. Fassbender, J. Appl. Phys. **105**, 064906 (2009).
[22] J. M. Gallego, S. Yu. Grachev, D. M. Borsa, D. O. Boerma, D. Écija, and R. Miranda, Phys. Rev. B **70**, 115417 (2004).
[23] S. W. Lee, Y. G. Ryu, G. Y. Ahn, S. -I. Park, and C. S. Kim, Phys. Status Solidi C **1**, 3550 (2004).

APPLIED PHYSICS LETTERS **95**, 252107 (2009)

Millisecond flash lamp annealing of shallow implanted layers in Ge

C. Wündisch,[1,a)] M. Posselt,[1] B. Schmidt,[1] V. Heera,[1] T. Schumann,[1] A. Mücklich,[1] R. Grötzschel,[1] W. Skorupa,[1] T. Clarysse,[2] E. Simoen,[2] and H. Hortenbach[3,b)]
[1]*Forschungszentrum Dresden-Rossendorf, Institute of Ion Beam Physics and Materials Research, P.O. Box 510119, D-01314 Dresden, Germany*
[2]*IMEC, Kapeldreef 75, B-3001 Leuven, Belgium*
[3]*Qimonda Dresden GmbH & Co OHG, Fraunhofer-Center Nanoelektronische Technologien (CNT), Königsbrücker Strasse 180, D-01099 Dresden, Germany*

(Received 3 November 2009; accepted 3 December 2009; published online 23 December 2009)

Shallow n^+ layers in Ge are formed by phosphorus implantation and subsequent millisecond flash lamp annealing. Present investigations are focused on the dependence of P redistribution, diffusion and electrical activation on heat input into the sample and flash duration. In contrast to conventional annealing procedures an activation up to 6.5×10^{19} cm^{-3} is achieved without any dopant redistribution and noticeable diffusion. Present results suggest that independently of pretreatment the maximum activation should be obtained at a flash energy that corresponds to the onset of P diffusion. The deactivation of P is explained qualitatively by mass action analysis which takes into account the formation of phosphorus-vacancy clusters. © *2009 American Institute of Physics*. [doi:10.1063/1.3276770]

Previous investigations on the formation of shallow junctions in Ge by ion beam processing have shown that p^+ doping using boron yields junctions that meet the requirements for the 22 nm technology node, whereas the formation of n^+ junctions by P or As is complicated by the high diffusivity and the low activation of these dopants.[1] The present work deals with millisecond flash lamp annealing (FLA) of shallow layers implanted by P. Dopant redistribution, diffusion, and activation are investigated. The dependence of these effects on flash energy and flash duration is discussed. Furthermore, the influence of pre-amorphization implantation (PAI) and preannealing as well as the solid phase epitaxial recrystallization (SPER) of amorphous layers are studied.

(100) Ge wafers (p-type) with a resistivity between 0.2 and 0.5 Ω cm were used. In order to prevent surface degradation by implantation and outdiffusion during annealing the wafers were capped with 10 nm SiO_2 by sputter deposition. Selected samples were preamorphized by Ge implantation at an energy of 200 keV and a fluence of 10^{15} cm^{-2}. All samples were implanted by P at 30 keV and 3×10^{15} cm^{-2}. The ion beam was tilted by 7° with respect to the normal of the sample surface. Some samples were first preannealed in N_2 ambient at 400 °C for 240 s. Flash-lamp annealing of all samples was carried out in Ar ambient using flash durations of 3 and 20 ms and different electrical energies required to produce the flash. The electrical energy is determined by the capacitors used in the flash lamp facility and the applied voltage. Details of the FLA equipment were elucidated elsewhere.[2] In a limited range the temperature of the sample is assumed to be proportional to the electrical energy of the flash E_{FLA} and, therefore, can be estimated by $T=cE_{FLA}+T_0$. The parameters c and T_0 are determined by complete SPER (Refs. 3 and 4) at about 600 °C and by melting of the sample surface at about 937 °C (3 ms flash: $c=5.81$ kJ^{-1} K, $T_0=373$ °C; 20 ms flash: $c=2.31$ kJ^{-1} K, $T_0=401$ °C). In the following the flash energy E_{FLA} is always used as a measure for the heat transfer to the sample.

Analysis by channeling Rutherford backscattering spectrometry (RBS/C) and cross-sectional transmission electron microscopy (XTEM) showed that the thickness of the amorphous layer formed by the PAI is about 178 nm, whereas the P implantation produces an amorphous layer of about 78 nm thickness. Furthermore, RBS/C and XTEM revealed that preannealing leads to complete SPER of the amorphous layers. If preannealing is not applied, samples recrystallize during FLA. The only exception is that treatment of preamorphized samples by 3 ms flashes leads to the formation of a polycrystalline layer by spontaneous nucleation and recrystallization.[4,5] In the recrystallized samples end-of-range defects cannot be found by XTEM. This is in contrast to silicon where such defects are always observed after SPER.

Depth profiles of P before and after annealing are shown in Fig. 1. The data were obtained by secondary ion mass spectrometry (SIMS). The difference between the as-implanted profiles in single-crystalline and preamorphized Ge is due to suppressed channelling in the latter case. Preannealing at 400 °C for 240 s leads to fast phosphorus redistribution by the snow plough effect [Figs. 1(a) and 1(b)]. A certain amount of P is incorporated into crystalline Ge, and the surplus is pushed ahead from the moving amorphous-crystalline interface. This leads to P loss of about 25% and the level of incorporation is about 3×10^{20} cm^{-3}. This value can be obtained from the plateau in the profiles shown in Figs. 1(a) and 1(b). The level of P incorporation found during SPER at 400 °C is higher than the maximum equilibrium solubility known from literature (2×10^{20} cm^{-3}, cf. Refs. 1, 6, and 7) and is therefore called metastable solubility.[8,9] On the other hand, SPER during FLA [Figs. 1(c) and 1(d)] does not show any significant snow plough effect. Obviously,

[a)]Author to whom correspondence should be addressed. Forschungszentrum Dresden-Rossendorf, Institute of Ion Beam Physics and Materials Research, P.O. Box 510119, D-01314 Dresden, Germany. Electronic mail: c.wuendisch@fzd.de.
[b)]Present address: SGS Institut Fresenius GmbH, Zur Wetterwarte 10, D-01109 Dresden, Germany.

 © 2009 American Institute of Physics

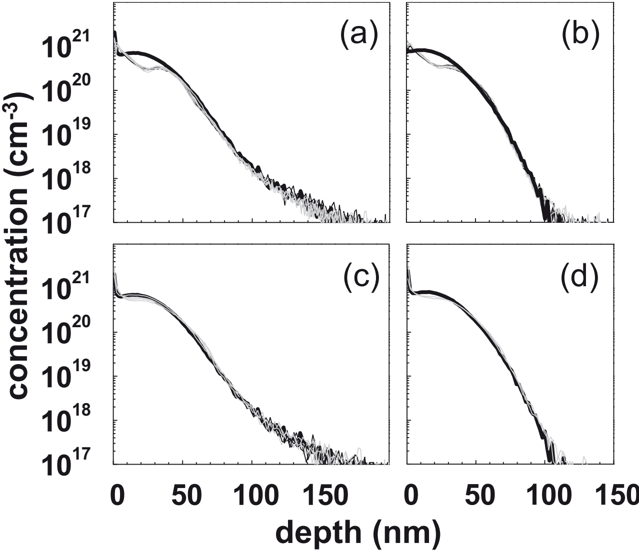

FIG. 1. Depth profiles of P in samples prepared without [(a) and (c)] and with [(b) and (d)] PAI as well as with [(a) and (b)] and without [(c) and (d)] preannealing. The as-implanted profiles are shown by thick black lines. Thin black and gray lines show P depth distributions after flash lamp annealing (FLA) for 3 and 20 ms, respectively. In the cases of 3 and 20 ms flashes the flash energy varied between 39 and 80 kJ as well as between 86 and 139 kJ, respectively.

nearly all phosphorus atoms are incorporated into crystalline Ge. This may be due to the fact that the temperature during SPER at millisecond FLA is higher than during preannealing, leading to a metastable solubility of at least 5–7 $\times 10^{20}$ cm^{-3}. The temperature dependence of the metastable solubility can be explained by the competition between the mobility of the impurity in the amorphous phase and the velocity of SPER (cf. Refs. 9 and 10, and references therein). The higher the temperature, the higher the speed of the amorphous-crystalline interface, the less likely the impurity can stay in front of it and, therefore, incorporation into the crystalline phase prevails.

Figures 1(a)–1(d) clearly demonstrate that no P diffusion occurs if the flash energy does not exceed 80 and 139 kJ for 3 and 20 ms flash duration, respectively. This is in striking contrast to conventional annealing with durations of seconds to hours. Significant concentration-dependent P diffusion is already observed in the case of annealing at 500 °C for 60 s.[8,11] However, some diffusion is also found at higher flash energies of 88 kJ (3 ms) and 183 kJ (20 ms) as shown in Fig. 2(a). In this case the temperature of the sample is so high that diffusion can even occur during some milliseconds. If the flash energy is further increased the near surface region of the sample melts and a huge diffusion of phosphorus is found [Fig. 2(b)].

The variable probe spacing technique[12] and micro-four-point-probe measurements[13] were applied to determine the sheet resistance of the samples.[14] Figures 3(a) and 3(c) depict the sheet resistance of the samples annealed by FLA for 3 and 20 ms, respectively. The flash energy E_{FLA} is given on the abscissa. In Fig. 3 data points obtained by the same preparation method are marked by the same symbols. These points are connected by straight lines if no P diffusion is observed [cf. Figs. 1(a)–1(d)] whereas the isolated points indicate diffusion in the solid phase [cf. Fig. 2(a)]. Since it is not useful to compare sheet resistance data for active layers with different depth distributions of charge carriers, the electrical properties are discussed in terms of the activation level of dopants. This quantity was roughly estimated using both the SIMS profile obtained after annealing and the corresponding value of sheet resistance.[15] The relation by Cuttriss[16] was used in order to transform resistivity to carrier concentration data. The resulting values for the activation are shown in Figs. 3(b) and 3(d). The figures demonstrate that below a certain threshold the activation level increases with increasing heat transfer to the sample, independently of the pretreatment. This effect is more pronounced for 3 ms flash duration. Below a certain flash energy preannealed samples show a lower activation than those without this treatment. If preannealing is used, samples that underwent PAI show a higher activation. In the case of 20 ms flash duration samples that did not undergo preannealing have a higher activation if they were preamorphized. The similar case for 3 ms duration was not investigated since a polycrystalline layer was formed.

The highest activation level of about 6.5×10^{19} cm^{-3} is achieved for the 3 ms flash and 97 kJ electrical energy. This corresponds to a case where slight P diffusion is observed

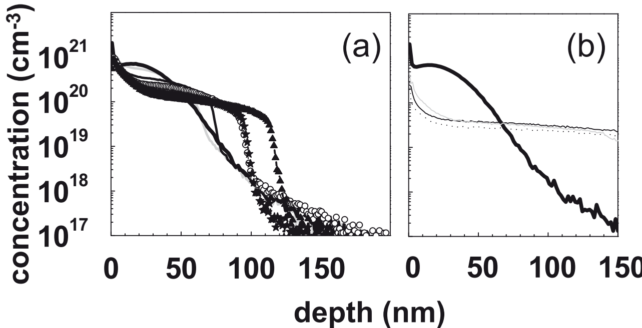

FIG. 2. P depth distributions obtained after different pretreatments and FLA at higher flash energies than in the case of Fig. 1. (a) Thin gray and black lines show the case of 3 ms FLA at 88 and 97 kJ, respectively, for samples without any pretreatment. The curves with lines and symbols were obtained for 20 ms FLA at 182 kJ (open circles – without any pretreatment, triangles-PAI, stars-PAI and preannealing). (b) Thin lines depict results obtained for 20 ms FLA at 232 kJ (black line – without any pretreatment, dotted line – PAI, gray line – PAI and preannealing).

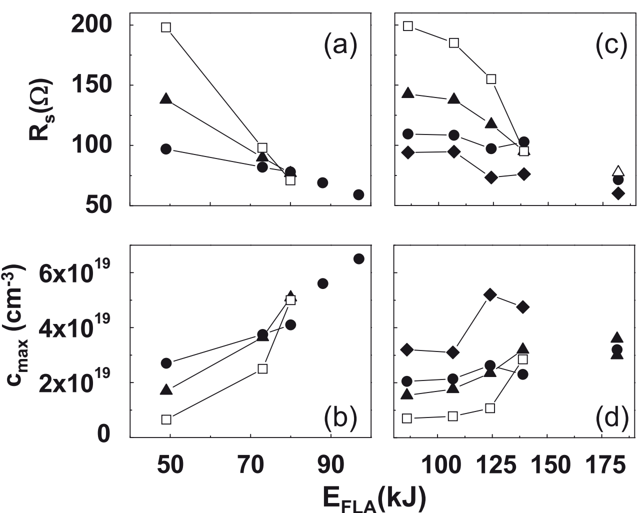

FIG. 3. Sheet resistance R_s and maximum carrier concentration c_{max} in the case of 3 ms [(a) and (b)] and 20 ms [(c) and (d)] FLA, for different flash energies and pretreatments. Circles: without any pretreatment, open squares: preannealing, diamonds: PAI, triangles: PAI and preannealing.

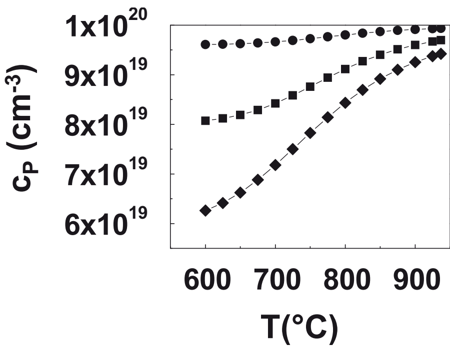

FIG. 4. Result of mass action analysis taking into account the formation of P_nV clusters ($n=1\ldots4$): concentration of unbound or active P vs temperature. Different values are assumed for the total vacancy concentration (circles: 10^{18} cm^{-3} squares: 5×10^{18} cm^{-3}, diamonds: 10^{19} cm^{-3}), and the total concentration of P is 10^{20} cm^{-3}.

[cf. Fig. 2(a)]. However, the comparison with results for the 20 ms flash shows that the activation level does not increase significantly or even decreases if P diffusion becomes stronger [cf. Figs. 3(d) and 2(a)]. Therefore, the optimum should be found at that electrical energy of the flash that corresponds to the onset of P diffusion. Taking into account the data depicted in Figs. 3(b) and 3(d) it may be concluded that this optimum should not strongly depend on the pretreatment. However, the highest activation level of P obtained in this work is far below the metastable and the equilibrium solubility. The fact that solubility returns to the equilibrium value during annealing after the completion of SPER or in subsequent annealing steps was also reported for dopants in Si. The reduction of solubility leads to less dopants on substitutional sites and to a concentration of activated dopants below or equal to equilibrium solubility. The decrease of solubility and activation may be accompanied by the formation of dopant-defect clusters.[9,17–19] However, in the considered samples such clusters were not found by XTEM. Therefore, it is assumed that deactivation is due to the formation of P-vacancy (PV) acceptor pairs[1] or other tiny clusters containing vacancies and dopant atoms[20] which are hardly detectable by standard XTEM. Indeed calculations using density functional theory and mass action analysis showed that the formation of P_nV clusters ($n=1,\ldots,4$) may be responsible for the deactivation of P.[21] Using the data from Ref. 21 a similar mass action analysis was performed. The temperature dependence of the concentration of unbound P is depicted in Fig. 4. In order to demonstrate qualitatively the effect of deactivation a total P concentration (10^{20} cm^{-3}) below equilibrium solid solubility is assumed and different values for the total concentration of vacancies were considered. These values are much higher than the equilibrium vacancy concentration due to defect formation by ion implantation. Figure 4 can be used to interpret the dependence of the P activation on flash energy and pretreatment: At low temperatures (or flash energies) and/or at high vacancy concentration many P_nV clusters are formed and, therefore, a relatively low level of unbound or electrically active P is found. At higher temperature and/or lower concentration of vacancies the concentration of active P increases. It should be emphasized that present mass action analysis considers equilibrium states as well as a homogeneous distribution of P and vacancies. Kinetics could prevent the ability of the system to reach such states so that the above interpretation should be used with some caution.

[1] E. Simoen, A. Satta, A. D'Amore, T. Janssens, T. Clarysse, K. Martens, B. De Jaeger, A. Benedetti, I. Hoflijk, B. Brijs, M. Meuris, and W. Vandervorst, Mater. Sci. Semicond. Process. **9**, 634 (2006).
[2] W. Skorupa, D. Panknin, W. Anwand, M. Voelskow, G. Ferro, Y. Monteil, A. Leycuras, J. Pezoldt, R. McMahon, M. Smith, J. Camassel, J. Stoemenos, E. Polychroniadis, P. Godignon, N. Mestres, D. Turover, S. Rushworth, and A. Friedberger, Mater. Sci. Forum **457**, 175 (2004).
[3] L. Csepregi, R. P. Küllen, J. W. Mayer, and T. W. Sigmon, Solid State Commun. **21**, 1019 (1977).
[4] B. C. Johnson, P. Gortmaker, and J. C. McCallum, Phys. Rev. B **77**, 214109 (2008).
[5] G. L. Olson and J. A. Roth, Mater. Sci. Rep. **3**, 1 (1988).
[6] V. I. Fistul, A. G. Yakovenko, A. A. Gvelesiani, V. N. Tsygankov, and R. L. Korchazhkina, Inorg. Mater. **11**, 457 (1975).
[7] F. A. Trumbore, Bell Syst. Tech. J. **39**, 205 (1960).
[8] A. Satta, E. Simoen, R. Duffy, T. Janssens, T. Clarysse, A. Benedetti, M. Meuris, and W. Vandervorst, Appl. Phys. Lett. **88**, 162118 (2006).
[9] R. Duffy, V. C. Venezia, K. van der Tak, M. J. P. Hopstaken, G. C. J. Maas, F. Roozeboom, Y. Tamminga, and T. Dao, J. Vac. Sci. Technol. B **23**, 2021 (2005).
[10] R. G. Elliman and Z. W. Fang, J. Appl. Phys. **73**, 3313 (1993).
[11] M. Posselt, B. Schmidt, W. Anwand, R. Grötzschel, V. Heera, A. Mücklich, C. Wündisch, W. Skorupa, H. Hortenbach, S. Gennaro, M. Bersani, D. Giubertoni, A. Möller, and H. Bracht, J. Vac. Sci. Technol. B **26**, 430 (2008).
[12] T. Clarysse, D. Vanhaeren, I. Hoflijk, and W. Vandervorst, Mater. Sci. Eng. R **47**, 123 (2004).
[13] T. Clarysse, W. Vandervorst, R. Lin, D. H. Petersen, and P. F. Nielsen, Nucl. Instrum. Methods Phys. Res. B **253**, 136 (2006).
[14] G. Hellings, C. Wündisch, G. Eneman, E. Simoen, T. Clarysse, M. Meuris, W. Vandervorst, M. Posselt, and K. De Meyer, Electrochem. Solid-State Lett. **12**, H417 (2009).
[15] W. Lerch, S. Paul, J. Niess, F. Cristiano, Y. Lamrani, P. Calvo, N. Cherkashin, D. F. Downey, and E. A. Arevalo, J. Electrochem. Soc. **152**, G787 (2005).
[16] D. B. Cuttris, Bell Syst. Tech. J. **40**, 509 (1961).
[17] Y. Takamura, S. H. Jain, P. B. Griffin, and J. D. Plummer, J. Appl. Phys. **92**, 230 (2002).
[18] Y. Takamura, P. B. Griffin, and J. D. Plummer, J. Appl. Phys. **92**, 235 (2002).
[19] Y. Takamura, A. Vailionis, A. F. Marshall, P. B. Griffin, and J. D. Plummer, J. Appl. Phys. **92**, 5503 (2002).
[20] W. Anwand, W. Skorupa, Th. Schumann, M. Posselt, B. Schmidt, R. Grötzschel, and G. Brauer, Appl. Surf. Sci. **255**, 81 (2008).
[21] A. Chroneos, H. Bracht, R. W. Grimes, and B. P. Uberuaga, Mater. Sci. Eng., B **154**, 72 (2008).

APPLIED PHYSICS LETTERS **94**, 011903 (2009)

The use of nanocavities for the fabrication of ultrathin buried oxide layers

Xin Ou,[1,a] Reinhard Kögler,[1] Arndt Mücklich,[1] Wolfgang Skorupa,[1] Wolfhard Möller,[1]
Xi Wang,[2] and Lasse Vines[3]
[1]*Forschungszentrum Rossendorf, PF 510119, D-01314 Dresden, Germany*
[2]*Shanghai Institute of Microsystem and Information Technology, Chinese Academy of Sciences, Shanghai 20050, People's Republic of China*
[3]*Department of Physics, University of Oslo, POB 1048 Blindern, 0316 Oslo, Norway*

(Received 6 November 2008; accepted 15 December 2008; published online 6 January 2009)

A continuous buried oxide layer with a thickness of only 58 nm is formed in silicon by oxygen implantation at 185 keV with a very low ion fluence of 1×10^{17} cm^{-2} and subsequent He implantation. Due to the implanted He efficient oxygen gettering occurs at the implantation induced damage and results in the accumulation of the implanted oxygen as well as of oxygen indiffused from the annealing atmosphere. The morphology and the resistivity of the resulting silicon-on-insulator structure are analyzed by cross section transmission electron microscopy and by cross section scanning spreading resistance microscopy. © *2009 American Institute of Physics*.
[DOI: 10.1063/1.3065478]

Point defects in silicon induced by ion implantation have been widely investigated with regard to doping in silicon device processing.[1,2] The forward momentum transfer from the implanted ions to the silicon atoms in the collision cascades results in the presence of two distinct layers of vacancy excess close to the surface and interstitial excess at larger depth.[3–6] These implantation induced excess defects may act as gettering centers for, e.g., impurities.[7,8] Excess vacancy defects induced by oxygen implantation also serve as trapping centers for the implanted atoms by acting as nucleation sites for SiO_2 precipitation. The empty volume generated in the vacancy excess region assists the growth of the precipitates by balancing their volume expansion (by about 120%).[9,10] This mechanism is employed in this study for ion beam synthesis of a buried oxide (BOX) layer in Si, which is commonly known as the separation-by-implanted-oxygen (SIMOX) process. In SIMOX, silicon-on-insulator (SOI) substrates are fabricated by high-fluence oxygen implantation at elevated temperature and subsequent high temperature annealing.[11] Most of the oxide precipitates formed during SIMOX processing are distributed around the mean projected ion range (R_p) where the oxygen concentration reaches its maximum. However, many large SiO_2 precipitates are also formed at a shallower depth position around the damage maximum (D_p) of about $0.8R_p$, where the change is from the vacancy rich region to the interstitial rich one.[12–14] This is a problem especially for the low-fluence SIMOX processing (at fluences well below the stoichiometric limit) as a discontinuous oxide layer forms consisting of isolated precipitates. In order to create a homogeneous continuous BOX layer, the accumulation of the implanted oxygen in only one narrow layer is essential.[9] This shrinking of the BOX layer thickness in the SOI structure is required in order to enable downscaling of the SOI complementary metal-oxide-semiconductor architecture at suppressed short channel effect[15] and in order to improve the thermal conductivity.[16]

Also implanted He is known to be trapped mainly by vacancy defects to form a He-filled bubble layer at the position of the vacancy dominated layer.[17–20] Such a layer of He bubbles or of empty cavities (after He outdiffusing during high temperature annealing[17]) is efficient for gettering of implanted oxygen into a narrow layer[21] and also for gettering of oxygen indiffused from the annealing atmosphere.[22] In our study, a subsequent helium implantation is employed after the oxygen implantation to stabilize the excess vacancy defects formed during oxygen implantation by He-induced bubbles and to better define the depth of oxide seeding.

Czochralski-Si (100) wafers were implanted at 550 °C with 185 keV O^+ ions to a fluence of 1×10^{17} cm^{-2}. For this fluence, the maximum concentration of the as-implanted oxygen profile is only 10% of the oxygen concentration in stoichiometric SiO_2 (4.4×10^{22} cm^{-3}). Subsequently 45 keV He^+ ions were implanted at room temperature to fluences of 4×10^{16}, 8×10^{16}, and 2×10^{17} cm^{-2}. High temperature annealing was preformed at 1300 or 1350 °C for 3 h in an atmosphere containing Ar and O_2 at the ratio $Ar/O_2 = 100/3$ or 100/30. In addition, a reference sample was fabricated by only oxygen implantation and subsequent annealing. The oxygen depth distribution was analyzed by means of secondary ion mass spectrometry (SIMS) using a Cameca IMS 7f instrument. The morphology and the resistance of the SOI structure were investigated by cross section transmission electron microscopy (XTEM) and cross section scanning spreading resistance microscopy (SSRM), respectively. For the cross section SSRM, the sample was cut manually and measured using a multimode atomic force microscopy (from Veeco instruments) equipped with a conductive Si tip coated with diamond.

Figure 1(a) presents the oxygen profiles obtained after the above processing. After annealing at 1300 °C, the oxygen profile of the reference sample shows only one peak located at the depth of 460 nm, which is close to R_p at 440 nm as calculated by the TRIM code.[23] For a low- and medium-fluence postimplantation of He, there are additional front peaks close to the depth of the calculated D_p position. The broadened R_p peak at lower He fluence may result from oxygen gettering at a certain amount of He, which is trapped by interstitial defects induced by the oxygen implantation,[20] which therefore cause the oxygen gettering there. As the He

[a]Electronic mail: x.ou@fzd.de.

 © 2009 American Institute of Physics

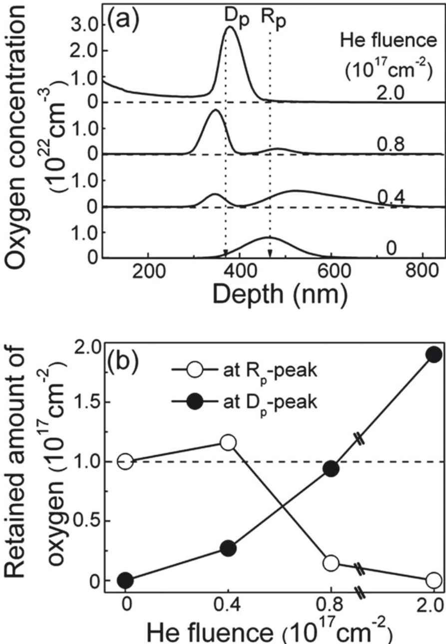

FIG. 1. (a) SIMS profiles of the oxygen distributions after postimplantation with He at different fluences and annealing at 1300 °C in 3% O_2 atmosphere for 3 h. The calculated positions of R_p and D_p are indicated. (b) Retained amount of the oxygen accumulated in the R_p peak and the D_p peak of the oxygen profiles vs He postimplantation fluence. The fluence of implanted oxygen is indicated by the dashed line.

fluence increases, more excess vacancies are generated in the vacancy rich region around D_p by the He implantation, in addition to those generated by the oxygen implantation. At the highest He fluence, all the oxygen is accumulated in the front peak at a depth of 370 nm. Figure 1(b) shows the retained amount of oxygen calculated by integrating the corresponding peaks of the profiles. The oxygen accumulation at the R_p region vanishes toward high He fluence, whereas the amount found around D_p even increases significantly above the implanted fluence. This indicates additional incorporation of oxygen by indiffusion from the annealing atmosphere. The corresponding XTEM image for the highest He fluence [Fig. 2(a)] shows a discontinuous BOX layer with a thickness of

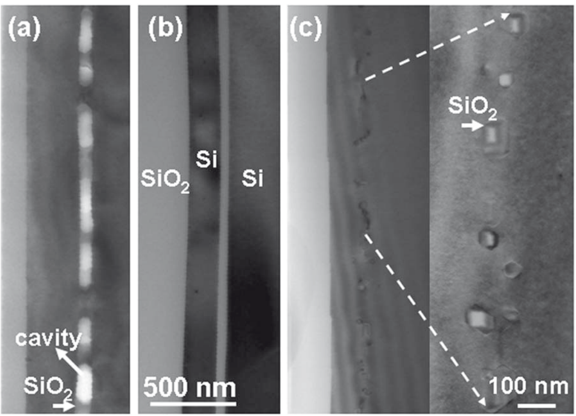

FIG. 2. Comparison of XTEM micrographs showing SOI structures formed by implantation of 185 keV ions to 1×10^{17} O cm^{-2}. (a) After 45 keV He postimplantation at 2×10^{17} cm^{-2} and annealing at 1300 °C in an atmosphere containing 3% O_2. The bright spots indicate cavities in the BOX layer. (b) Same, but after annealing at 1350 °C under 30% O_2, resulting in a continuous narrow BOX layer. (c) Reference sample annealed at 1350 °C in 30% O_2 showing widely distributed SiO_2 precipitates.

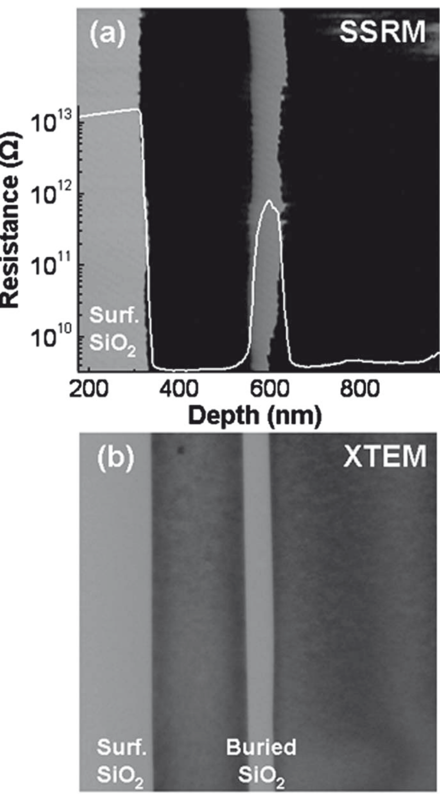

FIG. 3. (a) Cross section SSRM image of silicon implanted with 185 keV ions to 1×10^{17} O cm^{-2} plus 45 keV He ions to 2×10^{17} cm^{-2} and annealed at 1350 °C in 30% O_2. The dark and light colors indicate low and high resistance, respectively. A laterally averaged resistance scan curve is inserted. The scanning size is 0.8×0.8 μm^2. (b) Corresponding XTEM image with the same imaging area.

80 nm containing extended cavities (bright spots), which are similar to those recently reported by Ogura.[22] A continuous BOX layer [Fig. 2(b)] with a thickness of only 58 nm was achieved by enhanced oxygen indiffusion during annealing at increased temperature (1350 °C) and oxygen concentration (30%). Here, the total amount of retained oxygen of 2.6×10^{17} cm^{-2}, which is derived from the thickness of the BOX layer, exceeds the initially implanted fluence of 1×10^{17} cm^{-2} even more. Only few and disperse cavities remain in the BOX layer, and few dislocations in the top Si layer are observed by XTEM. The thickness of the BOX layer is not perfectly uniform, being slight larger at the positions of the remaining cavities. In comparison, a layer of isolated SiO_2 precipitates distributed over a thickness of about 110 nm is formed in the reference sample [see Fig. 2(c)]. The cross sectional SSRM analysis in Fig. 3 reveals the thermally formed surface oxide and confirms that the continuous BOX layer formed at the highest He postimplantation fluence [see Fig. 2(b)] is fully insulating. Any SiO_2 precipitates that would be larger than the tip diameter[24] cannot be seen in the top Si layer. The position in depth (at 400 nm) and the thickness (about 58 nm) of the BOX layer measured by SSRM are in agreement with the XTEM result shown in Fig. 2(b). Figure 3(a) demonstrates that the upper Si/SiO_2 interface of the BOX layer is as smooth as the SiO_2/Si interface obtained by thermal surface oxidation. The inserted curve shows the resistance laterally averaged over the scanned area. The top Si layer has the same resistance as the Si substrate, whereas the measured resistance of the BOX

layer is one order of magnitude lower than the surface oxide. This may be attributed to defects such as Si rich precipitates embedded in the BOX, which is usually obtained in the SIMOX process.[25] Together with this, the apparent less uniform BOX layer shown in the SSRM image may be attributed to artifacts of the SSRM measurement, such as electrical defects or partial oxidation of the cleaved surface.

The enhancement in oxygen accumulation around D_p caused by subsequently implanted He can be explained by vacancy clusters originally generated by the oxygen implantation, which form stable complexes[6] that are precursors of nanosized He-filled bubbles.[18–20] The empty volume and the internal surfaces associated with such bubbles act as the preferential trapping centers for He and oxygen, respectively (the latter is accumulated during the annealing process).[17,19,21,22] He escapes from bubbles leaving the Si substrate at the temperature above 300 °C.[26] An increase in the He fluence may result in a higher pressure inside the bubbles, which enhances their stability against the dissolution that may occur during the temperature ramping for high temperature annealing. A longer lasting oxygen gettering effect is achieved due to the stabilization of the gettering centers. By the conventional low-fluence SIMOX process for implantation energy of 185 keV, a continuous BOX layer was never achieved at such a low oxygen fluence and small thickness. BOX layers with a thickness of 100–125 nm were formed with oxygen fluences of $(4-5)\times 10^{17}$ cm^{-2}.[25,27] Nevertheless, the BOX thickness can also be decreased by reducing the ion energy according to the so-called "energy-dose" window,[9,28,29] which, however, would decrease the thickness of the superficial Si layer.

To summarize, oxygen gettering at the damage induced by the implantation of a very low implanted oxygen fluence of 1×10^{17} cm^{-2} at 185 keV is enhanced by using a subsequent He implantation and employing additional oxygen in-diffusion from the annealing atmosphere, which benefits the SOI structure formation at D_p. In this way, an extremely thin continuous BOX layer can be formed, which is demonstrated by cross section SSRM together with XTEM.

[1] P. M. Fahey, P. B. Griffin, and J. D. Plummer, Rev. Mod. Phys. **61**, 289 (1989).
[2] K. Kyllesbech Larsen, V. Privitera, S. Coffa, F. Priolo, S. U. Campisano, and A. Carnera, Phys. Rev. Lett. **76**, 1493 (1996).
[3] R. Kalyanaraman, T. E. Haynes, V. C. Venezia, D. C. Jacobson, H.-J. Gossmann, and C. S. Rafferty, Appl. Phys. Lett. **76**, 3379 (2000).
[4] P. Pellegrino, P. Lévêque, J. Wong-Leung, C. Jagadish, and B. G. Svensson, Appl. Phys. Lett. **78**, 3442 (2001).
[5] I. Danilov, H. Boudinov, J. P. de Souza, and Yu. N. Drozdov, J. Appl. Phys. **97**, 076106 (2005).
[6] O. W. Holland, J. D. Budai, and B. Nielsen, Mater. Sci. Eng., A **253**, 240 (1998).
[7] H. Wong, N. W. Cheung, P. K. Chu, J. Liu, and J. W. Mayer, Appl. Phys. Lett. **52**, 1023 (1988).
[8] R. Kögler, A. Peeva, A. Lebedev, M. Posselt, W. Skorupa, G. Özelt, H. Hutter, and M. Behar, J. Appl. Phys. **94**, 3834 (2003).
[9] R. Kögler, X. Ou, W. Skorupa, and W. Möller, Appl. Phys. Lett. **92**, 181906 (2008).
[10] R. Kögler, A. Mücklich, L. Vines, D. Krecar, A. Kuznetsov, W. Skorupa, Nucl. Instrum. Methods Phys. Res. B **257**, 161 (2007).
[11] *SIMOX*, edited by M. J. Anc (Institution of Electrical Engineers, Stevenage, 2004).
[12] S. Bagchi and S. J. Krause, Appl. Phys. Lett. **71**, 2136 (1997).
[13] M. Tamura, M. Ishimaru, K. Hinode, K. Tokiguchi, H. Seki, and H. Mori, Jpn. J. Appl. Phys., Part 1 **45**, 7592 (2006).
[14] A. Ogura, Appl. Phys. Lett. **74**, 2188 (1999).
[15] T. Ernst, C. Tinella, C. Raynaud, and S. Cristoloveanu, Solid-State Electron. **46**, 373 (2002).
[16] N. Bresson, S. Cristoloveanu, C. Mazuré, F. Letertre, and H. Iwai, Solid-State Electron. **49**, 1522 (2005).
[17] V. Raineri, M. Saggio, and E. Rimini, J. Mater. Res. **15**, 1449 (1999).
[18] A. Van Veen, H. Schut, R. A. Hakvoort, A. Fedorov, and K. T. Westerdin, Mater. Res. Soc. Symp. Proc. **373**, 499 (1995).
[19] G. F. Cerofolini, F. Corni, S. Frabboni, C. Nobili, G. Ottaviani, and R. Tonini, Mater. Sci. Eng. R. **27**, 1 (2000).
[20] F. Corni, C. Nobili, G. Ottaviani, R. Tonini, G. Calzolari, G. F. Cerofolini, and G. Queirolo, Phys. Rev. B **56**, 7331 (1997).
[21] X. Ou, R. Kögler, A. Mücklich, W. Skorupa, W. Möller, X. Wang, J. W. Gerlach, and B. Rauschenbach, Appl. Phys. Lett. **93**, 161907 (2008).
[22] A. Ogura, Appl. Phys. Lett. **82**, 4480 (2003).
[23] J. F. Ziegler, J. P. Biersack, and U. Littmark, in *The Stopping and Ranges of Ions in Solids*, edited by J. F. Ziegler (Pergamon, New York, 1985), Vol. 1.
[24] L. Vines, R. Kögler, and A. Kuznetsov, Microelectron. Eng. **84**, 547 (2007).
[25] S. Nakashima and K. Izumi, J. Mater. Res. **8**, 523 (1993).
[26] C. C. Griffioen, J. H. Evans, P. C. de Jong, and A. van Veen, Nucl. Instrum. Methods Phys. Res. B **27**, 417 (1987).
[27] Y. Tan, B. Johnson, S. Seraphin, J. Jiao, M. J. Anc, and L. P. Allen, J. Mater. Sci.: Mater. Electron. **12**, 537 (2001).
[28] M. Chen, X. Wang, J. Chen, Y. Dong, X. Liu, Y. Yu, and X. Wang, Appl. Phys. Lett. **80**, 880 (2002).
[29] X. Wang, J. Chen, Y. Dong, M. Chen, and X. Wang, Chem. Phys. Lett. **367**, 44 (2003).

APPLIED PHYSICS LETTERS **95**, 193501 (2009)

Light emitting field effect transistor with two self-aligned Si nanocrystal layers

V. Beyer,[1,a)] B. Schmidt,[1] K.-H. Heinig,[1] and K.-H. Stegemann[2]
[1]*Forschungszentrum Dresden-Rossendorf, Institute of Ion Beam Physics and Materials Research, P.O. Box 51 01 19, D-01314 Dresden, Germany*
[2]*Signet Solar GmbH, Am Fuchsloch 10, D-04720 Mochau, Germany*

(Received 8 February 2009; accepted 14 September 2009; published online 9 November 2009)

Light emitting field effect transistors based on narrow layers of silicon nanocrystals (NCs) in the gate oxide were fabricated. Direct quantum mechanical electron and hole tunneling into NCs was achieved by self-alignment of NCs-interface-distances to ~2 nm. The direct tunneling reduces oxide degradation, prolongs device lifetime and increases operation speed. Self-alignment occurs during thermal treatment of ion irradiated stacks of 50 nm polycrystalline silicon/15 nm SiO_2/(001)Si substrate. An alternating voltage (ac) was applied to the gate to inject charges into the NCs. Due to injection by direct tunneling, electroluminescence extends to higher ac frequencies than reported so far. © *2009 American Institute of Physics*. [doi:10.1063/1.3242379]

Ion beam synthesis (IBS) of nanocrystals (NCs) is compatible with modern complementary metal oxide semiconductor (CMOS) technology as it is a combination of ion implantation and subsequent annealing. Great effort is currently devoted to the IBS of semiconducting or metallic NCs for micro- and optoelectronic applications, respectively. An example is the nonvolatile multinanodot floating-gate memory.[1–4] Recently, Walters *et al.*[5] demonstrated a field effect driven electroluminescence (EL) by excitonic emission from Si NCs which are embedded in a gate oxide. An alternating current (ac) voltage is applied at the gate electrode of a MOS transistor device in order to charge the Si NCs sequentially with electrons and holes. Thereby, both charge carriers are injected from the transistor channel via Fowler–Nordheim (FN) tunneling through the oxide barrier. The excitons formed in the Si NCs recombine radiatively; the emitted wavelength depends on the NC bandgap energy, i.e., the NC size.[6]

Here, using an innovative fabrication process, a light emitting field effect transistor (LEFET) is demonstrated with two self-aligned luminescent layers of Si NCs. Compared to conventional Si NC synthesis by Si^+ ion implantation into the gate oxide (see Refs. 1 and 5, for instance), we take advantage of a self-alignment process, i.e., the Si NCs are formed in SiO_2 at a well-controlled small distance of ~2 nm from the Si/SiO_2 interfaces. This allows charge carrier injection into the NCs by direct tunneling, which leads to lower operation voltage and longer device life time. Additionally, excitonic light emission comes from two Si NC layers at the gate poly-Si/SiO_2 and the channel Si/SiO_2 interfaces. Figures 1(a)–1(c) illustrate the fabrication process. Ion irradiation through a MOS-like poly-Si/SiO_2/Si substrate stack [Fig. 1(a)] causes an ion-irradiation-induced mixing of both SiO_2/Si interfaces. At the formerly sharp SiO_2/Si interfaces nonstoichiometric SiO_x ($x<2$) regions are formed [Fig. 1(b)]. Subsequent annealing restores the upper and lower SiO_2/Si interfaces by phase separation (of SiO_x into SiO_2 and Si) [Fig. 1(c)]. In the tails of the ion beam mixed profile NCs form due to slow diffusion to the distance interfaces.[7–9] The competition between interface restoration and nucleation self-aligns the NCs into narrow layers parallel to the Si/SiO_2 interfaces. The competition between interface restoration and nucleation aligns the NCs into narrow layers parallel to the SiO_2/Si interfaces.[7] In comparison to the device reported by Walters *et al.*,[5] here, the light emission efficiency is improved due the additional second Si NC layer charged with opposite polarity from the poly-Si gate [see Fig. 1(d)]. The self-alignment of the NC layers with the SiO_2/Si interfaces allows to control shorter (direct) tunneling distances between the NCs and the Si electrodes with the potential of faster devices operating at reduced voltages. The charge storage

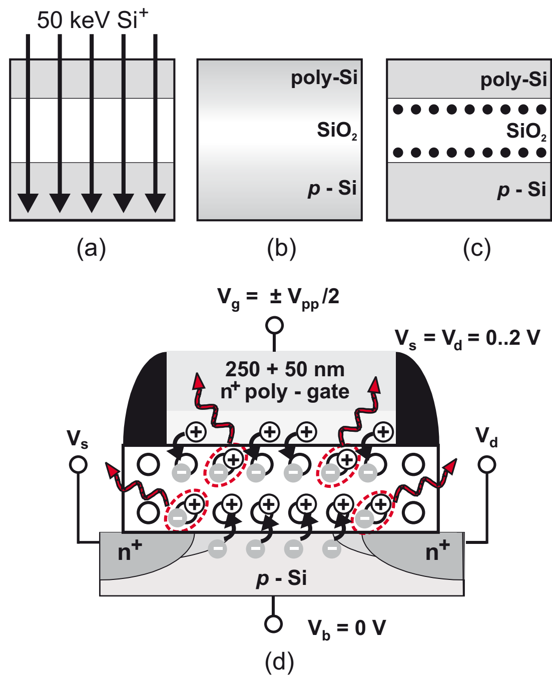

FIG. 1. (Color online) [(a)–(c)] Scheme of the fabrication of Si NCs in the gate oxide by ion irradiation through the Si/SiO_2 interfaces and subsequent annealing. (d) Schematic of light emission where an ac voltage is applied to the gate in order to inject charges of both polarities into the lower and upper Si NC layer from the channel and the poly-Si gate of the transistor, respectively.

[a)]Electronic mail: v.beyer@fzd.de.

 © 2009 American Institute of Physics

behavior of such a structure used as NCs based memory device is described elsewhere.[10,11]

In this article the performance of the LEFET devices as well as options of light emission with a NC double layer configuration are reported. A 14.5 nm thin SiO_2 layer was thermally grown at 900 °C for 50 min in dry O_2 on (001) *p*-type Si (1–10 Ω cm). A 50 nm thick poly-Si layer fabricated by low pressure chemical vapor deposition (LPCVD) covers this oxide. After 50 keV $^{28}Si^{+}$ ion irradiation of the poly-Si/SiO_2/*p*-Si layer stack to a fluence of 7×10^{15} cm^{-2} at room temperature [Fig. 1(a)], a highly n^+-doped 250 nm thick LPCVD poly-Si capping layer was deposited on top to form the poly-Si gate of the transistor. Rapid thermal annealing (RTA) was carried out at temperatures between 1000 and 1150 °C in N_2 for 10–160 s to prepare the Si NCs embedded in SiO_2 [see Fig. 1(c)]. The existence of the NCs was confirmed by EFTEM imaging using a FEI Tecnai 20 FEG microscope and a Gatan energy filter. Due to this protecting poly-Si layer the discussed fabrication approach profits by its insensitiveness to detrimental impacts.[4,8] The LEFETs were fabricated as *n*MOSFET devices with an active area of 20×20 μm^2 (gate length × gate width) using the standard 0.6 μm CMOS technology line of the Zentrum Mikroelektronik Dresden company. Originally prepared to study the memory characteristics of the embedded Si NCs, several layers of in total 3.2 μm thick Si_3N_4 and SiO_2 layers were deposited on top of the transistors. This device protection is usual in modern memory device fabrication but clearly not suitable for LEFET applications. Therefore, a second set of samples was prepared to study the photoluminescence (PL) properties of the embedded Si NCs, which was not possible on the integrated CMOS devices due to this multilayer coverage. For this sample series the preparation stopped after the 50 nm poly-Si layer deposition and subsequent ion irradiation. Here, the RTA treatment was carried out for 120 and 750 s and also for 3 h in a furnace, both at 1050 °C in N_2. Excited by the second-harmonics, 532 nm, of a Nd:YAG laser the PL spectra of the Si NCs were obtained by a liquid nitrogen cooled CD camera. ac square-wave voltage signals were applied to the gate with the *p*-Si substrate as the reference electrode and an amplitude between ±7 and ±11 V (peak-to-peak voltage V_{pp} of 14 to 22 V) by a 20 MHz NF1930 arbitrary function generator. The source and drain voltages were set to $V_s=V_d=0$ V. The EL spectra were recorded using an Andor DU401A-UV-BR-DD CCD camera working at $T=-70$ °C (thermoelectrical cooling), a Shamrock 303i grating spectrometer, and an optical microscope.

TRIDYN ion collision cascade simulations reveal[7,12] that the 50 keV Si^+ ion irradiation of the LEFET layer stack causes an ion beam mixing of the poly-Si/SiO_2 and SiO_2/(001)Si interfaces with a considerable Si excess in the gate oxide. As the projected ion range is located deeply inside the Si substrate, the majority of Si excess results from ion beam mixing of the interfaces. As shown in Fig. 2 during annealing well-aligned narrow layers of Si NCs with 2–3 nm in diameter form adjacent to the recovered interfaces. The layers are separated to the poly-Si gate and *p*-Si substrate, respectively, by an oxide of about 2 nm thickness, i.e., within a direct tunneling distance for electrons and holes. In the middle of the gate oxide an about 5 nm thin SiO_2 layer is found sandwiched between the NC arrays. Applying an ac voltage to the gate electrode—following the model of Walters *et al.*[5]—excitons are formed within the Si NCs due to alternating electron and hole injection from both electrodes. Since the emitted wavelength depends on the NC bandgap energy, i.e., the NC size, the luminescence with a center wavelength of about 750 nm as shown in Fig. 3 is attributed to radiative recombination of excitons within Si NCs of 2–3 nm in diameter which is consistent with the TEM result (Fig. 2).[5,6] The EL spectra in Figs. 3(a) and 3(c) were obtained from integrated devices of 20×20 μm^2 size. As confirmed by light transmission calculations (not shown here), the undulating modulations of the typically Gaussian-shaped luminescence profiles are related to multiple internal reflections within the Si_3N_4/SiO_2 multilayer stack covering the LEFET devices. These deviations are clearly not correlated with the NCs fabrication method since the PL spectra in Fig. 3(d), which are obtained at simple 50 nm poly-Si/14.5 nm SiO_2/Si stacks, reveal a typical behavior of tiny Si NCs. With the electro- and PL results in Fig. 3 different stages of NC evolution can be traced as a function of the annealing temperature and/or time. During the annealing at 1000 °C the overall EL intensity is close to its maximum value and

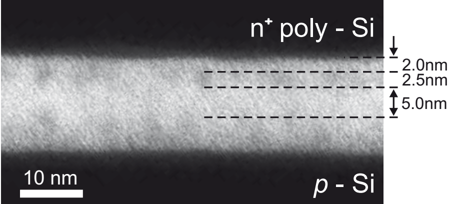

FIG. 2. Cross section EFTEM image of the poly-Si/SiO_2/*p*-Si layer stack revealing tiny Si NCs of about 2–3 nm size on both sides of the gate oxide in the late stage of ripening after 1100 °C, 160 s annealing.

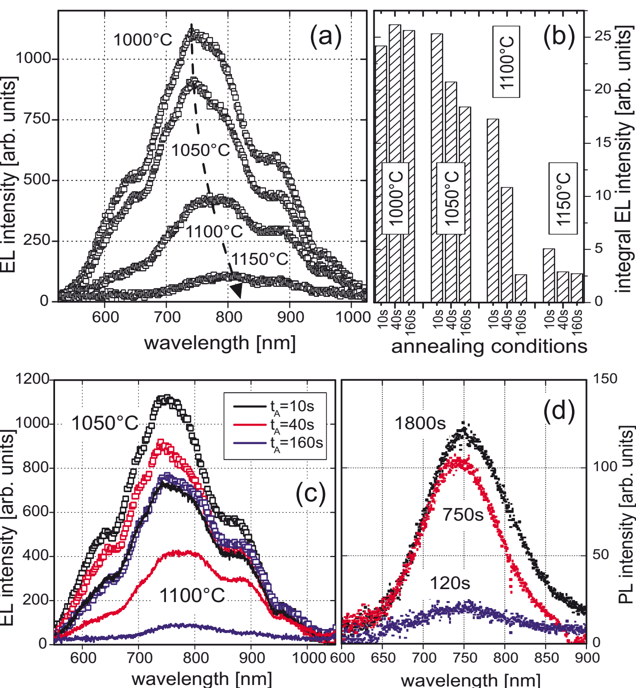

FIG. 3. (Color online) (a) EL spectra after 40 s annealing at different temperatures {$V_{pp}=22$ V and $f=10$ kHz in [(a)–(c)]}. (b) Bar graph plot of the integral EL intensities according to the total sample set (annealing for 10, 40, and 160 s at each temperature). (c) EL spectra after isothermal annealing at 1050 °C (squares) and 1100 °C (lines). The different annealing times are indicated by different colors. (d) PL spectra obtained at simplified structures after 120, 750 (RTA) and 1800 s (furnace) annealing at 1050 °C.

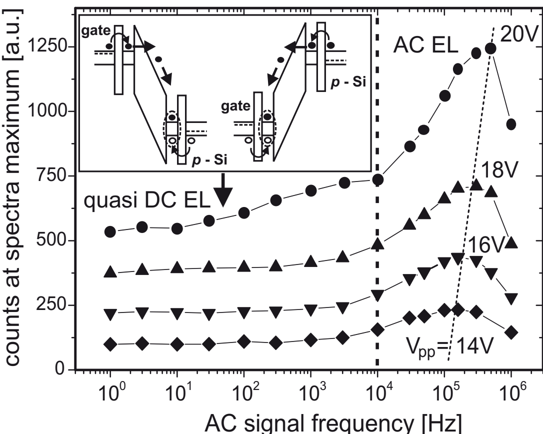

FIG. 4. Dependence of EL intensity on ac gate voltage amplitude and frequency for a LEFET annealed at 1050 °C for 40 s. A schematic band diagram illustrates the quasi DC mode EL mechanism in the inset ($f \lesssim 10$ kHz) for negative and positive ac square-wave gate voltage periods.

still slightly increasing [see the bar graph plot of Fig. 3(b)]. With a higher thermal budget (1050 °C) the intensity is decreasing especially during the 1100 °C annealing down to a very low but stable level such as for 1150 °C thermal treatment. Whereas an increasing intensity indicates that the process of precipitation and Si NC formation has not been finished up to this state (1000 °C), the dissolution of NCs is beginning at 1050 °C; the evolution of the NC size follows Gibbs-Thomson's relation, i.e., a diffusion controlled ripening process.[7,9] NCs adjacent to the Si substrate and poly-Si gate dissolve the faster, the closer they are located to the Si/SiO_2 interfaces.[7–9] This accelerates the dissolution of small, close NCs (1100 °C) and stabilizes bigger more distant ones (related to the Si substrate and gate, respectively) like for 1100 °C, 160 s and 1150 °C annealings in Fig. 3(b). During Ostwald ripening the Si NCs compete with each other in plane whereas some Si NCs grow at the expense of smaller ones. This corresponds at the same time to (i) the redshift of the EL spectra in Fig. 3(a), i.e., a radiative exciton recombination in larger NCs (which are characterized by a smaller bandgap), and (ii) the quenched luminescence due to a considerably reduced number of light emitting sites. It has to be mentioned that the denoted LEFET annealing temperatures represent only a part of the total thermal budget necessary for complete CMOS device fabrication. This explains why the overall PL intensity in Fig. 3(d) is still increasing during isothermal annealing indicating that the process of Si formation has not been finished after 1050 °C, 750 s, while seemingly the EL intensity already decreases with 1050 °C, 40 s thermal treatment [Fig. 3(c)].

The LEFET has two luminescence options depending on the applied gate signal frequency (Fig. 4). With similar EL spectra we refer both modes to radiative recombination of excitons in the Si NCs. At low frequencies, where both NC layers are saturated with charges of opposite sign, a quasi-direct current (dc) related EL is dominating (see the inset in Fig. 4). The applied gate voltage drops mainly across the remaining 5 nm thin SiO_2 layer sandwiched between the NC arrays. This enables a dc leakage current due to FN tunneling of electrons which recombine radiatively with stored holes at the NCs of the opposite side. The quasi-dc current can be easily suppressed increasing the gate oxide thickness to quench the tunneling probability (with positive consequences for the device long time reliability). In Fig. 4 for frequencies $f \gtrsim 10$ kHz an ac related EL emerges out of the quasi DC luminescence background. This type of EL—schematically illustrated in Fig. 1(d)—has been invented by Walters *et al.*[5] as a field effect driven mechanism. The luminescence intensity increases with increasing number of switching cycles up to 100–500 kHz and collapses at 1 MHz AC signal frequency. The highest EL intensity occurs at much higher AC frequencies than obtained by Walters *et al.*.[5] or predicted by Carreras *et al.*[13] ($f \leq 50$ kHz). Here, the gate capacitive charging time constant is clearly reduced due to our very small transistor. In addition the 2 nm thin direct tunneling oxide enables higher charging currents with shorter charging times (as confirmed by their memory device characteristics)[10,11] in comparison to FN tunneling as reported by Walters *et al.*[5] where the NCs are located closer to the oxide center. The dependence of the EL intensity maximum on the ac voltage amplitude reveals the significance of the charge transfer rate. The EL quenches at about $f = 1$ MHz which corresponds supposedly to the physical limit of radiative recombination of excitons in tiny Si NCs, i.e., their radiative lifetime.[5,13]

In conclusion, very small ($20 \times 20\ \mu m^2$) Si NC based light emitting nMOSFET devices are demonstrated where charge carriers are injected into NCs by direct tunneling, not by FN tunneling as in devices reported so far. The direct tunneling leads to a faster device operation which was proven by EL at one order of magnitude higher ac frequencies. Another advantage of direct tunneling is the lower operation voltage and the reduced oxide degradation which increases the device life time. The direct tunneling distances are achieved by a self-alignment process which yields an additional NC layer leading to a further increase of luminescence.

The authors would like to thank S. Probst and M. Klimenkov for the luminescence measurements and EFTEM support, respectively.

[1] S. Tiwari, F. Rana, H. Hanafi, A. Hartstein, E. F. Crabbé, and K. Chan, Appl. Phys. Lett. **68**, 1377 (1996).
[2] V. Beyer and J. von Borany, in *Materials for Information Technologies*, edited by E. Zschech, C. Whelan, and T. Mikolajick (Springer, Berlin, 2005), pp. 139–147.
[3] V. Beyer, J. von Borany, and M. Klimenkov, Appl. Phys. Lett. **89**, 193505 (2006).
[4] T. Müller, K.-H. Heinig, W. Möller, C. Bonafos, H. Coffin, N. Cherkashin, G. Ben Assayag, S. Schamm, G. Zanchi, A. Claverie, M. Tencé, and C. Colliex, Appl. Phys. Lett. **85**, 2373 (2004).
[5] R. J. Walters, G. I. Bourianoff, and H. A. Atwater, Nature Mater. **4**, 143 (2005).
[6] A. Puzder, A. J. Williamson, J. C. Grossman, and G. Galli, J. Chem. Phys. **117**, 6721 (2002).
[7] L. Röntzsch, K.-H. Heinig, B. Schmidt, A. Mücklich, W. Möller, J. Thomas, and T. Gemming, Phys. Status Solidi A **202**, R170 (2005).
[8] V. Beyer and J. von Borany, Phys. Rev. B **77**, 014107 (2008).
[9] K.-H. Heinig, T. Müller, B. Schmidt, M. Strobel, and W. Möller, Appl. Phys. A: Mater. Sci. Process. **77**, 17 (2003).
[10] B. Schmidt, K.-H. Heinig, L. Röntzsch, T. Müller, K.-H. Stegemann, and E. Votintseva, Nucl. Instrum. Methods Phys. Res. B **242**, 146 (2006).
[11] P. Dimitrakis, P. Normand, E. Votintseva, K.-H. Stegemann, K.-H. Heinig, and B. Schmidt, J. Phys.: Conf. Ser. **10**, 7 (2005).
[12] W. Möller and W. Eckstein, Nucl. Instrum. Methods Phys. Res. B **2**, 814 (1984).
[13] J. Carreras, J. Arbiol, B. Garrido, C. Bonafos, and J. Montserrat, Appl. Phys. Lett. **92**, 091103 (2008).

APPLIED PHYSICS LETTERS **94**, 051903 (2009)

Enhanced blue-violet emission by inverse energy transfer to the Ge-related oxygen deficiency centers via Er^{3+} ions in metal-oxide semiconductor structures

A. Kanjilal,[a] L. Rebohle, M. Voelskow, W. Skorupa, and M. Helm
Institute of Ion Beam Physics and Materials Research, Forschungszentrum Dresden-Rossendorf e.V., P.O. Box 51 01 19, 01314 Dresden, Germany

(Received 1 December 2008; accepted 7 January 2009; published online 4 February 2009)

It is generally believed that the 1.5 μm Er luminescence is enhanced by transferring energy from Si nanocrystals to the nearest Er^{3+} ions in Er-doped Si-rich SiO_2 layers during optical pumping. Here, the influence of Ge nanocrystals instead of excess Si in the same environment is studied using electroluminescence technique on metal-oxide-semiconductor structures. An increase of the 400 nm electroluminescence intensity with a concomitant reduction of the Er-related emission is observed. This is explained in the light of an inverse energy transfer process from Er^{3+} to the Ge-related oxygen-deficiency centers. © *2009 American Institute of Physics*. [DOI: 10.1063/1.3077169]

Recently, Si nanocrystals (NCs) in SiO_2 received much attention, since they can act as *sensitizers* for increasing the intensity of the 1.53 μm Er luminescence in layers codoped with Er ions.[1–4] The natural question arises, whether and/or how this behavior will change by using NCs of Ge, which is chemically very similar to Si. The optoelectronic properties of Ge NCs in SiO_2 have been investigated[5,6] to a much lesser extent than that of Si. The underlying physics behind such light emitting devices (LEDs) has generally been expressed in terms of recombination of charge carriers either in Ge NCs through bandgap opening[7] according to the quantum confinement model[5] or in defect states[6] during electrical/optical pumping. Emission of light at ~400 nm has been reported[6] as a result of optical and/or electrical excitation of the Ge-related oxygen-deficiency center (GeODC) into the first singlet state (S_1), followed by the intersystem crossing to the first triplet state (T_1), and a radiative transition back to the ground singlet state (S_0). Recent photoluminescence studies[8,9] revealed that this system could be used for visible range pumping of Er^{3+} ions where Ge nanoclusters behave as sensitizers. In fact, the application of such a system in Si-based electronic platform requires the fabrication of a metal-oxide semiconductor (MOS) structure while the electroluminescence (EL) efficiency is crucial for device performance.

In this letter, we present the fabrication of Si-based MOSLEDs where Ge NCs and/or Er^{3+} ions are dispersed into the SiO_2 layer. In particular, we demonstrate a pronounced increase in the 400 nm EL intensity by Er-doping with a concomitant reduction in the Er emission, implying an *inverse energy transfer* from Er^{3+} to the GeODCs. This is contrary to the phenomenon commonly accepted for Er-doped Si-rich SiO_2 layers where energy is known to transfer from Si NC to the nearby Er^{3+} ions,[1–4] keeping in mind the spatial location of the Er sites.[10]

Initially 130 keV Ge ions were implanted at room temperature (RT) with a dose of 2×10^{16} ions/cm^2 into a thermally grown SiO_2 layer of thickness 200 nm on *n*-type (100)Si wafers. The samples were subjected to rapid thermal annealing at 1050 °C for 180 s according to Ref. 11 in nitrogen ambience to produce Ge NCs. Subsequently, 250 keV Er ions were implanted with a dose of 1×10^{15} ions/cm^2 into the Ge-rich SiO_2 layer, followed by short-time annealing at 1050 °C for 6 s not only to remove ion-beam induced defects, but also to activate Er^{3+} ions. Both Ge and Er ions provide Gaussian-like profiles with maximum concentrations of ~3.5% and 0.3% at R_p of ~112 and 115 nm, respectively. Two reference samples were also prepared by implanting either Ge or Er ions into the SiO_2 layers followed by annealing at 1050 °C for 180 and 6 s, respectively. A semitransparent indium tin oxide and aluminum contacts were sputter deposited in the front and rear surfaces, respectively, to achieve a MOS structure. Circular electrodes with a diameter of 0.2–1.1 mm were subsequently patterned in the front surface by photolithography. The EL spectra were recorded at RT with a single grating monochromator and a photomultiplier, a liquid-nitrogen cooled InGaAs detector, or a charge-coupled device detector. The InGaAs detector or the photomultiplier in combination with a photon counting system were employed to study the time-resolved EL dynamics. Cross-sectional transmission electron microscopy (TEM) images were taken by means of a FEI Titan 80–300 S/TEM.

Formation of Er/Er-oxide clusters with dimension in the range of 2–5 nm (indicated by white arrows) [Fig. 1(a)] in Er-doped SiO_2 layers, called Er:SiO_2, was seen using high-resolution TEM (HRTEM), while Ge NCs with an in-plane diameter of ~4 nm (marked by black arrows) were observed in Ge-rich SiO_2 layers, called Ge-NCs:SiO_2 [Fig. 1(b)]. Although the composition of the clusters in Er:SiO_2 is not yet known, on the basis of the thermodynamic properties of Er and its oxide,[12] we feel that the formation of Er oxide is more favorable than that of Er. However, no specific variation in size and distribution of NC was observed in Er-doped Ge-NCs:SiO_2 layers, named Er:Ge-NCs:SiO_2 [Fig. 1(c)]; the corresponding HRTEM image is displayed in Fig. 1(d).

Figure 2 shows the EL spectra of the Ge-rich MOSLEDs with or without Er ions for a constant current density (J) of 0.17 mA/cm^2. The spectrum for the Er-doped MOSLED is characterized by four EL bands, namely, P_1 to P_4, in the spectral range between blue violet and infrared, which are assigned as the radiative transitions in Er^{3+} from the $^2H_{11/2}$, $^4S_{3/2}$, $^4F_{9/2}$ and $^4I_{13/2}$ states to the ground state ($^4I_{15/2}$), respectively.[13] Nevertheless, the Er emission in the short wavelength region, especially the $^2H_{9/2}\rightarrow{}^4I_{15/2}$ transition in-

[a]Electronic mail: a.kanjilal@fzd.de.

 © 2009 American Institute of Physics

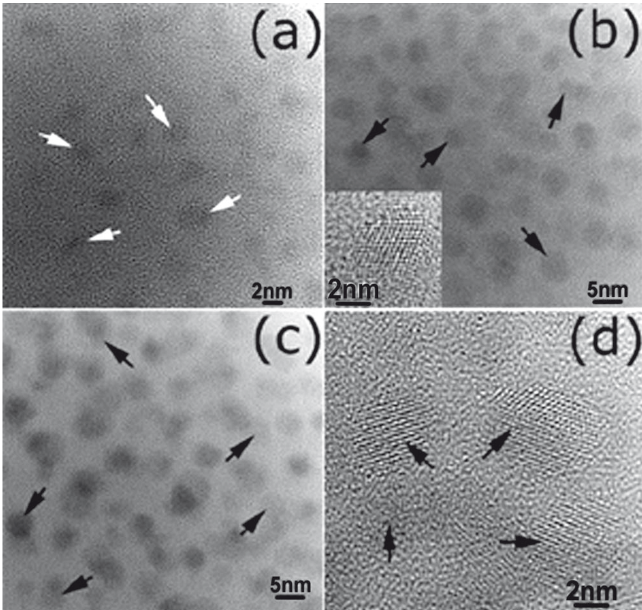

FIG. 1. Bright-field TEM images, with electron beam direction along the [110] zone axis for the (a) Er:SiO_2, (b) Ge-NCs:SiO_2, [(c) and (d)] and Er:Ge-NCs:SiO_2 are shown. Inset of (b) displays the HRTEM of a Ge NC of the Ge-NCs:SiO_2, where crystalline Ge core shows the {111} faceting. HRTEM of the Er:Ge-NCs:SiO_2 (d) depicts randomly oriented Ge-NCs (denoted by black arrows).

duced ~410 nm EL (inset of Fig. 2) can be distinguished for J=7.1 mA/cm^2. The EL peak of ~400 nm in Ge-NCs:SiO_2 is attributed to the GeODC (as a consequence of the $T_1 \rightarrow S_0$ transition).[6] Our key result is the increase in the 400 nm EL intensity at the expense of Er-related emission upon Er doping. Quantitative measurements show that the 1532 nm EL yield of the Er^{3+} is suppressed by a factor of ~3 in presence of Ge NCs. Whereas other Er EL bands are hardly distinguishable due to the broadening of the 400 nm peak and possible decrease in intensity of those Er emissions by a factor similar to the 1532 nm Er EL.

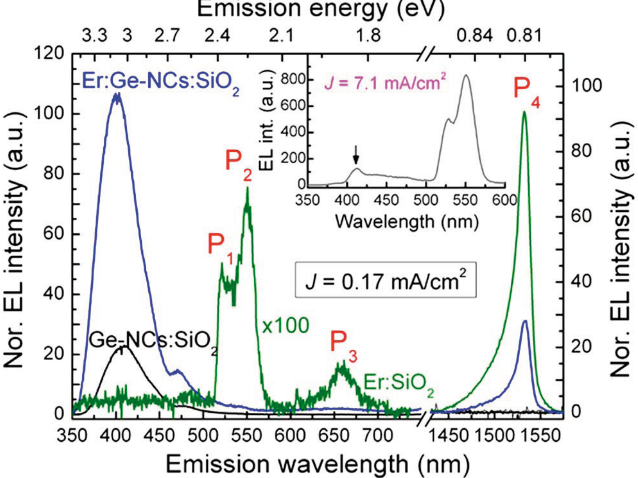

FIG. 2. (Color online) The visible and infrared EL spectra, plotted by solid lines in black, green, and blue for the Ge-NCs:SiO_2, Er:SiO_2, and Er:Ge-NCs:SiO_2, respectively, with J=0.17 mA/cm^2. Note that the scale given in the left and right ordinates are independent of each other as the signals in the visible and infrared regions were collected by two different detectors. 100 for better projection, where P_1 to P_4 represent radiative transitions from Inset shows an additional EL spectrum for Er:SiO_2 with J =7.1 mA/cm^2; a prominent peak at ~410 nm is indicated by the downward arrow.

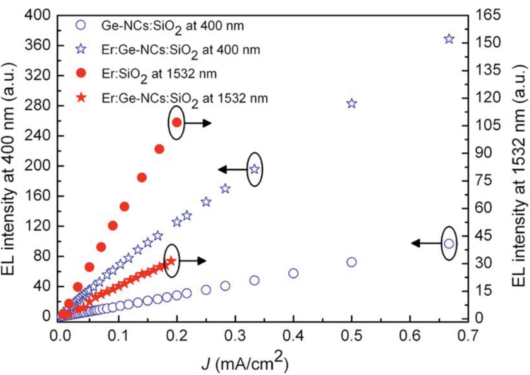

FIG. 3. (Color online) Relative intensities of the 400 nm peak for Ge-NCs:SiO_2 and Er:Ge-NCs:SiO_2 are denoted by blue open circles (○) and blue solid stars (☆), respectively. Similarly, the relative 1532 nm peak intensities for Er:SiO_2 and Er:Ge-NCs:SiO_2 are depicted by red solid circles (●) and red solid stars (★), respectively.

The current-voltage (I-V) characteristics of the working devices have also been tested (not shown), confirming that the device integrity is unaffected during device processing; the I-V profiles can be interpreted in the light of injection of electrons from the conduction band (CB) of the Si to the CB of SiO_2 via the Fowler–Nordheim or trap-assisted tunneling.[14] Furthermore, the 400 and 1532 nm EL intensities are found increasing linearly as a function of J (Fig. 3), where each of them can be fitted by EL(J) $=\mathrm{EL}_{max}[\sigma\tau\phi/(\sigma\tau\phi+1)]$;[15] $\phi=J/q$. The product of the excitation cross section (σ) and lifetime (τ) for the former peak increases from 2.3×10^{-20} to 5.4×10^{-17} cm^2 s by Er doping, while it varies from 6.5×10^{-17} to 1.7×10^{-16} cm^2 s for the later by incorporating Ge NCs.

It is assumed that during implantation Si and oxygen (O) atoms are released from the SiO_2 network. In the following phases of annealing, displaced O can either be reintegrated into the SiO_2 network or be used in oxidizing implanted element(s), where the formation enthalpies (ΔG_f) of GeO, GeO_2, SiO_2, and Er_2O_3 are −237.2, −521.4, −856.3, and −1808.7 kJ/mol, respectively.[12] Indeed, reconstruction of SiO_2 is favorable in Ge implanted SiO_2, where Ge atoms try to form NCs by Ostwald ripening and eventually triggers the formation of GeODCs near the NC/SiO_2 interface. The Er_2O_3 configuration is preferable in Er:SiO_2 due to high ΔG_f and leads to the formation of Er oxide clusters during annealing [Fig. 1(a)]. We should note here that in contrary to Ref. 16, HRTEM results reveal that Er doping does not give rise to (i) preferential nucleation of amorphous Ge, (ii) fragmentation of NCs by sputtering, (iii) evolution of bigger NCs, or (iv) dissolution of NCs via ion-beam-mixing for Ge-NCs:SiO_2 layers (Fig. 1). Therefore, even if we assume a variation in the cross-section without any change in microstructure, the two *independent* changes in Fig. 2 (quenching of the 1532 nm Er EL and the rise of the Ge-related 400 nm EL intensity) cannot be interpreted, unless we consider an energy transfer mechanism to the GeODC via Er^{3+}, called *inverse energy transfer* process.

The energy levels up to $^2H_{11/2}$ of an Er^{3+} ion lay below the level T_1 of GeODC and hence cannot take part in energytransfer process. Although the high energy level Er transitions are not evident in case of Er:SiO_2 by using a low J value (0.17 mA/cm^2), upon injection of electrons with a moderate J (~7.1 mA/cm^2), other Er-related EL peaks, es-

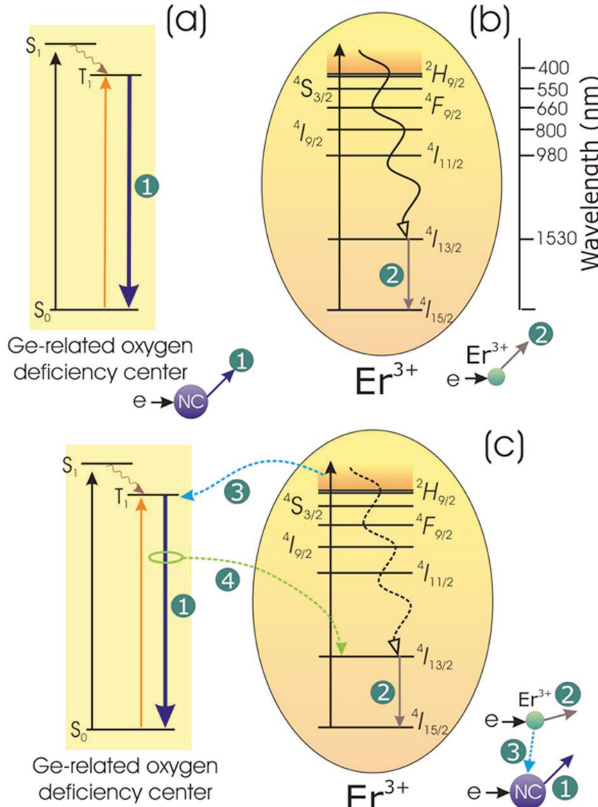

FIG. 4. (Color online) A hot electron excited Ge-related defect center in Ge-NCs:SiO_2 is shown in (a), where the radiative transition from the level T_1 is marked by 1. Electronic excitation of an Er^{3+} in Er:SiO_2 is shown in (b), while the downward arrow labeled as 2 represents the infrared emission of Er^{3+}. The downward wavy arrow up to $^4I_{13/2}$ represents a nonradiative transition. Both the radiative defect center and Er^{3+} are excited by colliding with hot electrons in Er:Ge-NCs:SiO_2 (c). Here, the downward wavy dashed arrow up to $^4I_{13/2}$ signifies nonradiative transition, which is either absent or strongly reduced. In all three cases, the corresponding impact-excitation processes are elucidated in the lower right corner of (a)–(c), respectively.

pecially the $^2H_{9/2}\rightarrow{}^4I_{15/2}$ transition mediated ~410 nm EL, can be visible (inset of Fig. 2). Clearly, the Er energy levels lying almost in the same height or above than that of T_1 in GeODC [schematically shown in Fig. 4(a)] can contribute to the energy transfer process. For 3.5% of Ge, the 400 nm EL yield reaches its maximum by doping Er up to 0.8%, while the peak intensity quenches by further increase in Er due to concentration quenching.[1] To follow the proposed energy transfer process, the EL lifetime of the Er^{3+} excited states has further been examined using a stretched exponential function,[17] which gives τ^{decay} of ~214 and 228 μs in Er:SiO_2 for the 410 and 550 nm EL, respectively. Because of close proximity, as the 410 nm Er peak is submerged into the Ge-related 400 nm EL intensity in Er:Ge-NCs:SiO_2, we estimate the corresponding rise (τ^{rise}) and decay (τ^{decay}) times for both Ge-NCs:SiO_2 and Er:SiO_2 layers (not shown). While the values of τ^{rise} and τ^{decay} are 46 and 66 μs for the former, the respective values are 27 and 214 μs for the latter. As expected from the energy transfer process, the radiative lifetime of the 400 nm EL hardly changes by Er doping,[2] revealing an increase in σ of the 400 nm EL by an order of three by introducing Er ions.

Based on our results, we believe that the transitions from the $^2H_{9/2}$ level or above to the ground $^4I_{15/2}$ level are likely to be accompanied by a nonradiative relaxation to the lower lying levels of Er^{3+} in Er:SiO_2 and as a consequence intensify the green, red, and infrared EL [Fig. 4(b)]. However, the decay time measurements indicate that the Er $^2H_{9/2}$ level is excited faster than that of the GeODC and can initiate an energy transfer process in Er:Ge-NCs:SiO_2 from Er^{3+} to the level T_1 of Ge-related defects (process 3) based on their respective lifetimes [Fig. 4(c)], analogous to the energy back transfer process as reported in Ref. 18. The 1532 nm EL quenching signifies either absence of an additional excitation path from the higher-energy levels to the state $^4I_{13/2}$ of Er^{3+} or excitation of the Er^{3+} ions staying apart from Ge NCs. A possible energy back transfer process (process 4) in Fig. 4(c) plays a minor role only.

In summary, we experimentally demonstrated an increase in the Ge-related 400 nm EL intensity at the expense of the Er emission in Er-doped SiO_2 layers containing Ge NCs, showing a strong coupling between the Er^{3+} ions and GeODCs. Since the microstructure of the Ge-rich SiO_2 layers is found unaffected by Er doping, based on the decay time measurements, we conclude that an energy transfer from Er^{3+} to the triplet state T_1 of the Ge-related defect centers can only justify the observed electroluminescence.

The authors thank J. Schneider and C. Neisser for the ion implantation and sample processing, respectively. The support of the Alexander von Humboldt Foundation is gratefully acknowledged.

[1]C. Maurizio, F. Iacona, F. D'Acapito, G. Franzò, and F. Priolo, Phys. Rev. B **74**, 205428 (2006).
[2]A. Kanjilal, L. Rebohle, M. Voelskow, W. Skorupa, and M. Helm, J. Appl. Phys. **104**, 103522 (2008).
[3]B. Garrido, C. García, S.-Y. Seo, P. Pellegrino, D. Navarro-Urrios, N. Daldosso, L. Pavesi, F. Gourbilleau, and R. Rizk, Phys. Rev. B **76**, 245308 (2007).
[4]T. Nakamura, M. Fujii, S. Miura, M. Inui, and S. Hayashi, Phys. Rev. B **74**, 045302 (2006).
[5]E. W. H. Kan, W. K. Chim, C. H. Lee, W. K. Choi, and T. H. Ng, Appl. Phys. Lett. **85**, 2349 (2004).
[6]L. Rebohle, J. von Borany, H. Fröb, and W. Skorupa, Appl. Phys. B: Lasers Opt. **71**, 131 (2000).
[7]C. Bulutay, Phys. Rev. B **76**, 205321 (2007).
[8]C. L. Heng, T. G. Finstad, P. Storås, Y. J. Li, and A. E. Gunnæs, Appl. Phys. Lett. **85**, 4475 (2004).
[9]J. S. Jensen, T. P. L. Pedersen, J. Chevallier, B. B. Nielsen, and A. N. Larsen, Nanotechnology **17**, 2621 (2006).
[10]R. A. Senter, C. Pantea, Y. Wang, H. Liu, T. W. Zerda, and J. L. Coffer, Phys. Rev. Lett. **93**, 175502 (2004).
[11]Q. Xu, I. D. Sharp, C. W. Yuan, D. O. Yi, C. Y. Liao, A. M. Glaeser, A. M. Minor, J. W. Beeman, M. C. Ridgway, P. Kluth, J. W. Ager III, D. C. Chrzan, and E. E. Haller, Phys. Rev. Lett. **97**, 155701 (2006).
[12]*CRC handbook of Chemistry and Physics*, edited by D. R. Lide (CRC, Boca Raton, FL, 2006).
[13]G. H. Dieke, *Spectra and Energy Levels of Rare Earth Ions in Crystals* (Interscience, New York, 1968).
[14]M. Perálvarez, J. Carreras, J. Barreto, A. Morales, C. Domínguez, and B. Garrido, Appl. Phys. Lett. **92**, 241104 (2008).
[15]A. Nazarov, J. M. Sun, W. Skorupa, R. A. Yankov, I. N. Osiyuk, I. P. Tjagulskii, V. S. Lysenko, and T. Gebel, Appl. Phys. Lett. **86**, 151914 (2005).
[16]M. C. Ridgway, G. de M. Azevedo, R. G. Elliman, C. J. Glover, D. J. Llewellyn, R. Miller, W. Wesch, G. J. Foran, J. Hansen, and A. Nylandsted-Larsen, Phys. Rev. B **71**, 094107 (2005).
[17]L. Pavesi and M. Ceschini, Phys. Rev. B **48**, 17625 (1993).
[18]I. Izeddin, A. S. Moskalenko, I. N. Yassievich, M. Fujii, and T. Gregorkiewicz, Phys. Rev. Lett. **97**, 207401 (2006).

APPLIED PHYSICS LETTERS **94**, 241105 (2009)

Resonant enhancement of second order sideband generation for intraexcitonic transitions in GaAs/AlGaAs multiple quantum wells

M. Wagner,[1,a)] H. Schneider,[1] S. Winnerl,[1] M. Helm,[1] T. Roch,[2] A. M. Andrews,[2] S. Schartner,[2] and G. Strasser[2]
[1]*Institute of Ion Beam Physics and Materials Research, Forschungszentrum Dresden-Rossendorf, P.O. Box 510119, 01314 Dresden, Germany*
[2]*Micro- and Nanostructure Center (ZMNS), TU Wien, Floragasse 7, 1040 Vienna, Austria*

(Received 5 May 2009; accepted 26 May 2009; published online 16 June 2009)

We present an experimental study on efficient second order sideband generation in symmetric undoped GaAs/AlGaAs multiple quantum wells. A near-infrared laser tuned to excitonic interband transitions is mixed with an in-plane polarized terahertz beam from a free-electron laser. The terahertz beam is tuned either to the intraexcitonic heavy-hole $1s$-$2p$ transition or to the interexcitonic heavy-hole light-hole transition. We find strong evidence that the intraexcitonic transition is of paramount influence on $n=\pm 2$ sideband generation, leading to an order-of-magnitude resonant enhancement of the conversion efficiency up to 0.1% at low temperature. At room temperature, the efficiency drops only by a factor of 7 for low terahertz powers. © *2009 American Institute of Physics*. [DOI: 10.1063/1.3155189]

Strong ac fields in the terahertz (THz) region are known to modify interband absorption of semiconductor heterostructures. Besides shifts of the excitonic energies, for instance due to the ac-Stark effect[1] or dynamical Franz–Keldysh effect,[2] strong THz fields can lead to spectral sidebands of an interband excitation. Sidebands have been studied in bulk GaAs,[3] but especially in semiconductor heterostructures using magnetoexcitons and excitonic and electronic intersubband transitions.[4–8] Besides high conversion efficiencies, semiconductor heterostructures have the advantage that intersubband energies can be tuned by applying a dc field,[9] making these devices potentially attractive for electrically controlled switches and modulators.

In THz sideband generation, the ac THz field with a frequency ω_{THz} modulates the polarization induced by a near-infrared (NIR) beam of frequency ω_{NIR}. New frequencies result at $\omega=\omega_{NIR}\pm n\omega_{THz}$. In symmetric structures, n is restricted to even integer numbers,[4] whereas in asymmetric quantum wells also odd sidebands are allowed.[10] Sideband generation at weak THz fields can be modeled using a nonlinear susceptibility and low-order perturbation theory.[10,11] Highest reported efficiencies in quantum wells for an $n=+1$ process were around 0.2% in a THz waveguide geometry with the THz beam tuned to an excitonic hole intersubband transition.[12] For $n=+2$, slightly lower efficiencies were reported for magnetoexcitons in strong magnetic fields.[5]

Here, we report on efficient $n=\pm 2$ sideband generation up to room temperature in a relatively simple geometry. We employ an in-plane THz field in an effective three-level system, consisting of the $1s$ and $2p$ states of the heavy-hole (hh) exciton, and the $1s$ state of the light-hole (lh) exciton in multiple quantum wells (MQWs). Note that no magnetic field is needed to separate the energy levels. We demonstrate experimentally how the $n=\pm 2$ sideband efficiency scales when the THz beam is tuned between interexcitonic hh-lh and intraexcitonic hh($1s$-$2p$) transitions.

The experimental scheme is indicated in Fig. 1(a). A tunable NIR Ti:sapphire laser delivering 2.5 ps long pulses is transmitted through the sample and detected by a charge coupled device camera attached to a grating spectrometer. The sample studied consists of 60 periods of undoped GaAs quantum wells, each 8.2-nm-thick and separated by 19.6-nm-thick barriers of $Al_{0.34}Ga_{0.66}As$. To allow transmission measurements, the sample was glued to NIR-transparent (100)-oriented ZnTe and the semi-insulating GaAs substrate has been etched away. The sample was kept in a liquid He flow cryostat equipped with a diamond window for the strong THz beam which is overlapped with the NIR beam near normal incidence on the sample. We employ FELBE, the free-electron laser (FEL) at the Forschungszentrum Dresden-

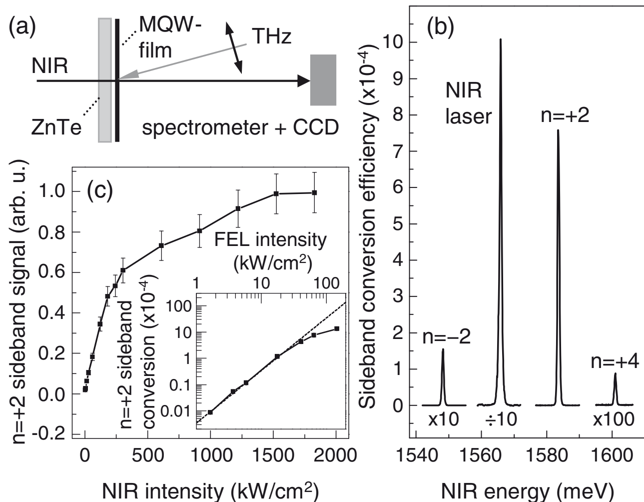

FIG. 1. (a) Experimental setup. (b) Transmitted sideband spectrum at 10 K for $\hbar\omega_{THz}=8.9$ meV near the hh($1s$-$2p$) transition. For clarity, the $n=-2$ and $n=+4$ sidebands are multiplied by 10 and 100, respectively, and the NIR laser is divided by 10. The THz peak intensity was around 65 kW/cm^2. The NIR intensity was 3 kW/cm^2. (c) For an FEL peak intensity of about 8 kW/cm^2 the $n=+2$ sideband signal depends linearly on NIR intensity until saturation is reached. The inset shows the quadratic behavior of the $n=+2$ sideband with FEL intensity (the dotted line is a quadratic fit).

[a)]Electronic mail: m.wagner@fzd.de.

 © 2009 American Institute of Physics

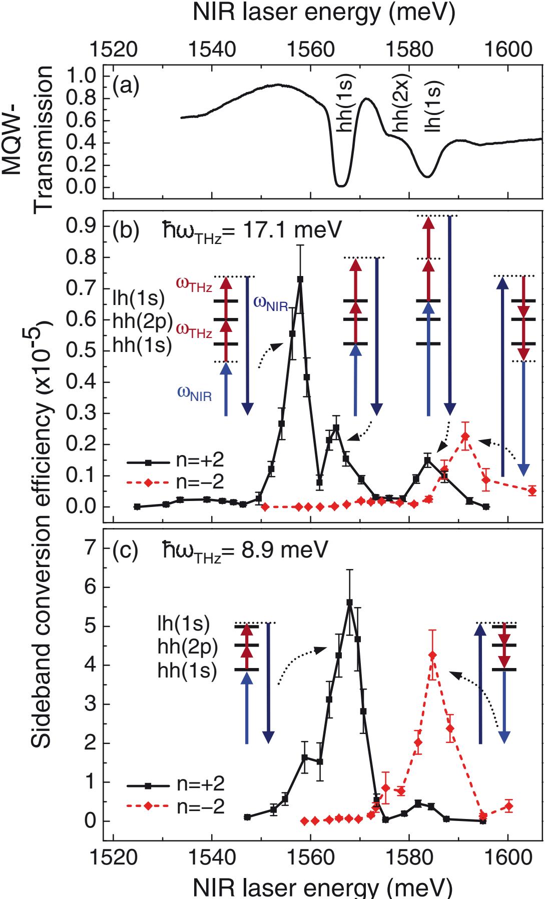

FIG. 2. (Color online) (a) MQW film transmission spectrum at 10 K with hh(1*s*), hh(2*x*), and lh(1*s*) transition (*x* marks the *s* and *p* state). (b) Sideband spectra for $n=+2$ (black line) and $n=-2$ (red dashed line) for an NIR intensity of 180 kW/cm^2, an FEL intensity around 18 kW/cm^2 and an FEL energy of 17.1 meV, corresponding to the hh(1*s*)-lh(1*s*) transition. Schematic level diagrams indicate the involved transitions. (c) Same as (b) for an FEL energy of 8.9 meV near the estimated hh(1*s*-2*p*) resonance.

Rossendorf. This THz source can be tuned continuously from 6 to 300 meV and delivers pulses at a repetition rate of 13 MHz with pulse durations of 10–25 ps for the energies used here. The NIR laser repetition rate was also reduced down to 13 MHz by an acousto-optical pulse picker to temporally overlap each NIR pulse with an FEL pulse. The polarizations of the FEL and NIR laser were linear and parallel to each other for maximum sideband signal.

Figure 2(a) shows the transmission spectrum of the thin MQW film, obtained through normalizing the signal by the ZnTe substrate transmission. hh and lh exciton transitions can be distinguished. At an energy of 1575 meV, the onset of the hh continuum transitions can be seen, starting with the interband allowed hh(2*s*) exciton state. The nearby 2*p* state is optically interband forbidden but should lie around 9 meV above the hh(1*s*) transition.[13] However, the excitonic intersubband transition between hh(1*s*) and hh(2*p*) exciton states is allowed and couples strongly to THz radiation.[2,5]

In Fig. 1(b), a typical low-temperature sideband spectrum is measured under FEL illumination with the NIR laser tuned near the hh(1*s*) exciton energy. Different even orders of sidebands could be observed. Due to slight asymmetry of the quantum wells resulting from MBE growth, also the odd sidebands $n=\pm 1$ appear with typical intensities 1000 times smaller than $n=\pm 2$ (not shown here). Corrected for the losses in the ZnTe substrate, the $n=+2$ sideband reveals a conversion efficiency between incoming NIR power and emitted sideband of 0.13% for an FEL intensity of 145 kW/cm^2, which is high for an $n=+2$ process.[12]

In Fig. 1(c), the $n=+2$ sideband power with the NIR laser at the hh(1*s*) resonance depends linearly on the NIR intensity until saturation is reached. The following experiments were performed at an NIR peak intensity of 180 kW/cm^2 on the quantum well film, resulting in an exciton density at the strongly absorbing hh(1*s*) exciton of 3×10^{10} cm^{-2}. A measurement with 10% of this relatively high exciton density was also taken but the trends presented here stayed the same and only a reduced linewidth was observed. The inset of Fig. 1(c) displays the quadratic dependence of the $n=+2$ power with FEL intensity, as expected for this $\chi^{(3)}$ process.

Now, in Fig. 2(b), the NIR laser energy was tuned at a fixed FEL energy, and at each position, the $n=+2$ (black line) and $n=-2$ (red dashed line) sideband power was recorded. First, we address the case where the FEL energy is fixed at 17.1 meV, corresponding to the interexcitonic hh(1*s*)-lh(1*s*) separation. For the $n=+2$ sideband, three pronounced resonances are observed and their origin can be seen qualitatively from the schematic energy level diagrams. The strongest resonance at 1557 meV lies slightly below the band edge. One FEL-photon energy above we find the hh(2*s*) and hh(2*p*) state in the transmission spectrum, serving as an intermediate state for the mixing. The relative strength of the resonance peak shows that the 1*s*-2*p* transition couples strongly to the THz radiation, although the NIR laser is only resonant with a virtual level and the final state lies in the continuum above the lh. The sideband resonance signal at the hh(1*s*) state is smaller, although one FEL photon is resonant with the hh(1*s*)-lh(1*s*) transition. However, for small in-plane wave vectors, this transition is weak.[14] The third resonance at the lh(1*s*) position is less pronounced since the lh exciton is coupled to continuum states and not to sharper excitonic states like in the aforementioned cases. Note that the intraband optically allowed hh(2*s*) state does not lead to a pronounced feature in the sideband resonance scan. The $n=-2$ sideband spectrum is consistent with this picture, showing highest conversion signal when the NIR laser is tuned 17.1 meV above the hh(2*p*) state. Thus we find that the hh(2*p*) state as an intermediate state for the nonlinear mixing dominates both the $n=+2$ and $n=-2$ sideband spectra.

We now address the case where the FEL energy is fixed at 8.9 meV near the estimated hh(1*s*-2*p*) resonance. The corresponding NIR sideband spectrum is shown in Fig. 2(c). One observes an increase in the $n=+2$ sideband signal at the hh exciton by a factor of 20. Now the FEL is resonant with the hh(1*s*-2*p*) transition and also approximately with the hh(2*p*)-lh(1*s*) transition, leading to an efficient $n=-2$ generation as well. The $n=+2$ spectrum shows a weak resonance at 1583 meV at the lh(1*s*) state, similar to Fig. 2(b). The additional small shoulders at 1575 meV (for $n=-2$) and 1559 meV (for $n=+2$) cannot be assigned with absolute certainty to a particular resonance.[15]

At a temperature of 77 K, there is no drop in efficiency compared to the low-temperature measurement. At room temperature, the $n=+2$ sideband resonance broadens, as shown in Fig. 3, for a THz intensity of 18 kW/cm^2 (black line) and 41 kW/cm^2 (red dashed line). The broadening

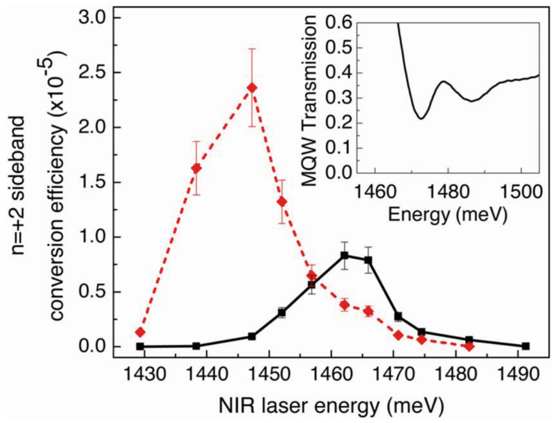

FIG. 3. (Color online) n=+2 sideband resonance taken above room temperature for an NIR intensity of 180 kW/cm^2, an FEL intensity of 18 kW/cm^2 (black line) and 41 kW/cm^2 (red dashed line). The FEL energy is fixed at 8.9 meV. Due to pronounced lattice heating, the sideband spectra appear shifted to lower energies by around 7 meV (black line) and 24 meV (red dashed line), respectively, with respect to the MQW transmission without FEL (inset, taken at 290 K).

stems from broader excitonic resonances in the transmission spectrum (Fig. 3 inset). Nevertheless, at lower THz intensities of 18 kW/cm^2, we still find an efficiency which is only reduced by a factor of 7 compared to the 10 K measurement. The FEL energy was kept at 8.9 meV, though the hh-lh splitting decreases from 17 to 14 meV. However, with the broader absorption lines, the need for matching the THz energy exactly with the energy levels is relaxed. Note that both spectra differ in the spectral position from the transmission measurement taken at 290 K. To overlap them with the transmission measurement, they have to be shifted to higher energies by 7 and 24 meV, respectively. This shift in bandgap is due to a pronounced FEL-induced lattice heating by roughly 17 and 52 K for 18 and 41 kW/cm^2, respectively.

In summary, we have demonstrated efficient $n = \pm 2$ sideband generation in a GaAs/AlGaAs MQW film with the THz beam under normal incidence. Relatively high conversion efficiencies of the 1.7 μm thin quantum well film above 0.1% were measured despite somewhat broad linewidths. By tuning the THz energy in resonance with the hh(1s-2p) transition, we showed that this intraexcitonic transition dominates the sideband spectra compared to a THz energy of the interexcitonic transition between hh and lh states. Slightly above room temperature, the sideband efficiency drops only by a factor of 7. Together with the possibility of shifting the sample's exciton transitions via an applied bias,[9] one could think of efficient room temperature switches or modulators based on such systems.

We gratefully acknowledge discussions with D. Citrin, J. Kono, and D. Stehr. We thank P. Michel and his ELBE team, as well as W. Seidel for their dedicated support. The Vienna group is supported by the Austrian FWF.

[1] J. F. Dynes, M. D. Frogley, M. Beck, J. Faist, and C. C. Phillips, Phys. Rev. Lett. **94**, 157403 (2005).
[2] K. B. Nordstrom, K. Johnsen, S. J. Allen, A.-P. Jauho, B. Birnir, J. Kono, T. Noda, H. Akiyama, and H. Sakaki, Phys. Rev. Lett. **81**, 457 (1998).
[3] M. A. Zudov, J. Kono, A. P. Mitchell, and A. H. Chin, Phys. Rev. B **64**, 121204 (2001).
[4] J. Černe, J. Kono, T. Inoshita, M. Sherwin, M. Sundaram, and A. C. Gossard, Appl. Phys. Lett. **70**, 3543 (1997).
[5] J. Kono, M. Y. Su, T. Inoshita, T. Noda, M. S. Sherwin, S. J. Allen, and H. Sakaki, Phys. Rev. Lett. **79**, 1758 (1997).
[6] A. V. Maslov and D. S. Citrin, Phys. Rev. B **62**, 16686 (2000).
[7] V. Ciulin, S. G. Carter, M. S. Sherwin, A. Huntington, and L. A. Coldren, Phys. Rev. B **70**, 115312 (2004).
[8] S. G. Carter, V. Ciulin, M. Hanson, A. S. Huntington, C. S. Wang, A. C. Gossard, L. A. Coldren, and M. S. Sherwin, Phys. Rev. B **72**, 155309 (2005).
[9] M. Y. Su, S. G. Carter, M. S. Sherwin, A. Huntington, and L. A. Coldren, Appl. Phys. Lett. **81**, 1564 (2002).
[10] M. Y. Su, C. Phillips, J. Ko, L. Coldren, and M. S. Sherwin, Physica B **272**, 438 (1999).
[11] T. Inoshita, J. Kono, and H. Sakaki, Phys. Rev. B **57**, 4604 (1998).
[12] S. G. Carter, V. Ciulin, M. S. Sherwin, M. Hanson, A. Huntington, L. A. Coldren, and A. C. Gossard, Appl. Phys. Lett. **84**, 840 (2004).
[13] I. Galbraith, R. Chari, S. Pellegrini, P. J. Phillips, C. J. Dent, A. F. G. van der Meer, D. G. Clarke, A. K. Kar, G. S. Buller, C. R. Pidgeon, B. N. Murdin, J. Allam, and G. Strasser, Phys. Rev. B **71**, 073302 (2005).
[14] F. Szmulowicz and G. J. Brown, Phys. Rev. B **51**, 13203 (1995).
[15] Such a mixing process would include normally forbidden hh(1s-2s) transitions, which could be possible by assuming a state consisting of mixed hh(2s) and hh(2p) contributions and thus relaxing the selection rules. Alternatively, the n=+2 shoulder (at 1559 meV) might be induced by an Autler–Townes splitting, see S. G. Carter, V. Birkedal, C. S. Wang, L. A. Coldren, A. V. Maslov, D. S. Citrin, and M. S. Sherwin, Science **310**, 651 (2005).

Statistics

Publications

Thin Films

1. Abd El-Rahman, A. M.; Mohamed, S. H.; Ahmed, M. R.; Richter, E.; Prokert, F.
Nitrocarburizing of AISI-304 stainless steel using high-voltage plasma immersion ion implantation
Nuclear Instruments and Methods in Physics Research B ***267****, 1792 (2009).*

2. Abrasonis, G.; Kovács, Gy. J.; Ryves, L.; Krause, M.; Mücklich, A.; Munnik, F.; Oates, T. W. H.; Bilek, M. M. M.; Möller, W.
Phase separation in carbon-nickel films during hyperthermal ion deposition
Journal of Applied Physics ***105****, 083518 (2009).*

3. Beckers, M.; Höglund, C.; Bähtz, C.; Martins, R. M. S.; Persson, P. O. Å.; Hultman, L.; Möller, W.
The influence of substrate temperature and Al mobility on the microstructural evolution of magnetron sputtered ternary Ti–Al–N thin films
Journal of Applied Physics ***106****, 0649157 (2009).*

4. Berndt, M.; Abrasonis, G.; Krause, M.; Mücklich, A.; Munnik, F.; Kolitsch, A.; Möller, W.
Morphology and structure of C:Co, C:V and C:Cu nanocomposite films
Plasma Processes and Polymers ***6****, 902 (2009).*

5. Cantelli, V.; Borany, J. von; Jeutter, N.; Grenzer, J.
In-situ grazing incidence scattering investigations during magnetron sputtering
Advanced Engineering Materials ***11****, 478 (2009).*

6. Cizek, J.; Prochazka, I.; Melikhova, O.; Vlach, M.; Zaludova, N.; Brauer, G.; Anwand, W.; Egger, W.; Sperr, P.; Hugenschmidt, C.; Gemma, R.; Pundt, A.; Kirchhelm, R.
Hydrogen-induced defects in Pd films
Physica Status Solidi (C) ***6****, 2364 (2009).*

7. Cornelius, S.; Vinnichenko, M.; Shevchenko, N.; Rogozin, A.; Kolitsch, A.; Möller, W.
Achieving high free electron mobility in ZnO:Al thin films grown by reactive pulsed magnetron sputtering
Applied Physics Letters ***94****, 042103 (2009).*

8. Donchev, A.; Kolitsch, A.; Schütze, M.; Yankov, R.
Plasma-immersion-ion-implantation of fluorine to protect TiAl-components against high-temperature oxidation
Plasma Processes and Polymers ***6****, 434 (2009).*

9. Emmerlich, J.; Music, D.; Braun, M.; Fayek, P.; Munnik, F.; Schneider, J. M.
A proposal for an unusually stiff and moderately ductile hard coating material: Mo_2BC
Journal of Physics D ***42****, 185406 (2009).*

10. Fahland, M.; Vogt, T.; Meyer, B.; Fahlteich, J.; Schiller, N.; Vinnichenko, M.; Munnik, F.
Deposition of functional coatings on polyethylene terephthalate films by magnetronplasma-enhanced chemical vapour deposition
Thin Solid Films ***517****, 3043 (2009).*

11. Gago, R.; Redondo-Cubero, A.; Endrino, Jl.; Jimenez, I.; Shevchenko, N.
Aluminum incorporation in $Ti_{1-x}Al_xN$ films studied by X-ray absorption near-edge structure
Journal of Applied Physics ***105****, 113521 (2009).*

12. Hämäläinen, J.; Munnik, F.; Ritala, M.; Leskelä, M.
Study on atomic layer deposition of amorphous rhodium oxide thin films
Journal of the Electrochemical Society ***156****, D418 (2009).*

13. Kölpin, H.; Music, D.; Emmerlich, J.; Munnik, F.; Schneider, J. M.
Phase stability of $AlYB_{14}$ sputtered thin films
Journal of Physics: Condensed Matter ***21****, 355006 (2009).*

14. Krause, M.; Bedel, L.; Taupeau, A.; Kreissig, U.; Munnik, F.; Abrasonis, G.; Kolitsch, A.; Radnoczi, G.; Zsolt, C.; Vanhulsel, A.
Structural and mechanical characterization of BC_xN_y thin films deposited by pulsed reactive magnetron sputtering
Thin Solid Films ***518****, 77 (2009).*

15. Martinavicius, A.; Abrasonis, G.; Möller, W.; Templier, C.; Riviere, J. P.; Declemy, A.; Chumlyakov, Y.
Anisotropic ion-enhanced diffusion during ion nitriding of single-crystalline austenitic stainless steel
Journal of Applied Physics ***105****, 093502 (2009).*

16. Martins, R. M. S.; Schell, N.; Gordo, P. R.; Maneira, M. J. P.; Silva, R. J. C.; Braz Fernandes, F. M.
Development of sputtered shape memory alloy Ni–Ti films for actuation in ice cooled environments
Vacuum ***83****, 1299 (2009).*

17. Martins, R. M. S.; Schell, N.; Silva, R.; Pereira, L.; Mahesh, K. K.; Braz Fernandes, F. M.
Texture development and phase transformation behaviour of sputtered Ni-Ti films
Journal of Materials Engineering and Performance ***18****, 543 (2009).*

18. Piekoszewski, J.; Kempinski, W.; Barlak, M.; Werner, Z.; Los, Sz.; Andrzejewski, B.; Stankowski, J.; Piekara-Sady, L.; Skladnik-Sadowska, E.; Szymczyk, W.; Kolitsch, A.; Grötzschel, R.; Starosta, W.; Sartowska, B.
Superconductivity of Mg-B layers prepared by a multi-energy implantation of boron into magnesium and magnesium into boron bulk substrates followed by the furnace and pulsed plasma annealing
Surface and Coatings Technology ***203****, 2694 (2009).*

19. Pilvi, T.; Puukilainen, E.; Munnik, F.; Leskelä, M.; Ritala, M.
ALD of YF_3 thin films from TiF_4 and $Y(thd)_3$ precursors
Chemical Vapor Deposition ***15****, 27 (2009).*

20. Rogozin, A.; Vinnichenko, M.; Shevchenko, N.; Kreissig, U.; Kolitsch, A.; Möller, W.
Real-time evolution of electrical properties and structure of indium oxide and indium tin oxide during crystallization
Scripta Materialia ***60****, 199 (2009).*

21. Romero-Gomez, P.; Palmero, A.; Yubero, F.; Vinnichenko, M.; Kolitsch, A.; Gonzalez-Elipe, A. R.
Surface nanostructuring of TiO_2 thin films by ion beam irradiation
Scripta Materialia ***60****, 574 (2009).*

22. Saly, M. J.; Munnik, F.; Baird, R. J.; Winter, C. H.
Atomic layer deposition growth of BaB_2O_4 thin films from an exceptionally thermally stable tris(pyrazolyl)borate-based precursor
Chemistry of Materials ***21****, 3742 (2009).*

23. Stenzel, O.; Wilbrandt, S.; Kaiser, N.; Vinnichenko, M.; Munnik, F.; Kolitsch, A.; Chuvilin, A.; Kaiser, U.; Ebert, J.; Jakobs, S.; Kaless, A.; Wüthrich, S.; Treichel, O.; Wunderlich, B.; Bitzer, M.; Grössl, M.
The correlation between mechanical stress, thermal shift and refractive index in HfO_2, Nb_2O_5, Ta_2O_5 and SiO_2 layers and its relation to the layer porosity
Thin Solid Films ***517****, 6058 (2009).*

24. Tavares, C. J.; Marques, S. M.; Viseu, T.; Teixeira, V.; Carneiro, J. O.; Alves, E.; Barradas, N. P.; Munnik, F.; Girardeau, T.; Rivière, J.-P.
Enhancement in the photocatalytic nature of nitrogen-doped PVD-grown titanium dioxide thin films
Journal of Applied Physics ***106****, 113535 (2009).*

25. Vinnichenko, M.; Rogozin, A.; Grambole, D.; Munnik, F.; Kolitsch, A.; Möller, W.; Stenzel, O.; Wilbrandt, S.; Chuvilin, A.; Kaiser, U.
Highly dense amorphous Nb_2O_5 films with closed nano-sized pores
Applied Physics Letters ***95****, 081904 (2009).*

26. Werner, Z.; Szymczyk, W.; Piekoszewski, J.; Seah, M. P.; Ratajczak, R.; Nowicki, L.; Barlak, M.; Richter, E.
Stoichiometric MgB_2 layers produced by multi-energy implantation of boron into magnesium
Surface and Coatings Technology ***203****, 2712 (2009).*

27. Wirth, E.; Munnik, F.; Pranevicius, L. L.; Milcius, D.
Dynamic surface barrier effects on hydrogen storage capacity in Mg-Ni films
Journal of Alloys and Compounds ***475****, 917 (2009).*

Nanoscale Magnetism

28. Adam, J.-P.; Rohart, S.; Jamet, J.-P.; Mougin, A.; Ferre, J.; Bernas, H.; Faini, G.; Faßbender, J.
Single Pt/Co(0.5 nm)/Pt nano-discs: Beyond the coherent spin reversal model and thermal stability
Journal of the Magnetics Society of Japan ***33****, 498 (2009).*

29. Bürger, D.; Zhou, S.; Grenzer, J.; Reuther, H.; Anwand, W.; Gottschalch, V.; Helm, M.; Schmidt, H.
The influence of annealing on manganese implanted GaAs films
Nuclear Instruments and Methods in Physics Research B ***267****, 1626 (2009).*

30. Cantelli, V.; Grenzer, J. ; Borany, J. von; Faßbender, J.
The effect of the sputtering gas (Ar, Xe) on FePt clusters formation: Structural and magnetic properties
Journal of Applied Physics ***105****, 07B529 (2009).*

31. Faßbender, J.; Grenzer, J.; Roshchupkina, O.; Choi, Y.; Jiang, J. S.; Bader, S. D.
The effect of ion irradiation and annealing on exchange spring magnets
Journal of Applied Physics ***105****, 023902 (2009).*

32. Faßbender, J.; Strache, T.; Liedke, M. O.; Marko, D.; Wintz, S.; Lenz, K.; Keller, A.; Facsko, S.; Mönch, I.; McCord, J.
Introducing artificial length scales to tailor magnetic properties
New Journal of Physics ***11****, 125002 (2009).*

33. Gaier, O.; Hamrle, J.; Hillebrands, B.; Kallmayer, M.; Pörsch, P.; Schönhense, G.; Elmers, H. J.; Faßbender, J.; Gloskovskii, A.; Jenkins, C. A.; Felser, C.; Ikenaga, E.; Sakuraba, Y.; Tsunegi, S.; Oogane, M.; Ando, Y.
Improvement of structural, electronic, and magnetic properties of Co_2MnSi thin films by He^+-irradiation
Applied Physics Letters ***94****, 122508 (2009).*

34. González-Arrabal, R.; González, Y.; González, L.; García-Hernández, M.; Munnik, F.; Martín-González, M. S.
Room-temperature ferromagneticlike behavior in Mn-implanted and postannealed InAs layers deposited by molecular beam epitaxy
Journal of Applied Physics ***105****, 073911 (2009).*

35. Jaworowicz, J.; Maziewski, A.; Mazalski, P.; Kisielewski, M.; Sveklo, I.; Tekielak, M.; Zablotskii, V.; Ferre, J.; Vernier, N.; Mougin, A.; Henschke, A.; Faßbender, J.
Spin reorientation transitions in Pt/Co/Pt films under low dose Ga^+ ion irradiation
Applied Physics Letters ***95****, 022502 (2009).*

36. Khalid, M.; Ziese, M.; Setzer, A.; Esquinazi, P.; Lorenz, M.; Hochmuth, H.; Grundmann, M.; Brauer, G.; Anwand, W.; Fischer, G.; Adeagbo, W. A.; Hergert, W.; Ernst, A.
Defect-induced magnetic order in pure ZnO films
Physical Review B ***80****, 035331 (2009).*

37. Körner, M.; Lenz, K.; Liedke, M. O.; Strache, T.; Mücklich, A.; Keller, A.; Facsko, S.; Faßbender, J.
Interlayer exchange coupling of Fe/Cr/Fe thin films on rippled substrates
Physical Review B ***80****, 214401 (2009).*

38. Küpper, K.; Räkers, M.; Taubitz, C.; Prinz, M.; Derks, C.; Neumann, M.; Postnikov, A. V.; de Groot, F. M. F.; Piamonteze, C.; Prabhakaran, D.; Blundell, S. J.
Charge order, enhanced orbital moment, and absence of magnetic frustration in layered multiferroic $LuFe_2O_4$
Physical Review B ***80****, 220409 (2009).*

39. Küpper, K.; Wintz, S.; Raabe, J.; Buess, M.; Akhmadaliev, C.; Bischoff, L.; Quitmann, C.; Faßbender, J.
Magnetization dynamics of Landau structures: Tuning the response of mesoscopic magnetic objects using defects
Journal of Physics: Condensed Matter ***21****, 436003 (2009).*

40. Martin, N.; McCord, J.; Gerber, A.; Strache, T.; Gemming, T.; Mönch, I.; Farag, N.; Schäfer, R.; Faßbender, J.; Quandt, E.; Schultz, L.
Local stress engineering of magnetic anisotropy in soft magnetic thin films
Applied Physics Letters ***94****, 062506 (2009).*

41. McCord, J.; Mönch, I.; Faßbender, J.; Gerber, A.; Quandt, E.
Local setting of magnetic anisotropy in amorphous films by Co ion implantation
Journal of Physics D ***42****, 055006 (2009).*

42. Menendez, E.; Sort, J.; Liedke, M. O.; Faßbender, J.; Gemming, T.; Weber, A.; Heydermann, L. J.; Surinach, S.; Rao, K. V.; Deevi, S. C.; Baro, M. D.; Nogues, J.
Creation of sub-100 nm ferromagnetic dots by selective irradiation of a paramagnetic intermetallic alloy
Small ***5****, 229 (2009).*

43. Menendez, E.; Sort, J.; Liedke, M. O.; Faßbender, J.; Surinach, S.; Baro, M. D.; Nogues, J.
Controlled generation of ferromagnetic martensite from paramagnetic austenite in AISI 316L austenitic stainless steel
Journal of Materials Research ***24****, 565 (2009).*

44. Mikuszeit, N.; Baraban, L.; Vedmedenko, E.; Erbe, A.; Leiderer, P.; Wiesendanger, R.
Quasiantiferromagnetic 120° Néel state in two-dimensional clusters of dipole-quadrupole-interacting particles on a hexagonal lattice
Physical Review B ***80****, 014402 (2009).*

45. Potzger, K.; Shalimov, A.; Zhou, S.; Schmidt, H.; Mücklich, A.; Helm, M.; Faßbender, J.; Arenholz, M.; Liberati, E.
Amorphous clusters in Co implanted ZnO induced by boron pre-implantation
Journal of Applied Physics ***105**, 123917 (2009).*

46. Potzger, K.; Zhou, S.
Non-DMS related ferromagnetism in transition metal doped zinc oxide
Physica Status Solidi (B) ***246**, 11247 (2009).*

47. Räkers, M.; Küpper, K.; Bartkowski, S.; Prinz, M.; Postnikov, A. V.; Potzger, K.; Zhou, S.; Arulraj, A.; Stüßer, N.; Uecker, R.; Yang, W. L.; Neumann, M.
Electronic and magnetic structure of $RScO_3$ (R = Sm, Gd, Dy) from X-ray spectroscopies and first-principles calculations
Physical Review B ***79**, 125114 (2009).*

48. Scarlat, C.; Vinnichenko, M.; Xu, Q.; Bürger, D.; Zhou, S.; Kolitsch, A.; Grenzer, J.; Helm, M.; Schmidt, H.
Mn-implanted, polycrystalline indium tin oxide and indium oxide films
Nuclear Instruments and Methods in Physics Research B ***267**, 1616 (2009).*

49. Shalimov, A.; Potzger, K.; Geiger, D.; Lichte, H.; Talut, G.; Misiuk, A.; Reuther, H.; Stromberg, F.; Zhou, S.; Bähtz, C.; Faßbender, J.
Fe nanoparticles embedded in MgO crystals
Journal of Applied Physics ***105**, 064906 (2009).*
Virtual Journal of Nanoscale Science and Technology ***19**, 13 (2009).*

50. Talut, G.; Grenzer, J.; Reuther, H.; Shalimov, A.; Bähtz, C.; Novikov, D.; Walz, B.
In-situ observation of secondary phase formation in Fe implanted GaN annealed in low pressure N_2 atmosphere
Applied Physics Letters ***95**, 232506 (2009).*

51. Tripathi, J. K.; Kanjilal, A.; Rajput, P.; Gupta, A.; Som, T.
Modification of the magnetic and the structural properties of Pt/Cr/Co multilayers by He^+-ion irradiation
Nuclear Instruments and Methods in Physics Research B ***267**, 1608 (2009).*

52. Xu, Q.; Zhou, S.; Markó, D.; Potzger, K.; Faßbender, J.; Vinnichenko, M.; Helm, M.; Hochmuth, H.; Lorenz, M.; Grundmann, M.; Schmidt, H.
Paramagnetism in Co-doped ZnO films
Journal of Physics D ***42**, 085001 (2009).*

53. Xu, Q.; Zhou, S.; Schmidt, B.; Mücklich, A.; Schmidt, H.
Paramagnetic Mn-implanted amorphous Si
Nuclear Instruments and Methods in Physics Research B ***267**, 3358 (2009).*

54. Xu, Q.; Zhou, S.; Schmidt, H.
Magnetic properties of ZnO nanopowders
Journal of Alloys and Compounds ***487**, 665 (2009).*

55. Ye, S.; Ney, V.; Kammermeier, T.; Ollefs, K.; Zhou, S.; Schmidt, H.; Wilhelm, F.; Rogalev, A.; Ney, A.
Absence of ferromagnetic-transport signatures in epitaxial paramagnetic and superparamagnetic $Zn_{0.95}Co_{0.05}O$ films
Physical Review B ***80**, 245321 (2009).*

56. Zhou, S.; Abrasonis, G.; Mücklich, A.; Potzger, K.; Faßbender, J.; Helm, M.; Schmidt, H.
Spin-dependent transport in hard superparamagnetic C:Ni nanocomposites
Proceedings of SPIE ***7364**, 736406 (2009).*

57. Zhou, S.; Berndt, M.; Bürger, D.; Heera, V.; Potzger, K.; Abrasonis, G.; Radnóczi, Gy.; Kovács, Gy. J.; Kolitsch, A.; Helm, M.; Faßbender, J.; Möller, W.; Schmidt, H.
Spin-dependent transport in nanocomposite C:Co films
Acta Materialia ***57**, 4758 (2009).*

58. Zhou, S.; Bürger, D.; Helm, M.; Schmidt, H.
Anomalous Hall resistance in Ge:Mn systems with low Mn concentrations
Applied Physics Letters ***95**, 172103 (2009).*

59. Zhou, S.; Cizmar, E.; Potzger, K.; Krause, M.; Talut, G.; Helm, M.; Faßbender, J.; Zvyagin, S. A.; Wosnitza, J.; Schmidt, H.
Origin of the ferromagnetism in defective TiO_2 single crystals
Physical Review B ***79**, 113201 (2009).*

60. Zhou, S.; Potzger, K.; Bürger, D.; Küpper, K.; Helm, M.; Faßbender, J.; Schmidt, H.
Inverse spinel $ZnFe_2O_4$ nanoparticles synthesized by ion implantation and post-annealing: An

investigation using X-ray spectroscopy and magneto-transport
Nuclear Instruments and Methods in Physics Research B ***267**, 1620 (2009).*

61. Zhou, S.; Potzger, K.; Xu, Q.; Küpper, K.; Talut, G.; Shalimov, A.; Mücklich, A.; Helm, M.; Faßbender, J.; Arenholz, E.; Schmidt, H.
Spinel ferrite nanocrystals embedded inside ZnO: Magnetic, electronic and magneto-transport properties
Physical Review B ***80**, 094409 (2009).*
Virtual Journal of Nanoscale Science and Technology ***20**, 14 (2009).*

62. Zhou, S.; Potzger, K.; Xu, Q.; Lorenz, M.; Skorupa, W.; Helm, M.; Faßbender, J.; Grundmann, M.; Schmidt, H.
Ferromagnetic transition metal implanted ZnO: A diluted magnetic semiconductor?
Vacuum ***83**, S13 (2009).*

63. Zhou, S.; Shalimov, A.; Potzger, K.; Helm, M.; Faßbender, J.; Schmidt, H.
$MnSi_{1.7}$ nanoparticles embedded in Si: Superparamagnetism with collective behaviour
Physical Review B ***80**, 174423 (2009).*

64. Zhou, S.; Shalimov, A.; Potzger, K.; Helm, M.; Faßbender, J.; Schmidt, H.
Memory effect of Mn_5Ge_3 nanomagnets embedded inside a Mn-diluted Ge matrix
Applied Physics Letters ***95**, 192505 (2009).*

65. Zhang, G.; Potzger, K.; Zhou, S.; Mücklich, A.; Ma, Y.; Faßbender, J.
Memory effect of magnetic nanoparticle systems originating from particle size distribution
Nuclear Instruments and Methods in Physics Research B ***267**, 1596 (2009).*

Nanostructures

66. Abrasonis, G.; Kovacs, Gy. J.; Mücklich, A.; Zhou, S. Q.; Babonneau, D.; Martinavicius, A.; Berndt, M.; Munnik, F.; Vinnichenko, M.; Heinig, K.-H.; Grenzer, J.; Kolitsch, A.; Schmidt, H.; Möller, W.
Substrate effects on the morphology of carbon encapsulated nickel nanoparticles grown by surface diffusion assisted phase separation
Journal of Physical Chemistry C ***113**, 8645 (2009).*

67. Batabyal, R.; Patra, S.; Roy, A.; Roy, S.; Bischoff, L.; Dev, B. N.
Estimation of diffusion coefficient by photoemission electron microscopy in ion-implanted nanostructures
Applied Surface Science ***256**, 536 (2009).*

68. Bauer, J.; Pietsch, U.; Davydok, A.; Biermanns, A.; Grenzer, J.; Gottschalch, V.; Wagner, G.
X-ray investigation of the interface structure of free standing InAs nanowires grown on GaAs[$\overline{111}$]$_B$
Applied Physics A ***96**, 851 (2009).*

69. Beyer, R.; Borany, J. von
Evidence of a thermally stimulated charge transfer mechanism and interface defect formation in metal-oxide-semiconductor structures with germanium nanocrystals
Journal of Applied Physics ***105**, 064513 (2009).*

70. Beyer, R.; Borany, J. von; Burghardt, H.
Interface and border trap relaxation in Si/SiO_2 structures with Ge nanocrystals examined by transient capacitance spectroscopy
Microelectronic Engineering ***86**, 1859 (2009).*

71. Beyer, V.; Schmidt, B.; Heinig, K.-H.; Stegemann, K.-H.
Light emitting field effect transistor with two self-aligned Si nanocrystal layers
Applied Physics Letters ***95**, 193501 (2009).*

72. Beyer, V.; Borany, J. von; Klimenkov, M.; Müller, T.
Current-voltage characteristics of metal-oxide-semiconductor devices containing Ge or Si nanocrystals in thin gate oxides
Journal of Applied Physics ***106**, 064505 (2009).*

73. Bischoff, L.; Schmidt, B.; Lange, H.; Donzev, D.
Nano-structures for sensors on SOI by writing FIB implantation and subsequent anisotropic wet chemical etching
Nuclear Instruments and Methods in Physics Research B ***267**, 1372 (2009).*

74. Chini, T. K.; Datta, D. P.; Lucchesi, U.; Mücklich, A.
Photoluminescence from Si: Effect of ripple microstructures induced by argon ion irradiation
Surface and Coatings Technology ***203**, 2690 (2009).*

75. Davydok, A.; Biermanns, A.; Pietsch, U.; Grenzer, J.; Pätzelt, H.; Gottschalch, V.; Bauer, J.
Submicron resolution X-ray diffraction from periodically patterned GaAs nanorods grown onto Ge[111]
Physica Status Solidi (A) ***206****, 1704 (2009).*

76. Dimitrakis, P.; Mouti, A.; Bonafos, C.; Schamm, S.; Ben Assayag, G.; Ioannou, V.; Schmidt, B.; Becker, J.; Normand, P.
Ultra-low energy ion beam synthesis of Ge nanocrystals in thin ALD Al_2O_3 layers for memory applications
Microelectronic Engineering ***86****, 1838 (2009).*

77. Gemming, S.; Seifert, G.; Bertram, N.; Fischer, T.; Götz, M.; Ganteför, G.
One-dimensional $(Mo_3S_3)_n$ clusters: Building blocks of clusters materials and ideal nanowires for molecular electronics
Chemical Physics Letters ***474****, 127 (2009).*

78. Grenzer, J.; Biermanns, A.; Mücklich, A.; Grigorian, S. A.; Pietsch, U.
Ripple structures on surfaces and underlying crystalline layers in ion beam irradiated Si wafers
Physica Status Solidi (A) ***206****, 1731 (2009).*

79. Järvi, T. T.; Pohl, D.; Albe, K.; Rellinghaus, B.; Schultz, L.; Faßbender, J.; Kuronen, A.; Nordlund, K.
From multiply twinned to fcc nanoparticles via irradiation-induced transient amorphization
Europhysics Letters ***85****, 26001 (2009).*

80. Keller, A.; Biermanns, A.; Carbone, G.; Grenzer, J.; Facsko, S.; Plantevin, O.; Gago, R.; Metzger, T. H.
Transition from smoothing to roughening of ion-eroded GaSb surfaces
Applied Physics Letters ***94****, 193103 (2009).*

81. Keller, A.; Cuerno, R.; Facsko, S.; Möller, W.
Anisotropic scaling of ripple morphologies on high-fluence sputtered silicon
Physical Review B ***79****, 115437 (2009).*

82. Keller, A.; Facsko, S.; Möller, W.
Evolution of ion-induced ripple patterns on SiO_2 surfaces
Nuclear Instruments and Methods in Physics Research B ***267****, 656 (2009).*

83. Krause, M.; Virsek, M.; Remskar, M.; Kolitsch, A.; Möller, W.
Diameter dependent Raman scattering of WS_2 nanotubes
Physica Status Solidi (B) ***246****, 2786 (2009).*

84. Krause, M.; Virsek, M.; Remskar, M.; Salacan, N.; Fleischer, N.; Chen, L.; Hatto, P.; Kolitsch, A.; Möller, W.
Diameter and morphology dependent Raman signatures of WS_2 nanostructures
ChemPhysChem ***10****, 2221 (2009).*

85. Krzyzanowska, H.; Kulik, M.; Zuk, J.; Rzodkiewicz, W.; Kobzev, A. P.; Skorupa, W.
Optical investigations of germanium nanoclusters - rich SiO_2 layers produced by ion beam synthesis
Journal of Non-Crystalline Solids ***355****, 1347 (2009).*

86. Kumar, M.; Chatterjee, R.; Milikisiyants, S.; Kanjilal, A.; Voelskow, M.; Grambole, D.; Lakshmi, K. V.; Singh, J. P.
Investigating the role of hydrogen in indium oxide tubular nanostructures as a donor or oxygen vacancy passivation center
Applied Physics Letters ***95****, 013102 (2009).*

87. Müller, C.; Leonhardt, A.; Kutz, M. C.; Büchner, B.; Reuther, H.
Growth aspects of iron-filled carbon nanotubes obtained by catalytic chemical vapor deposition of ferrocene
Journal of Physical Chemistry C ***113****, 2736 (2009).*

88. Odor, G.; Liedke, B.; Heinig, K.-H.
Mapping of 2+1 dimensional KPZ growth onto driven lattice gas model of dimmers
Physical Review E ***79****, 021125 (2009).*

89. Pécz, B.; Stoemenos, J.; Voelskow, M.; Skorupa, W.; Dobos, L.; Pongrácz, A.; Battistig, G.
Epitaxial 3C-SiC nanocrystal formation at the SiO_2/Si interface by combined carbon implantation and annealing in CO atmosphere
Journal of Applied Physics ***105****, 083508 (2009).*

90. Schmidt, B.; Heinig, K.-H.; Mücklich, A.; Akhmadaliev, C.
Swift-heavy-ion-induced shaping of spherical Ge nanoparticles into disks and rods
Nuclear Instruments and Methods in Physics Research B ***267****, 1345 (2009).*

91. Sule, P.; Heinig, K.-H.
The molecular dynamics simulation of ion-induced ripple growth
Journal of Chemical Physics ***131****, 204704 (2009).*

92. Virsek, M.; Krause, M.; Kolitsch, A.; Remskar, M.
Raman characterisation of MoS_2 microtube
Physica Status Solidi (B) ***246****, 2782 (2009).*

Microelectronic Materials

93. Alves, E.; Franco, N.; Barradas, N. P.; Munnik, F.; Monteiro, T.; Peres, M.; Wang, J.; Martins, R.; Fortunato, E.
Structural and optical properties of nitrogen doped ZnO films
Vacuum ***83****, 1274 (2009).*

94. Andreadou, A.; Pezoldt, J.; Förster, Ch.; Polychroniadis, E. K.; Voelskow, M.; Skorupa, W.
Buckling stabilization and stress reduction in SiC on Si by i-FLASiC processing
Materials Science Forum ***600-603****, 239 (2009).*

95. Baleva, M.; Zlateva, G.; Tsvetkova, T.; Balabanov, S.; Bischoff, L.
Vibrational spectra of silicon implanted polymethyl-methacrylate (PMMA) and poly-propylene (PP)
Journal of Optoelectronics and Advanced Materials ***11****, 1420 (2009).*

96. Baumgart, C.; Helm, M.; Schmidt, H.
Quantitative dopant profiling in semiconductors: A Kelvin probe force microscopy model
Physical Review B ***80****, 085305 (2009).*

97. Baumgart, C.; Schmidt, H.
Mikroskopische Aufnahmen neu gedeutet - Revolution in der Raster-Kelvin-Mikroskopie?
GIT Labor-Fachzeitschrift ***53****, 680 (2009).*

98. Bracht, H.; Schneider, S.; Klug, J. N.; Liao, C. Y.; Lundsgaard Hansen, J.; Haller, E. E.; Nylandsted Larsen, A.; Bougeard, D.; Posselt, M.; Wündisch, C.
Interstitial-mediated diffusion in germanium under proton irradiation
Physical Review Letters ***103****, 255501 (2009).*

99. Brauer, G.; Anwand, W.; Grambole, D.; Egger, W.; Sperr, P.; Beinik, I.; Wang, L.; Teichert, Ch.; Kuriplach, J.; Lang, J.; Zviagin, S.; Cizmar, E.; Ling, C. C.; Hsu, Y. F.; Xi, Y. Y.; Chen, X.; Djurisic, A. B.; Skorupa, W.
Characterization of ZnO nanostructures: A challenge to positron annihilation spectroscopy and other methods
Physica Status Solidi (C) ***6****, 2556 (2009).*

100. Brauer, G.; Anwand, W.; Grambole, D.; Grenzer, J.; Skorupa, W.; Cizek, J.; Kuriplach, J.; Prochazka, I.; Ling, C. C.; So, C. K.; Schulz, D.; Klimm, D.
Evidence for Zn vacancy – hydrogen complexes in ZnO single crystals
Physical Review B ***79****, 115212 (2009).*

101. Darakchieva, V.; Barradas, N. P.; Xie, M.-Y.; Lorenz, K.; Alves, E.; Schubert, M.; Persson, P. O. A.; Giuliani, F.; Munnik, F.; Hsiao, C. L.; Tu, L. W.; Schaff, W. J.
Role of impurities and dislocations for the unintentional n-type conductivity in InN
Physica B ***404****, 4476 (2009).*

102. Das Kanungo, P. ; Kögler, R.; Nguyen-Duc, K.; Zhakarov, N.; Werner, P.; Gösele, U.
Ex-situ n and p doping of vertical epitaxial short silicon nanowires by ion implantation
Nanotechnology ***20****, 165706 (2009).*

103. Fan, J. C.; Zhu, C. Y.; Fung, S.; Zhong, Y. C.; Wong, K. S.; Xie, Z.; Brauer, G.; Anwand, W.; Skorupa, W.; To, C. T.; Yang, B.; Beling, C. D.; Ling, C. C.
Arsenic doped p-type zinc oxide films grown by radio frequency magnetron sputtering
Journal of Applied Physics ***106****, 073709 (2009).*

104. Fitting, H.-J.; Fitting Kourkoutis, L.; Salh, R.; Schmidt, B.
EFTEM, EELS, and cathodoluminescence in Si-implanted SiO_2 layers
Microscopy and Microanalysis ***15****, 1104 (2009).*

105. Gao, F.; Xiao, H.; Posselt, M.; Weber, William J.
Defect-enhanced charge transfer by ion-solid interactions in SiC using large-scale ab initio molecular dynamics simulations
Physical Review Letters ***103****, 027405 (2009).*

106. Hellings, G.; Wündisch, C.; Eneman, G.; Simoen, E.; Clarysse, T.; Meuris, M.; Vandervorst, W.; Posselt, M.; de Meyer, K.
Implantation, diffusion, activation, and recrystallization of gallium implanted in preamorphized and

crystalline germanium
Electrochemical and Solid State Letters ***12****, H417 (2009).*

107. Herrmannsdörfer, T.; Heera, V.; Ignatchik, O.; Uhlarz, M.; Mücklich, A.; Posselt, M.; Reuther, H.; Schmidt, B.; Heinig, K.-H.; Skorupa, W.; Voelskow, M.; Wündisch, C.; Skrotzki, R.; Helm, M.; Wosnitza, J.
Superconducting state in a gallium-doped germanium layer at low temperatures
Physical Review Letters ***102****, 217003 (2009).*

108. Kube, R.; Bracht, H.; Chroneos, A.; Posselt, M.; Schmidt, B.
Intrinsic and extrinsic diffusion of indium in germanium
Journal of Applied Physics ***106****, 063534 (2009).*

109. Kups, Th.; Tonisch, K.; Voelskow, M.; Skorupa, W.; Konkin, A. L.; Pezoldt, J.
Structure and lattice location of Ge implanted 4H-SiC
Materials Science Forum ***600-603****, 623 (2009).*

110. Kuriplach, J.; Brauer, G.; Melikhova, O.; Čížek, J.; Procházka, I.; Anwand, W.; Skorupa, W.
Vacancy-hydrogen complexes in ZnO
Materials Science Forum ***607****, 117 (2009).*

111. Leisegang, T.; Stöcker, H.; Levin, A. A.; Weißbach, T.; Zschornak, M.; Gutmann, E.; Rickers, K.; Gemming, S.; Meyer, D. C.
Switching Ti valence in $SrTiO_3$ by a dc electric field
Physical Review Letters ***102****, 087601 (2009).*

112. Lubk, A.; Gemming, S.; Spaldin, N. A.
First-principles study of ferroelectric domain walls in multiferroic bismuth ferrite
Physical Review B ***80****, 104110 (2009).*

113. Morawetz, K.; Gemming, S.; Luschtinetz, R.; Kunze, T.; Lipavský, P.; Eng, L. M.; Seifert, G.; Milde, P.; Pankoke, V.
Transport and noise in organic field effect devices
Physical Review B ***79****, 1 (2009).*

114. Novak, P.; Chaplygin, I.; Seifert, G.; Gemming, S.; Laskowski, R.
Ab-initio calculation of exchange interactions in $YMnO_3$
Computational Materials Science ***44****, 79 (2008).*

115. Ou, X.; Kögler, R.; Skorupa, W.; Möller, W.; Wang, X.; Gerlach, J. W.
Gettering layer for oxygen accumulation in the initial stage of SIMOX processing
Nuclear Instruments and Methods in Physics Research B ***267****, 1273 (2009).*

116. Ou, X.; Kögler, R.; Skorupa, W.; Möller, W.; Wang, X.; Vines, L.
The use of nanocavities for the fabrication of ultrathin buried oxide layers
Applied Physics Letters ***94****, 011903 (2009).*

117. Pankoke, V.; Gemming, S.
Binding properties between ferroic oxides and metals
European Physical Journal B ***67****, 57 (2009).*

118. Pantchev, B.; Danesh, P.; Schmidt, B.; Grambole, D.; Möller, W.
Ion beam-induced hydrogen migration in a SiO_2/a-Si:H/SiO_2 layer stack
Semiconductor Science and Technology ***24****, 035012 (2009).*

119. Peyre, H.; Pezoldt, J.; Voelskow, M.; Skorupa, W.; Camassel, J.
SIMS investigation of $Ge_x(4H\text{-}SiC)_{1-x}$ solid solutions synthesized by Ge-ion implantation up to $x = 0.2$
Materials Science Forum ***615-617****, 465 (2009).*

120. Posselt, M.; Gabriel, A.
Atomistic simulation of amorphous germanium and its solid phase epitaxial recrystallization
Physical Review B ***80****, 045202 (2009).*

121. Posselt, M.; Gao, F.; Bracht, H.
Correlation between self-diffusion in Si and the migration mechanisms of vacancies and self-interstitials: An atomistic study
Physical Review B ***79****, 119901(E) (2009).*

122. Riedl, T.; Gemming, T.; Weissbach, T.; Seifert, G.; Gutmann, E.; Zschornak, M.; Meyer, D. C.; Gemming, S.
ELNES study of chemical solution deposited $SrO(SrTiO_3)_n$ Ruddlesden-Popper films: Experiment and simulation
Ultramicroscopy ***110****, 26 (2009).*

123. Roushdey, S.; Kourkoutis, L.; Zamoryanskaya, M. V.; Schmidt, B.; Fitting, H.-J.
Ion implantation, luminescence, and cluster growth in silica layers
*Journal of Non-Crystalline Solids **355**, 1107 (2009).*

124. Salh, R.; Fitting-Kourkoutis, L.; Zamoryanskaya, M. V.; Schmidt, B.; Fitting, H.-J.
Ion implantation and cluster formation in silica
*Superlattices and Microstructures **45**, 362 (2009).*

125. Sarov, Y.; Frank, A.; Ivanov, T.; Zöllner, J.-P.; Ivanova, K.; Volland, B.; Rangelow, I. W.; Brogan, A.; Wilson, R.; Zawierucha, P.; Zielony, M.; Gotszalk, T.; Nikolov, N.; Zier, M.; Schmidt, B.; Kostic, I.
Parallel proximal probe arrays with vertical interconnections
*Journal of Vacuum Science and Technology B **27**, 3132 (2009).*

126. Schmidt, M.; Ellguth, M.; Czekalla, C.; von Wenckstern, H.; Pickenhain, R.; Grundmann, M.; Brauer, G.; Skorupa, W.; Helm, M.; Gu, Q.; Ling, C. C.
Defects in zinc-implanted ZnO thin films
*Journal of Vacuum Science and Technology B **27**, 1597 (2009).*

127. Schmidt-Grund, R.; Rheinländer, B.; Kaidashev, E. M.; Lorenz, M.; Fritsch, D.; Schubert, M.; Schmidt, H.; Herzinger, C. M.
Vacuum ultraviolet dielectric function and band structure of ZnO
*Journal of the Korean Physical Society **53**, 88 (2008).*

128. Seidel, J.; Martin, L. W.; He, Q.; Zhan, Q.; Chu, Y.-H.; Rother, A.; Hawkridge, M. E.; Maksymovych, P.; Yu, P.; Gajek, M.; Balke, N.; Kalinin, S. V.; Gemming, S.; Wang, F.; Catalán, G.; Scott, J. F.; Spaldin, N. A.; Orenstein, J.; Ramesh, R.
Conduction at domain walls in oxide multiferroics
*Nature Materials **8**, 229 (2009).*

129. Thieme, M. B.; Gemming, S.
Elastic properties and electronic structure of vanadium silicides - a density functional investigation
*Acta Materialia **57**, 50 (2009).*

130. Tyschenko, I. E.; Voelskow, M.; Cherkov, A. G.; Popov, V. P.
Endotaxial growth of InSb nanocrystals at the bonding interface of the In^+ and Sb^+ ion implanted SOI structure
*Nuclear Instruments and Methods in Physics Research B **267**, 1360 (2009).*

131. Tyschenko, I. E.; Voelskow, M.; Cherkov, A. G.; Popov, V. P.
Nanometer-thick SGOI structures produced by Ge^+ ion implantation of SiO_2 film and subsequent hydrogen transfer of Si layer
*Nuclear Instruments and Methods in Physics Research B **267**, 1277 (2009).*

132. Tyschenko, I. E.; Voelskow, M.; Cherkov, A. G.; Popov, V. P.
Growth and electrical properties of the (Si/Ge)-on-insulator structures formed by ion implantation and subsequent hydrogen-assisted transfer
*Fizika i Tekhnika Poluprovodnikov **43**, 58 (2009).*
*Semiconductors **43**, 52 (2009).*

133. Voelskow, M.; Pécz, B.; Stoemenos, J.; Skorupa, W.
Epitaxial 3C-SiC nanocrystal formation at the SiO_2/Si interface after carbon implantation and annealing in CO atmosphere
*Nuclear Instruments and Methods in Physics Research B **267**, 1364 (2009).*

134. Voelskow, M.; Pezoldt, J.; Kups, T.; Skorupa, W.
Controlled localised melting in silicon by high dose germanium implantation and flash lamp annealing
*Nuclear Instruments and Methods in Physics Research B **267**, 1269 (2009).*

135. Wenckstern, H. von; Schmidt, H.; Brandt, M.; Lajn, A.; Pickenhain, R.; Lorenz, M.; Grundmann, M.; Hofmann, D.; Polity, A.; Meyer, B. K.; Saal, H.; Binnewies, M.; Börger, A.; Becker, K.-D.; Tikhomirov, V. A.; Jug, K.
Anionic and cationic substitution in ZnO
*Progress in Solid State Chemistry **37**, 153 (2009).*

136. Wündisch, C.; Posselt, M.; Schmidt, B.; Heera, V.; Schumann, T.; Mücklich, A.; Grötzschel, R.; Skorupa, W.; Clarysse, T.; Simoen, E.; Hortenbach, H.
Millisecond flash lamp annealing of shallow implanted layers in Ge
*Applied Physics Letters **95**, 252107 (2009).*

137. Zatsepin, A. F.; Fitting, H.-J.; Kortov, V. S.; Pustovarov, V. A.; Schmidt, B.; Buntov, E. A.
Photosensitive defects in silica layers implanted with germanium ions
*Journal of Non-Crystalline Solids **355**, 61 (2009).*

138. Zuk, J.; Romanek, J.; Skorupa, W.
Micro-Raman depth profile investigations of beveled Al^+-ion implanted 6H-SiC samples
Nuclear Instruments and Methods in Physics Research B ***267****, 1251 (2009).*

Optoelectronic Materials

139. Bregolin, F.; Behar, M.; Sias, U.; Reboh, S.; Lehmann, J.; Rebohle, L.; Skorupa, W.
Electroluminescence induced by Ge nanocrystals obtained by hot ion implantation into SiO_2
Journal of Applied Physics ***106****, 106103 (2009).*

140. Chandramohan, S.; Kanjilal, A.; Sarangi, S. N.; Majumder, S.; Sathyamoorthy, R.; Som, T.
Implantation-assisted Co-doped CdS thin films: Structural, optical, and vibrational properties
Journal of Applied Physics ***106****, 063506 (2009).*

141. Chandramohan, S.; Kanjilal, A.; Strache, T.; Tripathi, J. K.; Sarangi, S. N.; Sathyamoorthy, R.; Som, T.
Modifications in structural and optical properties of Mn-ion implanted CdS thin films
Applied Surface Science ***256****, 465 (2009).*

142. Chandramohan, S.; Kanjilal, A.; Tripathi, J. K.; Sarangi, S. N.; Sathyamoorthy, R.; Som, T.
Structural and optical properties of Mn-doped CdS thin films prepared by ion implantation
Journal of Applied Physics ***105****, 123507 (2009).*

143. Cherkouk, C.; Rebohle, L.; Skorupa, W.; Strache, T.; Reuther, H.; Helm, M.
Spraying spin coating silanization at room temperature of a SiO_2 surface for silicon-based integrated light emitters
Journal of Colloid and Interface Science ***337****, 375 (2009).*

144. Drachenko, O.; Kozlov, D. V.; Aleshkin, V. Ya.; Gavrilenko, V. I.; Maremyanin, K. V.; Ikonnikov, A. V.; Zvonkov, B. N.; Goiran, M.; Leotin, J.; Fasching, G.; Winnerl, S.; Schneider, H.; Wosnitza, J. Sc; Helm, M.
High-field splitting of the cyclotron resonance absorption in strained p-InGaAs/GaAs quantum wells
Physical Review B ***79****, 073301 (2009).*

145. Golde, D.; Wagner, M.; Stehr, D.; Schneider, H.; Helm, M.; Andrews, A. M.; Roch, T.; Strasser, G.; Kira, M.; Koch, S. W.
Fano signatures in the intersubband terahertz response of optically excited semiconductor quantum wells
Physical Review Letters ***102****, 127403 (2009).*

146. Hudert, F.; Bruchhausen, A.; Issenmann, D.; Schecker, O.; Waitz, R.; Erbe, A.; Scheer, E.; Dekorsy, Th.; Mlayah, A.; Huntzinger, J.-R.
Confined longitudinal acoustic phonon modes in free-standing Si membranes coherently excited by femtosecond laser pulses
Physical Review B ***79****, 201307 (2009).*

147. Kanjilal, A.; Rebohle, L.; Baddela, N. K.; Zhou, S.; Voelskow, M.; Skorupa, W.; Helm, M.
Probing the impact of microstructure on the electroluminescence properties of Ge-nanocrystal enriched Er-doped SiO_2 layers
Physical Review B ***79****, 161302 (2009).*

148. Kanjilal, A.; Rebohle, L.; Prucnal, S.; Voelskow, M.; Skorupa, W.; Helm, M.
Temperature dependence of the crossover between the near-infrared Er and defect-related photoluminescence bands of Ge-rich Er-doped SiO_2 layers
Physical Review B ***80****, 241313 (2009).*

149. Kanjilal, A.; Rebohle, L.; Skorupa, W.; Helm, M.
Correlation between the microstructure and electroluminescence properties of Er-doped metal-oxide semiconductor structures
Applied Physics Letters ***94****, 101916 (2009).*

150. Kanjilal, A.; Rebohle, L.; Voelskow, M.; Skorupa, W.; Helm, M.
Enhanced blue-violet emission by inverse energy transfer to the Ge-related oxygen deficiency centers via Er^{3+} ions in metal-oxide semiconductor structures
Applied Physics Letters ***94****, 051903 (2009).*

151. Kanjilal, A.; Rebohle, L.; Voelskow, M.; Skorupa, W.; Helm, M.
Defect-engineered blue-violet electroluminescence from Ge nanocrystal rich SiO_2 layers by Er doping
Journal of Applied Physics ***106****, 026104 (2009).*

152. Kanjilal, A.; Tsushima, S.; Götz, C.; Rebohle, L.; Voelskow, M.; Skorupa, W.; Helm, M.
The role of Ge-related oxygen-deficiency centers in controlling the blueviolet photo- and electroluminescence in Ge-rich SiO_2 via Er doping
Journal of Applied Physics ***106****, 063112 (2009).*

153. Nazarov, A. N.; Tyagulskii, I. P.; Tyagulskii, S. I.; Rebohle, L.; Skorupa, W.; Biskupek, J.; Kaiser, U.
Correlation between electroluminescence and charge trapping in multi-color Eu-implanted Si-based light-emitting diodes
*Physica E **41**, 902 (2009).*

154. Patanè, A.; Feu, W. H. M.; Makarovsky, O.; Drachenko, O.; Eaves, L.; Krier, A.; Zhuang, Q. D.; Helm, M.; Goiran, M.; Hill, G.
Effect of low nitrogen concentrations on the electronic properties of $InAs_{1-x}N_x$
*Physical Review B **80**, 115207 (2009).*

155. Prucnal, S.; Rebohle, L.; Kanjilal, A.; Krzyzanowska, H.; Skorupa, W.
White electroluminescence from a gadolinium doped Si nanocluster enriched SiO_2-SiON interface region
*Electrochemical and Solid State Letters **12**, H333 (2009).*

156. Prucnal, S.; Rebohle, L.; Skorupa, W.
Electroluminescence (at 316 nm) and electrical stability of a MOS light-emitting device operated at different temperatures
*Applied Physics B **94**, 289 (2009).*

157. Prucnal, S.; Wójtowicz, A.; Pyszniak, K.; Drozdziel, A.; Zuk, J.; Turek, M.; Rebohle, L.; Skorupa, W.
Defect engineering in the MOSLED structure by the ion implantation
*Nuclear Instruments and Methods in Physics Research B **267**, 1311 (2009).*

158. Rebohle, L.; Cherkouk, C.; Prucnal, S.; Helm, M.; Skorupa, W.
Rare earth implanted Si-based light emitters and their use for smart biosensor applications
*Vacuum **83**, S24 (2009).*

159. Rebohle, L.; Lehmann, J.; Kanjilal, A.; Prucnal, S.; Nazarov, A.; Tyagulskii, I.; Skorupa, W.; Helm, M.
The correlation between electroluminescence properties and the microstructure of Eu-implanted MOS light emitting devices
*Nuclear Instruments and Methods in Physics Research B **267**, 1324 (2009).*

160. Rebohle, L.; Lehmann, J.; Prucnal, S.; Nazarov, A.; Tyagulskii, I.; Tyagulskii, S.; Kanjilal, A.; Voelskow, M.; Grambole, D.; Skorupa, W.; Helm, M.
Anomalous wear-out phenomena of Europium-implanted light emitters based on a metal–oxide-semiconductor structure
*Journal of Applied Physics **106**, 123103 (2009).*

161. Schneider, H.; Liu, H. C.; Winnerl, S.; Drachenko, O.; Helm, M.; Walther, M.; Faist, J.
Quadratic detection with two-photon quantum well infrared photodetectors
*Infrared Physics and Technology **52**, 419 (2009).*

162. Schneider, H.; Liu, H. C.; Winnerl, S.; Song, C. Y.; Walther, M.; Helm, M.
Terahertz two-photon quantum well infrared photodetector
*Optics Express **17**, 12279 (2009).*

163. Stehr, D.; Morris, C. M.; Talbayev, D.; Wagner, M.; Kim, H. C.; Taylor, A. J.; Schneider, H.; Petroff, P. M.; Sherwin, M. S.
Ultrafast carrier capture in InGaAs quantum posts
*Applied Physics Letters **95**, 251105 (2009).*

164. Tsvetkova, T.; Balabanov, S.; Avramov, L.; Borisova, E.; Angelov, I.; Sinning, S.; Bischoff, L.
Photoluminescence enhancement in Si^+ implanted PMMA
*Vacuum **83**, S252 (2009).*

165. Tyagulskiy, S.; Tyagulskyy, I.; Nazarov, A.; Lysenko, V.; Rebohle, L.; Lehmann, J.; Skorupa, W.
Electroluminescence, charge trapping and quenching in Eu implantes SiO_2-Si structures
*Microelectronic Engineering **86**, 1954 (2009).*

166. Wagner, M.; Golde, D.; Stehr, D.; Schneider, H.; Helm, M.; Andrews, A. M.; Roch, T.; Strasser, G.; Kira, M.; Koch, S. W.
Fano profile in the intersubband THz response of photoexcited GaAs/AlGaAs quantum wells
*Journal of Physics: Conference Series **193**, 012073 (2009)*

167. Wagner, M.; Schneider, H.; Winnerl, S.; Helm, M.; Roch, T.; Andrews, A. M.; Schartner, S.; Strasser, G.
Resonant enhancement of second order sideband generation for intraexcitonic transitions in GaAs/AlGaAs multiple quantum wells
*Applied Physics Letters **94**, 241105 (2009).*

168. Wang, C. Y.; Kuznetsova, L.; Gkortsas, V. M.; Diehl, L.; Kärtner, F. X.; Belkin, M. A.; Belyanin, A.; Li, X.; Ham, D.; Schneider, H.; Grant, P.; Song, C. Y.; Haffouz, S.; Wasilewski, Z. R.; Liu, H. C.; Capasso, F.

Mode-locked pulses from mid-infrared quantum cascade lasers
Optics Express ***17**, 12929 (2009).*

169. Winnerl, S.; Zimmermann, B.; Peter, F.; Schneider, H.; Helm, M.
Terahertz Bessel-Gauss beams of radial and azimuthal polarization from microstructured photoconductive antennas
Optics Express ***17**, 1571 (2009).*

170. Zibik, E. A.; Grange, T.; Carpenter, B. A.; Porter, N. E.; Ferreira, R.; Bastard, G.; Stehr, D.; Winnerl, S.; Helm, M.; Liu, H. Y.; Skolnick, M. S.; Wilson, L. R.
Long lifetimes of quantum-dot intersublevel transitions in the terahertz range
Nature Materials ***8**, 803 (2009).*

Others

171. Abd El-Al, S.; Korman, A.; Stonert, A.; Munnik, F.; Turos, A.
Ion beam analysis of ancient Egyptian wall paintings
Vacuum ***83**, S4 (2009).*

172. Barlak, M.; Piekoszewski, J.; Werner, Z.; Stanislawski, J.; Skladnik-Sadowska, E.; Borkowska, K.; Miskiewicz, M.; Kolitsch, A.; Grötzschel, R.; Starosta, W.; Sartowska, B.; Kierzek, J.
Wettability improvement of carbon ceramic materials by mono- and multi-energy plasma pulses
Surface and Coatings Technology ***203**, 2536 (2009).*

173. Chen, T.; Yao, S.; Hua, W.; Fa, T.; Li, L.; Zhou, S.
Charge transport and magnetotransport properties of polyimide irradiated by 80 keV Co ions
Chinese Physics Letters ***26**, 087201 (2009).*

174. Chen, T.; Yao, S.; Wang, K.; Wang, H.; Zhou, S.
Modification of the electrical properties of polyimide by irradiation with 80 keV Xe ions
Surface and Coatings Technology ***203**, 3718 (2009).*

175. Cizek, J.; Procházka, I.; Daniš, S.; Brauer, G.; Anwand, W.; Gemma, R.; Nikitin, E.; Kirchheim, R.; Pundt, A.; Islamgaliev, R. K.
Hydrogen-vacancy complexes in electron-irradiated niobium
Physical Review B ***79**, 054108 (2009).*

176. Constantinescu, B.; Bugoi, R.; Cojocaru, V.; Simon, R.; Grambole, D.; Munnik, F.; Oberländer-Târnoveanu, E.
Elemental analysis through X-ray techniques applied in archeological gold authentication — the case of Transylvanian gold and of the Dacian bracelets
Spectrochimica Acta B ***64**, 1198 (2009).*

177. Dekov, V. M.; Arnaudov, V.; Munnik, F.; Boycheva, T. B.; Fiore, S.
Native aluminum: Does it exist?
American Mineralogist ***94**, 1283 (2009).*

178. Dekov, V. M.; Hålenius, U.; Billström, K.; Kamenov, G. D.; Munnik, F.; Eriksson, L.; Dyer, A.; Schmidt, M.; Botz, R.
Native Sn-Pb droplets in a zeolitic amygdale (Isle of Mull, Inner Hebrides)
Geochimica et Cosmochimica Acta ***73**, 2907 (2009).*

179. Geissler, A.; Merroun, M.; Geipel, G.; Reuther, H.; Selenska-Pobell, S.
Biogeochemical changes induced in uranium mining waste pile samples by uranyl nitrate treatments under anaerobic conditions
Geobiology ***7**, 282 (2009).*

180. Gemming, S.; Kunze, T.; Morawetz, K.; Pankoke, V.; Luschtinetz, R.; Seifert, G.
The role of homophase and heterophase interfaces on transport properties in structured material
European Physical Journal - Special Topics ***177**, 83 (2009).*

181. González-Posada Flores, F.; Redondo-Cubero, A.; Gago, R.; Bengoechea, A.; Jiménez, A.; Grambole, D.; Braña, A. F.; Muñoz, E.
High-resolution hydrogen profiling in AlGaN/GaN heterostructures grown by different epitaxial methods
Journal of Physics D: Applied Physics ***42**, 055406 (2009).*

182. Heintze, C.; Recknagel, C.; Bergner, F.; Hernández-Mayoral, M.; Kolitsch, A.
Ion-irradiation-induced damage of steels characterized by means of nanoindentation
Nuclear Instruments and Methods in Physics Research B ***267**, 1505 (2009).*

183. Kavan, L.; Janda, P.; Krause, M.; Ziegs, F.; Dunsch, L.
A rotating cell for in situ Raman spectroelectrochemical studies of photosensitive redox systems
*Analytical Chemistry **81**, 2017 (2009).*

184. Kolacek, J.; Lipavský, P.; Morawetz, K.; Brandt, E. H.
Boundary condition for Ginzburg-Landau theory of superconducting layers
*Physical Review B **79**, 174510 (2009).*

185. Krause-Rehberg, R.; Anwand, W.; Brauer, G.; Butterling, M.; Cowan, T.; Jungmann, M.; Krille, A.; Schwengner, R.; Wagner, A.
Progress of the EPOS project: Gamma-induced positron spectroscopy (GiPS)
*Physica Status Solidi (C) **6**, 2451 (2009).*

186. Kundin, J.; de Cuba, M. R.; Emmerich, H.; Gemming, S.
Two-scale modeling of adsorption processes at structured surfaces
*Physica D **238**, 117 (2009).*

187. Lebelt, P.; Gehrke, J.; Hallmeier, K.-H.; Reuther, H.; Dörfel, I.
Qualitative und quantitative Analysen dünner Funktionsschichten für das Kleben durch XPS-, AES-, REM- und TEM-Untersuchungen
*Galvanotechnik **100**, 930 (2009).*

188. Markov, A. B.; Reuther, H.; Shevchenko, N.
Polishing of titanium and enhancing the wear resistance of the titanium alloys with a low-energy high-current electron beam
*Isvestia VUZov Fizika **8**, 425 (2009).*

189. Mazarov, P.; Wieck, A. D.; Bischoff, L.; Pilz, W.
Alloy liquid metal ion source for carbon focused ion beams
*Journal of Vacuum Science and Technology B **27**, L47 (2009).*

190. Melikhova, O.; Cizek, J.; Prochazka, I.; Kuriplach, J.; Lukac, F.; Cieslar, M.; Brauer, G.; Anwand, W.
Quenched-in vacancies in Fe-Al alloys
*Physica Status Solidi (C) **6**, 2367 (2009).*

191. Melikhova, O.; Kuriplach, J.; Cizek, J.; Prochazka, I.; Brauer, G.
Structure and positron characteristics of basic open volume defects in zirconia
*Materials Science Forum **607**, 125 (2009).*

192. Mello, C. B.; Ueda, M.; Silva, M. M.; Reuther, H.; Pichon, L.; Lepienski, C. M.
Tribological effects of plasma immersion ion implantation heating treatments on Ti-6Al-4V alloy
*Wear **267**, 867 (2009).*

193. Morawetz, K.; Lipavsky, P.; Mares, J. J.
Discontinuity of capacitance at the onset of surface superconductivity
*New Journal of Physics **11**, 1 (2009).*

194. Oliveira, R. M.; Ueda, M.; Silva, L. L. G.; Reuther, H.; Lepienski, C. M.
Characteristics of austenitic stainless steel nitrided in a hybrid glow discharge plasma
*Brazilian Journal of Physics **39**, 554 (2009).*

195. Oswald, S.; Hermanna, R.; Schmidt, B.
SIMS measurement of oxygen content in γ-TiAl single crystals and polycrystalline alloys with Nb addition
*Materials Science and Engineering A **516**, 54 (2009).*

196. Preoteasa, E. A.; Preoteasa, E.; Kuczumow, A.; Gurban, D.; Harangus, L.; Grambole, D.; Herrmann, F.
Broad-beam PIXE and μ-PIXE analysis of normal and in vitro demineralized dental enamel
*X-Ray Spectrometry **37**, 517 (2008).*

197. Vasilescu, A.; Constantinescu, B.; Bugoi, R.; Ceccato, D.; Grambole, D.; Herrmann, F.
Micro-elemental analysis of some transylvanian meteorites and lunar samples
*Nuclear Instruments and Methods in Physics Research B **267**, 2233 (2009).*

198. Wang, T. S.; Lv, H. Y.; Grambole, D.; Yang, Z.; Peng, H. B.; Han, Y. C.
Hydrogen micro-kinetics in titanium under mechanical stress studied by ion beam analysis
*Journal of Nuclear Materials **386**, 214 (2009).*

199. Zharnylskaya, A. L.; Volkhin, V. V.; Shcherban, M. G.; Reuther, H.
Synthesis of a precursor for an alumina ceramic reinforced by zirconium dioxide from inorganic compounds in the presence of urea
*Zhurnal Prikladnoi Khimii **81**, 1069 (2008).*
*Russian Journal of Applied Chemistry **81**, 1147 (2008).*

200. Zharnylskaya, A. L.; Volkhin, V. V.; Reuther, H.
Effect of the nature of anions of aluminum salts used to synthesize a precursor of the Al_2O_3-ZrO_2 ceramics on the stabilization of the tetragonal modification of zirconium dioxide
Zhurnal Prikladnoi Khimii ***82****, 1268 (2009).*
Russian Journal of Applied Chemistry ***82****, 1364 (2009)*

Invited Conference Talks

1. Abrasonis, G.
Surface diffusion assisted phase separation during the growth of carbon:transition metal nanocomposite thin films
2nd Plasma-Nano International Workshop at Australia's Commonwealth Scientific and Industrial Research Organisation (CSIRO), 9.02.2009, Lindfield, Australia

2. Brauer, G.; Anwand, W.; Grambole, D.; Egger, W.; Sperr, P.; Beynik, I.; Hofer, C.; Teichert, C.; Kuriplach, J.; Lang, J.; Zviagin, S.; Cizmar, E.; Ling, C. C.; Hsu, Y. F.; Xi, Y. Y.; Djurisic, A. B.; Skorupa, W.
Characterization of ZnO nanostructures: A challenge to positron annihilation spectroscopy and other methods
15th International Conference on Positron Annihilation, 18.-23.01.2009, Kolkata, India

3. Facsko, S.; Ranjan, M.; Keller, A.; Oates, T. W. H.; Rosen, J.
Self-aligned metal nanoparticles and nanowires grown on ripple-templates
MRS 2009 Fall Meeting, Symposium "Nanosclae Pattern Formation", 30.11.-4.12.2009, Boston MA, USA

4. Faßbender, J.
Engineering surfaces, interfaces and structural phases to tailor magnetic properties
Gaede-Preis-Vortrag, Frühjahrstagung der Deutschen Physikalischen Gesellschaft, 24.03.2009, Dresden, Germany

5. Faßbender, J.; Liedke, M. O.; Strache, T.; Marko, D.; Lenz, K.; Keller, A.; Facsko, S.; Tibus, S.; Springer, F.; Albrecht, M.; Rohrmann, H.
Periodically modulated surfaces and interfaces: Introducing artificial length scales to tailor magnetic properties
MRS 2009 Spring Meeting, Symposium "Ion Beams and Nano-Engineering", 13.-17.04.2009, San Francisco, USA
6. *2nd International Conference on Physics at Surfaces and Interfaces, 23.-27.02.2009, Puri, Orissa, India*

7. Faßbender, J.
Nanomagnets - Created and tailored by ions
International Seminar and Workshop on Magnonics: From Fundamentals to Applications, 2.-7.08.2009, Dresden, Germany
8. *International Workshop "Nanoscale Modification of Surfaces and Thin Films", 30.08.-3.09.2009, Rathen, Germany*

9. Faßbender, J.; Liedke, M. O.; Körner, M.; Markó, D.; Lenz, K.; Facsko, S.
Ion-erosion-induced pattern as template for layers with magnetic anisotropy and coupling
MRS 2009 Fall Meeting, Symposium "Nanosclae Pattern Formation" 30.11.-4.12.2009, Boston MA, USA

10. Gemming, S.
First-principles investigation of metal/oxide contacts and related metal/group-IV interfaces
CECAM-Workshop on Metal-Ceramic Interfaces, 20.-22.07.2009, Zürich, Switzerland

11. Heinig, K.-H.
Fundamentals of ion beam synthesis of nanostructures
12. **Formation of nanodots, nanowires, wormholes etc. driven by capillary forces-reaction pathways predicted by atomistic simulations**
13. **Spontaneous formation of regular nanopattern on surfaces during thin film deposion and ion beam erosion**
3 Talks given at Winter School on Nanoelectronics and Nanophotonics, 19.-25.01.2009, Ankara, Turkey

14. Heinig, K.-H.; Beyer, V.; Schmidt, B.; Stegemann, K.-H.
Novel LEFET with two self-aligned Si nanocrystal layers
Workshop on Nanoelectronics and Nanophotonics, 26.-28.01.2009, Ankara, Turkey

15. Heinig, K.-H.; Liedke, B.; Numazawa, S.; Ranjan, M.; Möller, W.; Facsko, S.
Ion-beam-assisted nanostructure formation – Atomistic reaction pathways
International Conference on Ion-Surface Interactions 2009, 21.-25.08.2009, Zvenigorod, Russia

16. Heinig, K.-H.; Schmidt, B.; Vredenberg, A.; Polman, A.; Toulemonde, M.
Shaping of Au and Ge nanoparticles in SiO_2 with swift heavy ions
International Workshop on Nanostructures in Silica, 6.-9.09.2009, Ivalo, Finland

17. Kosmata, M.; Grötzschel, R.; Munnik, F.; Vieluf, M.; Möller, W.
Quantitative ion beam analysis of ultra thin films with magnetic spectrometers using heavy MeV ions
5th International Workshop on High-Resolution Depth Profiling, 15.-19.11.2009, Kyoto, Japan

18. Leiderer, P.; Erbe, A.
Colloids: Mesoscopic model systems of matter on a nano scale
Juelich Soft Matter Days 2009, 10.-13.11.2009, Bonn, Germany

19. Lorenz, K.; Magalhães, S.; Franco, N.; Darakchieva, V.; Barradas, N. P.; Alves, E.; Pereira, S.; Correia, M. R.; Munnik, F.; Martin, R. W.; O'Donnell, K. P.; Watson, I. M.
$Al_{1-x}In_xN$/GaN bilayers: Structure, morphology and optical properties
International Conference on Nitride Semiconductors, 18.-23.10.2009, JeJu, South Korea

20. McCord, J.; Hamann, C.; Martin, N.; Mönch, I.; Kaltofen, R.; Schultz, L.; Strache, T.; Faßbender, J.; Mattheis, R.
Static and dynamic magnetization processes in magnetic property patterned thin films
International Magnetics Conference, 4.-8.05.2009, Sacramento, USA

21. McCord, J.; Faßbender, J.
Designing soft magnetic materials by ion irradiation
18th International Materials Research Congress, 16.-20.08.2009, Cancun, Mexiko

22. Posselt, M.; Wündisch, C.; Schmidt, B.; Schumann, T.; Mücklich, A.; Skorupa, W.; Clarysse, T.; Simoen, E.; Hortenbach, H.
Millisecond flash lamp annealing of ultra-shallow implanted layers in Ge
216th Meeting of the Electrochemical Society, Symposium "ULSI Process Integration", 4.-9.10.2009, Vienna, Austria

23. Schneider, H.; Liu, H. C.; Maier, T.; Walther, M.
Two-photon photocurrent spectroscopy of quantum well intersubband relaxation and dephasing
SPIE Photonics West, 24.-29.01.2009, San Jose CA, USA

24. Schneider, H.; Liu, H. C.; Winnerl, S.; Drachenko, O.; Helm, M.; Walther, M.; Faist, J.
Resonant two-photon transitions, quadratic detection, and photocurrent autocorrelation using multiple quantum wells
SPIE Photonics West, 24.-29.01.2009, San Jose CA, USA

25. Schneider, H.
Quantum well infrared photodetectors for dual-band thermal imaging and two-photon detection
3rd International Symposium on Photoelectronic Detection and Imaging, 17.-19.06.2009, Beijing, China

26. Schneider, H.; Winnerl, S.; Drachenko, O.; Helm, M.; Liu, H. C.; Song, C.; Maier, T.; Walther, M.; Faist, J.
Two-photon intersubband transition physics and detectors
10th International Conference on Intersubband Transitions in Quantum Wells, 6.-11.09.2009, Montréal, Canada

27. Skorupa, W.
Nanostructuring of semiconductors with ion beams
LENS 2009 Summer School, 11.-14.06.2009, Reykjavik, Iceland

28. Skorupa, W.
Advances in Si & Ge millisecond processing: From silicon-on-insulator to superconducting Ge
17th IEEE International Conference on Advanced Thermal Processing of Semiconductors, 29.09.-2.10.2009, Albany NY, USA

29. Sort, J.; Menendez, E.; Varea, A.; Pi, F.; Surinach, S.; Baro, M. D.; Nogues, J.
Nanoscale magnetic lithography on FeAl alloys by ion irradiation and nanoindentation
International Conference on Advanced Materials, 20.-25.09.2009, Rio de Janeiro, Brazil

30. Stehr, D.; Wagner, M.; Schneider, H.; Helm, M.; Andrews, A. M.; Roch, T.; Strasser, G.
Two color pump-probe studies of intraminiband relaxation in doped GaAs/AlGaAs superlattices
SPIE Photonics West, 24.-29.01.2009, San Jose CA, USA

31. Vinnichenko, M.; Cornelius, S.; Rogozin, A.; Shevchenko, N.; Gago, R.; Kolitsch, A.; Möller, W.
Properties of transparent conductive oxides deposited by magnetron sputtering
16th International Summer School on Vacuum, Electron and Ion Technologies, 28.09.-2.10.2009, Sunny Beach, Bulgaria

32. Zhou, S.
Transition metal implanted ZnO: A correlation between structure and magnetism
Thyssen Krupp Electrical Steel Dissertationspreis der AG Magnetismus, Frühjahrstagung der Deutschen Physikalischen Gesellschaft, 22.-27.03.2009, Dresden, Germany

Conference Contributions

1. Abrasonis, G.; Kovacs, Gy. J.; Ryves, L.; Mücklich, A.; Krause, M.; Munnik, F.; Oates, T. W. H.; Bilek, M. M. M.; Kolitsch, A.; Möller, V.
Comparison of the structural developments in the C:Ni films grown by ion beam sputtering and pulsed filtered cathodic vacuum arc
E-MRS 2009 Spring Meeting, 8.-12.06.2009, Strasbourg, France

2. Abrasonis, G.; Kovacs, Gy. J.; Oates, T. W. H.; Tucker, M.; Munnik, F.; Bilek, M. M. M.; Möller, W.
Hyperthermal ion induced self-organization during the growth of carbon-transition metal films
MRS 2009 Fall Meeting, 30.11.-4.12.2009, Boston MA, USA

3. Al-Motasem, A. T.; Posselt, M.; Bergner, F.; Birkenheuer, U.
Atomic-level computer simulations of copper-vacancy clusters in alpha-Fe
1st International School on Materials for Nuclear Reactors, 18.-23.10.2009, Rochehaut-sur-Semois, Belgium

4. Arnold, M.; Merchel, S.; Bourlès, Didier L.; Braucher, R.; Benedetti, L.; Finkel, Robert C.; Aumaître, G.; Gottdang, A.; Klein, M.
The French accelerator mass spectrometry facility ASTER: Improved performance and developments
19th International Conference on Ion Beam Analysis, 7.-11.09.2009, Cambridge, United Kingdom

5. Bähtz, C.; Jeutter, N.; Grenzer, J.; Borany, J. von
In-situ X-ray scattering investigations at ROBL
European Congress and Exhibition on Advances Materials and Processes, 7.-10.09.2009, Glasgow, United Kingdom

6. Batabyal, R.; Patra, S.; Roy, A.; Roy, S.; Bischoff, L.; Dev, B. N.
Estimation of diffusion coefficient by photoemission electron microscopy in ion-implanted nanostructures
2nd International Conference on Physics at Surfaces and Interfaces, 23.-27.02.2009, Puri, India

7. Baumgart, C.; Jänsch, S.; Helm, M.; Schmidt, H.
Kelvin probe force and scanning capacitance microscopy on MOS structures
DPG Frühjahrstagung 2009 der Sektion Kondensierte Materie, 22.-27.03.2009, Dresden, Germany

8. Baumgart, C.; Müller, A.-D.; Müller, F.; Helm, M.; Möller, A.; Schmidt, H.
Kelvin probe force microscopy imaging of cross-sections of Si multilayer structures
DPG Frühjahrstagung 2009 der Sektion Kondensierte Materie, 22.-27.03.2009, Dresden, Germany

9. Baumgart, C.; Helm, M.; Schmidt, H.
Frequency dependent Kelvin probe force microscopy on locally doped Si
MRS 2009 Fall Meeting, 30.11.-4.12.2009, Boston MA, USA

10. Beinik, I.; Teichert, C.; Brauer, G.; Anwand, W.; Chen, X.; Hsu, Y. F.; Djurisic, A. B.
Characterization of single ZnO nanorods by conductive atomic force microscopy
International Symposium Piezoresponse Force Microscopy and Nanoscale Phenomena in Polar Materials, 23.-27.06.2009, Aveíro, Portugal

11. Beinik, I.; Kratzer, M.; Wang, L.; Brauer, G.; Anwand, W.; Teichert, C.
Characterization of single ZnO nanorods by conductive atomic force microscopy
Joint Annual Meeting of the Austrian Physical Society, 2.-4.09.2009, Innsbruck, Austria

12. Bernert, K.; Schönlebe, J.; Oestreich, C.; Mikolajick, T.
Extraction of nitride trap density distribution in SONOS structures based on an advanced thermal emission model
DPG Frühjahrstagung 2009 der Sektion Kondensierte Materie, 26.03.2009, Dresden, Germany

13. Beyer, R.; Borany, J. von; Burghardt, H.
Interface and border trap relaxation in Si/SiO_2 structures with Ge nanocrystals examined by transient capacitance spectroscopy
16th Conference of Insulating Films on Semiconductors, 29.06.-1.07.2009, Cambridge, United Kingdom

14. Beyer, R.; Borany, J. von
Determination of size and density of embedded nanocrystals in SiO_2 by scanning force microscopy using a tomographic approach
15. Tagung Festkörperanalytik, 12.-16.07.2009, Chemnitz, Germany

15. Bischoff, L.; Pilz, W.; Mazarov, P.; Wieck, A.
Alloy liquid metal ion sources for new FIB applications
DPG Frühjahrstagung 2009 der Sektion Kondensierte Materie, 22.-27.03.2009, Dresden, Germany

16. Bischoff, L.; Schmidt, B.; Lange, H.; Donzev, D.
Crossbeam processing for nano-structures on SOI substrates
4th FIB-Workshop: Focused Ion Beams in Research, Science and Technology, 29.-30.06.2009, Halle/Saale, Germany

17. Bischoff, L.; Schmidt, B.; Lange, H.; Donzev, D.
3D nanostructures by combined FIB and electron beam processing
35th International Conference on Micro Nano Engineering 2009, 28.09.-1.10.2009, Ghent, Belgium

18. Bürger, D.; Pandey, M.; Zhou, S.; Grenzer, J.; Reuther, H.; Anwand, W.; Helm, M.; Schmidt, H.
Structural and magnetic properties of pulsed laser annealed GaMnAs
DPG Frühjahrstagung 2009 der Sektion Kondensierte Materie, 22.-27.03.2009, Dresden, Germany

19. Bürger, D.; Zhou, S.; Grenzer, J.; Reuther, H.; Anwand, W.; Pandey, M.; Gottschalch, V.; Helm, M.; Schmidt, H.
Influence of annealing on Mn implanted GaAs films
5th International School and Conference on Spintronics and Quantum Information Technology, 7.-11.07.2009, Kraków, Poland

20. Camargo, E. N.; Silva, M. M.; Baldissera, S.; Ueda, M.; Otubo, J.; Reuther, H.
Modificação da superfície da liga Ni-Ti pela implantação iônica por imersão em plasma
64º Congresso da ABM – Associação Brasileira de Metalurgia, Materiais e Mineração, 13.-17.07.2009, Expominas, Belo Horizonte, Brasil

21. Cantelli, V.; Grenzer, J.; Borany, J. von; Faßbender, J.
Tailoring the FePt orientation on amorphous substrates by magnetron sputtering, structural and magnetic investigations
DPG Frühjahrstagung 2009 der Sektion Kondensierte Materie, 22.-27.03.2009, Dresden, Germany

22. Cantelli, V.; Grenzer, J.; Borany, J. von; Faßbender, J.
The effect of the sputtering gas (Ar, Xe) on FePt clusters formation: Structural and magnetic properties
DPG Frühjahrstagung 2009 der Sektion Kondensierte Materie, 22.-27.03.2009, Dresden, Germany

23. Cherkouk, C.; Rebohle, L.; Skorupa, W.; Helm, M.
Nachweis von Östrogen- wirkenden Substanzen in wässrigen Lösungen
6. Deutsches BioSensor Symposium (LOC-Lab-on-a-Chip und Point-of-Care Diagnostik), 30.03.-1.04.2009, Freiburg, Germany

24. Cornelius, S.; Vinnichenko, M.; Rogozin, A.; Shevchenko, N.; Kolitsch, A.; Möller, W.
Influence of substrate temperature and oxygen partial pressure on the electrical properties of Al-doped ZnO grown by reactive pulsed magnetron sputtering
DPG Frühjahrstagung 2009 der Sektion Kondensierte Materie, 22.-27.03.2009, Dresden, Germany

25. Cornelius, S.; Vinnichenko, M.; Kolitsch, A.; Möller, W.
Electrical properties of reactively sputtered ZnO thin films with a wide range of Al impurity concentrations
16th International Summer School on Vacuum, Electron and Ion Technologies, 28.09.-2.10.2009, Sunny Beach, Bulgaria

26. Da Silva, G.; Ueda, M.; Otani, C.; Reuther, H.
Corrosion resistance of aeronautics alloys treated by plasma immersion ion implantation (PIII)
11th International Conference on Advanced Materials, 20.-25.09.2009, Rio de Janeiro, Brasil

27. Dimitrakis, P.; Mouti, A.; Bonafos, C.; Schamm, S.; Ben Assayag, G.; Ioannou, V.; Schmidt, B.; Becker, J.; Normand, P.
Ultra-low-energy ion-beam-synthesis of Ge nanocrystals in thin ALD Al_2O_3 layers for memory applications
16th Biannual Conference of Insulating Films on Semiconductors, 29.06.-1.07.2009, Cambridge, United Kingdom

28. Donchev, A.; Kolitsch, A.; Schütze, M.; Yankov, R.
Enhancing the resistance of Ti-alloys against environmental high temperature degradation by a combination of Al-enrichment and F-treatment
European Congress and Exhibition on Advanced Materials and Processing, 7.-10.09.2009, Glasgow, United Kingdom

29. Donchev, A.; Kolitsch, A.; Schütze, M.; Yankov, R.
Combined Al- plus F-treatment of Ti-alloys for improved behaviour at elevated temperatures
European Federation of Corrosion Workshop, 30.09.-2.10.2009, Frankfurt/Main, Germany

30. Drachenko, O.; Winnerl, S.; Schneider, H.; Helm, M.; Wosnitza, J.; Kozlov, D.; Maremyanin, K.; Ikonnikov, A.; Gavrilenko, V.; Zvonkov, B.; Goiran, M.; Leotin, J.; Fasching, G.
Cyclotron resonance absorption of 2D holes in strained InGaAs/GaAs quantum wells under high magnetic fields
International Conference on Research in High Magnetic Fields, 22.-25.07.2009, Dresden, Germany

31. Dupuy, J. C.; Dubois, C.; Prudon, G.; Gautier, B.; Kögler, R.; Akhmadaliev, S.; Perrat-Mabilon, A.; Peaucelle, C.
Isotopic comparative method (ICM) for the determination of variations of the useful ion yields in boron doped silicon as a function of oxygen concentration in the 0 - 10 at.% range
17th International Conference on Secondary Ion Mass Spectrometry, 13.-17.09.2009, Toronto, Canada

32. Fischer, H.; Koczur, K.; Lindner, M.; Jennissen, H. P.; Meissner, M.; Zurlinden, K.; Mueller-Mai, C.; Seifert, G.; Oliveira, A.; Morawetz, K.; Gemming, S.
Functionalized mineral surfaces: Sorption mechanisms of growth proteins on the surface of bone replacement materials (BioMin)
GeoDresden 2009, 30.09.-2.10.2009, Dresden, Germany

33. Fritsch, D.; Schmidt, H.
Electronic bandstructure of the ZnTe absorber material
DPG Frühjahrstagung 2009 der Sektion Kondensierte Materie, 22.-27.03.2009, Dresden, Germany

34. Gago, R.; Redondo-Cubero, A.; Vinnichenko, M.; Jiménez, I.; Czigány, Zs.; Vázquez, L.
Correlation between morphology and bonding structure in titanium oxide films produced by reactive pulsed magnetron sputtering
E-MRS 2009 Spring Meeting, 8.-12.06.2009, Strasbourg, France

35. Garroni, S.; Menendez, E.; Lopez Ortega, A.; Estrader, M.; Milanese, C.; Nolis, P.; Nogues, J.; Surinach, S.; Baro, M. D.
Sorption properties of the $NaBH_4/MgH_2$ system: Dehydrogenation mechanism and pathway
MRS 2009 Fall Meeting, 30.11.-4.12.2009, Boston MA, USA

36. Gemming, S.; Lubk, A.; Lichte, H.; Spaldin, N. A.
Dichtefunktional-Studie zu Domänengrenzen in $BiFeO_3$
17. Jahrestagung der Deutschen Gesellschaft für Kristallographie, 9.-12.02.2009, Hannover, Germany

37. Gemming, S.; Kunze, T.; Numazawa, S.; Schreiber, M.
Novel concepts for anisotropic Heisenberg modeling of multiferroic oxides
45th Symposium on Theoretical Chemistry, 8.-12.09.2009, Neuss, Germany

38. Hamann, C.; McCord, J.; Faßbender, J.; Mattheis, R.; Kaltofen, R.; Schäfer, R.; Schultz, L.
Tuning the static and dynamic magnetization properties of exchange bias modulated thin films
DPG Frühjahrstagung 2009 der Sektion Kondensierte Materie, 22.-27.03.2009, Dresden, Germany

39. Hanisch, A.; Grenzer, J.; Biermanns, A.; Pietsch, U.
Xe^+ ion beam induced rippled structures on Si miscut wafers
DPG Frühjahrstagung 2009 der Sektion Kondensierte Materie, 22.-27.03.2009, Dresden, Germany

40. Heera, V.; Herrmannsdörfer, T.; Heinig, K.-H.; Ignatchik, O.; Mücklich, A.; Posselt, M.; Schmidt, B.; Skrotzki, R.; Skorupa, W.; Uhlarz, M.; Voelskow, M.; Wündisch, C.; Helm, M.; Wosnitza, J.
Superconductivity in heavily Ga-doped Ge
Workshop Ionenstrahlphysik, 6.-8.04.2009, Jena, Germany

41. Heinig, K.-H.; Schmidt, B.
Swift heavy ions: A tool for nanotechnology?
Workshop Ionenstrahlphysik, 6.-8.04.2009, Jena, Germany

42. Jeutter, N. M.; Zschintzsch, M.; Borany, J. von; Bähtz, C.
In-situ X-ray studies of Ge nanocrystals formation out of (GeO_x/SiO_2) superlattices
DPG Frühjahrstagung 2009 der Sektion Kondensierte Materie, 22.-27.03.2009, Dresden, Germany
43. *E-MRS 2009 Spring Meeting, 8.-12.06.2009, Strasbourg, France*

44. Jeutter, N. M.; Zschintzsch, M.; Borany, J. von; Bähtz, C.
Formation of Ge NCs out of (GeO_x-SiO_2) superlattice structures
DPG Frühjahrstagung 2009 der Sektion Kondensierte Materie, 22.-27.03.2009, Dresden, Germany

45. Kanjilal, A.; Rebohle, L.; Voelskow, M.; Skorupa, W.; Helm, M.
Metal-oxide semiconductor light-emitting devices based on Ge nanocrystals co-implanted with Er ions
SPIE Europe - Microtechnologies for the New Millennium, 4.-6.05.2009, Dresden, Germany

46. Keller, A.; Nicoli, M.; Cuerno, R.; Facsko, S.; Möller, W.
Ripple rotation in the anisotropic Kuramoto-Sivashinsky equation
MRS 2009 Spring Meeting, 13.-17.04.2009, San Francisco CA, USA

47. Keller, A.; Nicoli, M.; Cuerno, R.; Facsko, S.; Möller, W.
Pattern rotation in the anisotropic Kuramoto-Sivashinsky equation
Workshop "Nanoscale Modification of Surfaces and Thin Films", 30.08.-3.09.2009, Rathen, Germany

48. Khan, S. A.; Tripathi, A.; Gerlach, J. W.; Grambole, D.; Toulemonde, M.; Assmann, W.
^{13}C-detection for sputtering investigations
19th International Conference on Ion Beam Analysis, 7.-11.09.2009, Cambridge, United Kingdom

49. Kögler, R.
Implantation induced point defects and their role in silicon-on-insulator (SOI) materials processing
Workshop Ionenstrahlphysik, 6.-8.04.2009, Jena, Germany

50. Körner, M.; Liedke, M. O.; Strache, T.; Dzenisevich, S.; Keller, A.; Facsko, S.; Faßbender, J.
Influence of rippled substrate morphology on the interlayer exchange coupling in Fe/Cr/Fe thin films
DPG Frühjahrstagung 2009 der Sektion Kondensierte Materie, 22.-27.03.2009, Dresden, Germany

51. Kosmata, M.; Grötzschel, R.; Hanf, D.; Munnik, F.; Akhmadaliev, C.; Vieluf, M.; Möller, W.
The QQDS magnetic spectrometer "Little John" for high resolution depth profiling
Workshop Ionenstrahlphysik, 6.-8.04.2009, Jena, Germany

52. Kosmata, M.; Grambole, D.; Grötzschel, R.; Möller, W.; Munnik, F.; Neelmeijer, C.; Vieluf, M.
Ionenstrahlanalyse ultradünner Schichten mit Nanometertiefenauflösung
15. Tagung Festkörperanalytik, 12.-16.07.2009, Chemnitz, Germany

53. Kosmata, M.; Grötzschel, R.; Munnik, F.; Vieluf, M.; Möller, W.
Release of light elements from ultra thin films during high resolution depth profiling using heavy ion ERDA
19th International Conference on Ion Beam Analysis, 7.-11.09.2009, Cambridge, United Kingdom

54. Kovacs, Gy. J.; Oates, T. W. H.; Mücklich, A.; Abrasonis, G.; Kolitsch, A.; Möller, W.
Structure and optical properties of boron nitride capped silver nanoparticles grown by magnetron sputtering
MRS 2009 Fall Meeting, 30.11.-4.12.2009, Boston MA, USA

55. Krause, M.; Viršek, M.; Salacan, N.; Chen, L.; Abrasonis, G.; Kolitsch, A.; Remškar, M.; Fleischer, N.; Hatto, P.; Möller, W.
Size and shape dependent Raman scattering of WS_2 nanomaterials
23rd International Winterschool on Electronic Properties of Novel Materials, 7.-14.03.2009, Kirchberg, Austria

56. Krause-Rehberg, R.; Anwand, W.; Brauer, G.; Butterling, M.; Cowan, T.; Jungmann, M.; Krille, A.; Schwengner, R.; Wagner, A.
Progress of the EPOS project: Gamma-induced positron spectroscopy (GiPS)
15th International Conference on Positron Annihilation, 18.-23.01.2009, Kolkata, India

57. Krickl, R.; Nasdala, L.; Grambole, D.; Kaindl, R.
Radio-induced alteration in cordierite – Implications for petrology, gemmology and materials science
General Assembly 2009 of the European Geosciences Union, 19.-24.04.2009, Vienna, Austria

58. Krickl, R.; Götze, J.; Grambole, D.; Nasdala, L.; Kaindl, R.
Radiohaloes in feldspar group minerals
Jahrestagung der Deutschen Mineralogischen Gesellschaft, 13.-16.09.2009, Halle, Germany

59. Kunze, T.; Gemming, S.
Novel concepts for anisotropic Heisenberg modelling of multiferroic oxides
DPG Frühjahrstagung 2009 der Sektion Kondensierte Materie, 22.-27.03.2009, Dresden, Germany

60. Kunze, T.; Gemming, S.; Luschtinetz, R.; Pankoke, V.; Morawetz, K.; Schreiber, M.; Eng, L.; Seifert, G.
Modelling the transport through organic layers on a ferroelectric substrate
DPG Frühjahrstagung 2009 der Sektion Kondensierte Materie, 22.-27.03.2009, Dresden, Germany

61. Kunze, T.; Gemming, S.; Luschtinetz, R.; Pankoke, V.; Morawetz, K.; Schreiber, M.
Conductivity through an organic field-effect transistor with ferroelectric gating
DPG Frühjahrstagung 2009 der Sektion Kondensierte Materie, 22.-27.03.2009, Dresden, Germany

62. Kuriplach, J.; Melikhova, O.; Cizek, J.; Prochazka, I.; Brauer, G.; Anwand, W.
Positron trapping at vacancy-hydrogen complexes in zinc oxide
Advanced Science Research, Symposium "Positron, Muon, and other Exotic Particle Beams for Materials Science and Atomic/Molecular Sciences", 10.-12.11.2009, Tokai, Japan

63. Kuriplach, J.; Brauer, G.; Melikhova, O.; Cizek, J.; Prochazka, I.; Anwand, W.
Divacancy-hydrogen complexes in zinc oxide
MRS 2009 Fall Meeting, 30.11.-4.12.2009, Boston MA, USA

64. Kuznetsova, L.; Wang, C. Y.; Gkortsas, V. M.; Diehl, L.; Kärtner, F.; Belkin, M. A.; Belyanin, A.; Li, X.; Ham, D.; Schneider, H.; Liu, H. C.; Capasso, F.
Mode-locking via active gain modulation in quantum cascade lasers

Conference on Lasers and Electro-Optics, 2009 and 2009 Conference on Quantum Electronics and Laser Science Conference, 2.-4.06.2009, Baltimore MD, USA

65. Lenz, K.; Körner, M.; Liedke, M. O.; Strache, T.; Dzenisevich, S.; Keller, A.; Facsko, S.; Faßbender, J.
Tailoring the Néel- and interlayer exchange coupling of Fe/Cr/Fe trilayers using rippled substrates
Advances in Magnetic Nanostructures, 4.-9.10.2009, Vail CO, USA

66. Lenz, K.; Marko, D.; Strache, T.; Faßbender, J.
Determination of the saturation magnetization from perpendicular magnetic anisotropy measurements
Advances in Magnetic Nanostructures, 4.-9.10.2009, Vail CO, USA

67. Liedke, B.; Heinig, K.-H.
Competition ion beam mixing and phase separation: A novel program combining TRIM with kinetic Monte Carlo
Workshop Ionenstrahlphysik, 6.-7.04.2009, Jena, Germany

68. Liedke, B.; Heinig, K.-H.; Facsko, S.; Möller, W.
Ion-induced surface pattern evolution in computer simulations with a new approach – unification of collision cascade and kinetic 3D Monte Carlo calculations
Workshop "Nanoscale Modification of Surfaces and Thin Films", 30.08.-3.09.2009, Rathen, Germany

69. Liedke, B.; Heinig, K.-H.; Facsko, S.; Möller, W.
Classification of simulated surface morphologies induced by ion irradiation using combined TRIM an kinetic Monte-Carlo calculations
MRS 2009 Fall Meeting, 30.11.-4.12.2009, Boston MA, USA

70. Liedke, B.; Heinig, K.-H.; Odor, G.
Efficient numerical studies of scaling properties and pattern formation during surface growth / erosion by surface mapping on a binary lattice gas model
MRS 2009 Fall Meeting, 30.11.-4.12.2009, Boston MA, USA

71. Lubk, A.; Spaldin, N.; Gemming, S.; Lichte, H.
First principle calculations of domain boundaries in multiferroic $BiFeO_3$
DPG Frühjahrstagung 2009 der Sektion Kondensierte Materie, 22.-27.03.2009, Dresden, Germany

72. Luschtinetz, R.; Enyashin, A. N.; Milek, T.; Frenzel, J.; Gemming, S.; Seifert, G.
DFT-study of the adsorption of organic molecules on low-index titanium dioxide surfaces
DPG Frühjahrstagung 2009 der Sektion Kondensierte Materie, 22.-27.03.2009, Dresden, Germany

73. Markó, D.; Strache, T.; Lenz, K.; Faßbender, J.; Kaltofen, R.
Ion irradiation induced modification of magnetic properties in Py-Ta multilayers
DPG Frühjahrstagung 2009 der Sektion Kondensierte Materie, 22.-27.03.2009, Dresden, Germany

74. Markov, A. B.; Reuther, H.; Shevchenko, N.
Polishing of titanium and enhancing the wear resistance of the titanium alloys with a low-energy high-current electron beam
14th International Conference on Radiation Physics and Chemistry of Inorganic Materials, 6.-10.10.2009, Astana, Kazakhstan

75. Martin, N.; McCord, J.; Gerber, A.; Strache, T.; Gemming, T.; Mönch, I.; Schäfer, R.; Faßbender, J.; Quandt, E.; Schultz, L.
Local setting of magnetic anisotropy in FeCoSiB thin films by means of indirect ion implantation
DPG Frühjahrstagung 2009 der Sektion Kondensierte Materie, 22.-27.03.2009, Dresden, Germany

76. Martinavicius, A.; Abrasonis, G.; Möller, W.
Temperature dependence of nitrogen diffusion in single crystalline austenitic stainless steel during ion beam nitriding
15th International Summer School on Vacuum, Electron and Ion Technologies, 28.09.-2.10.2009, Sunny Beach, Bulgaria

77. Masset, P. J.; Yankov, R. A.; Kolitsch, A.; Schütze, M.
Comparison of fluorination treatments to improve the high temperature oxidation resistance of TiAl alloys in SO_2-containing environments
International Conference on Processing and Manufacturing of Advanced Materials, 25.-29.08.2009, Berlin, Germany

78. Masset, P. J.; Neve, S.; Zschau, H.-E.; Yankov, R. A.; Kolitsch, A.; Schütze, M.
Oxidation resistance improvement of TiAl alloys by the halogen effect in industrial environments
European Congress and Exhibition on Advanced Materials and Processes, 7.-10.09.2009, Glasgow, United Kingdom

79. Mazarov, P.; Bischoff, L.; Pilz, W.; Wieck, A.
A silver containing liquid alloy ion source
DPG Frühjahrstagung 2009 der Sektion Kondensierte Materie, 22.-27.03.2009, Dresden, Germany

80. Melikhova, O.; Cizek, J.; Kuriplach, J.; Prochazka, I.; Cieslar, M.; Brauer, G.; Anwand, W.
Quenched-in vacancies in Fe-Al alloys
15th International Conference on Positron Annihilation, 18.-23.01.2009, Kolkata, India

81. Melikhova, O.; Cizek, J.; Kuriplach, J.; Prochazka, I.; Cieslar, M.; Brauer, G.; Anwand, W.
Hydrogen-induced defects in Pd films
15th International Conference on Positron Annihilation, 18.-23.01.2009, Kolkata, India

82. Melikhova, O.; Kuriplach, J.; Cizek, J.; Prochazka, I.; Brauer, G.; Anwand, W.
Investigation of hydrogen interaction with defects in zirconia
Advanced Science Research Symposium "Positron, Muon, and other Exotic Particle Beams for Materials Science and Atomic/Molecular Sciences", 10.-12.11.2009, Tokai, Japan

83. Melikhova, O.; Kuriplach, J.; Cizek, J.; Prochazka, I.; Brauer, G.; Anwand, W.
Investigation of interaction of hydrogen with defects in zirconia
MRS 2009 Fall Meeting, 30.11.-4.12.2009, Boston MA, USA

84. Mello, C. B.; Ueda, M.; Silva, M. M.; Reuther, H.; Pichon, L.; Lepienski, C. M.
Tribological effects of plasma immersion ion implantation heating treatments on Ti-6Al-4V alloy
17th International Conference on Wear of Materials, 19.-23.04.2009, Las Vegas, USA

85. Mello, C. B.; Ueda, M.; Oliveira, R. M.; Reuther, H.; Lepienski, C. M.
Enhancement of surface properties of SAE 1070 by chromium plasma immersion ion implantation and deposition
10th International Workshop on Plasma Based Ion Implantation and Deposition, 7.-11.09.2009, São José dos Campos, Brazil

86. Merchel, S.; Bremser, W.; Alfimov, V.; Arnold, M.; Aumaître, G.; Benedetti, L.; Bourlès, Didier L.; Braucher, R.; Caffee, M.; Christl, M.; Fifield, L. Keith; Finkel, Robert C.; Freeman, Stewart P. H. T.; Ruiz-Gómez, A.; Kubik, Peter W.; Rood, Dylan H.; Sasa, K.; Steier, P.; Tims, Stephen G.; Wallner, A.; Wilcken, Klaus M.; Xu, S.
Be-10 and Cl-36 interlaboratory comparisons
73. Jahrestagung der DPG und DPG Frühjahrstagung 2009 der Sektion AMOP, 2.-6.03.2009, Hamburg, Germany

87. Merchel, S.; Bremser, W.; Alfimov, V.; Arnold, M.; Aumaître, G.; Benedetti, L.; Bourlès, Didier L.; Braucher, R.; Caffee, M.; Christl, M.; Fifield, L. Keith; Finkel, Robert C.; Freeman, Stewart P. H. T.; Ruiz-Gómez, A.; Kubik, Peter W.; Rood, Dylan H.; Sasa, K.; Steier, P.; Tims, Stephen G.; Wallner, A.; Wilcken, Klaus M.; Xu, S.
Be-10 and Cl-36 interlaboratory comparisons: Implications for terrestrial production rates?
19th V.M. Goldschmidt™ Conference, 21.-26.06.2009, Davos, Switzerland

88. Merchel, S.; Bremser, W.
Quality assurance in accelerator mass spectrometry: Results from international round-robin exercises for Be-10 and Cl-36
19th International Conference on Ion Beam Analysis, 7.-11.09.2009, Cambridge, United Kingdom

89. Mironov, O. A.; Goiran, M.; Galibert, J.; Drachenko, O.; Helm, M.; Wosnitza, J.; Kozlov, D. V.; Ikonnikov, A. V.; Gavrilenko, V. I.; Kummer, M.; von Känel, H.; Morris, R. J. H.; Leadley, D. R.
Cyclotron resonance of extremely conductive 2D holes in high Ge content strained heterostructures
9th International Conference on Research in High Magnetic Fields, 22.-25.07.2009, Dresden, Germany

90. Möller, W.; Kolitsch, A.; Merchel, S.; Zier, M.; The Spirit Consortium (www. Spirit-Ion. Eu)
The SPIRIT project: Fast ions for everybody in Europe
GDCh-Wissenschaftsforum Chemie 2009, 30.08.-2.09.2009, Frankfurt am Main, Germany

91. Mücklich, A.; Potzger, K.
Clusters in cobalt implanted boron pre-doped ZnO
Microscopy Conference 2009, 30.08.-4.09.2009, Graz, Austria

92. Munnik, F.; Grambole, D.; Grötzschel, R.; Merchel, S.; Neelmeijer, C.
Accelerator mass spectrometry (AMS) and ion beam analysis (IBA) with the new 6 MV accelerator at FZ Dresden-Rossendorf
Deutschsprachige Analytiker Konferenz 2009, 17.-20.03.2008, Berlin, Germany

93. Munnik, F.
Characterisation of thin films using ion beams
Materials Science Workshop II, 23.-25.03.2009, Sohag, Egypt

94. Munnik, F.; Cabral, A. R.; Lehmann, B.
Micro-ERDA measurements of hydrogen distribution in natural Pd–Pt compounds
19th International Conference on Ion Beam Analysis, 7.-11.09.2009, Cambridge, United Kingdom

95. Nasdala, L.; Grambole, D.; Wildner, M.; Zaitsev, Alexander M.; Götze, J.; Kempe, U.; Hanchar, John M.; Harris, Jeffrey W.

Radiation-induced defect centers: Luminescence and optical absorption study of helium-irradiated diamond and zircon
AGU Joint Assembly 2009 - The Meeting of the Americas, 24.-27.05.2009, Toronto, Canada

96. Nasdala, L.; Grambole, D.; Váczi, T.; Götze, J.
Is there alpha-assisted annealing of radiation damage? A helium implantation study of radiation-damaged zircon and monazite
Annual Meeting 2009 of the Mineralogical Society of Great Britain and Ireland: Micro-Analysis, Processes, Time (MAPT), 31.08.-2.09.2009, Edinburgh, United Kingdom

97. Neelmeijer, C.; Grambole, D.; Grötzschel, R.; Merchel, S.; Munnik, F.
Ion beam analysis (IBA) and accelerator mass spectrometry (AMS) with the new 6 MV accelerator at FZ Dresden-Rossendorf
GDCh-Wissenschaftsforum Chemie 2009, 30.08.-2.09.2009, Frankfurt/Main, Germany

98. Nomura, K.; Németh, Z.; Reuther, H.
^{57}Fe implantation effect of Sb doped SnO_2 films
International Conference on the Applications of the Mössbauer Effect, 19.-24.07.2009, Vienna, Austria

99. Nomura, K.; Iio, S.; Hirose, Y.; Nemeth, Z.; Yamamoto, K.; Reuther, H.
Characterization of ^{57}Fe implanted and annealed SnO_2 (3% Sb) films by depth selective conversion electron Mossbauer spectroscopy (DCEMS)
Asia-Pacific Symposium on Radiochemistry, 29.11.-4.12.2009, Napa CA, USA

100. Nomura, K.; Németh, Z.; Rykov, A.; Reuther, H.
Characterization of ^{57}Fe implanted SnO_2 films by Mössbauer spectroscopy and nuclear inelastic scattering
Asia-Pacific Symposium on Radiochemistry, 29.11.-4.12.2009, Napa CA, USA

101. Numazawa, S.; Heinig, K.-H.; Ranjan, M.; Facsko, S.
Mechanisms of metal self-ordering at grazing PVD on ion-erosion-induced surface pattern
Workshop "Nanoscale Modification of Surfaces and Thin Films", 30.08.-3.09.2009, Rathen, Germany

102. Numazawa, S.; Heinig, K.-H.
Prediction of surface pattern formation by surface defect generation and diffusion
MRS 2009 Fall Meeting, 30.11.-4.12.2009, Boston MA, USA

103. Numazawa, S.; Heinig, K.-H.; Ranjan, M.; Facsko, S.
Mechanisms of metal self-ordering at oblique PVD on nanopatterned surfaces
MRS 2009 Fall Meeting, 30.11.-4.12.2009, Boston MA, USA

104. Odor, G.; Liedke, B.; Heinig, K.-H.
Mapping two-dimensional surface patterns and scaling onto driven lattice gases
34th Conference of the Middle European Cooperation in Statistical Physics, 30.03.-1.04.2009, Leipzig, Germany

105. Odor, G.; Liedke, B.; Heinig, K.-H.
KPZ growth mapping onto driven lattice gas model of n-mers
Workshop on Statistical Physics, 16.04.2009, Budapest, Hungary

106. Ogiewa, M.; Zier, M.; Schmidt, B.
Electrical Characterisation of USJs in doped Si
DPG Frühjahrstagung 2009 der Sektion Kondensierte Materie, 22.-27.03.2009, Dresden, Germany

107. Oliveira, R. M.; Ueda, M.; Silva, L. L. G.; Reuther, H.; Lepienski, C. M.
Characteristics of austenitic stainless steel nitrided in a hybrid glow discharge plasma
17th International Conference on Wear of Materials, 19.-23.04.2009, Las Vegas, USA

108. Ou, X.; Kögler, R.; Skorupa, W.; Möller, W.; Wang, X.
Oxygen gettering in thin buried oxide layer fabrication
5th Workshop of the Thematic Network on Silicon on Insulator Technology, Devices and Circuits, 19.-21.01.2009, Göteborg, Sweden

109. Pankoke, V.; Gemming, S.
Effects of film thickness and Co doping on the magnetism of Pd structures
DPG Frühjahrstagung 2009 der Sektion Kondensierte Materie, 22.-27.03.2009, Dresden, Germany

110. Peter, F.; Winnerl, S.; Schneider, H.; Helm, M.; Köhler, K.
Terahertz emission from an InGaAsN large area emitter
International Workshop on Optical Terahertz Science and Technology, 7.-11.03.2009, Santa Barbara, USA

111. Peter, F.; Winnerl, S.; Schneider, H.; Helm, M.; Köhler, K.
Terahertz wave emission from InGaAsN large area emitter
DPG Frühjahrstagung 2009 der Sektion Kondensierte Materie, 22.-27.03.2009, Dresden, Germany

112. Peter, F.; Winnerl, S.; Schneider, H.; Helm, M.; Köhler, K.
Large-area terahertz emitters based on GaInAsN
SPIE Europe Microtechnologies for the New Millenium, 4.-6.05.2009, Dresden, Germany

113. Peter, S.; Günther, M.; Hauschild, D.; Grambole, D.; Richter, F.
Mid-frequency deposition of a-C:H films using five different precursors
4th Symposium on Vacuum based Science and Technology in conjunction with 8th Annual Meeting of German Vacuum Society, 21.-23.09.2009, Koszalin- Kołobrzeg, Poland

114. Popov, I.; Seifert, G.; Gemming, S.
A structure-induced metal-insulator transition in thin MoS nanowires
DPG Frühjahrstagung 2009 der Sektion Kondensierte Materie, 22.-27.03.2009, Dresden, Germany

115. Posselt, M.
Atomistic simulation of ion-beam-induced defect formation
International Workshop "Exchange on Laser-Plasma Interaction Theory", 1.-3.04.2009, Dresden, Germany

116. Posselt, M.; Gabriel, A.
Atomistic simulation of recrystallization of amorphous Si and Ge
13th International Autumn Meeting on Gettering and Defect Engineering in Semiconductor Technology, 26.09.-2.10.2009, Döllnsee-Schorfheide, Germany

117. Potzger, K.; Zhou, S.; Mücklich, A.; Xu, Q.; Schmidt, H.; Helm, M.; Faßbender, J.
'Invisible' ferromagnetic secondary phases in Co doped ZnO
DPG Frühjahrstagung 2009 der Sektion Kondensierte Materie, 22.-27.03.2009, Dresden, Germany

118. Prochazka, I.; Cizek, J.; Melikhova, O.; Kuriplach, J.; Kuzel, R.; Brauer, G.; Anwand, W.; Konstantinova, T. E.; Danilenko, I. A.
Defects in nanostructured yttria-stabilized zirconia studied by positron annihilation spectroscopy
15th International Conference on Positron Annihilation, 18.-23.01.2009, Kolkata, India

119. Rebohle, L.
Physical limitations of the hot electron impact excitation mechanism in electrically driven Si-based light emitters
IBEDM 2009, 2.10.2009, Tossa de Mar, Spain

120. Reuther, H.; Müller, C.; Leonhardt, A.; Kutz, M. C.
Investigation of the formation of Fe-filled Carbon nanotubes
International Conference on the Applications of the Mössbauer Effect, 19.-24.07.2009, Vienna, Austria

121. Roshchupkina, O.; Grenzer, J.; Faßbender, J.; Choi, Y.; Jiang, J. S.; Bader, S. D.
Tuning exchange spring magnets by ion irradiation and annealing: X-ray investigations
DPG Frühjahrstagung 2009 der Sektion Kondensierte Materie, 22.-27.03.2009, Dresden, Germany

122. Scarlat, C.; Zhou, S.; Vinnichenko, M.; Kolitsch, A.; Bürger, D.; Faßbender, J.; Potzger, K.; Shalimov, A.; Grenzer, J.; Helm, M.; Schmidt, H.
Optical and magnetic properties of indium oxides implanted with Cr
E-MRS 2009 Spring Meeting, 8.-12.06.2009, Strasbourg, France

123. Schlosser, M.; Iskra, P.; Abelein, U.; Lange, H.; Lochner, H.; Sulima, T.; Wiest, F.; Zilbauer, T.; Schmidt, B.; Eisele, I.; Hansch, W.
The impact ionization MOSFET (IMOS) as low-voltage optical detector
11th European Symposium on Semiconductor Detectors, New Developments in Radiation Detectors, 7.-11.06.2009, Wildbad Kreuth, Germany

124. Schmidt, B.; Heinig, K.-H.; Beyer, V.; Stegemann, K.-H.
Ion beam mixing as basic technology for a light-emitting silicon nanocrystal field-effect transistor
Workshop Ionenstrahlphysik, 6.-8.04.2009, Jena, Germany

125. Schmidt, B.; Zier, M.; Potfajova, J.
Ion implantation in AFM cantilever array fabrication
54th Internationales Wissenschaftliches Kolloquium, Workshop „PRONANO", 10.09.2009, Ilmenau, Germany

126. Schmidt, M.; Ellguth, M.; Lüder, T.; Wenckstern, H. von; Pickenhain, R.; Grundmann, M.; Brauer, G.; Skorupa, W.; Helm, M.
Investigation of defects in nitrogen implanted n-type ZnO by capacitance spectroscopy and simultaneous optical excitation
25th International Conference on Defects in Semiconductors, 20.-24.07.2009, St. Petersburg, Russia

127. Schmidt, M.; Ellguth, M.; Brachwitz, K.; Brandt, M.; Wenckstern, H. von; Pickenhain, R.; Grundmann, M.; Brauer, G.; Skorupa, W.

Deep levels in Ni doped ZnO materials research society
MRS 2009 Fall Meeting, 30.11.-4.12.2009, Boston MA, USA

128. Schneider, H.; Liu, H. C.; Winnerl, S.; Drachenko, O.; Helm, M.; Walther, M.; Faist, J.
Quadratic detection with two-photon quantum well infrared photodetectors
International Conference "Quantum Structure Infrared Photodetector", 18.-23.01.2009, Yosemite, USA

129. Schneider, H.; Bracht, H.; Klug, J. N.; Lundsgaard Hansen, J.; Bourgeard, D.; Liao, C. Y.; Haller, E. E.; Posselt, M.; Wündisch, C.
Radiation enhanced diffusion in germanium
25th International Conference on Defects in Semiconductors, 20.-24.06.2009, St. Petersburg, Russia

130. Seeger, M.; Bürger, D.; Rebohle, L.; Skorupa, W.; Helm, M.; Schmidt, H.
Photocapacitance measurements on MOS light emitting devices
DPG Frühjahrstagung 2009 der Sektion Kondensierte Materie, 22.-27.03.2009, Dresden, Germany

131. Shalimov, A.; Potzger, K.; Geiger, D.; Lichte, H.; Talut, G.; Misiuk, A.; Reuther, H.; Stromberg, F.; Zhou, S.; Bähtz, C.
Fe nanoparticles embedded in MgO crystals
DPG Frühjahrstagung 2009 der Sektion Kondensierte Materie, 22.-27.03.2009, Dresden, Germany

132. Shevchenko, N.; Kolitsch, A.
Porous steel surfaces produced by plasma immersion ion implantation
International Conference on Physical Mesomechanics and Computer-Aided Design and Development of Advanced Materials, 8.-11.09.2009, Tomsk, Russia

133. Siqueira, R. H. M.; Ueda, M.; Lepienski, C. M.; Reuther, H.
Improvement of satellite imaging camera components made of SS304 by nitrogen PIII treatments
10th International Workshop on Plasma Based Ion Implantation and Deposition, 7.-11.09.2009, São José dos Campos, Brazil

134. Skorupa, W.; Anwand, W.; Gebel, T.
Energy pulse modification of electronic materials: From electronics via photonics to other advanced materials
European Project Meeting "Teramagstor", 28.-29.05.2009, Santorini, Greece

135. Strache, T.; Reichel, L.; Wintz, S.; Fritzsche, M.; Mönch, I.; Raabe, J.; Martin, N.; McCord, J.; Körner, M.; Markó, D.; Romstedt, F.; Faßbender, J.
Ion irradiation of permalloy: From thin magnetic films to lateral exchange spring nanostructures
Workshop Ionenstrahlphysik, 6.-8.04.2009, Jena, Germany

136. Strache, T.; Tibus, S.; Springer, F.; Rohrmann, H.; Albrecht, M.; Lenz, K.; Faßbender, J.
Tuning coercivity in CoCrPt-SiO_2 hard disk material
DPG Frühjahrstagung 2009 der Sektion Kondensierte Materie, 22.-27.03.2009, Dresden, Germany

137. Talut, G.; Reuther, H.; Grenzer, J.; Bähtz, C.; Novikov, D.; Walz, B.
On the formation of secondary phases in Fe implanted GaN
DPG Frühjahrstagung 2009 der Sektion Kondensierte Materie, 22.-27.03.2009, Dresden, Germany

138. Talut, G.; Grenzer, J.; Reuther, H.; Bähtz, C.; Novikov, D.; Walz, B.
Repeatable phase change in Fe implanted GaN induced by multi-annealing in reduced atmosphere
International Conference on the Applications of the Mössbauer Effect, 19.-24.07.2009, Vienna, Austria

139. Thieme, M.; Gemming, S.; Potzger, K.
Vanadium:silicon - an ion-beam generated diluted magnetic semiconductor? - Integration of vanadium into the silicon host crystal
DPG Frühjahrstagung der Sektion Kondensierte Materie 2009, 25.03.2009, Dresden, Germany

140. Thieme, M.; Gemming, S.; Potzger, K.
Vanadium:silicon - an ion-beam generated diluted magnetic semiconductor? Vanadium diffusion and concentration predictions in silicon
23rd Nordic Semiconductor Meeting, 14.-17.06.2009, Reykjavik, Iceland

141. Thorn, A.; Ritter, E.; Ullmann, F.; Zschornack, G.; Bischoff, L.; Pilz, W.
Investigations on Dresden EBIS/T as charge breeders
5th SPARC Collaboration Symposium, 1.-4.09.2009, Lisboa, Portugal

142. Turos, A.; Nowicki, L.; Stonert, A.; Pagowska, K.; Jagielski, J.; Mücklich, A.
Monte Carlo simulations of ion channeling in crystals containing extended defects
19th International Conference on Ion Beam Analysis, 7.-11.09.2009, Cambridge, United Kingdom

143. Valenzuela, M.; Rochette, P.; Bourlès, Didier L.; Braucher, R.; Faestermann, T.; Finkel, Robert C.; Gattacceca, J.; Korschinek, G.; Merchel, S.; Morata, D.; Poutivtsev, M.; Rugel, G.; Suavet, C.

The age of the Monturaqui impact crater
72nd Annual Meeting of the Meteoritical Society, 13.-18.07.2009, Nancy, France

144. Vinnichenko, M.; Rogozin, A.; Grambole, D.; Munnik, F.; Kolitsch, A.; Möller, W.; Stenzel, O.; Wilbrandt, S.; Chuvilin, A.; Kaiser, U.
Highly dense amorphous Nb_2O_5 films with closed nano-sized pores
E-MRS 2009 Spring Meeting, 8.-12.06.2009, Strasbourg, France

145. Virsek, M.; Krause, M.; Kolitsch, A.; Mrzel, A.; Iskra, I.; Remskar, M.
Structural properties of MoS_2 "mama"- tubes and related materials
23rd International Winterschool on Electronic Properties of Novel Materials, 7.-14.03.2009, Kirchberg, Austria

146. Wagner, M.; Schneider, H.; Helm, M.; Schartner, S.; Andrews, A. M.; Roch, T.; Strasser, G.
THz sideband generation in GaAs/AlGaAs multi quantum wells
DPG Frühjahrstagung 2009 der Sektion Kondensierte Materie, 22.-27.03.2009, Dresden, Germany

147. Wagner, M.; Schneider, H.; Winnerl, S.; Helm, M.; Roch, T.; Andrews, A. M.; Schartner, S.; Strasser, G.
Efficient THz sideband generation in GaAs/AlGaAs multi quantum wells
16th International Conference on Electron Dynamics in Semiconductors, Optoelectronics and Nanostructures, 24.-28.08.2009, Montpellier, France

148. Wagner, M.; Golde, D.; Stehr, D.; Schneider, H.; Helm, M.; Andrews, A. M.; Roch, T.; Strasser, G.; Kira, M.; Koch, S. W.
Fano profile in the intersubband THz response of photoexcited GaAs/AlGaAs quantum wells
16th International Conference on Electron Dynamics in Semiconductors, Optoelectronics and Nanostructures, 24.-28.08.2009, Montpellier, France

149. Wagner, M.; Golde, D.; Stehr, D.; Schneider, H.; Helm, M.; Andrews, A. M.; Roch, T.; Strasser, G.; Kira, M.; Koch, S. W.
Fano interference in the intersubband THz response of photoexcited GaAs/AlGaAs quantum wells
10th International Conference on Intersubband Transitions in Quantum Wells, 6.-11.09.2009, Montreal, Canada

150. Weißbach, T.; Lubk, A.; Leisegang, T.; Führlich, T.; Wunderlich, F.; Souptel, D.; Behr, G.; Chaplygin, I.; Seifert, G.; Meyer, D. C.; Gemming, S.
Structural and DFT studies on $YFeMnO_5$
DPG Frühjahrstagung 2009 der Sektion Kondensierte Materie, 22.-27.03.2009, Dresden, Germany

151. Weißbach, T.; Riedl, T.; Gemming, T.; Gemming, S.; Zschornak, M.; Gutmann, E.; Stöcker, H.; Leisegang, T.; Meyer, D. C.
Electronic properties of defects in $SrTiO_3$ - theory and experiments
DPG Frühjahrstagung 2009 der Sektion Kondensierte Materie, 22.-27.03.2009, Dresden, Germany

152. Wilde, L.; Bähtz, C.; Borany, J. von; Krügener, J.; Teichert, S.
Simultaneous structural and electrical measurements on Si-doped $Ge_2Sb_2Te_5$ for PCRAM applications
12th International Conference on the Formation of Semiconductor Interfaces, 5.-10.07.2009, Weimar, Germany

153. Winnerl, S.; Zimmermann, B.; Peter, F.; Schneider, H.; Helm, M.
Terahertz emitters and detectors for radially and azimuthally polarized beams
SPIE Europe Microtechnologies for the New Millenium, 4.-6.05.2009, Dresden, Germany

154. Winnerl, S.; Zimmermann, B.; Hubrich, R.; Peter, F.; Schneider, H.; Helm, M.
Free-space propagation of radially and azimuthally polarized terahertz Bessel-Gauss beams
European Conference on Lasers and Electro-Optics and 11th European Quantum Electronics Conference, 14.-19.06.2009, München, Germany

155. Winnerl, S.; Zimmermann, B.; Hubrich, R.; Peter, F.; Schneider, H.; Helm, M.
Photoconductive emitters and detectors for radially and azimuthally polarized terahertz beams
CNRS Workshop "Semiconductor Sources and Detectors of THz Radiation", 16.-17.11.2009, Montpellier, France

156. Wolff, T.; Denker, A.; Hahn, O.; Merchel, S.; Radtke, M.; Reinholz, U.
Quantitative analysis of corroded coins with four non-destructive X-ray methods
19th International Conference on Ion Beam Analysis, 7.-11.09.2009, Cambridge, United Kingdom

157. Wündisch, C.; Posselt, M.; Schmidt, B.; Mücklich, A.; Skorupa, W.; Clarysse, T.; Simoen, E.; Hortenbach, H.
Preparation of shallow n^+-layers in Ge using flash lamp annealing
Nordic Semiconductor Meeting, 14.-17.06.2009, Reykjavik, Iceland

158. Yang, K.; Ruf, H.; Neuhaus, J.; Dekorsy, T.; Villas-Boas Grimm, C.; Helm, M.; Heumann, E.; Huber, G.; Biermann´, K.; Künzel, H.
Saturable absorption mode-locking based on intersubband transitions in quantum wells at 2 µm
European Conference on Lasers and Electro-Optics and 11th European Quantum Electronics Conference, 14.-19.06.2009, München, Germany

159. Yankov, R. A.; Kolitsch, A.; Borany, J. von; Munnik, F.; Donchev, A.; Schütze, M.
Surface modification of Ti and low Al-content Ti alloys for enhanced environmental stability at elevated temperatures
E-MRS 2009 Spring Meeting, 8.-12.06.2009, Strasbourg, France

160. Zhou, S.; Berndt, M.; Bürger, D.; Abrasonis, G.; Heera, V.; Faßbender, J.; Helm, M.; Schmidt, H.
Magneto-transport properties of nanocomposite cobalt/carbon systems
Magnetism Meets Semiconductors: Spin Phenomena in Heterostructures and Novel Materials, 5.-7.01.2009, Bad Honnef, Germany
161. *SPIE Europe Microtechnologies for the New Millennium, 4.-6.05.2009, Dresden, Germany*
162. *International Conference on Magnetism, 26.-31.07.2009, Karlsruhe, Germany*

163. Zhou, S.; Berndt, M.; Bürger, D.; Abrasonis, G.; Radnoczi, G.; Schmidt, H.; Kolitsch, A.; Helm, M.
Spin-dependent transport in C:Co and C:Ni nanocomposite thin films
MRS 2009 Fall Meeting, 30.11.-4.12.2009, Boston MA, USA

164. Zhou, S.; Bürger, D.; Heera, V.; Potzger, K.; Faßbender, J.; Helm, M.; Schmidt, H.
Dilution of Mn in Ge: The evidence from samples' electrical and magneto-transport properties
International Conference on Magnetism, 26.-31.07.2009, Karlsruhe, Germany

165. Zhou, S.; Cizmar, E.; Potzger, K.; Krause, M.; Talut, G.; Helm, M.; Faßbender, J.; Zvyagin, S. A.; Wosnitza, J.; Schmidt, H.
Origin of the ferromagnetism in defective TiO_2 single crystals
International Conference on Magnetism, 26.-31.07.2009, Karlsruhe, Germany

166. Zhou, S.; Potzger, K.; Xu, Q.; Shalimov, A.; Schmidt, H.; Helm, M.; Faßbender, J.
Granular magnetic ZnO: Structure, magnetism and transport properties
Magnetism Meets Semiconductors: Spin Phenomena in Heterostructures and Novel Materials, 5.-7.01.2009, Bad Honnef, Germany
167. *5th International School and Conference on Spintronics and Quantum Information Technology, 4.-11.07.2009, Krakow, Poland*

168. Zhou, S.; Xu, Q.; Hartmann, L.; Mücklich, A.; Helm, M.; Biehne, G.; Hochmuth, H.; Lorenz, M.; Grundmann, M.; Schmidt, H.
ZnO-based magnetic tunnel junctions
DPG Frühjahrstagung 2009 der Sektion Kondensierte Materie, 22.-27.03.2009, Dresden, Germany

169. Zhou, S.; Xu, Q.; Potzger, K.; Talut, G.; Faßbender, J.; Vinnichenko, M.; Grenzer, J.; Helm, M.; Hochmuth, H.; Lorenz, M.; Grundmann, M.; Schmidt, H.
Room temperature ferromagnetism in carbon-implanted ZnO
DPG Frühjahrstagung 2009 der Sektion Kondensierte Materie, 22.-27.03.2009, Dresden, Germany

170. Zschintzsch, M.; Jeutter, N. M.; Borany, J. von; Mücklich, A.
Reactive magnetron sputtering of (GeO_x-SiO_2) superlattices for nanocrystal synthesis
DPG Frühjahrstagung 2009 der Sektion Kondensierte Materie, 22.-27.03.2009, Dresden, Germany
171. *E-MRS 2009 Spring Meeting, 8.-12.06.2009, Strasbourg, France*

Lectures / Talks

1. Bischoff, L.
Application of focused ion and electron beams in materials research
Symposium at Imdea Nanociencia, 4.11.2009, Madrid, Spain
2. *Kolloquiumsvortrag am Leibniz Institut für Oberflächenmodifizierung Leipzig, 10.12.2009, Leipzig, Germany*

3. Brauer, G.
Positron annihilation spectroscopy in connection with activities towards p-type doping of ZnO
Seminar at University of Orissa, Institute of Physics, 16.01.2009, Bhubaneswar, India

4. Brauer, G.
Characterisation of ZnO single crystals – A challenge to positron annihilation spectroscopy
Seminar am Institut für Kristallzüchtung Berlin, 17.08.2009, Berlin, Germany
5. *Seminar at Charles University Prague, 2.11.2009, Prague, Czech Republic*

6. Eng, L. M.; Grafström, S.; Seifert, G.; Gemming, S.
Polarisationsinduzierte Oberflächenfunktionalität an Ferroelektrika
Abschlusskolloquium SPP 1157 „Integrierte elektrokeramische Funktionsstrukturen „ 21.-22.09.2009, Bonn, Germany

7. Erbe, A.
Capped colloidal particular: A model system for spin arrangements
Workshop SPP 1296 "Heterogene Keim- und Mikrostrukturbildung", 13.-14.10.2009, Bayreuth, Germany

8. Faßbender, J.
Künstliche magnetische Materialien durch Nanostrukturierung
Kolloquiumsvortrag, Institut für Physik, Universität Mainz, 16.02.2009, Mainz, Germany

9. Faßbender, J.
Nanomagnets - Created and tailored by ions
Forschungsseminar, Institut für Physik, HU Berlin, 13.05.2009, Berlin, Germany
10. *SFB 668 - Kolloquium „Magnetismus vom Einzelatom zur Nanostruktur", Institut für Angewandte Physik und Zentrum für Mikrostrukturforschung der Universität Hamburg, 16.06.2009, Hamburg, Germany*
11. *Kolloquiumsvortrag Fachbereich Physik, Universität Paderborn, 2.07.2009, Paderborn, Germany*

12. Gemming, S.
Unusual transport phenomena in nanostructured materials
NanoSeminar, 5.02.2009, Dresden, Germany

13. Gemming, S.
Modelling electronic and transport properties in ferroic devices
Fraunhofer IWM - Seminarreihe zur Materialforschung, 13.02.2009, Freiburg, Brsg., Germany

14. Gemming, S.
Transport through nanostructures
Sächsisches Landesseminar Theoretische Chemie, 26.02.2009, Leipzig, Germany

15. Gemming, S.
Simulation of bone replacement materials
Seminar "Topical Problems in Theoretical Physics", TU Chemnitz, 16.12.2009, Chemnitz, Germany

16. Gemming, S.
Multi-scale approaches for structure and conductivity of complex materials
Colloquium on Multi-Scale Modeling, 4.05.2009, Vienna, Austria

17. Gemming, S.
Density-functional theory in materials science
FZD Theory Seminar Series, 17.12.2009, Dresden-Rossendorf, Germany

18. Grebing, J.; Dietsche, R.; Ganteför, G.; Kirchner, T.; Scheer, E.
Electronic transport measurements on Si_4 clusters
Clustertreffen 2009, 4.-9.10.2009, Herzogenhorn, Schwarzwald, Germany

19. Grenzer, J.
X-ray investigations off nanostructures manufactured by focused ion beam techniques
Seminar, Charles University Prague, 6.01.2009, Prague, Czech Republic

20. Helm, M.
Nanometrologie für die Nanoelektronik
Talk at BMBF Cluster of Excellence Meeting „Cool Silicon", 6.05.2009, Dresden, Germany

21. Helm, M.
Solid state spectroscopy using an infrared free-electron laser
Colloquium at Institute for Molecules and Materials, Radboud University, 10.11.2009, Nijmegen, The Netherlands

22. Helm, M.
Infrared solid state spectroscopy using a free-electron laser
Seminarvortrag bei ANKA, 2.03.2009, Karlsruhe, Germany

23. Helm, M.
Silicon based light emitters: From rare-earth doped MOS devices to resonant-cavity LEDs
Seminar at van der Waals - Zeeman Institute, University Amsterdam, 27.03.2009, Amsterdam, The Netherlands

24. Hubrich, R.
Radiale Moden in THz-Feldern
Drittes THz-Frischlinge-Meeting 2009, 7.-10.06.2009, Berlin, Germany

25. Keller, A.; Facsko, S.; Möller, W.
Self-organized ripple patterns by ion erosion - Experiment, theory, and application
Seminar, Institute of Solid State Electronics, TU Vienna, 16.06.2009, Vienna, Austria

26. Kosmata, M.
Ion beam analysis with sub nanometer depth resolution
4th Graduate Students Seminar, 16.-18.09.2009, Krögis, Germany

27. Lenz, K.
Spin dynamics in ferromagnets: Gilbert damping vs. two-magnon scattering
Talk at the Physics Seminar Series, 12.10.2009, Colorado Springs, USA
28. *Talk at the Electromagnetics Group Seminar, 13.10.2009, Boulder, Colorado, USA*

29. Lenz, K.
Tailoring magnetic properties using ion beam irradiation
Division Seminar of the Condensed Matter Theory Group, 15.10.2009, Irvine, CA, USA

30. Lenz, K.; Marko, D.; Strache, T.; Faßbender, J.
Spin wave excitations: coupling and damping effects in ultrathin films
448. WE-Heraeus-Seminar: Excitement in Magnetism: Spin-dependent Scattering and Coupling of Excitations in Ferromagnets, 22.-25.11.2009, Ringberg, Germany

31. Liedke, B.; Heinig, K.-H.; Möller, W.
Modelling of ion beam mixing with phase separation - Simulation of damage formation and thermally activated relaxation
Seminar at Department of Physics, University of Bialystok, 21.11.2009, Bialystok, Poland

32. Liedke, B.; Heinig, K.-H.; Möller, W.
Atomistic description of ion-induced surface patterning - Role of surface / bulk defects and viscous flow
Meeting DFG Forschergruppe 845 "Selbstorganisierte Nanostrukturen durch niederenergetische Ionenstrahlerosion", 31.03.2009, Köln, Germany

33. Merchel, S.; Bichler, M.; Sterba, J. H.
On the reliability of target element data for cosmogenic nuclide exposure dating
Seminar Activation Analysis and Gamma-Spectroscopy, 25.-27.02.2009, TU Vienna, Austria

34. Merchel, S.; Grambole, D.; Grötzschel, R.; Munnik, F.; Neelmeijer, C.
Accelerator mass spectrometry (AMS) and ion beam analysis (IBA) with the new 6 MV accelerator at FZ Dresden-Rossendorf
Seminar Activation Analysis and Gamma-Spectroscopy, 25.-27.02.2009, TU Vienna, Austria

35. Merchel, S.
Terrestrial cosmogenic radionuclides and the new AMS facility DREAMS
Seminar über aktuelle Themen aus Kosmochemie und Astrophysik, 06.05.2009, Universität Mainz, Germany

36. Merchel, S.; Munnik, F.
Beschleunigermassenspektrometrie und Ionenstrahlanalytik
Seminarreihe "Moderne analytische Methoden der Physik", 14.07.2009, Berlin, Germany

37. Merchel, S.
Cosmogenic nuclides: Endless opportunities?
GeoKolloquium - Geowissenschaftliches Kolloquium der Fakultät für Geowissenschaften, Geotechnik & Bergbau, TU Bergakademie Freiberg, 8.04.2009, TU Bergakademie Freiberg, Germany

38. Möller, W.
Nanostructures by ion-driven self-organisation: Can ions induce order?
Colloquium at Shanghai Institute of Microsystems and Information Technology, 5.05.2009, Shanghai, China

39. Möller, W.
Self-organized nanostructures by ion irradiation
Polymer-Physics-Seminar, Charles University Prague, 10.11.2009, Prague, Czech Republic

40. Munnik, F.; Merchel, S.
Ion beam analysis (IBA) for thin film studies
Seminarreihe "Moderne analytische Methoden der Physik", 14.07.2009, Berlin, Germany

41. Neelmeijer, C.
Zerstörungsfreie Materialanalyse an Kunstwerken
Gastvorlesung, 24.02.2009, HfBK Dresden, Germany

42. Neidhardt, J.
Atomic billiard – Materials science using hyperthermal ions
Lecture, 16.11.2009, University Linköping, Sweden

43. Odor, G.; Liedke, B.; Heinig, K.-H.
Mapping of 2+1 dimensional KPZ growth onto driven lattice gas model of dimers

International Seminar on "Many-body systems far from equilibrium: Fluctuations, slow dynamics and long-range interactions", 16.-27.02.2009, Dresden, Germany

44. Rebohle, L.
Rare earth implanted MOS light emitting devices
Seminar Talk, Department of Physics, University of Hong Kong 8.05.2009, Hong Kong, China

45. Rebohle, L.
Si-based light emitters: How bright is the future?
Seminar Talk, Department of Electronics, University of Barcelona, 29.09.2009, Barcelona, Spain

46. Schneider, H.
Time-resolved infrared and terahertz spectroscopy of semiconductor quantum structures
Seminar, Institute of Optics and Precision Mechanics, Xi'an University of Technology, 22.06.2009, Xi'an, China

47. Schneider, H.
Ultrafast infrared and terahertz spectroscopy of semiconductor quantum structures
Physics Colloquium, Shanghai Jiao Tong University, 30.12.2009, Shanghai, China

48. Schneider, H.
Infrared and THz spectroscopy of semiconductor quantum structures with modelocked tabletop and free-electron lasers
Seminar, Rensslaer Polytechnic Institute, 14.09.2009, Troy NY, USA

49. Skorupa, W.; Anwand, W.; Gebel, T.
Energy pulse modification of electronic materials: From electronics via photonics to other advanced materials
European Project Meeting "Teramagstor", 28.-29.05.2009, Santorini, Greece

50. Skorupa, W.; Anwand, W.; Gebel, T.
Energy pulse modification of electronic materials: from electronics via photonics to other advanced materials
Seminar at the University of Hong Kong, 8.05.2009, Hong Kong, China

51. Zhou, J.; Facsko, S.; Keller, A.; Möller, W.
Ion sputtering of Si surfaces at normal incidence: roughening versus smoothening
Meeting DFG-Forschergruppe 845 "Selbstorganisierte Nanostrukturen durch niederenergetische Ionenstrahlerosion", 31.03.2009, Köln, Germany

PhD Theses

1. Berndt, M.
Phase separation in carbon: transition metal nanocomposite thin films
TU Dresden, 21.12.2009

2. Beyer, V.
Nanocrystals for nanodot memories - Ion beam synthesis and electrical studies
Leibniz Universität Hannover, 11.12.2009

3. Güttler, D.
An investigation of target poisoning during reactive magnetron sputtering
TU Dresden, 12.03.2009, Wissenschaftlich-Technische Berichte FZD-515 (2009)

4. Heller, R.
Wechselwirkung langsamer hochgeladener Ionen mit der Oberfläche von Ionenkristallen
TU Dresden, 30.06.2009, Wissenschaftlich-Technische Berichte FZD-520 (2009)

5. Keller, A.
Evolution of ion-induced ripple patterns - Anisotropy, nonlinearity, and scaling
TU Dresden, 8.06 2009

6. Ou, X.
Defect engineering in SIMOX processing
Shanghai Institute of Microsystems and Information Technology, Chinese Academy of Science, Shanghai, China, 1.07.2009

7. Potfajova, J.
Silicon based microcavity enhanced light emitting diodes
TU Dresden, 15.12.2009, Wissenschaftlich-Technische Berichte FZD-526 (2009)

Master & Diploma Theses

1. Buhl, M.
   Herstellung und magnetische Charakterisierung von Co-Nanopartikeln auf ionenstrahlerodierten Substraten
   Westsächsische Hochschule Zwickau, 30.09.2009
2. Hubrich, R.
   Untersuchung von Terahertz-Moden unterschiedlicher Polarisation
   TU Dresden, 17.11.2009
3. Lehmann, J.
   Correlation between electrical and optical properties of europium doped SiO_2-layers
   TU Dresden, 7.10.2009
4. Seeger, M.
   Charakterisierung von Si- MOS-Dioden mittels Kapazitätsspektroskopie
   TU Dresden, 28.08.2009

Organization of Conferences / Workshops

1. Borany, J. von, Jäger, C.
   Workshop "He-Ion Microscopy and its Applications"
   9.12.2009, Forschungszentrum Dresden-Rossendorf, Germany
2. Chason, E., Cuerno, R., Gray, J., Heinig, K.-H.
   MRS 2009 Fall Meeting, Symposium "Nanoscale Pattern Formation"
   30.11.-3.12.2009, Boston MA, USA
3. Facsko, S., Heinig, K.-H., Keller, A., Rauschenbach, B.
   International Workshop "Nanoscale Modification of Surfaces and Thin Films"
   30.08.–3.09.2009, Rathen, Germany
4. Liu, H. C., Gmachl, C., Helm, M.
   10th International Conference on Intersubband Transitions in Quantum Wells (ITQW 2009)
   6.-11.09.2009, Montreal, Canada
5. Rafaja, D., Bähtz, C.
   EUROMAT 2009, Symposium "X-ray Characterization of Microstructure Features",
   7.-10.09.2009, Glasgow, United Kingdom

Laboratory Visits

1. Abrasonis, G.
   ESRF Grenoble, France; 30.06.-5.07., 27.08.-5.09.2009
2. Bischoff, L.
   University of Madrid, Spain; 2.-6.11.2009
3. Borany, J. von
   ESRF Grenoble, France; 21.-28.01.2009
4. Bunce, C.
   Swiss Light Source, PSI Villigen, Switzerland; 13.-22.12.2009
5. Drachenko, O.
   Kurchatov Institute Moscow/Institute for Microstructures Nishni Novgorod, Russia; 7.-14.04.2009
6. Drachenko, O.
   Laboratoire Nationale des Champs Magnetiques Pulses, Toulouse, France; 12.-21.06.2009
7. Grenzer, J.
   ESRF Grenoble, France; 14.-21.04., 20.-26.05., 13.-17.07., 13.-15.10., 7.-14.12.2009
8. Grebing, J.
   Swiss Light Source, PSI Villigen, Switzerland; 7.-10.09.2009

9. Grötzschel, R.
CMAM Madrid, Spain; 4.-7.05., 11.-14.05.,21.-23.05.2009
10. Hanf, D.
MPI Halbleiterlabor, München, Germany; 5.-9.04.2009
11. Hanisch, A.
ESRF Grenoble, France; 30.01.-3.02., 4.-10.07.2009
12. Hanisch, A.
DESY Hamburg, Germany; 2.-8.12.2009
13. Heinig, K.-H.
KFKI Budapest, Hungary; 14.-18.06.2009
14. Höwler, M.
IPHT Jena, Germany; 23.-25.05.2009
15. Höwler, M.
Universität Kaiserslautern, 23.-27.08.2009
16. Keller, A.
TU Wien, Austria; 16.-27.06.2009
17. Kögler, R.
SMIT Shanghai, Hangzhou University, China; 3.-10.05.2009
18. Körner, M.
Swiss Light Source, PSI Villigen, Switzerland; 16.-25.02., 6.-10.09., 13.-22.12.2009
19. Kovacs, G.
ESRF Grenoble, France; 16.-23.06., 30.06.-5.07., 27.08.-1.09.2009
20. Liedke, B.
KFKI Budapest, Hungary; 14.-28.06.2009
21. Liedke, B.
University Bialystok, Poland; 24.09.-4.10., 18.-22.11.2009
22. Liedke, M.O.
Swiss Light Source, PSI Villigen, Switzerland; 26.04.-3.05.2009
23. Marko, D.
Swiss Light Source, PSI Villigen, Switzerland; 16.-25.02., 13.-22.12.2009
24. Martinavisius, A.
ESRF Grenoble, France; 27.08.-5.09.2009
25. Merchel, S.
Aix-en-Provence, France; 2.-9.07.2009
26. Merchel, S.
Ljubljana, Slovenien; 17.-22.07.2009
27. Möller, W.
SMIT Shanghai, China; 3.-7.05.2009
28. Morawetz, K.
ICCMP Brasilia, Brazil; 7.-30.01., 5.-19.03., 15.-29.04., 4.-19.06.2009
29. Numazawa, S.
KFKI Budapest, Hungary; 6.-18.07., 25.11.-6.12.2009
30. Rebohle, L.
SMIT Shanghai, City University Hong Kong, China; 3.-12.05.2009
31. Schneider, H.
Xi'an University, Beijing, China; 15.-24.06.2009
32. Schumann, T.
Oslo University, Norway; 7.-20.06.2009
33. Shalimov, A.
ESRF Grenoble, France; 16.-23.06., 17.-24.11.2009
34. Shevchenko, N.
ESRF Grenoble, France; 13.-17.07.2009

35. Skorupa, W.
KFKI Budapest, Hungary; 22.-26.04.2009

36. Skorupa, W.
SMIT Shanghai, City University Hong Kong, China; 3.-12.05.2009

37. Skorupa, W.
Uppsala, Sweden; 5.-9.08.2009

38. Strache, T.
Swiss Light Source, PSI Villigen, Switzerland; 16.-25.02., 26.04.-3.05., 6.-10.09., 5.-11.10., 13.-22.12.2009

39. Strache, T.
Glasgow University, United Kingdom; 11.-15.05., 29.11.-4.12.2009

40. Voelskow, M.
KFKI Budapest, Hungary; 22.-26.04.2009

41. Wintz, S.
Swiss Light Source, PSI Villigen, Switzerland; 16.-25.02., 26.04.-3.05., 6.-10.09., 5.-11.10., 13.-18.12.2009

42. Wintz, S.
Advanced Light Source, Berkeley, USA; 7.-27.05., 26.10.-9.11.2009

43. Wintz, S.
Canadian Light Source, Saskatoon, Canada; 5.-12.12.2009

44. Zschornak, M.
DESY Hamburg, Germany; 10.-15.09.2009

Guests

1. Akhmerov, G.
Izhevsk State Technical University, Russia; 9.03.-1.05.2009

2. Andermann, C.
Universite de Rennes, France and TU Bergakademie Freiberg, Germany; 28.09.-17.10.2009

3. Arpaci, S.
Ankara University, Turkey; 1.07.-31.08.2009

4. Avashti, D. K.
Inter-University Accelerator Centre, New Delhi, India; 3.-6.06.2009

5. Bergmaier, A.
Institut für Angewandte Physik, Universität der Bundeswehr, München, Germany; 8.-12.12.2009

6. Bhattacharyya, J.
Tata Institute of Fundamental Research, Mumbai, India; 7.01.-28.02.2009

7. Bichler, M.; Eder, F.; Sterba, J.H.
Atominstitut der Österreichischen Universitäten, TU Wien, Austria 15.-18.12.2009

8. Bregolin, F.
Universidade Federal do Rio Grande do Sul, Departamento de Física, Porto Alegre, Brazil; 1.02.-24.04.2009

9. Dzenisevich, S.
Yanka Kupala State University, Grodno, Belarus; 31.08.-1.11.2009

10. Enyashin, A.
Institute of Solid State Chemistry, Ekaterinburg, Russia; 27.05.-1.06.2009

11. Gieniusz, R.
University of Bialystok, Poland; 30.01.-28.02.2009

12. Ionescu, M.
Austrian Nuclear Science and Technology Organization, Sydney, Australia; 3.-4.09.2009

13. Ivkova, T.
Institute of Nuclear Fusion, Kurchatov Institute, Moscow; 5.-26.04.2009

14. John, V.
Manipal Institute of Technology, Manipal , India; 9.06.-28.07.2009

15. Khan, S.
Inter-University Accelerator Centre, New Delhi, India; 22.03.-14.05.2009
16. Kumar, H.
Indian Institute of Technology, New Delhi, India; 26.07.-15.10.2009
17. Kutschera, W.
Fakultät für Physik, Beschleunigerlabor (VERA), Universität Wien, Austria; 30.11.-1.12.2009
18. Liechtenstein, V.
Institute of Nuclear Fusion, Kurchatov Institute, Moscow; 5.-26.04.2009
19. Li, L.
Department of Nuclear Physics and Nuclear Technology, Beijing University , China; 1.10.-31.12.2009
20. Mackova, A.
Laboratory of Nuclear Analytical Methods, Nuclear Institute of ASCZ, Rez, Czech Republic; 19.-20.03.2009
21. Markov, A.
Institute of High Current Electronics, Tomsk, Russia; 5.10.-13.11.2009
22. Mazalski, P.
University Bialystok, Poland; 16.05.-14.06., 11.07.-15.08., 18.09.-11.10.2009
23. Menendez Dalmau, E.
Universidad Autonoma de Barcelona, Spain; 3.08.-6.11.2009
24. Moiseev, K.
Ioffe Physical-Technical Institute, St. Petersburg, Russia; 1.-9.05.2009
25. Nazarov, A.
Institute of Semiconductor Physics, Kiew, Ukraine; 15.06.-7.08.2009
26. Oates, T.
Linköping University, Sweden; 12.10.-6.11.2009
27. Odor, G.
KFKI Budapest, Hungary; 15.-20.02., 24.-30.03., 31.10.-13.11.2009
28. Om, P.S.
Amity Institute of Nanotechnology, Noida, India; 25.05.-30.07.2009
29. Ou, X.
Shanghai Institute of Microsystems and Information Technology, China; 1.07.-31.12.2009
30. Poljotow, J.
Izhevsk State Technical University, Russia; 31.08.-1.11.2009
31. Prucnal, S.
University Marie Sklodowska Curie, Lublin, Poland; 1.03.-30.04.2009
32. Pryadko, E.
Institute of High Current Electronics, Tomsk, Russia; 30.10.-18.12.2009
33. Sasaki, T.
Tohoku University, Sendai, Japan; 1.09.-31.10.2009
34. Shoshan, N.
Technion, Haifa, Israel; 1.01.-1.02.2009
35. Song, J.
Advanced Analysis Center, Korea Institute of Science and Technology, Seoul, South Korea; 19.-20.05.2009
36. Süle, P.
KFKI Budapest, Hungary; 30.08.-20.09., 25.10.-13.11.2009
37. Sundaravel, B.
Materials Science Division, Indira Gandhi Centre for Atomic Research, Kalpakkam, India; 13.-18.09.2009
38. Tyagulskiy, I.
Institute of Semiconductor Physics, Kiew, Ukraine; 15.06.-7.08.2009
39. Virsek, M.
Jozef Stefan Institute, Ljubljana, Slovenia; 19.-31.01.2009

40. Yao, S.
School of Microelectronics and Solid-State Electronics, University of Electronic Science and Technology of China , Chengdu, Sichuan, China; 20.09.-31.12.2009
41. Ye, S.
Universität Duisburg-Essen, Germany; 10.-17.02.2009
42. Yilgin, R.
Gebze Institute of Technology, Department of Physics, Gebze-Kocaeli, Turkey; 16.06.-25.11.2009
43. Zhou, J.
University Shanghai, China; 1.01.-9.10.2009

AIM Visitors

1. Abrasheva, M.
University of Sofia, Bulgaria; 22.02.-4.03.2009
2. Barlak, M.
Soltan Institute for Nuclear Studies, Otwock, Poland; 22.-27.11.2009
3. Barquinha, P.
CENIMAT Lisboa, Portugal; 26.-31.07.2009
4. Bugoi, R.
Institute for Nuclear Physics, Bucharest, Romania; 6.-13.12.2009
5. Caciolli, A.
INFN Padova, Italy; 1.-14.03., 18.-22.10.2009
6. Capogrosso, V.
INFN Padova, Italy; 8.-13.03.2009
7. Constantinescu, B.
Institute for Nuclear Physics, Bucharest, Romania; 6.-13.12.2009
8. Dekov, V.
University of Sofia, Bulgaria; 22.02.-4.03.2009
9. Erhard, M.
INFN Padova, Italy; 22.02.-7.03.2009
10. Franz, R.
University Leoben, Austria; 31.03.-3.04.2009
11. Gomez, P.R.
University Sevilla, Spain; 30.10.-6.11.2009
12. Gösselsberger, C.
TU Vienna, Austria; 25.01.-7.02., 26.04.-1.05.2009
13. Gonzalez Arrabal, R.
Universidad Politécnica de Madrid, Spain; 13.-19.12.2009
14. Igreja, R.
CENIMAT Lisboa, Portugal; 26.-31.07.2009
15. Kotb, H.
IEMT Warsaw, Poland; 23.-30.05.2009
16. Martins, R.
INT Sacavem, Portugal; 3.-19.12.2009
17. Meissl, W.
TU Vienna, Austria; 25.01.-7.02.2009
18. Nasdala, L.
University Vienna, Austria; 6.-9.04.2009
19. Pagowska, K.
IEMT Warsaw, Poland; 6.-15.01.2009
20. Preuschl, F.
University Vienna, Austria; 6.-9.04.2009

21. Sartowska, N.
Soltan Institute for Nuclear Studies, Otwock, Poland; 22.-27.11.2009

22. Sicinski, M.
Unversity Lodz, Poland; 12.-15.10.2009

23. Stonert, A.
IEMT Warsaw, Poland; 23.-30.05.2009

24. Turos, A.
IEMT Warsaw, Poland; 6.-15.01., 2.-4.03.2009

25. Vasko, C.
TU Vienna, Austria; 26.04.-1.05.2009

26. Winklehner, D.
TU Vienna, Austria; 6.-17.07.2009

FEL Visitors

1. Aleksa, V.
Vilnius University, Lithuania; 5.-11.04., 6.-10.05.2009

2. Balocco, C.
Manchester University, United Kingdom; 6.-9.02., 28.02.-1.03.2009

3. Kasjoo, S.R.
Manchester University, United Kingdom; 6.-9.02., 28.02.-5.03., 23.-27.07., 11.-14.08.2009

4. Lu, X.
Manchester University, United Kingdom; 28.02.-1.03.2009

5. Orlita, M.
High Field Laboratory Grenoble, France; 20.-25.09.2009

6. Porter, N.
University of Sheffield, United Kingdom; 27.-31.01., 25.02.-1.03.2009

7. Sablinskas, V.
Vilnius University, Lithuania; 5.-11.04., 6.-10.05.2009

8. Sandall, I.
University of Sheffield, United Kingdom; 27.-31.01., 25.02.- 1.03.2009

9. Song, A. M.
Manchester University, United Kingdom; 6.-8.02., 23.-25.07.2009

10. Vaskevicius, K.
Vilnius University, Lithuania; 5.-11.04.2009

ROBL-MRH Visitors

1. Bartels, M.
Institut für Röntgenphysik, Georg-August Universität Göttingen, Germany; 21.-24.02.2009

2. Bayer, B.
Department of Engineering, University of Cambridge, United Kingdom; 22.-28.04.2009

3. Biermanns, A.
Fachbereich Physik, Universität Siegen, Germany; 31.01.- 3.02., 5.-10.07.2009

4. Birch, J.
Department of Physics, Chemistry and Biology, Linkoeping University, Sweden; 6.-12.05.2009

5. Braz Fernades, F.
CENIMAT - Materials Science Department, Caparica, Portugal; 23.-27.01.2009

6. Buljan, M.
Department of Condensed Matter Physics, Charles University Praha, Czech Republic; 15.–21.04.; 9.–15.12.2009

7. Dopita, M.
Institute of Materials Science, Technische Universität Bergakademie Freiberg, Germany; 28.-31.01., 21.-27.10.2009

8. Gaca, J.
Institute of Electronic Materials Technology, Warsaw, Poland; 10.–14.07.2009

9. Hoefer, S.
Fachbereich Röntgenoptik, Friedrich-Schiller Universität Jena, Germany; 18.–21.02.2009

10. Höglund, C.
Department of Physics, Chemistry and Biology, Linkoeping University, Sweden; 6.-12.05., 16.-21.12.2009

11. Holy, V.
Department of Condensed Matter Physics, Charles University Praha, Czech Republic; 15.–21.04.; 9.–15.12.2009

12. Karimbi Koosappa, M.
CENIMAT - Materials Science Department, Caparica, Portugal; 23. - 27.01.2009

13. Kalinichenka, S.
Fraunhofer Institut IFAM, Dresden, Germany; 18.–22.09.2009

14. Kräußlich, J.
Fachbereich Röntgenoptik, Friedrich Schiller Universität Jena, Germany; 18.–21.02.2009

15. Krüger, S. .
Institut für Röntgenphysik, Georg-August Universität Göttingen, Germany; 21 -24.02.2009

16. Lechner, R.
Institute of Physics, University of Leoben, Austria, 27.02.–3.03.; 23.–29.09.2009

17. Mazur, K.
Institute of Electronic Materials Technology, Warsaw, Poland; 10.–14.07.2010

18. Meduna, M.
Institute of Condensed Matter Physics, Masaryk University Brno, Czech Republic; 27.02.–3.03.2009

19. Motylenko, M.
Institute of Materials Science, Technische Universität Bergakademie Freiberg, Germany; 28.-31.01., 21.-27.10.2009

20. Navarro Quezada, A.
Institut für Halbleiterphysik, Johannes Kepler Universität Linz, Austria; 27.02.–3.03.; 23.– 29.09.2009

21. Neubauer, H.
Institut für Röntgenphysik, Georg-August Universität Göttingen, Germany; 21.-24.02.2009

22. Radic, N.
Materials Physics, Rudjer Boskovic Institute, Zagreb, Croatia; 9.–15.12.2009

23. Röntzsch, L.
Fraunhofer Institut IFAM, Dresden, Germany; 18.–22.09.2009

24. Rovezzi, M.
Institute of Semiconductor Physics, Johannes Kepler University Linz, Austria; 27.02.– 3.03.; 23.–29.09.2009

25. Silva Cordeiro, R.
CENIMAT - Materials Science Department, Caparica, Portugal; 23.-27.01.2009

26. Vales, V.
Department of Condensed Matter Physics, Charles University Praha, Czech Republic; 15.–21.04.2009

27. Wirth, C.
Department of Engineering, University of Cambridge, United Kingdom; 22.-28.04.2009

28. Wojcik, M.
Institute of Electronic Materials Technology, Warsaw, Poland; 10.–14.07.2009

29. Wüstefeld, C.
Institute of Materials Science, Technische Universität Bergakademie Freiberg, Germany; 28.-31.01., 21.-27.10.2009

30. Zastrau, U.
Fachbereich Röntgenoptik, Friedrich Schiller Universität Jena, Germany; 18.–21.02.2009

Colloquium

1. Aumayr, F. - Institut für Allgemeine Physik, TU Wien, Austria
   Interaction of slow highly-charged ions with solid surfaces
   29.06.2009
2. van den Berg, J. - Joule Physics Laboratory and Institute for Materials Research, University of Salford, United Kingdom
   Medium energy ion scattering (MEIS) for the high depth resolution characterisation of ultra shallow implant effects and high k-dielectric gate oxide layers
   10.12.2009
3. Golser, R. - Fakultät für Physik - Isotopenforschung, TU Wien, Austria
   Beschleunigermassenspektrometrie und Ionenstrahlanalyse bei VERA
   4.06.2009
4. Grützmacher, D. - Institut für Bio- und Nanosysteme (IBN-1), Forschungszentrum Jülich, Germany
   Semiconductor nanostructures: On the search for ultimately scaled devices
   5.03.2009
5. Jörg, G. - Institut für Radiochemie, TU München, Germany
   Determination of long-lived radionuclides, which are relevant for final disposal, by radiometric and sophisticated mass-spectrometic methods
   16.04.2009
6. Lerch, W. - Centrotherm thermal solutions GmbH, Blaubeuren, Germany
   Advanced activation strategies for boron and arsenic by combinations of single, multiple flash anneals and spike rapid thermal annealing
   24.09.2009
7. Masselink, T. - Institut für Physik, Humboldt Universität Berlin, Germany
   Strained epitaxy for high-performance mid-infrared quantum-cascade lasers
   9.07.2009
8. McCord, J. - Leibniz Institut für Festkörper- und Werkstoffforschung Dresden, Germany
   Aspects of magnetic heterostructures - statics and dynamics
   19.11.2009
9. Michel, R. - Zentrum für Strahlenschutz und Radioökologie, Leibnitz Universität Hannover, Germany
   Untersuchung langlebiger Radionuklide in der Umwelt mittels AMS: Aktuelle Entwicklungen und Anwendungen in den Umweltwissenschaften
   11.06.2009
10. Schneider, C. M. - Institut für Festkörperforschung, Forschungszentrum Jülich, Germany
    Magnetism and sprintronics: Research activities at the IFF in Jülich
    2.04.2009
11. Schreyer, A. - Institute for Materials Research, GKSS Research Center, Germany
    Material science with photons and neutrons at GKSS
    5.11.2009
12. Schroer, C. - Institut für Strukturphysik, TU Dresden, Germany
    Microscopy and tomography using hard X-rays
    8.10.2009
13. Schubert, M. - Department of Electrical Engineering and Center for Materials Research and Analysis, University of Nebraska-Lincoln, USA
    Generalized terahertz to ultraviolet ellipsometry in nanoscience: Optical, electrical and structrural properties of glancing angle deposited hybrid nanostructures
    13.08.2009
14. Tautz, S. - Institut für Bio-und Nanosysteme (IBN-3), Forschungszentrum Jülich, Germany
    Organic molecules on metals: From surface science to molecular electronics
    17.12.2009
15. Timm, C. - Institut für Theoretische Physik, TU Dresden, Germany
    Magnetism and transport: From molecules to semiconductors
    14.05.2009

16. Toulemonde, M. - Center of Research on Ions Materials and Photonics at GANIL, Caen, France
Surface material modifications by slow and high charge ions: Role of the electron-phonon coupling
29.01.2009

FZD Materials Science Seminar

1. Erbe, A.
Colloids: Mesoscopic model systems for matter on the nanoscale
16.12.2009
2. Heera, V.
Superconductivity in Ga doped Ge
20.10.2009
3. Heinig, K.-H.
Nanodots, nanowires, surface pattern –Atomistic simulations in materials science
23.02.2009
4. Kanjilal, A.
Interplay between the microstructure and the optical properties of Er-doped Ge-rich SiO_2 layers
17.11.2009
5. Krause-Rehberg, R.
Materials research with positrons - The EPOS Project at FZD
21.04.2009
6. Rebohle, L.
Rare earth implanted MOS light emitting devices
17.03.2009
7. Kögler, R.
Silicon-on-insulator (SOI) materials: Intention, production, prospects
8.09.2009

IIM Seminars

1. Giraud, R. - Laboratoire de Photonique et de Nanostructures, Marcoussis, France
Quantum spin transport in GaMnAs nanomagnets
8.05.2009
2. Grebing, J. - Universität Konstanz, Germany
Elektronische Transportmessungen durch Si4-Cluster
1.04.2009
3. Heine, T. - School of Engineering and Science, Jacobs University, Bremen, Germany
Computational science on the nanoscale: Nanoelectromechanics and nanopores
5.10.2009
4. Kelling, J. - TU Dresden, Germany
NVIDIA-Grafikkarten zum parallelen Rechnen von Monte-Carlo-Simulationen
29.09.2009
5. Kirchner, T. - Universität Konstanz, Germany
Electrical conduction through single molecule junctions
8.07.2009
6. Ling, F. C. C. - Department of Physics, The University of Hong Kong, China
p-type doping of ZnO by ion implantation and radio frequency magnetron sputtering
11.08.2009
7. Löser, M. - Institut für Angewandte Physik, Universität Münster, Germany
Fasergestützte Repetitionsratenstabilisierung eines diodengepumpten Ultrakurzpuls-Erbium-Faserlasers
9.01.2009
8. Meier, G. - Universität Hamburg, Germany
Current-induced magnetization dynamics: x-ray microscopy and rf-transport experiments
26.10.2009

9. Moiseev, K. - Ioffe Physical-Technical Institute of the Russion Academy of Science, St. Petersburg, Russia
Low-dimensional nanoobjects in narrow-gap type II antymonide-based heterostructures
6.05.2009

10. Nazarov, A.N. - Lashkaryov Institute of Semiconductor Physics, National Academy of Sciences of Ukraine, Kiev, Ukraine
Study of amorphous Si_xC_{1-x}:H and $Si_xC_yO_z$:H films on crystalline silicon for light-emission
7.07.2009

11. Oesterlin, P. - INNOVAVENT GmbH, Göttingen, Germany
Laser–Annealing mit frequenzverdoppelten Festkörperlasern: Anwendungen und Technologie
26.2.2009

12. Przybylski, M. - MPI für Mikrostrukturphysik Halle, Germany
Oscillatory magnetic anisotropy originating from quantum well states in Fe films
5.10.2010

13. Reichel, D. - TU Dresden, Germany
T-Messung bei Kurzzeittemperung: Eine Übersicht
17.02.2009

14. Sadewasser, S. - Humboldtzentrum Berlin, Germany
Kelvin probe force microscopy on semiconductors
2.11.2009

15. Sharma, R. - MPI for the Science of Light, University Erlangen-Nürnberg, Germany
Electrodynamically confined microscale lasers
21.09.2009

16. Villis, B.J. - School of Physics, University of Melbourne, Australia
The electrical and optical properties of defects in ion implanted silicon
26.11.2009

17. Vogel, A. - Universität Hamburg, Germany
Enhanced spin injection and detection in spin valves with integrated tunnel barriers
1.07.2009

18. Wiesenhütter, U. - IFW Dresden, Germany
Hochauflösende Transmissionselektronenmikroskopie an Übergangsmetall-Partikeln
30.06.2009

19. Windl, W. - Materials Science and Engineering Department, Ohio State University, USA
Ab-initio calculations for silicon as spintronics material
29.07.2009

20. Zeh, C. - TU Dresden, Germany
Interferometrie mit polarisationserhaltenden Glasfasern und Anwendungen auf die streuende optische Nahfeldmikroskopie
4.02.2009

Projects

1. 03/2004 – 02/2009 European Union EU
IA-SFS - Integrating activity on synchrotron and free electron laser science
Prof. M. Helm Tel.: 0351 260-2260 m.helm@fzd.de

2. 11/2004 – 12/2009 Silicon Sensor Berlin GmbH Industry
Hochenergie-Ionenimplantation für optische Sensoren
Dr. J. von Borany Tel.: 0351 260 3378 j.v.borany@fzd.de

3. 04/2005 – 03/2010 European Union EU
Technology for the production of massively parallel intelligent cantilever-probe platforms for nanoscale analysis and synthesis (PRONANO)
Dr. B. Schmidt Tel.: 0351 260 2726 bernd.schmidt@fzd.de

4. 06/2005 – 03/2010 Deutsche Forschungsgemeinschaft DFG
Mössbauerspektroskopie an ionenimplantierten magnetischen Halbleitern
Dr. H. Reuther Tel.: 0351 260 2898 h.reuther@fzd.de

5. 09/2005 – 02/2010 European Union EU
Fullerene-based opportunities for robust engineering:

Making optimised surfaces for tribology (FOREMOST)
Prof. A. Kolitsch Tel.: 0351 260 3348 a.kolitsch@fzd.de

6. 01/2006 – 06/2010 European Union EU
Ion technology and spectroscopy at low energy ion beam facilities (ITS-LEIF)
Dr. S. Facsko Tel.: 0351 260 2987 s.facsko@fzd.de

7. 04/2006 – 03/2010 European Union EU
Center for application of ion beams to materials research (AIM)
Prof. A. Kolitsch Tel.: 0351 260 3348 a.kolitsch@fzd.de

8. 07/2006 – 10/2009 Deutsche Forschungsgemeinschaft DFG
Magnetische Übergangsmetallschichten auf Piezosubstraten
(Teilprojekt C3 der DFG-Forschergruppe 520: Ferroische Funktionselemente)
Dr. S. Gemming Tel.: 0351 260 2470 s.gemming@fzd.de

9. 12/2006 – 12/2009 VKTA e.V. Dresden Bilateral
Durchführung von REM- bzw. EDX- sowie Mössbauer-spektroskopischen
Untersuchungen an Metallproben
Dr. H. Reuther Tel.: 0351 260 2898 h.reuther@fzd.de

10. 04/2007 – 03/2009 Arbeitsgemeinschaft industrieller Forschungsvereinigungen AiF
Unterdrückung der Sauerstoffversprödung von Titanlegierungen
Prof. A. Kolitsch Tel.: 0351 260 3348 a.kolitsch@fzd.de

11. 04/2007 – 03/2009 Deutsche Forschungsgemeinschaft DFG
Ion-beam induced rippling at the amorphous-crystalline interface in silicon
Dr. J. Grenzer Tel.: 0351 260 3389 j.grenzer@fzd.de

12. 05/2007 – 06/2009 Deutsche Forschungsgemeinschaft DFG
Strukturübergänge eingebetteter magnetischer Nanopartikel
Dr. K. Potzger Tel.: 0351 260 3148 k.potzger@fzd.de

13. 07/2007 – 01/2013 Deutsche Forschungsgemeinschaft DFG
Hybride Magnetische Materialien
Prof. J. Faßbender Tel.: 0351 260 3096 j.faßbender@fzd.de

14. 08/2007 - 07/2009 Arbeitsgemeinschaft industrieller Forschungsvereinigungen AiF
Grenzen des Halogeneffektes für TiAl-Hochtemperaturleichtbaulegierungen unter
industriellen Bedingungen
Prof. A. Kolitsch Tel.: 0351 260 3348 a.kolitsch@fzd.de

15. 08/2007 – 11/2010 Deutsche Forschungsgemeinschaft DFG
Nanostrukturierung von Oberflächen mit direkter Extraktion der Ionen aus Plasmaquellen
Dr. S. Facsko Tel.: 0351 260 2987 s.facsko@fzd.de

16. 08/2007 – 10/2010 Deutsche Forschungsgemeinschaft DFG
Selbstorganisierte Nanostrukturen durch niederenergetische Ionenstrahlerosion
Dr. K.-H. Heinig Tel.: 0351 260 3288 k.h.heinig@fzd.de

17. 08/2007 - 08/2010 Deutsche Forschungsgemeinschaft DFG
Ferromagnetism in transition metal doped ZnO
Dr. H. Schmidt Tel.: 0351 260 2724 heidemarie.schmidt@fzd.de

18. 09/2007 – 08/2009 European Union EU
TEMPUS courses of materials science
Prof. W. Möller Tel.: 0351 260 2245 w.moeller@fzd.de

19. 09/2007 – 10/2010 Deutsche Forschungsgemeinschaft DFG
Infrared scattering near-field optical microscopy near dielectric (polaritonic)
resonances using a free-electron laser
Prof. M. Helm Tel.: 0351 260 2260 m.helm@fzd.de

20. 10/2007 – 08/2009 Alexander-von-Humboldt-Stiftung AvH
Gastaufenthalt Herr Dr. A. Kanjilal
Prof. M. Helm Tel.: 0351 260 2260 m.helm@fzd.de

21. 10/2007 – 09/2009 Dechema Bilateral
Haifischhaut
Prof. A. Kolitsch Tel.: 0351 260 3348 a.kolitsch@fzd.de

22. 11/2007 – 10/2010 Eifeler GmbH Industry
Technologietransfer c-BN II
Prof. A. Kolitsch Tel.: 0351 260 3348 a.kolitsch@fzd.de

23. 12/2007 – 01/2009 Qimonda Dresden GmbH Industry
NanoAnalytik
Dr. J. von Borany Tel.: 0351 260 3378 j.v.borany@fzd.de

24. 01/2008 – 01/2009 IXYS Semiconductor GmbH Industry
Laserannealing
Dr. J. von Borany Tel.: 0351 260 3378 j.v.borany@fzd.de

25. 01/2008 – 12/2009 Deutscher Akademischer Austauschdienst DAAD
Projektbezogener Personenaustausch mit Hong Kong
Dr. W. Skorupa Tel.: 0351 260 3612 w.skorupa@fzd.de

26. 01/2008 – 12/2009 Deutscher Akademischer Austauschdienst DAAD
Projektbezogener Personenaustausch mit Ungarn
Dr. K.-H. Heinig Tel.: 0351 260 3288 k.h.heinig@fzd.de

27. 01/2008 – 12/2009 Deutsche Forschungsgemeinschaft DFG
Bildung, Stabilität und Struktur nanoskaliger Phasen in funktionellen Oxiden und ihre Auswirkung auf die Materialwissenschaft (Oxidkristalle II)
Dr. S. Gemming Tel.: 0351 260 2470 s.gemming@fzd.de

28. 01/2008 – 12/2009 Deutsche Forschungsgemeinschaft DFG
Polarisationsinduzierte Oberflächenfunktionalität an Ferroelektrika
Dr. S. Gemming Tel.: 0351 260 2470 s.gemming@fzd.de

29. 02/2008 – 02/2010 Deutsche Forschungsgemeinschaft DFG
Adsorption von Molekülen an strukturierten Fluid-Feststoff-Grenzflächen
Dr. S. Gemming Tel.: 0351 260 2470 s.gemming@fzd.de

30. 05/2008 – 04/2010 FHR Anlagenbau Ottendorf-Okrilla/IHP Frankfurt/O. Industry
Blitztemperung 200
Dr. W. Skorupa Tel.: 0351 260 3612 w.skorupa@fzd.de

31. 07/2008 – 12/2010 Bundesministerium für Bildung und Forschung BMBF
WTZ Russland: Duplexbehandlung rostfreier Stähle
Prof. A. Kolitsch Tel.: 0351 260 3348 a.kolitsch@fzd.de

32. 07/2008 – 06/2011 Deutsche Forschungsgemeinschaft DFG
Morphologie-induzierte magnetische Anisotropie- und Dämpfungsphänomene
Prof. J. Faßbender Tel.: 0351 260 3096 j.faßbender@fzd.de

33. 07/2008 – 07/2011 Bundesministerium für Bildung und Forschung BMBF
Multifunktionale Speicherkonzepte
Prof. J. Faßbender Tel.: 0351 260 3096 j.faßbender@fzd.de

34. 08/2008 – 02/2009 Deutsche Forschungsgemeinschaft DFG
International Conference on Nonequilibrium Nanostructures
Dr. K. Morawetz Tel.: 0351 260 2470 k.morawetz@fzd.de

35. 09/2008 – 06/2009 AMD Industry
TEM-Untersuchungen
Dr. J. von Borany Tel.: 0351 260 3378 j.v.borany@fzd.de

36. 09/2008 – 12/2010 TU Dresden
Modellieren der Bedeckung keramischer Oberflächen mit Wachstumsproteinen (BIOMIN) BMBF
Dr. S. Gemming Tel.: 0351 260 2470 s.gemming@fzd.de

37. 11/2008 – 02/2009 BASF Ludwigshafen Industry
Ionenimplantation BASF
Prof. A. Kolitsch Tel.: 0351 260 3348 a.kolitsch@fzd.de

38. 11/2009 – 03/2010 Burgmann Industries Wolfratshausen Industry
Abscheidung hochhaftender TiN-Hartstoffschichten
Prof. A. Kolitsch Tel.: 0351 260 3348 a.kolitsch@fzd.de

39. 01/2009 – 12/2009 KETEK GmbH München Industry
Wafer-Prozessierung
Dr. B. Schmidt Tel.: 0351 260 2726 bernd.schmidt@fzd.de

40. 01/2009 – 12/2010 Deutscher Akademischer Austauschdienst DAAD
Projektbezogener Personenaustausch mit Polen
Prof. J. Faßbender Tel.: 0351 260 3096 j.faßbender@fzd.de

41. 02/2009 – 12/2009 Deutsche Forschungsgemeinschaft DFG
Magnetismus von nanoskaligen CoCrPt-SiO_2-Filmen in templatbedingt geometrisch eingeschränkten Dimensionen (Magtemplat)
Prof. J. Faßbender Tel.: 0351 260 3096 j.faßbender@fzd.de

42. 02/2009 – 12/2009 Johannes Kepler Universität Linz Bilateral
Speicherprogrammierte Steuerung
Dr. J. von Borany Tel.: 0351 260 3378 j.v.borany@fzd.de

43. 03/2009 – 06/2009 Sächsisches Staatsministerium für Wissenschaft und Kunst SMWK
Verbesserung der Forschungsinfrastruktur mit Mitteln des Europäischen Fonds für regionale Entwicklung
Prof. A. Kolitsch Tel.: 0351 260 3348 a.kolitsch@fzd.de

44. 03/2009 – 02/2013 European Union EU
Support of Public and Industrial Research using Ion Beam Technology (SPIRIT)
Prof. W. Möller Tel.: 0351 260 2245 w.moeller@fzd.de

45. 03/2009 – 08/2011 European Union EU
European Light Sources Activities: Synchrotrons and Free Electron Lasers (ELISA)
Prof. M. Helm Tel. 0351 260 2260 m.helm@fzd.de

46. 05/2009 – 04/2010 Alexander-von-Humboldt-Stiftung AvH
Gastaufenthalt Frau Dr. J. Bhattacharyya
Dr. H. Schneider Tel.: 0351 260 2880 h.schneider@fzd.de

47. 05/2009 – 04/2011 Bundesministerium für Bau, Verkehr und Stadtentwicklung BMBVS
FZD-Applikationslabor Ionentechnologie
Prof. A. Kolitsch Tel.: 0351 260 3348 a.kolitsch@fzd.de

48. 06/2009 – 05/2012 Bundesministerium für Bildung und Forschung BMBF
Rezeptor-selektive Anreicherung und Bio-LED-Sensorik zur qualitativen und quantitativen Detektion von (anti-) östrogen- und (anti-) androgenwirkenden Substanzen (Bio-LED-Sensorik)
Dr. L. Rebohle Tel.: 0351 260 3368 l.rebohle@fzd.de

49. 07/2009 – 12/2009 GLOBALFOUNDRIES Dresden Industry
TEM-Untersuchungen
Dr. J. von Borany Tel.: 0351 260 3378 j.v.borany@fzd.de

50. 07/2009 – 06/2011 Deutscher Akademischer Austauschdienst DAAD
Projektbezogener Personenaustausch mit Großbritannien
Prof. J. Faßbender Tel.: 0351 260 3096 j.faßbender@fzd.de

51. 07/2009 – 06/2011 TU Bergakademie Freiberg Bilateral
Eigenschaften nano- und mikrokristalliner Si-Dünnfilme
Dr. W. Skorupa Tel.: 0351 260 3612 w.skorupa@fzd.de

52. 09/2009 – 02/2011 Alexander-von-Humboldt-Stiftung AvH
Gastaufenthalt Herr Dr. A.S. El-Said
Dr. S. Facsko Tel.: 0351 260 2987 s.facsko@fzd.de

53. 09/2009 – 08/2012 Deutsche Forschungsgemeinschaft DFG
Bestimmung der lagespezifischen und räumlich aufgelösten elektronischen Struktur um Punktdefekte in Kristallen aus dem Streufaktortensor für Röntgenstrahlung unter resonanter Anregung
Dr. S. Gemming Tel.: 0351 260 2470 s.gemming@fzd.de

54. 11/2009 – 04/2010 Wilhelm- und Else-Heraeus-Stiftung WEH
Physikschule zur Festkörper-DFT an der RWTH Aachen (7.-11.02.2010)
Dr. S. Gemming Tel.: 0351 260 2470 s.gemming@fzd.de

Experimental Equipment

1. Accelerators, Ion Implanters and Ion-Assisted-Deposition

⇒	Van de Graaff Accelerator	(VdG)	1.8 MV	*TuR Dresden, DE*
⇒	Tandem Accelerator	(Td)	5 MV	*NIIEFA, RU*
⇒	Tandetron Accelerator	(Tdt)	3 MV	*HVEE, NL*
⇒	Tandetron Accelerator (commissioning)		6 MV	*HVEE, NL*
⇒	Low-Energy Ion Implanter		0.5 - 50 kV	*Danfysik, DK*
⇒	High-Current Ion Implanter		20 - 200 kV	*Danfysik, DK*
⇒	High-Energy Ion Implanter		40 - 500 kV	*HVEE, NL*
⇒	Plasma Immersion Ion Implantation		5 - 60 keV	*GBR, DE/Home-built*
⇒	Focused Ion Beam (15 nm, variable ions)		30 keV, 10 A/cm^2	*Orsay Physics, FR*
⇒	Highly-Charged Ion Facility		25 eV – 25 keV × Q Q = 1…40 (Xe)	*Home-built*
⇒	Dual-Beam Magnetron Sputter Deposition			*Roth & Rau, DE*
⇒	Ion-Beam-Assisted Deposition			*Danfysik, DK*
⇒	Ion-Beam Sputtering		200 - 2000 V	*Home-built*
⇒	UHV Ion Irradiation (Ar, He, etc.)		0 - 5 keV Scan 10×10 mm^2	*VG, USA*

2. Ion Beam Analysis (IBA)

A wide variety of advanced IBA techniques are available at the MeV accelerators (see figure).

⇒	RBS	Rutherford Backscattering	(1), (2), (3), (8)	*VdG, Td, Tdtr*
⇒	RBS/C	RBS + Channelling	(1), (2), (3), (8)	*VdG, Td, Tdtr*
		High-Resolution RBS/C	(7), (10)	*Tdtr*
⇒	ERDA	Elastic Recoil Detection Analysis	(2), (4), (5)	*VdG, Td*
		High-resolution ERDA	(7)	*Td*
⇒	PIXE	Proton-Induced x-ray Emission	(3)	*Td*
⇒	PIGE	Proton-Induced γ Emission	(3)	*Td*
⇒	NRA	Nuclear Reaction Analysis	(4)	*Td*
⇒	NRRA	Nuclear Resonance Reaction Analysis	(6)	*Td*
⇒	NμP	Nuclear Microprobe	(9)	*Tdtr*
⇒	AMS	Accelerator Mass Spectrometry	(commissioning)	
		(focused to cosmogenic radionuclides:	^{10}Be, ^{26}Al, ^{36}Cl, ^{41}Ca, ^{129}J	

Some stations are equipped with additional process facilities which enable *in-situ* IBA investigations during ion irradiation, sputtering, deposition, annealing etc.

3. Other Particle Based Analytical Techniques

⇒	SEM	Scanning Electron Microscope	1 - 30 keV + EDX	*Hitachi, JP*
⇒	TEM	Transmission Electron Microscope (Titan 80-300 with Image Corrector)	80 - 300 keV + EDX, +GIF	*FEI, NL*
⇒	FIB/SEM	Focused Ion / Electron Cross Beam (NVision 40 with Elphy Plus Litho)	0.5 – 30 keV + IL, + EDX	*Zeiss-NTS, DE* *Raith, Bruker, DE*
⇒	AES	Auger Electron Spectroscopy	+ XPS	*Fisions, UK*
⇒	CEMS	Mössbauer Spectroscopy	^{57}Fe source	*Home-built*
⇒	PAS	Positron Annihilation Spectroscopy	^{22}Na source 30 V - 36 kV	*Home-built*

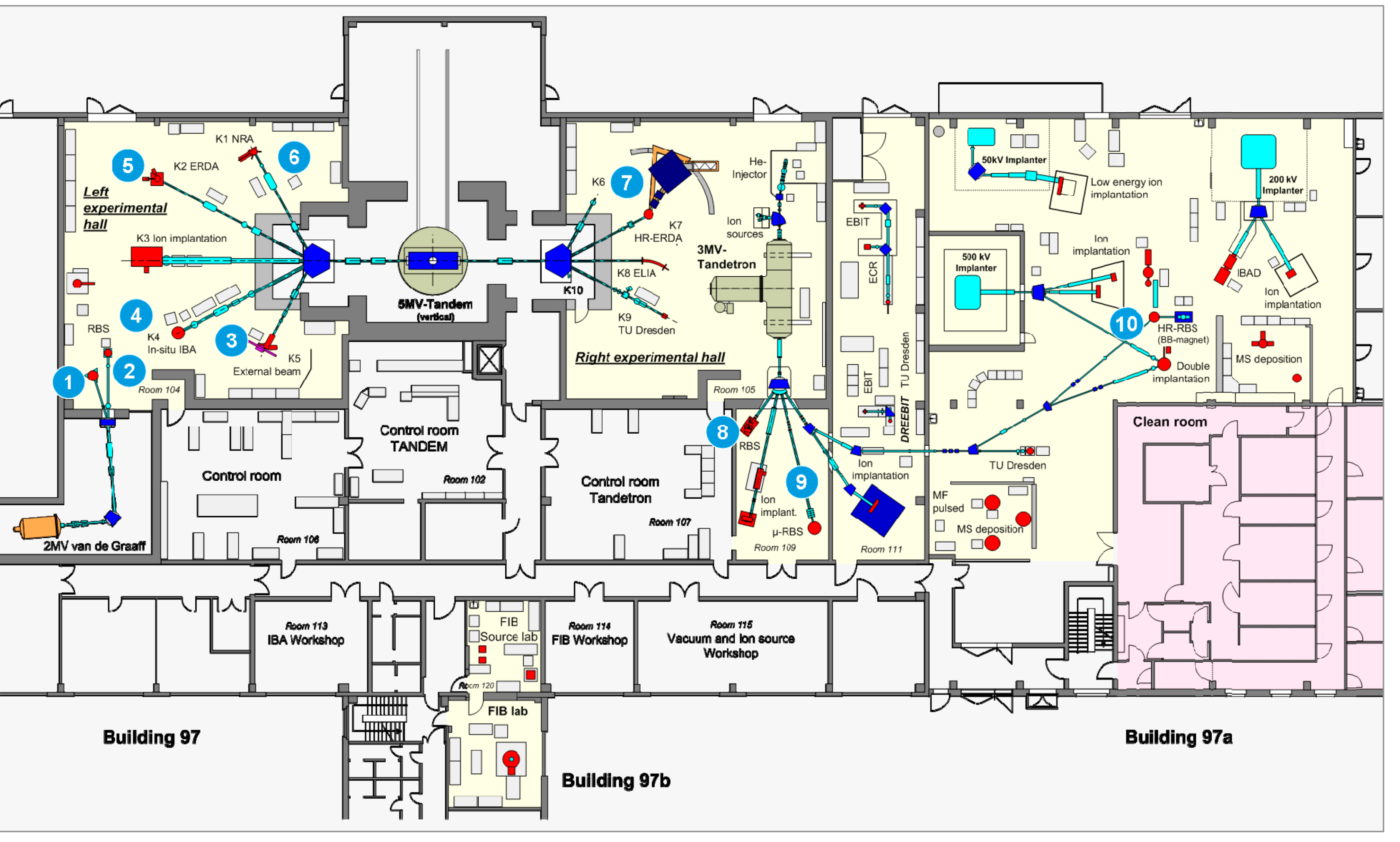

Ion Beam Centre: Schematic Overview of Installations.

4. Photon Based Analytical Techniques

⇒	XRD/XRR	X-Ray Diffraction and Reflection	$Cu-K_{\alpha}$	*Bruker axs, DE*
	HR-XRD	High-Resolution XRD	$Cu-K_{\alpha}$	*GE Inspection, DE*
⇒	XRD/XRR	with Synchrotron Radiation	5 – 35 keV	*ROBL at ESRF, FR*
⇒	SE	Spectroscopic Ellipsometry	250 - 1700 nm	*Woolam, US*
⇒	FTIR	Fourier-Transform Infrared Spectr.	600 - 7000 cm^{-1}	*Nicolet, US*
⇒	FTIR	Fourier-Transform Infrared Spectr.	50 - 15000 cm^{-1}	*Bruker, DE*
⇒		Ti:Sapphire Femtosecond Laser		*Spectra Physics, US*
⇒		Femtosecond Optical Parametric Osci.		*APE, DE*
⇒		Ti:Sapphire Femtosecond Amplifier		*Femtolasers, AT*
⇒		Femtosecond Optical Parametric Amplifier		*Light Conversion, LI*
⇒	THz-TDS	Terahertz Time-Domain Spectroscopy	0.1 - 4 THz	*Home-built*
⇒	Raman	Raman Spectroscopy	45 cm^{-1} shift	*Jobin-Yvon-Horiba, FR*
⇒	PL	Photoluminescence	300 - 1500 nm	*Jobin-Yvon-Horiba, FR*
⇒	TRPL	Time-Resolved PL	τ = 3 ps - 2 ns	*Hamamatsu Phot., JP*
			τ > 5 ns	*Stanford Research, US*
⇒	EL	Electroluminescence (10-300 K)	300 - 1500 nm	*Jobin-Yvon-Horiba, FR*
		Optical Split-Coil Supercond. Magnet	7 T	*Oxford Instrum., UK*
⇒	PR	Photomodulated Reflectivity	300 - 1500 nm	*Jobin-Yvon-Horiba, FR*
⇒	PLE	Photoluminescence Excitation	300 - 1500 nm	*Jobin-Yvon-Horiba, FR*

5. Magnetic Thin Film Deposition and Analysis

⇒	MBE	Molecular Beam Epitaxy with in-situ FIB		*CreaTec, DE*
⇒	MBE	Molecular Beam Epitaxy		*Home-built*
⇒	PLD	Pulsed Laser Deposition		*SURFACE, DE*
⇒	MFM	Magnetic Force Microscope	~ 50 nm resol.	*VEECO / DI, US*
⇒	SQUID	Supercond. Quantum Interf. Device	± 7 T	*Quantum Design, US*
⇒	MOKE	Magneto-Optic Kerr Effect (in-plane)	± 0.35 T	*Home-built*
⇒	MOKE	Magneto-Optic Kerr Effect (perpend.)	± 2 T	*Home-built*
⇒	SKM	Scanning Kerr Microscope		*Home-built*
⇒		Kerr Microscope		*Evico Magnetics, DE*
⇒	TR-MOKE	Time-Resolved MOKE (Pump-Probe)		*Home-built*
⇒	VNA-FMR	Vector Network Analyzer Ferromagnetic Resonance		*Agilent / Home-built*
⇒	ME	Magnetoellipsometer		*LOT, DE; AMAC, US*

6. Other Analytical and Measuring Techniques

⇒	STM	Scanning Tunneling Microscope (with AFM-Option)		*DME, DK*
⇒	STM	*In-situ* Scanning Tunneling Microscope (T variable)		*Omicron, DE*
⇒	AFM	Atomic Force Microscope (Tapping Mode)		*SIS, DE*
⇒	AFM	Atomic Force Microscope (with c-AFM, SCM-Module)		*Veeco Instruments, UK*
⇒	KFM	Kelvin Probe Force Microscopy		*Anfatec, DE*
⇒		Dektak Surface Profilometer		*Veeco, US*
⇒		Micro Indenter / Scratch Tester		*Shimatsu, JP*
⇒		Wear Tester (pin-on disc)		*Home-built*
⇒	HE	Hall Effect Equipment	(2 - 400 K, ≤ 9 T)	*LakeShore, US*
⇒	RS	Sheet-Rho-Scanner		*AIT, South Korea*
⇒	DLTS	Deep Level Transient Spectroscopy	(+ I-U / C-V) (10 - 300 K, 1 MHz)	*PhysTech, DE*
⇒		Photocapacitance (+I-U/G-V)	(250 - 2500 nm)	*Home-built*
⇒		I-V and C-V Analyzer		*Keithley, US*

⇒	I-V and C-V Semi-Automatic Prober	(-60 – 300°C)	*Süss, DE; Keithley, US*
⇒	I-V Prober	(4.2 – 600 K)	*LakeShore, Agilent, US*

7. Processing and Preparation Techniques

⇒	Physical Deposition	Sputtering DC / RF, Evaporation	*Nordiko, UK*
		Electron Beam Evaporation System	*Leybold Optics, DE*
		Thermal Evaporation	*Bal-Tec, LI*
⇒	Chemical Deposition	Plasma Enhanced CVD (for a-Si, SiO_2, SiON, Si_3N_4)	*Oxford Instruments, UK*
⇒	Dry Etching	Plasma and RIE Mode	*Sentech, DE*
⇒	Reactive Ion Beam Etching	∅ 6”, Ar, CF_4	*Roth & Rau, DE*
⇒	Etching / Cleaning	incl. Anisotropic Selective KOH Etching	
⇒	Photolithography	Mask-Aligner, 2 µm-level	*Süss, DE*
⇒	Electron Beam Lithography	Raith 150-TWO: ∅ 6”, 10 nm res.	*Raith, DE*
⇒	Thermal Treatment	Room Temperature - 2000°C	
	• Furnace		*InnoTherm, DE*
	• Rapid Thermal Annealing		*ADDAX, FR*
	• Flash-Lamp Units (0.5 – 20 ms)		*Home-built; FHR, DE*
	• RF Heating (Vacuum)		*JIP.ELEC, FR*
⇒	Bonding Techniques	Ultrasonic Wire Bonding	*Kulicke & Soffa, US*
⇒	Cutting, Grinding, Polishing		*Bühler, DE*
⇒	TEM Sample Preparation	Plan View and Cross Section incl. Ion Milling Equipment	*Gatan, US*

SPIRIT

The Institute of Ion Beam Physics and Materials Research is coordinating the Integrated Infrastructure SPIRIT under the FP7 Capacities Programme of the European Union. The duration of the project is from March 2009 to February 2013, the total funding is 6.991.000 €.

SUPPORT OF PUBLIC AND INDUSTRIAL RESEARCH USING ION BEAM TECHNOLOGY

Integrated Activity,
EU Project No. 227012
www.spirit-ion.eu

SPIRIT integrates 11 leading ion beam facilities from six European Member States and two Associated States. Seven of the partners provide Transnational Access to European researchers and industry at their infrastructures. Ion beams in an energy range from ~10 keV to ~100 MeV are supplied for modification and analysis of solid surfaces, interfaces, thin films and nanostructured systems, being mainly applied in research related to materials, biomedicine, environment, and cultural heritage. SPIRIT aims at increasing user access and the quality of research by sharing best practice, balancing supply and demand, harmonizing procedures and extending the services into new emerging fields and to new users especially from the New European Member States and industry. The project comprises a management section (4% of the total funding) and three interlinked activities, which are Transnational Access (45%), Networking (19%) and Joint Research (32%).

Analysis Techniques		Materials Modification Techniques	
Rutherford Backscattering Spectrometry	RBS	Ion Implantation	II
Elastic Recoil Detection	ERD	High-Energy Ion Irradiation	HEIR
High-Resolution Ion Beam Analysis	HRIBA	Plasma-Immersion-Ion-Implantation	PIII
Proton-Induced X-ray (γ-ray) Emission	PIXE/ PIGE	Ion Beam Lithography	IBL

Potential users from public of industrial research are invited for free use of the ion beam facilities at the SPIRIT partners laboratories, either by conducting experiments personally or by sending samples in case of standard ion implantation or ion beam materials analysis. Regularly, access is given on a transnational basis, i.e. the user has to be employed in a European Member or Associate State in which the specific infrastructure is not situated. However, there are exceptions in particular in case of industrial use and/or non-conventional use of ion technologies.

Proposals may be turned in continuously through the SPIRIT website and will be evaluated promptly by an international User Selection Panel. Any successful proposer will be granted free access to the infrastructure, with the associated travel costs and daily expenses being covered by the European Commission.

Until 31-March-2010, the institute is still providing Transnational User Access under the FP6 project AIM, which then will be followed up by access under SPIRIT.

The SPIRIT Consortium

Forschungszentrum Dresden-Rossendorf	Germany
CNRS – CENBG Bordeaux	France
Katholieke Universiteit Leuven	Belgium
Jozef Stefan Institut Ljubljana	Slovenia
Universität der Bundeswehr München	Germany
CEA – JANNUS Saclay and CIMAP Caen	France
University of Surrey	U.K.
Institute Tecnologico e Nuclear Lisboa	Portugal
University de Pierre et Marie Curie Paris	France
Ruder Boskovic Institute Zagreb	Croatia
Swiss Federal Institute of Technology Zurich	Switzerland

(The top seven partners provide Transnational Access)

Free Electron Laser FELBE

ELBE is an acronym for the free-electron laser (FEL) at the Electron Linear accelerator with high Brilliance and Low Emittance (ELBE) located at the Forschungszentrum Dresden-Rossendorf, Germany. The heart of ELBE is a superconducting linear accelerator operating in cw mode with a pulse repetition rate of 13 MHz. The electron beam (40 MeV, 1 mA max.) is guided to several laboratories where secondary beams (particle and electromagnetic) are generated. Two free-electron lasers (U27-FEL and U100-FEL) produce intense, coherent electromagnetic radiation in the mid and far infrared, which is tunable over a wide wavelength range (4 – 250 µm) by changing the electron energy or the undulator magnetic field. Main parameters of the infrared radiation produced by FELBE are as follows:

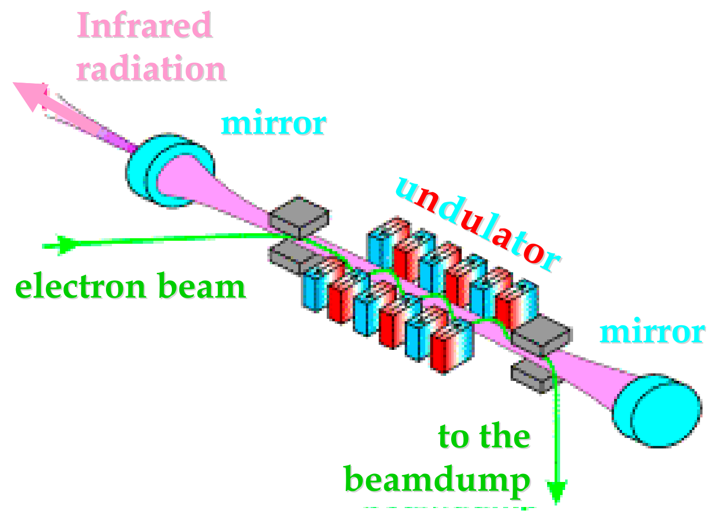

Parameter	Range / Value	Remarks
Wavelength	4 - 22 µm 18 – 250 µm	FEL with undulator U27 FEL with undulator U100
Pulse energy	0.01 – 2 µJ	depends on wavelength
Pulse length	1 – 25 ps	depends on wavelength
Repetition rate	13 MHz	3 modes: cw / macropulsed (> 100 µs, < 25 Hz) / single pulsed (Hz…kHz)

The free electron laser is a user facility. Applications for beam time can be submitted twice a year, typically by April, 15 and October, 15. User from EU countries can receive support through the FP7 Integrated Infrastructure Initiative (I3) ELISA (**E**uropean **LI**ght **S**ources **A**ctivities). Typical applications are picosecond pump-probe spectroscopy (also in combination with several other femtosecond lasers, which are synchronized to the FEL), near-field microscopy and nonlinear optics. The FELBE facility also serves as a far-infrared source for experiments at the High-Field Laboratory Dresden (HLD) involving pulsed magnetic fields up to 70 Tesla.

The statistics shows that the FEL used 2136 hours beamtime of the ELBE accelerator, which corresponds to 40% of total beamtime. These 40% were again distributed among internal and external users as shown in the graph.

For further information please contact Prof. Manfred Helm (m.helm@fzd.de) or visit the FELBE webpage www.fzd.de/FELBE.

Beamtime Distribution at ELBE 2009
Scheduled: 5.412 h; Used: 4.395 h

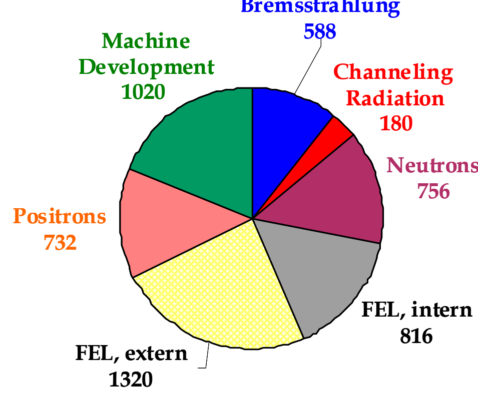

ROBL

The **RO**ssendorf **B**eam**L**ine (ROBL), operated by the FZD since 1998, is a bending magnet synchrotron beam line located at the European Synchrotron Radiation Facility (ESRF) in Genoble, France. The set-up and main parameters are sketched as follows:

Energy range	6 – 35 keV
Energy resolution	$< 5x10^{-4}$
Photon flux density	$8x10^9$ phot./(s·mm²)
Divergence	(0.08 x 2.5) mrad
Beam size (typ.)	(0.4 x 5) mm²

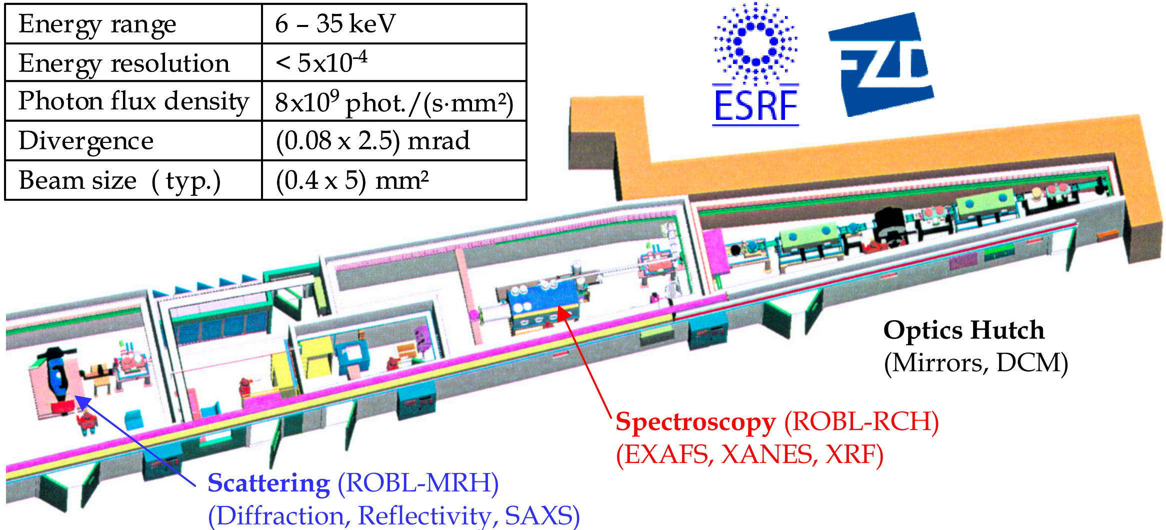

The activeness of ROBL is based upon the high specialization of its two end-stations for Radiochemistry (RCH) and Materials Research (MRH). ROBL-RCH is one of only two stations in Europe dedicated to X-ray absorption spectroscopy of actinides and other radionuclides. The core competence of ROBL-MRH is the analysis of thin films, multilayers and (ion-beam-synthesized) nanostructures using X-ray scattering techniques. A continuously increasing number of experiments are performed as *in-situ* X-ray studies using process chambers for magnetron sputter deposition, ion irradiation or annealing under vacuum or various (including reactive) atmospheres, respectively. Non-destructive X-ray analysis during materials processing is applied to characterize the formation or transformation of crystalline phases, their texture, the evolution of nanostructures, surfaces and interfaces properties or strain/stress development at thin films. These data are the key to understand the underlying physical or chemical processes and to interpret the corresponding macroscopic materials properties with the general aim to design materials with well defined properties.

ROBL has the status of an user facility. Applications for ROBL beam time can be submitted twice a year, typically by March, 1 and September, 1 via the official ESRF proposal submission portal. Successfully reviewed proposals will be financially supported by the ESRF by covering the travel and accommodation costs. In addition, there is the possibility to use in-house research beam time for collaborative experiments between external users and FZD scientists for studies of common interest.

With more than 5000 beam time hours per year ROBL belongs to the most reliable and booked beam lines at the ESRF. The diagram at the right plots the beam time distribution of ROBL which reveal an availability of about 90% for experimental research studies. In 2009 visitors from more than 20 European and Overseas Universities and Research Institutions were involved in ROBL experiments.

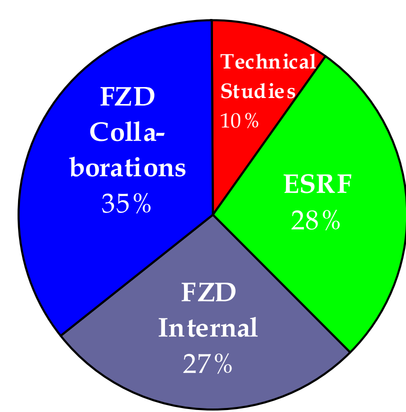

For further information please contact

Dr. A. Scheinost (ROBL-RCH): scheinost@esrf.fr
Dr. C. Bähtz (ROBL-MRH): baehtz@esrf.fr

or visit the ROBL webpage www.fzd.de/ROBL.

Services

Main Areas of Competence:

- Ion implantation in a broad range of ion energy (~ 200 eV to ~ 50 MeV) and substrate temperature
- Advanced ion beam technologies (high energy ion implantation, plasma immersion ion implantation, focused ion beam) for (micro)electronic applications
- Deposition of functional coatings using ion-assisted physical vapor deposition
- Development and fabrication of sensors and detectors for charged particle spectroscopy
- High energy ion implantation service for power devices and laser structures
- Doping of semiconductors, in particular wide bandgap semiconductors
- Surface analysis of solid materials with high energy ion beams
- Optical characterization of materials (luminescence, FTIR, Raman)

Offers:

- Consultation and problem evaluation for ion beam applications
- Process development for ion beam processing of metals, ceramics, semiconductors, thin films
- Preparation and treatment of material samples, tools or complex parts of devices
- Ion implantation and ion beam analysis services
- Electron beam lithography and focused ion beam patterning
- Fabrication of silicon radiation sensors under clean room conditions
- Structural diagnostics of materials including e-beam and X-ray techniques

Contact:

Please direct your inquiry about the application of ion beams for modification and analysis of materials to one of the following experts:

Field of application	Name	Phone / Fax	E-mail
Ion implantation (metals, ceramics, polymers, biomaterials)	Prof. Andreas Kolitsch	3348 / 2703	a.kolitsch@fzd.de
Ion implantation (semiconductors, in particular high energy)	Dr. Johannes von Borany	3378 / 3438	j.v.borany@fzd.de
Thin film deposition	Prof. Andreas Kolitsch	3348 / 2703	a.kolitsch@fzd.de
High energy ion beam analysis	Dr. Silke Merchel	2802 / 3701	s.merchel@fzd.de
Semiconductor preparation Detector / Sensor fabrication	Dr. Bernd Schmidt	2726 / 3285	bernd.schmidt@fzd.de
Electron beam lithography	Dr. Artur Erbe	2366	a.erbe@fzd.de
Focused ion beams	Dr. Lothar Bischoff	2963 / 3285	l.bischoff@fzd.de
Structural diagnostics	Dr. Johannes von Borany	3378 / 3438	j.v.borany@fzd.de
Materials research with Synchrotron radiation at ROBL (ESRF)	Dr. Carsten Bähtz	2367	baehtz@esrf.fr
Optical materials characterization	Dr. Harald Schneider	2880 / 3285	h.schneider@fzd.de

For all phone/ fax-numbers choose the country / local code: +49 351 260 - xxxx (for FZD)
+33 47 688 - xxxx (for ROBL)

The institute also recommends the homepages of its spin-off companies

- "GeSiM mbH" Si- Mikrosysteme www.gesim.de
- "APT Dresden" Angewandte Pulstechnik www.apt-dresden.de
- "DFT GmbH" Dünnschichttechnologie www.dtf-technology.de

Forschungszentrum Dresden - Rossendorf e.V.

Institute of Ion Beam Physics and Materials Research (IIM)

P.O. Box 51 01 19
01314 Dresden

Phone: +49 351 260 2245
Fax: + 49 351 260 3285
http://www.fzd.de/FWI

DIRECTORS

Prof. Dr. Wolfhard Möller / Prof. Dr. Manfred Helm / Prof. Dr. Jürgen Faßbender
2245 / 2260 / 3096

DIVISIONS

ION TECHNOLOGY
(FWII)
Prof. Dr. Andreas Kolitsch / 3326

- MeV accelerators
- Ion Implanter / PIII operation
- Ion Beam and Plasma Assisted Deposition
- Biotechnological Materials
- Industrial Services and Projects

SEMICONDUCTOR MATERIALS
(FWIM)
Dr. Wolfgang Skorupa / 3612

- Semiconductors
- Optoelectronic Applications
- Rapid Thermal Annealing Processes
- Defect Engineering
- Positron Annihilation Spectroscopy

NANOFUNCTIONAL FILMS
(FWIN)
Prof. Dr. Jürgen Faßbender / 3096

- Modification of Magnetic Materials
- High Anisotropy Nanoparticles
- Magnetic Semiconductors / Spintronics
- Magnetization Dynamics
- Fullerene-like Materials

SEMICONDUCTOR SPECTROSCOPY
(FWIH)
Dr. Harald Schneider / 2880

- Semiconductor Quantum Structures
- Terahertz Spectroscopy
- Femtosecond Spectroscopy
- Free Electron Laser at ELBE
- Optical Characterization (PL, FTIR, Raman)

ION BEAM ANALYSIS
(FWIA)
Dr. Silke Merchel / 2802

- Ion-Solid-Interaction
- High-Energy Ion Beam Analysis
- Accelerator Mass Spectrometry
- Non-destructive Analysis of Art Objects
- Composition / Modification of Materials

STRUCTURAL DIAGNOSTICS
(FWIS)
Dr. Johannes von Borany / 3378

- Electron Microscopy (TEM, SEM)
- Electron Spectroscopy (AES, XPS)
- Mössbauer Spectroscopy
- X-ray Analysis
- Materials Research with Synchr. Radiation

THEORY
(FWIT)
Dr. Matthias Posselt / 3279

- Ion-Beam Synthesis of Nanostructures
- Formation and Evolution of Defects
- Atomistic Simulation of Ion implantation and Ion-Assisted Deposition
- Interatomic Potentials for Solids Reaction-Diffusion-Models

PROCESS TECHNOLOGY
(FWIP)
Dr. Bernd Schmidt / 2726

- Semiconductor Technology
- Focused Ion Beam Technology
- Thin Film Deposition
- Computer Aided Structure Design
- Electrical Characterization
- Clean Room Operation

List of Personnel 2009

Directors:

Prof. W. Möller
Prof. M. Helm
Prof. J. Faßbender

Office:

S. Kirch, L. Post, A. Schiemann

Scientific Staff:

Permanent:

Dr. G. Abrasonis
Dr. C. Akhmadaliev
Dr. C. Bähtz
Dr. L. Bischoff
Dr. J. von Borany
Dr. S. Facsko
Dr. S. Gemming
Dr. J. Grenzer
Dr. V. Heera
Dr. K.-H. Heinig
Dr. R. Kögler
Prof. A. Kolitsch
Dr. S. Merchel
Dr. A. Mücklich
Dr. F. Munnik
Dr. C. Neelmeijer
Dr. M. Posselt
Dr. K. Potzger
Dr. L. Rebohle
Dr. H. Reuther
Dr. B. Schmidt
Dr. H. Schneider
Dr. W. Skorupa
Dr. D. Stehr
Dr. M. Voelskow
Dr. S. Winnerl

Post Docs:

Dr. R. Heller
Dr. N. Jeutter
Dr. G. Kovacs
Dr. K. Lenz

Projects:

Dr. J. Bhattacharyya
Dr. C. Bunce
Dr. W. Bürger
Dr. O. Drachenko
Dr. A. S. El-Said
Dr. A. Erbe
Dr. M. Friedrich
Dr. D. Grambole
Dr. R. Grötzschel
Dr. J. Grebing
D. Henke
Dr. A. Kanjilal
Dr. M. Krause
Dr. M. O. Liedke
Dr. K. Morawetz
Dr. J. Neidhart
V. Pankoke
Dr. W. Pilz
Dr. S. Prucnal
D. Reichel
Dr. A. Rogozin
Dr. H. Schmidt
Dr. A. Shalimov
Dr. N. Shevchenko
Dr. M. Vinnichenko
Dr. R. Yankov
Dr. S. Zhou
Dr. M. Zier

PhD Students:

D. Ball
C. Baumgart
M. Berndt
K. Bernert
M. Buhl
D. Bürger
V. Cantelli
C. Cherkouk
S. Cornelius
M. Fritsche
A. Hanisch
M. Höwler
R. Jacob
A. Keller
M. Körner
M. Kosmata
T. Kunze
J. Lehmann
B. Liedke
D. Markó
A. Martinavicius
K. M. Mok
S. Numazawa
X. Ou
F. Peter
J. Potfajova
M. Ranjan
H. G. von Ribbeck
O. Roshchupkina
C. Scarlat
M. Schmidt
M. Seeger
T. Strache
G. Talut
M. Thieme
A. Thorn
M. Vieluf
M. Wagner
S. Wintz
C. Wündisch
J. Zhou
M. Zschintzch
M. Zschornak
S. Zybell

Diploma Students:

F. Fischer
S. Germer
R. Hubrich
J. König
A. Mrotzek
J. Osten
P. Philipp
E. Ritter
T. Schönherr
R. Wiemann
M. Wieser
C. Wilde

Technical Staff:

Permanent:

Rb. Aniol
Ry. Aniol
E. Christalle
H. Felsmann
B. Gebauer
H.-J. Grahl
D. Hanf
J. Haufe
A. Henschke
M. Kiebler
S. Klare
J. Kreher
A. Kunz
H. Lange
U. Lucchesi
F. Ludewig
R. Mester
M. Mißbach
C. Neisser
S. Probst
A. Reichel
M. Roch
B. Scheumann
G. Schnabel
A. Schneider
J. Schneider
A. Scholz
T. Schumann
M. Steinert
U. Strauch
K. Thiemig
A. Vetter
J. Wagner
R. Weidauer
A. Weise
J. Winkelmann
U. Strauch
G. Winkler
I. Winkler
L. Zimmermann
J. Zscharschuch

Projects:

S. Eisenwinder
V. Kühn
I. Skorupa
A. Weißig